Investigation of Background from the Inter-Spectrometer Penning Trap and Secondary Electron Emission in the KATRIN Experiment

Luke Kippenbrock

A dissertation
submitted in partial fulfillment of the
requirements for the degree of

Doctor of Philosophy

University of Washington

2019

Reading Committee:

Diana S. Parno, Chair

Jason Detwiler

Sanshiro Enomoto

Gerald Miller

Program Authorized to Offer Degree:
Physics

University of Washington

Abstract

Investigation of Background from the Inter-Spectrometer Penning Trap and Secondary Electron Emission in the KATRIN Experiment

Luke Kippenbrock

Chair of the Supervisory Committee:
Affiliate Assistant Professor Diana S. Parno
Department of Physics

The KATRIN experiment aims to determine the neutrino mass with unprecedented precision by measuring the tritium β-decay spectrum with a tandem of MAC-E-filter spectrometers. The background rate measured at the β-detector is a crucial parameter affecting the sensitivity of the experiment. The detector energy resolution affects the intrinsic background contribution from the detector system and, therefore, must be well-characterized. Additionally, the increased size of the main spectrometer compared with predecessor experiments necessitates understanding and quantifying various sources of background electrons originating from the spectrometer.

Secondary electron emission from the inner spectrometer surface, induced by environmental gamma radiation and cosmic-ray muons, is investigated as a potentially large source of background electrons. A background source unique to the beamline geometry of KATRIN is the inter-spectrometer Penning trap formed during tandem operation of the spectrometers. Detailed measurements and simulations were performed to quantify the background induced by the Penning trap and to confirm the electron-production model. However, by maintaining ultra-high vacuum conditions inside the spectrometers, the effect of the trap on the total background rate is found to be insignificant compared with contributions from other sources.

TABLE OF CONTENTS

LIST OF FIGURES

LIST OF TABLES

LIST OF ABBREVIATIONS

ΛCDM Lambda cold dark matter

ADC analog-to-digital converter

CMB cosmic microwave background

CPS Cryogenic Pumping Section

DAQ data acquisition

DET detector magnet

DPS Differential Pumping Section

ELIOTT ELectron impact Ion source to Test the Transport section

ELOG Electronic Logbook

EMCS Earth Magnetic field Compensation System

ENC equivalent noise charge

FBM Forward Beam Monitor

FPD Focal Plane Detector

FWHM full width at half maximum

HPGe high-purity germanium

HV High Voltage

IE inner electrode

KATRIN KArlsruhe TRItium Neutrino experiment

KIT Karlsruhe Institute of Technology

LFCS Low Field Correction System

MAC-E Magnetic Adiabatic Collimation with an Electrostatic filter

MoS Monitor Spectrometer

MS Main Spectrometer

NEG non-evaporable getter

ORCA Object-oriented Real-time Control and Acquisition

PAE post-acceleration electrode

PCH pinch magnet

PDG Particle Data Group

PID particle identification

PMT photomultiplier tube

PS Pre-Spectrometer

PS1 first Pre-Spectrometer magnet

PS2 second Pre-Spectrometer magnet

PULCINELLA Precision Ultra-Low Current Integrating Normalization Electrometer for Low-Level Analysis

RGA residual gas analyzer

RMS root mean square

ROI region of interest

RS Rear Section

SDS Spectrometer and Detector Section

SDS-I first SDS commissioning phase

SDS-II second SDS commissioning phase

SDS-IIa second SDS commissioning phase, part A

SDS-IIb second SDS commissioning phase, part B

SDS-III third SDS commissioning phase

SDS-IIIa third SDS commissioning phase, part A

SDS-IIIb third SDS commissioning phase, part B

SDS-IIIc third SDS commissioning phase, part C

SE secondary electron

STS Source and Transport Section

STS-IIIa STS commissioning phase IIIa

TLK Tritium Laboratory Karlsruhe

TMP turbo-molecular pump

UHV ultra-high vacuum

UW University of Washington

WGTS Windowless Gaseous Tritium Source

XML Extensible Markup Language

ACKNOWLEDGMENTS

I must first express my indebtedness to Diana Parno, who has faithfully advised me through all the vicissitudes of graduate school. Her patience and tireless comments allowed this thesis to come to fruition.

I would like to thank Hamish Robertson, for accepting me into the KATRIN group at CENPA. I am also grateful for Peter Doe, Sanshiro Enomoto, and Eric Martin for their assistance on a multitude of fronts. Additionally, I am thankful for the oversight and suggestions provided by Florian Fränkle during my stays at KIT, without whom large portions of this thesis would not have been possible. Many other KATRIN collaborators have also supported my work in a number of ways, but I will refrain from trying to name them all, lest I forget any.

I want to thank my parents, Stanley and Kathy, for their unfailing love and support. My siblings have also continuously provided motivation for me to finish my degree. Finally, I need to thank the guys in my men's group, who have provided an essential social and human dimension to my time in Seattle. I would not have reached this point without all their encouragement.

The work presented in this thesis was funded by the United States Department of Energy under grant #DE-FG02-97ER41020.

AMDG

DEDICATION

To my parents, Stanley and Kathy

Chapter 1

NEUTRINO PHYSICS

In this chapter, the formulation and detection of the electron (anti-)neutrino is presented, as well as an overview of neutrinos in the Standard Model. The discovery and theory of neutrino oscillations are then described, with particular focus given to the implication of non-zero neutrino mass. Finally, experimental attempts to measure the neutrino mass are described, with β-decay experiments given additional attention.

1.1 Formulation and Discovery

1.1.1 Motivation for the Neutrino

By the 1920s, it was believed that nuclear structure could be explained by two massive particles, the proton and the electron [1]. For a neutral atom with atomic mass A and atomic number Z, the nucleus was thought to consist of A protons and $A - Z$ electrons, with Z electrons in the atomic shell. In β^- decay, it was observed that the nucleus emitted a β-electron and changed its atomic number from Z to $Z + 1$:

$$^{A}_{Z}\mathrm{X} \ \rightarrow \ ^{\ \ A}_{Z+1}\mathrm{X} \ + \ \beta^- \tag{1.1}$$

Such a decay could be explained by the escape of an electron from the nucleus. However, measurements of the energy of the emitted β-particle indicated a continuous energy spectrum; such a result is incompatible with the kinematics of a two-body decay. Additionally, certain nuclei with odd Z and even A (e.g., $^{14}_{7}\mathrm{N}$) were known to be spin-1 particles, which could not be recovered from an odd number of spin-1/2 particles in the nucleus [1].

To explain these and other observations, Wolfgang Pauli in 1930 posited the existence of a neutral particle ν in the nucleus that was also emitted during β^- decay [1]:

$$ {}^{A}_{Z}\mathrm{X} \;\rightarrow\; {}^{\;\;A}_{Z+1}\mathrm{X} \;+\; \beta^- + \;\nu \tag{1.2} $$

Originally called a “neutron”, the ν shares the decay energy with the β^- and so explains the continuous energy spectrum. Pauli’s hypothesized particle would soon become known as the “neutrino” (through the suggestion of Enrico Fermi) to differentiate it from the neutron discovered by James Chadwick in 1932 [1].

In 1934, Fermi published his theory of β-decay [2]. He assumed the “transition from a neutron to a proton is associated with the creation of an electron and a neutrino” [3]:

$$ n \;\rightarrow\; p^+ \;+\; e^- + \;\nu \tag{1.3} $$

Using his theory, Fermi calculated the shape of the β spectrum at the highest allowed β energies assuming different magnitudes for the neutrino mass. Fermi was able to show, by comparing the shape of the observed spectrum to theoretical spectra, that “the rest mass of the neutrino is either zero, or, in any case, very small in comparison with the electron mass” [3].

Conservation of lepton number, although not formulated until much later, allows a determination of whether the ν emitted in β^- decay is a particle or an anti-particle. The initial neutron has a lepton number of 0, while the proton and electron have lepton numbers equal to 0 and +1, respectively. This implies that the emitted ν has a lepton number of -1, which means that it is an “anti-neutrino”, $\bar{\nu}$. Conversely, β^+ decay (the decay of a proton into a neutron) results in the emission of a positron and a neutrino. As is common in the field, the term “neutrino” will be used in the remainder of this thesis to refer to both neutrinos and anti-neutrinos. Context will dictate which particle is being referenced.

1.1.2 Detection

Due to the weak interaction of the neutrinos, it would take many years before the particle would be directly observed. Calculations by H. Bethe and R. Peierls in 1934 indicated that a

2.3 MeV neutrino had an interaction cross section of less than $10^{-44}\,\mathrm{cm}^2$ [4]. The smallness of this number can be realized when compared to the electromagnetic interaction cross section for a photon with similar energy: $\sim 10^{-25}\,\mathrm{cm}^2$ [5].

However, Cowan and Reines were able to make the first detection of the neutrino using a nuclear reactor [6]; a preliminary detection was made in 1953 at the Hanford site in Washington state [7], which was followed up with a more definitive detection at the Savannah River site in South Carolina in 1956 [8, 9]. Fission products in the reactor produced anti-neutrinos while a nearby cadmium-loaded scintillator, surrounded by photomultiplier tubes (PMTs), served as the detector. In the scintillator, the inverse β-decay reaction occurs:

$$\bar{\nu} \; + \; p^{+} \; \rightarrow \; n \; + \; e^{+} \tag{1.4}$$

The resultant positron quickly annihilates with an electron, producing two back-to-back gamma rays which can be detected by the PMTs. The neutron scatters in the scintillator before eventually being captured by the cadmium nucleus, resulting in the emission of several gamma rays that can also be measured.

A delayed-coincidence technique was used to distinguish the inverse β-decay reaction from other background events. The delayed-coincidence rate consisted of events with prompt and delayed signals consistent with electron-positron annihilation and a subsequent neutron capture on cadmium. An excess in the delayed-coincidence rate was observed when the reactor was at full power, compared to when the reactor was inactive. The value of this excess roughly matched the value derived from calculations of the neutrino cross section. Thus, the neutrino was finally observed.

1.2 Neutrinos in the Standard Model

1.2.1 Neutrino Flavors

The neutrino measured by Cowan and Reines was the “electron” anti-neutrino. It was later discovered that two additional type of neutrinos exist in nature: the “muon” neutrino and the “tau” neutrino.

Muon Neutrino

The first direct detection of the muon neutrino occurred in 1962 at the Brookhaven National Laboratory [10]. Pions were produced via proton interactions with a beryllium target; these subsequently decayed into muons and neutrinos (ν_μ):

$$\begin{aligned} \pi^+ &\rightarrow \mu^+ + \nu_\mu \\ \pi^- &\rightarrow \mu^- + \bar{\nu}_\mu \end{aligned} \tag{1.5}$$

The neutrinos were detected using an aluminum target placed near the beamline but behind several meters of steel. Observations were made of the neutrinos via the following muon-producing reactions:

$$\begin{aligned} \bar{\nu}_\mu + p^+ &\rightarrow n + \mu^+ \\ \nu_\mu + n &\rightarrow p^+ + \mu^- \end{aligned} \tag{1.6}$$

If the neutrino produced in interactions with a muon (ν_μ) is the same as the neutrino produced in interactions with an electron (ν_e), then one also expects to observe electron production from the following reactions:

$$\begin{aligned} \bar{\nu}_\mu + p^+ &\rightarrow n + e^+ \\ \nu_\mu + n &\rightarrow p^+ + e^- \end{aligned} \tag{1.7}$$

However, electron events from this reaction were not observed. Thus, it seemed as though $\nu_\mu \neq \nu_e$. The conclusion was that there were at least two types of neutrinos, each associated with one of the two known types of charged leptons ($e^\pm$ and $\mu^\pm$).

Tau Neutrino

In 1975, the tau lepton was discovered at SLAC [11]. Because the other leptons (the electron and muon) each had an associated neutrino, it was presumed that a tau neutrino also existed. However, it was only in 2001 that the DONuT experiment at Fermilab published the first results showing the direct detection of the tau neutrino [12]. Using a beam of neutrinos, of which a fraction were predicted to be tau neutrinos, observations were made of the production of the tau lepton. In a way similar to electron and muon neutrinos (see Eqns. 1.4 and 1.6, respectively), the following charged-current interactions were expected:

$$\begin{aligned} \bar{\nu}_\tau \; + \; p^+ \; &\rightarrow \; n \; + \; \tau^+ \\ \nu_\tau \; + \; n \; &\rightarrow \; p^+ \; + \; \tau^- \end{aligned} \tag{1.8}$$

The final results of DONuT indicated 9 observed ν_τ charged current events, with an estimated background of 1.5 events [13].

Number of Neutrinos

Thus, in the standard model of physics, three types, or flavors, of neutrinos have been discovered. Each neutrino flavor is associated with a charged lepton: the electron, the muon, and the tau.

Observations from the Large Electron-Positron (LEP) collider confirm that only three flavors of weakly interacting neutrinos exist [14]. The Z boson was produced at the collider from e^+e^- collisions and can decay into both visible (e.g., hadrons and charged leptons) and invisible particles (i.e., neutrinos). By measuring the decay width of the Z boson and subtracting out the visible decay width, it is possible to determine the invisible decay width, which depends on the number of neutrinos[1]. Using this method, the number of light neutrinos was found to be 2.9840 ± 0.0082 [16], which is consistent with three flavors.

Measurements from the Planck satellite [17] also confirm this result. (More details about the Planck mission will be given in section 1.4.2.) The contribution of neutrinos to the energy density of the universe depends on N_{eff}, the effective number of neutrinos [17]. The Planck collaboration found N_{eff} to be 2.99 ± 0.17, in good agreement with the prediction of 3.046 from cosmology [18].

However, it is possible that in addition to the three "active" neutrino flavors, one or more non-active, or so-called "sterile", neutrinos may exist. Such neutrinos would not couple

---

[1] This only holds for light neutrinos, which are defined to have a mass $m_\nu < \frac{1}{2} m_Z$, where $m_Z = 91.2\,\text{GeV}$ is the Z boson mass [15].

strongly to Standard Model particles and would not contribute to the Z-boson width or the effective number of neutrinos observed from cosmology. One method to indirectly confirm the existence of sterile neutrinos is to look for the disappearance of the three active neutrinos in oscillation experiments. (Neutrino oscillations are described in section 1.3.) The KATRIN experiment (discussed in chapter 2) may be sensitive to distortions in the β-decay spectrum originating from sterile neutrinos with masses in the keV [19] and eV [20] range.

1.2.2 Weak Interaction

It is now understood that Fermi's theory of β-decay is part of a larger theory of weak decays. Considering the example of β-decay, a down quark in the neutron decays into an up quark (thereby turning the neutron into a proton) with the emission of a W^- boson; this latter particle quickly decays into an electron and electron anti-neutrino. A Feynman diagram of this process is shown in Figure 1.1a. A related process is electron capture, in which an electron is absorbed by a proton via the interaction of a W^+ boson, resulting in the production of a neutron and a neutrino (Figure 1.1b). Depending on the nuclear environment (i.e., the number of protons and neutrons in the nucleus), the probability for these processes to occur can change dramatically, resulting in a wide variety of β-decay half-lives for different isotopes.

The electromagnetic and the weak forces can be understood as part of a single theory, known today as the electroweak theory. In this framework, charged current interactions are mediated by the W^+ and W^- bosons, and neutral current interactions are mediated by the Z boson and the photon [22–25]. Because neutrinos lack electric charge, they can only interact weakly via the $W^\pm$ and the Z bosons. This explains the small interaction cross section for neutrinos.

1.2.3 Massless Particle

In 1958, Goldhaber, Grodzins, and Sunyar performed an experiment to determine the helicity of the neutrino [26, 27]. The helicity of a particle is defined to be +1 (right-handed) if the

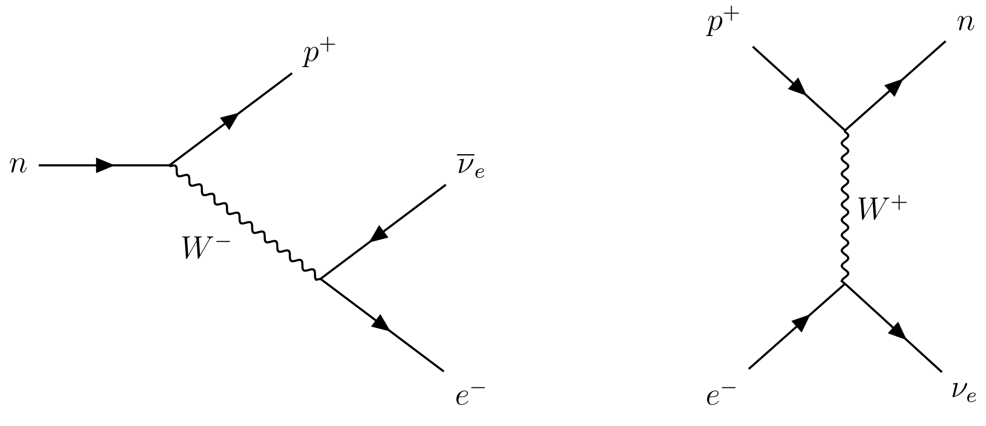

(a) β-decay (b) Electron capture

Figure 1.1: Feynman diagrams of common weak decays, where time increases from left to right. (a) The β-decay of the neutron into a proton, with the emission of a W^- boson, which subsequently decays into a electron and an electron anti-neutrino. (b) A proton captures an electron via the emission of a W^+ boson, resulting in the production of a neutron and an electron neutrino. Figures made with Ti*k*Z-Feynman [21].

momentum and spin of the particle point in the same direction, and -1 (left-handed) if they point in opposite directions. The scientists studied the electron capture of ^{152m}Eu, which produces ^{152}Sm and a neutrino. Because ^{152}Sm is produced in an excited state, it quickly emits a photon to reach the ground state. Because of the spins of the involved particles, the resultant photon must have the same helicity as the neutrino. Thus, the scientists could indirectly determine the helicity of the neutrino by measuring the helicity of the photon. They found that neutrinos are left-handed particles, i.e., the spin of the neutrino is opposite its momentum vector. Conversely, anti-neutrinos are now known to be right-handed [28].

In the Standard Model, particles acquire mass via interactions with the Higgs boson [27]. The interaction mechanism requires both left-handed and right-handed versions of the particle. However, only left-handed neutrinos are known to exist in nature. Because it lacks a right-handed partner, a neutrino cannot interact via the Higgs mechanism and thus cannot acquire mass in the Standard Model.

1.3 Neutrino Oscillations

However, it is now known that neutrinos do in fact have mass. This surprising result originates from the solution to the so-called "solar neutrino problem".

1.3.1 The Solar Neutrino Problem

Inside the Sun, several nuclear processes generate electron neutrinos. The largest flux of neutrinos originate from the *pp*-fusion reaction [29]:

$$p \ + \ p \ \rightarrow \ {}^{2}\mathrm{H} \ + \ e^{+} \ + \nu_{e} \tag{1.9}$$

However, the neutrinos produced in this process are low-energy ($< 0.5\,\mathrm{MeV}$), which means that low-threshold detectors are required to measure them. Much easier to measure are the solar neutrinos produced from the decay of ^{8}B [14] with energies up to 15 MeV [30]:

$$^{8}\mathrm{B} \ \rightarrow \ {}^{8}\mathrm{Be}^{*} \ + \ e^{+} \ + \nu_{e} \tag{1.10}$$

Beginning in the 1960s, Ray Davis began an experiment to measure the neutrino flux coming from the sun [30]. The experiment was performed with a tank filled with 615 metric tons of tetrachloroethylene (C_2Cl_4) in the Homestake Gold Mine in South Dakota. Solar neutrinos could interact with the chlorine nucleus in the following manner:

$$\nu_{e} \ + \ {}^{37}\mathrm{Cl} \ \rightarrow \ {}^{37}\mathrm{Ar} \ + \ e^{-} \tag{1.11}$$

The above reaction has an energy threshold of 0.814 MeV, meaning that ^{8}B neutrinos could be detected. The number of ^{37}Ar atoms was counted to determine the rate of the interaction and thus the ν_e flux. The observed rate was $(2.56 \pm 0.16(\mathrm{stat.}) \pm 0.16(\mathrm{syst.})) \times 10^{-36}$ neutrino captures per target atom per second [30]. The observed flux of solar neutrinos was about a third of the value predicted by standard solar model calculations [31]. Including the results from other solar neutrino experiments (GALLEX, SAGE, Kamiokande), only about half of the predicted ^{8}B neutrino flux was experimentally observed [30].

1.3.2 Theory of Oscillations

The solution to the solar neutrino problem was neutrino oscillations. Electron neutrinos were being produced in the Sun at the rates given by the standard solar model. However, before reaching Earth, a portion of the electron neutrinos changed into muon and tau neutrinos; these flavors of neutrinos could not be detected by the Davis experiment.

The following formulation of neutrino oscillations is taken from several sources [32–34]. The phenomenon of neutrino oscillations assumes that the flavor states of the neutrino, necessary for determining the weak interactions of the neutrino, are not the same as the mass states, which determine how the neutrino propagates in space and time. Instead, the flavor states of the neutrino ($\alpha = e, \mu, \tau$) are quantum superpositions of the mass states ($k = 1, 2, 3$):

$$|\nu_\alpha\rangle = \sum_k U^*_{\alpha k} |\nu_k\rangle, \tag{1.12}$$

where U is a unitary matrix. The flavor state at a position x and time t can be written as

$$|\nu_\alpha(x,t)\rangle = \sum_k U^*_{\alpha k} |\nu_k(x,t)\rangle. \tag{1.13}$$

The mass states propagate freely through vacuum with momentum p_k and energy E_k according to the plane wave solution to the Schrödinger equation [33]:

$$|\nu_k(x,t)\rangle = e^{ip_k(x-x_0)-iE_k(t-t_0)} |\nu_k\rangle, \tag{1.14}$$

where x_0 and t_0 are the initial position and time, respectively, and natural units have been used. Thus, Equation 1.13 can be written as

$$|\nu_\alpha(x,t)\rangle = \sum_k U^*_{\alpha k} e^{ip_k(x-x_0)-iE_k(t-t_0)} |\nu_k\rangle. \tag{1.15}$$

Akin to Equation 1.12, a neutrino in mass state k can be written as a linear combination of the flavor states ($\beta = e, \mu, \tau$):

$$|\nu_k\rangle = \sum_\beta U_{\beta k} |\nu_\beta\rangle. \tag{1.16}$$

Using this formulation, Equation 1.15 can be rewritten solely in terms of the flavor eigenstates:

$$|\nu_\alpha(x,t)\rangle = \sum_k \sum_\beta U^*_{\alpha k} U_{\beta k} e^{ip_k(x-x_0)-iE_k(t-t_0)} |\nu_\beta\rangle. \tag{1.17}$$

The probability for a neutrino created with flavor α to be detected at a position x_D and time t_D with flavor $\beta \neq \alpha$ is

$$\begin{aligned} P_{(\nu_\alpha\to\nu_\beta)}(x_D,t_D) &= |\langle\nu_\beta|\nu_\alpha(x_D,t_D)\rangle|^2 \\ &= \left|\langle\nu_\beta| \sum_k \sum_\beta U^*_{\alpha k} U_{\beta k} e^{ip_k(x_D-x_0)-iE_k(t_D-t_0)} |\nu_\beta\rangle\right|^2 \\ &= \left|\sum_k U^*_{\alpha k} U_{\beta k} e^{ip_k L - iE_k T}\right|^2, \end{aligned} \tag{1.18}$$

where the final step uses the orthogonality of the flavor states ($\langle\nu_\alpha|\nu_\beta\rangle = \delta_{\alpha\beta}$). $L = x_D - x_0$ is the distance from the source to the detector and $T = t_D - t_0$ is the propagation time.

Further simplification is possible when considering relativistic neutrinos [32]. Consider the relativistic dispersion relation:

$$E_k^2 = p_k^2 + m_k^2. \tag{1.19}$$

If $E_k >> m_k$, then $p_k \approx E_k$. Additionally, each mass state has approximately the same energy ($E_k \approx E$). Therefore, one can write:

$$E_k = p_k\sqrt{1+\frac{m_k^2}{p_k^2}} \approx E\sqrt{1+\frac{m_k^2}{E^2}} \approx E + \frac{m_k^2}{2E}. \tag{1.20}$$

For relativistic neutrinos, the propagation time T is approximately equal to the propagation distance L in natural units. Thus, the exponent in Equation 1.18 becomes

$$ip_k L - iE_k T \approx i(E)L - i(E + \frac{m_k^2}{2E})L = \frac{-im_k^2 L}{2E}, \tag{1.21}$$

and Equation 1.18 can be approximated as

$$\begin{aligned} P_{(\nu_\alpha\to\nu_\beta)}(L,E) &\approx \left|\sum_k U^*_{\alpha k} U_{\beta k} e^{\frac{-im_k^2 L}{2E}}\right|^2 \\ &\approx \sum_k |U_{\alpha k}|^2 |U_{\beta k}|^2 + 2\,\mathrm{Re}\left(\sum_{k>j} U^*_{\alpha k} U_{\beta k} U_{\alpha j} U^*_{\beta j} e^{\frac{i\Delta m^2_{jk} L}{2E}}\right), \end{aligned} \tag{1.22}$$

where $\Delta m^2_{jk} = m^2_j - m^2_k$ [32].

Two-Flavor Case

Consider the simplified case where there are only two neutrino flavors. The probability to change flavors (Equation 1.22) can be written as:

$$P_{(\nu_\alpha \to \nu_\beta)}(L, E) \approx |U_{11}|^2 |U_{21}|^2 + |U_{12}|^2 |U_{22}|^2 + 2\,\mathrm{Re}\left(U^*_{12} U_{22} U_{11} U^*_{21} e^{\frac{i\Delta m^2 L}{2E}}\right), \tag{1.23}$$

where $\Delta m^2 = \Delta m^2_{12}$. The 2×2 form of U is a rotation matrix with a single parameter, θ:

$$U = \begin{bmatrix} \cos\theta & \sin\theta \\ -\sin\theta & \cos\theta \end{bmatrix} \tag{1.24}$$

Using this form, Equation 1.23 can be simplified to [34]:

$$\begin{aligned} P_{(\nu_\alpha \to \nu_\beta)}(L, E) &= \cos^2\theta \sin^2\theta + \cos^2\theta \sin^2\theta - 2\cos^2\theta \sin^2\theta \cos\left(\frac{\Delta m^2 L}{2E}\right) \\ &= 2(\cos^2\theta \sin^2\theta)\left[1 - \cos\left(\frac{\Delta m^2 L}{2E}\right)\right] \\ &= 2\left[\frac{1}{4}\sin^2(2\theta)\right]\left[2\sin^2\left(\frac{1}{2}\frac{\Delta m^2 L}{2E}\right)\right] \\ P_{(\nu_\alpha \to \nu_\beta)}(L, E) &= \sin^2(2\theta)\sin^2\left(\frac{\Delta m^2 L}{4E}\right) \end{aligned} \tag{1.25}$$

Several insights can be drawn from Equation 1.25. First, neutrino oscillations will only occur if the difference in the squared masses (Δm^2) is finite. This requires the neutrino mass states to have distinct masses and at least one of the masses must be nonzero. Thus, any observation of neutrino oscillations requires that neutrinos have mass. Second, oscillations can be observed by looking at different values of L/E, as is shown in Figure 1.2. By properly choosing the distance from the source and/or the neutrino energy, it is possible to maximize the appearance or disappearance of certain neutrino flavors.

Three-Flavor Case

For the case of three neutrino flavors, the mixing matrix U is known as the Pontecorvo-Maki-Nakagawa-Sakata (PMNS) matrix [36, 37]. Three angles (θ_{12}, θ_{13}, θ_{23}, running from 0

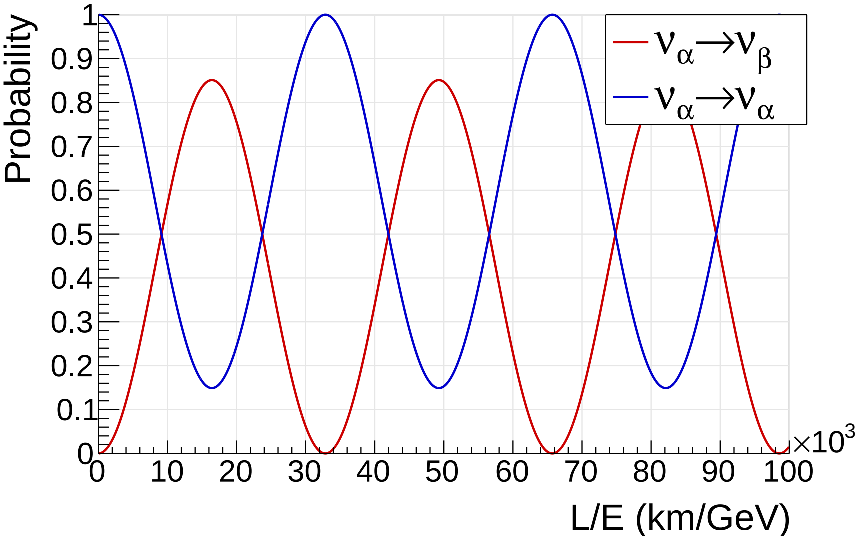

Figure 1.2: The probability for a neutrino to change its flavor (red) or retain its flavor (blue) as a function of L/E, for the case of two-flavor oscillations. The values $\Delta m^2 = 7.53 \times 10^{-5}\,\text{eV}^2$ and $\sin^2(2\theta) = 0.851$ were used. Figure based on work found in [35].

to $\pi/2$) and one CP-violating phase (δ, running from 0 to 2π) are used to parameterize this matrix, which has the following form [14]:

$$U = \begin{bmatrix} c_{12}c_{13} & s_{12}c_{13} & s_{13}e^{-i\delta} \\ -s_{12}c_{23} - c_{12}s_{23}s_{13}e^{i\delta} & c_{12}c_{23} - s_{12}s_{23}s_{13}e^{i\delta} & s_{23}c_{13} \\ s_{12}c_{23} - c_{12}c_{23}s_{13}e^{i\delta} & -c_{12}s_{23} - s_{12}c_{23}s_{13}e^{i\delta} & c_{23}c_{13} \end{bmatrix}, \tag{1.26}$$

where $c_{ij} = \cos\theta_{ij}$ and $s_{ij} = \sin\theta_{ij}$. If the neutrino is a Majorana particle (see section 1.4.2), then U is modified by the inclusion of two Majorana CP-violating phases, α_{21} and α_{31}:

$$U' = U \cdot \begin{bmatrix} 1 & 0 & 0 \\ 0 & e^{i\alpha_{21}/2} & 0 \\ 0 & 0 & e^{i\alpha_{31}/2} \end{bmatrix}. \tag{1.27}$$

The probability for a neutrino to change its flavor can be calculated from Equation 1.22 using the PMNS matrix. Because there are three neutrino flavors (and thus three mass states), two unique mass splittings exist (Δm^2_{21} and Δm^2_{31}). The observation of three-flavor oscillations therefore requires three distinct mass values, with at least two non-zero masses.

1.3.3 Observation of Oscillations

Atmospheric Neutrinos

The earliest indication for neutrino oscillations came from observations of atmospheric neutrinos with the Super-Kamiokande (Super-K) experiment, which is located in an underground mine in Japan [38]. Cosmic rays, interacting in the Earth's atmosphere, produce pions which subsequently decay and produce electron and muon neutrinos. Super-K can detect these neutrinos using an experimental apparatus consisting of 50 kilotons of water surrounded by over 10^4 PMTs. An electron (muon) neutrino that interacts with a nucleus N in the water can result in the production of an electron (muon) with enough energy to produce Cherenkov light that is detected by the PMTs [38]:

$$\begin{aligned} \nu_e/\bar{\nu}_e \ + \ N \ \rightarrow \ e^-/e^+ \ + \ X \\ \nu_\mu/\bar{\nu}_\mu \ + \ N \ \rightarrow \ \mu^-/\mu^+ \ + \ X \end{aligned} \tag{1.28}$$

By studying the characteristics of the Cherenkov light cone, it is possible to distinguish between electrons and muons [39].

When analyzing the neutrino events, the Super-K collaboration discovered that the flux of muon neutrinos as a function of entrance angle disagreed with model predictions [38]. Specifically, a deficit of upward-going muon neutrinos was observed. One possibility to explain this fact was that muon neutrinos were oscillating into tau neutrinos during their transit through the Earth. Indeed, Super-K found that their results were consistent with two-flavor neutrino oscillations [38].

Solar Neutrinos

Additional measurements were required to show that neutrino oscillations could explain the discrepancy between the observed and predicted flux of electron neutrinos from the Sun. The Sudbury Neutrino Observatory (SNO) was initiated in 1984 [40] to get a handle on the flavor of ^{8}B solar neutrinos [41].

Built in an underground mine in Ontario, Canada, the SNO experiment detected Cherenkov light from neutrino interactions using an array of PMTs, in a way similar to Super-K. However, what made SNO unique was that the active volume consisted of 10^6 kg of heavy water (D_2O), allowing for neutrino interactions with the deuteron. The neutral current (NC) reaction occurs with all flavors of neutrinos:

$$\nu_x \ + \ d \ \rightarrow \ p \ + \ n \ + \ \nu_x \tag{1.29}$$

By contrast, the charged current (CC) reaction only occurs with electron neutrinos:

$$\nu_e \ + \ d \ \rightarrow \ p \ + \ p \ + \ e^- \tag{1.30}$$

An additional channel, elastic scattering (ES), is available to all neutrino flavors but has a larger cross section for electron neutrinos [41]:

$$\nu_x \ + \ e^- \ \rightarrow \ \nu_x \ + \ e^- \tag{1.31}$$

By observing the rates for these reactions, SNO could determine both the total and electron neutrino flux coming from the Sun.

The experiment went through three phases, beginning in 1999 [40], which were distinguished by the method of detecting the resultant neutrons from the NC reaction (capture on deuterons, ^{35}Cl, and ^{3}He, respectively). The NC reaction rate indicated ^{8}B neutrino flux was $(5.25 \pm 0.16(\text{stat.})^{+0.11}_{-0.13}(\text{syst.})) \times 10^6\,\text{cm}^2/\text{s}$ [41, 42]. This result was in agreement with calculations, which, depending on the exact solar model, predicted the neutrino flux to be $(4.66 \text{ to } 5.88) \times 10^6\,\text{cm}^2/\text{s}$, not including errors [41, 43]. The flux derived from the CC reaction rate was $(1.67^{+0.05}_{-0.04}(\text{stat.})^{+0.07}_{-0.08}(\text{syst.})) \times 10^6\,\text{cm}^2/\text{s}$ [42, 44]. This result, combined with the NC result, indicates that about a third of detected ^{8}B neutrinos were electron flavor, even though essentially all neutrinos produced in the sun should be electron flavor. SNO thus validated the idea of neutrino oscillations, ruling out the null hypothesis by over 7σ [41].

Reactor and Beam Neutrinos

After the observation of neutrino oscillations by Super-K and SNO, a number of other experiments produced confirming evidence, primarily through measurements of neutrino disappearance. The KamLAND experiment measured the neutrino flux from reactors using a liquid-scintillator detector [45]. Looking at distant nuclear reactors, a deficit was observed in the flux of $\bar{\nu}_e$; this result was in agreement with oscillation calculations.

The K2K experiment observed evidence of oscillations using muon neutrinos produced from an accelerator [46]. A proton synchrotron at KEK was used to generate a beam of pions, which then decayed to produce muon neutrinos. When the muon neutrino beam was measured 250 km away at the Super-K detector, fewer events were observed than expected. The MINOS experiment also saw evidence of oscillations from a muon neutrino beam originating at Fermilab and measured over 700 km away in the Soudan mine [47].

Combining these results with other, newer experiments, the theory of neutrino oscillations has been rigorously confirmed, and the three mixing angles and the magnitudes of the two mass splittings have been experimentally determined. For instance, the Daya Bay Reactor Neutrino Experiment made the first non-zero measurement of θ_{13}; the results were published in 2012 [48]. The most up-to-date values of the oscillation parameters are listed in Table 1.1. However, several questions still remain, in particular the quadrant of θ_{23} and the value of the CP-violating phase δ [42]. The CP violation from δ may contribute to the known baryon asymmetry in the universe, so determining its value is of critical importance [42]. Several current beam experiments (including NOνA [49] and T2K [50]) are working to constrain δ, and the recently formed DUNE collaboration [51] has the determination of this parameter as one of its primary physics goals. The other unresolved question, that of the neutrino mass ordering, is discussed in section 1.4.1.

Parameter	**Value**
$\sin^2\theta_{12}$	$0.307^{+0.013}_{-0.012}$
$\sin^2\theta_{23}$	$0.417^{+0.025}_{-0.028}$ if normal ordering, quadrant I $0.597^{+0.024}_{-0.030}$ if normal ordering, quadrant II $0.421^{+0.033}_{-0.025}$ if inverted ordering, quadrant I $0.592^{+0.023}_{-0.030}$ if inverted ordering, quadrant II
$\sin^2\theta_{13}$	$(2.12 \pm 0.08) \times 10^{-2}$
Δm^2_{21}	$(7.53 \pm 0.18) \times 10^{-5}\,\text{eV}^2$
Δm^2_{32}	$(2.51 \pm 0.05) \times 10^{-3}\,\text{eV}^2$ if normal ordering $(-2.56 \pm 0.04) \times 10^{-3}\,\text{eV}^2$ if inverted ordering

Table 1.1: Neutrino oscillation parameters. Values are taken from the Particle Data Group (PDG) [42].

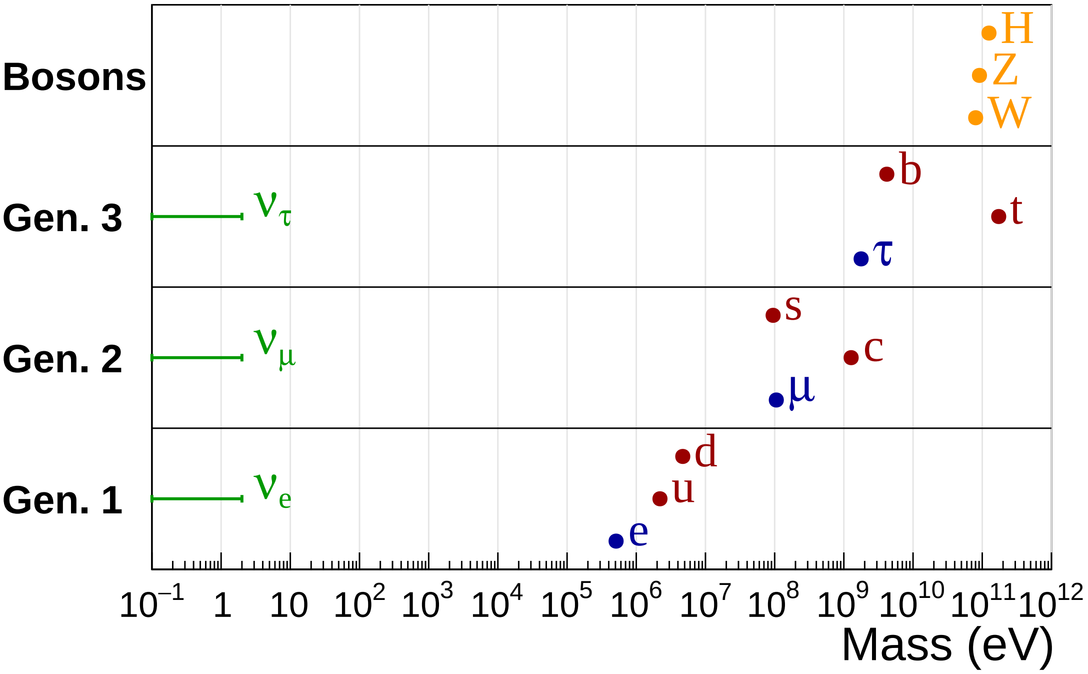

Figure 1.3: Masses of Standard Model particles, separated by generation, including bosons (orange), quarks (red), charged leptons (blue), and neutrinos (green). The approximate upper limit on the neutrino masses is also shown. The values of the masses are taken from the PDG [42]. Figure inspired by [27, 52].

1.4 Neutrino Mass Scale

As was mentioned in section 1.2.3, the neutrino is massless in the Standard Model since no right-handed partner is available to allow for interactions with the Higgs boson. However, neutrino oscillations require that neutrinos have mass. Therefore, some extension to the Standard Model must be made to realize massive neutrinos.

The simplest method to give neutrinos mass is to propose a right-handed partner to the neutrino that doesn't interact with other Standard Model particles [27]. The existence of this particle would allow the neutrino to obtain mass via the Higgs mechanism. However, this mechanism for neutrino mass is rather unappealing since no explanation is given for why the neutrino mass is so tiny. Although the exact value for the neutrino mass scale has not yet been determined, it is already apparent that the neutrino masses are orders of magnitude smaller than other particles. This disparity can be seen schematically in Figure 1.3. To account for this large difference in mass, the coupling to the Higgs field for neutrinos must be arbitrarily small [53].

The lack of any explanation for the mass scale difference has led many physicists to consider other extensions to the Standard Model; one popular extension is the so-called "seesaw" mechanism, which can explain the smallness of the neutrino mass by positing the existence of a very massive right-handed neutrino but requires neutrinos to be Majorana particles [54, 55]. No matter the exact mechanism responsible for setting the neutrino mass scale, a determination of the neutrino mass will certainly provide clues about new physics beyond the Standard Model. This fact makes finding the neutrino mass a very exciting and active area of research in experimental physics.

1.4.1 Mass Ordering

At present, two possible orderings of the neutrino masses are allowed: the so-called "normal" ordering ($m_1 < m_2 < m_3$) and the "inverted" ordering ($m_3 < m_1 < m_2$). The relationship between m_1 and m_2 has already been determined from solar neutrino observations of the

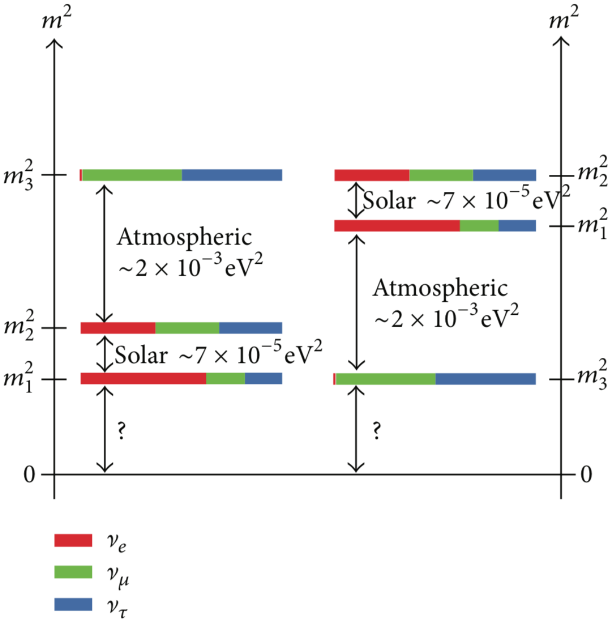

Figure 1.4: The two possible neutrino mass orderings: normal ordering (left) and inverted ordering (right). The value of the lightest mass state is not known. Figure taken from [56]. Used under the CC BY 4.0 license [57].

Mikheyev-Smirnov-Wolfenstein (MSW) effect, in which the varying matter density inside the Sun causes a resonant enhancement of neutrino oscillations [58]. The observation of the MSW effect requires that $\Delta m_{21}^2 \cos 2\theta_{12} > 0$, which subsequently implies that $\Delta m_{21}^2 > 0$ [59].

In the normal ordering, Δm_{21}^2 corresponds to the squared mass-splitting between the two lightest neutrinos, while in the inverted ordering it corresponds to the mass difference between the two heaviest neutrinos. This is shown schematically in Figure 1.4. Although current oscillation experiments have some sensitivity to distinguish between the two orderings[2], several new collaborations (including DUNE and JUNO) are aiming to definitively determine the mass ordering [61]. The sign of Δm_{32}^2 can be determined by observing the matter effects that either resonantly enhance or suppress $\nu_\mu \leftrightarrow \nu_e$ (or $\bar{\nu}_\mu \leftrightarrow \bar{\nu}_e$) oscillations [42]. However, oscillation experiments are only sensitive to mass splittings, not the absolute values of the

---

[2] Combined results from current experiments indicate a preference for normal ordering, with the inverted ordering disfavored at the 3σ level [60].

masses. Thus, an independent method must be used to set the scale of the neutrino mass.

1.4.2 Mass Determination

A variety of complementary methods can be used to measure the neutrino mass. These include cosmological fits, searches for rare nuclear decays, supernova kinematics, and spectroscopy of β-decays.

Cosmology

The universe is composed of several distinct components: dark energy, dark matter, and ordinary matter. Lambda cold dark matter (ΛCDM) is the well-motivated theory that explains many of the measured quantities in the universe (Λ is the cosmological constant that results from dark energy). One method of testing this model has been through observations of the cosmic microwave background (CMB), which consists of photons emitted during an early stage of the universe. The CMB was first observed by Penzias and Wilson in 1965 [17, 62]. Although the CMB is isotropic to first order, measurements of small anisotropies allow one to probe the sum of the neutrino masses, which is a parameter in ΛCDM. Essentially, neutrino mass affects structure formation in the universe and thus must be accounted for in the cosmological fit.

The Planck space mission was the most recent satellite to probe the CMB [17]. The limit on the sum of the mass of the neutrinos quoted by the Planck collaboration is [18]:

$$\sum_{i=1}^{3} m(\nu_i) < 0.12\,\mathrm{eV/c^2},\ (95\,\%\ \mathrm{C.L.}). \tag{1.32}$$

This limit is found by combining Planck data with several external datasets (e.g., measurements of lensing and baryon acoustic oscillations).

Future CMB experiments, combined with galaxy surveys, hope to determine the sum of the neutrino masses to within an error of 16 meV [63]. However, deriving a neutrino mass from cosmological data is complicated by the fact that the sum of neutrino masses is partly degenerate with other parameters of the model. For instance, the Hubble constant H_0 determined by Planck, which is anticorrelated with the sum of the neutrino masses, disagrees with direct measurements of H_0 (using Cepheid variables in the Milky Way [64]) at the 3.6σ level [18]. Any mass value derived from cosmology should therefore be independently confirmed through laboratory-based experiments. Another benefit to measuring the neutrino mass with a different method is the prospect of fixing the neutrino mass in the cosmological model, thus allowing cosmologists to probe other ΛCDM parameters with greater sensitivity.

Neutrinoless Double Beta Decay

For some nuclei, it is energetically unfavorable to undergo a single β-decay. However, two simultaneous β-decays are allowed, and this process is referred to as $\beta\beta$-decay. The simplest type of $\beta\beta$-decay is the two neutrino channel (known as $2\nu\beta\beta$), where two β-particles and two anti-neutrinos are produced. Although a rare process, $2\nu\beta\beta$-decay has been observed in over a dozen nuclei [65].

If neutrinos are Majorana particles, a second decay channel is possible. A Majorana particle is a particle which is its own anti-particle; for the case of neutrinos, this would mean that $\nu = \bar{\nu}$. For $\beta\beta$-decay, if the neutrino were a Majorana particle, this would allow the neutrino emitted from one of the decaying neutrons to be absorbed by the other neutron, resulting in zero neutrinos being emitted ($0\nu\beta\beta$). All of the decay energy (excluding the nuclear recoil) would thus be transferred to the two emitted electrons. The signature for $0\nu\beta\beta$-decay is thus an excess number of events at the Q-value (i.e., endpoint) of the $2\nu\beta\beta$-decay spectrum.

The calculated rate for $0\nu\beta\beta$-decay has a dependence on the neutrino mass:

$$(T^{0\nu}_{1/2})^{-1} = G^{0\nu}|M^{0\nu}|^2\langle m_{\beta\beta}\rangle^2, \tag{1.33}$$

where $G^{0\nu}$ is the phase space factor, $M^{0\nu}$ is the nuclear matrix element, and $\langle m_{\beta\beta}\rangle$ is the effective Majorana mass [14]. The squared effective Majorana mass has the form

$$\langle m_{\beta\beta} \rangle^2 = \left| \sum_{i=1}^{3} U_{ei}^2 m(\nu_i) \right|^2 . \tag{1.34}$$

At present, $0\nu\beta\beta$-decay has not been experimentally observed. Only limits on the rate (and thus limits on $\langle m_{\beta\beta} \rangle$) can be set. One of the most stringent limits on $\langle m_{\beta\beta} \rangle$ comes from the KamLAND-Zen experiment, which uses ^{136}Xe as its $\beta\beta$-decay isotope [66]:

$$\langle m_{\beta\beta} \rangle < 61 - 165\,\mathrm{meV},\ (90\,\%\ \mathrm{C.L.}). \tag{1.35}$$

The range in the limit is due to uncertainties in the nuclear matrix element. Besides ^{136}Xe, $\beta\beta$-decay experiments are also setting limits on $\langle m_{\beta\beta} \rangle$ using ^{130}Te [67] and ^{76}Ge [68, 69].

If a non-zero rate for $0\nu\beta\beta$-decay is eventually measured, extracting an accurate value for the neutrino mass would be difficult for a couple of reasons. First, as just noted, there are fairly large uncertainties on the calculated values of the nuclear matrix elements. Nuclear models only agree on $M^{0\nu}$ to within a factor of 2 or 3 [14]. Second, even if a value for $\langle m_{\beta\beta} \rangle$ can be obtained experimentally, converting this parameter to a neutrino mass requires knowing the values of the CP and Majorana phases. These phases can produce negative terms in the sum in Equation 1.34, thereby making it impossible to determine $m(\nu_i)$ from $\langle m_{\beta\beta} \rangle$ without first measuring the phases.

Supernova

The most straightforward and model-independent way of determining the neutrino mass is to use kinematics. This technique relies on the fact that mass has a definite relationship with energy and momentum. By constraining the neutrino energy and momentum, one thereby constrains the neutrino mass.

One application of this technique is observing the time of flight of neutrinos from supernovae. In 1987, a supernova (given the name SN 1987A) from the Large Magellanic Cloud produced a burst of neutrinos that was observed in several detectors on Earth [70]. By attributing the spread in the arrival time of the neutrinos on Earth to the spread in energies of finite-mass neutrinos, it is possible to deduce a value for the neutrino mass [71]. However, an accurate result requires an a priori knowledge of both the energy and time distributions of the emitted supernova neutrinos.

Using a supernova model that assumes neutrino emission during cooling and accretion, the upper limit on the electron antineutrino mass is [70]

$$m(\nu_e) < 5.7\,\mathrm{eV/c^2}, (95\,\%\ \mathrm{C.L.}). \tag{1.36}$$

Since the observation of SN 1987A, a wide array of neutrino detectors have come online. Any future nearby supernova should produce a large number of detected neutrino events on Earth. With sufficient statistics, it may be possible to reach a neutrino mass limit below 1 eV [72]. However, it is not possible to know when or where the next supernova may occur. Additionally, a greater understanding of supernova physics will be required to reach a limit competitive with other laboratory experiments [73].

1.5 Neutrino Mass from Beta Decay

The kinematic method that has provided the best laboratory limits on the neutrino mass to date are β-decay experiments, which look for the spectral distortion coming from a finite neutrino mass. During β-decay, the decay energy is shared between the daughter nucleus, the electron, and the anti-neutrino. A tiny fraction of the decay energy is used to produce the neutrino mass, and this energy is thus kinetically unavailable to the other particles. β-decay experiments thus attempt to determine the neutrino mass by looking for the effect from the “missing” electron kinetic energy. This type of measurement, unlike many of the previously described methods, is essentially free from model dependencies.

1.5.1 Tritium Beta Decay Spectrum

Before describing past and present β-decay experiments, a brief derivation of the β-particle energy spectrum is given; the content has been taken from several sources [71, 73, 74]. Only tritium β-decay is considered, since this isotope is used by the KATRIN experiment. Tritium decays into ^{3}He with the emission of an electron and an electron anti-neutrino [74]:

$$^3\text{H} \;\rightarrow\; ^3\text{He} \;+\; e^- \;+\; \bar{\nu}_e \tag{1.37}$$

The total decay rate Γ can be calculated starting from Fermi's Golden Rule, in which one sums and integrates over all discrete and continuous final states f, respectively[3]:

$$\Gamma = 2\pi \sum \int |M^2| df, \tag{1.38}$$

where M is the transition matrix element and $\hbar = c = 1$. The number of available final states dn for an emitted particle in a volume V with momentum between p and $p + dp$ at a solid angle $d\Omega$ is

$$dn = \frac{V}{(2\pi)^3} p^2 \cdot dp d\Omega, \tag{1.39}$$

where natural units have been used. Because $E^2 = p^2 + m^2$ and $E \cdot dE = p \cdot dp$, Equation 1.39 can be rewritten in terms of the particle energy:

$$dn = \frac{V}{(2\pi)^3} E\sqrt{E^2 - m^2} \cdot dE d\Omega. \tag{1.40}$$

Although there are three outgoing particles in β-decay, the daughter nucleus is much more massive than the electron and the neutrino, and so its momentum is approximately fixed. Therefore, one can ignore (to first order) the final states of the nucleus and only consider the final states of the electron and the neutrino:

$$df = dn_e dn_\nu = \frac{V^2}{(2\pi)^6} E_e\sqrt{E_e^2 - m_e^2} \cdot E_\nu\sqrt{E_\nu^2 - m_\nu^2} \cdot dE_e d\Omega_e dE_\nu d\Omega_\nu, \tag{1.41}$$

where E_e and m_e (E_ν and m_ν) are the electron (neutrino) energy and mass, respectively.

Combining Equations 1.38 and 1.41, one finds

$$\begin{aligned}\Gamma = \frac{V^2}{(2\pi)^5} \int |M^2| E_e\sqrt{E_e^2 - m_e^2} \cdot E_\nu\sqrt{E_\nu^2 - m_\nu^2} \\ \cdot\delta(E_0 - (E_e - m_e) - E_\nu) \cdot dE_e d\Omega_e dE_\nu d\Omega_\nu,\end{aligned} \tag{1.42}$$

---

[3] Equation 1.38 is written according to the notation given in [71]. This notation should be interpreted as meaning that one adds the sum over the discrete states and the integral over the continuous states; it should not be interpreted as meaning that one takes the sum of the integral.

where the delta function δ ensures energy conservation. The endpoint energy E_0 is defined to be the Q-value for the decay minus the recoil energy of the daughter nucleus (which is essentially fixed near the endpoint). E_0 is the kinetic energy available to the electron and neutrino, assuming the neutrino has zero mass.

The energy spectrum is the derivative of the decay rate with respect to the kinetic energy of the electron $E = E_e - m_e$. Rewriting Equation 1.42 in terms of E, one finds the energy spectrum to be

$$\begin{aligned}\frac{d\Gamma}{dE} = \frac{V^2}{(2\pi)^5} \int |M^2| d\Omega_e d\Omega_\nu \cdot (E + m_e)\sqrt{(E + m_e)^2 - m_e^2} \\ \cdot (E_0 - E)\sqrt{(E_0 - E)^2 - m_\nu^2} \cdot \Theta(E_0 - E - m_\nu),\end{aligned} \tag{1.43}$$

where the integral over the neutrino energy was removed via the delta function. The Heaviside function Θ ensures that the sum of the electron kinetic energy and neutrino mass is less than the endpoint energy.

The matrix element M can be written as a function of a leptonic element M_{lep} and a nuclear element $\overline{M}_{\text{nuc}}$:

$$M = G_F \cos\theta_C \overline{M}_{\text{nuc}} M_{\text{lep}}, \tag{1.44}$$

where G_F is Fermi's constant and θ_C is the Cabibbo angle. The integral in Equation 1.43 thus becomes:

$$\int |M^2| d\Omega_e d\Omega_\nu = G_F^2 \cos^2\theta_C \int |\overline{M}^2_{\text{nuc}}||M^2_{\text{lep}}| d\Omega_e d\Omega_\nu \tag{1.45}$$

The leptonic nuclear matrix element can be calculated for the case of tritium and is simply

$$|M^2_{\text{lep}}| = \frac{1}{V^2} \cdot F(E, Z'), \tag{1.46}$$

where $F(E, Z')$ is the Fermi function, which accounts for the electromagnetic interaction between the electron and the daughter nucleus with charge Z'. The nuclear matrix element is also calculable for tritium β-decay. Including the angular correlation of the electron and the neutrino, one finds that

$$\int |\overline{M}^2_{\text{nuc}}| d\Omega_e d\Omega_\nu = (4\pi)^2 \cdot |M^2_{\text{nuc}}|, \tag{1.47}$$

where $|M_{\text{nuc}}^2| = 5.55$ for the case of tritium [71]. Equation 1.45 thus becomes:

$$\int |M^2| d\Omega_e d\Omega_\nu = \frac{(4\pi)^2 G_F^2}{V^2} \cos^2\theta_C |M_{\text{nuc}}^2| F(E, Z'). \tag{1.48}$$

Combining Equations 1.43 and 1.48 gives the β-particle energy spectrum:

$$\begin{aligned} \frac{d\Gamma}{dE} &= C \cdot F(E, Z') \cdot (E + m_e)\sqrt{(E + m_e)^2 - m_e^2} \\ &\quad \cdot (E_0 - E)\sqrt{(E_0 - E)^2 - m_\nu^2} \cdot \Theta(E_0 - E - m_\nu), \end{aligned} \tag{1.49}$$

where C is

$$C = \frac{G_F^2}{2\pi^3} \cos\theta_C{}^2 |M_{\text{nuc}}^2|. \tag{1.50}$$

The effect of the neutrino mass in Equation 1.49 is quite small, since generally $(E_0 - E)^2 \gg m_\nu^2$. However, for electrons with energies near the endpoint, the effect of a non-zero neutrino mass on the spectrum becomes pronounced. It should be noted that Equation 1.49 is a simplified form of the β-particle energy spectrum; additional correction terms (e.g., molecular and relativistic effects) must be included for a precise calculation of the spectrum shape [75].

Figure 1.5 shows an approximate β-decay spectrum for the case of tritium. If the neutrino were massless (red curve), it would be possible for the β-particle to have an energy up to the endpoint energy. However, if the neutrino has mass (blue curve), some of the decay energy goes into the rest mass of the neutrino, leaving less energy available to the electron and also reducing its available phase space. The goal of a β-decay experiment is to look for the change in the spectral shape near the endpoint that indicates a finite neutrino mass.

In reality, multiple distortions to the endpoint spectrum are present due to the existence of three distinct mass states. However, if the mass splitting between the neutrinos is not experimentally resolvable, then the observed squared-mass is just the incoherent sum of the squared-mass of each mass state [74]:

$$m_\nu^2 = m(\nu_e)^2 = \sum_{i=1}^{3} |U_{ei}|^2 m(\nu_i)^2. \tag{1.51}$$

Notice that, unlike the case of the effective Majorana mass in $0\nu\beta\beta$-decay, any phases in U play no role in the calculation of m_ν. Thus, a firm determination of $m(\nu_i)$ can be achieved using β-decay experiments.

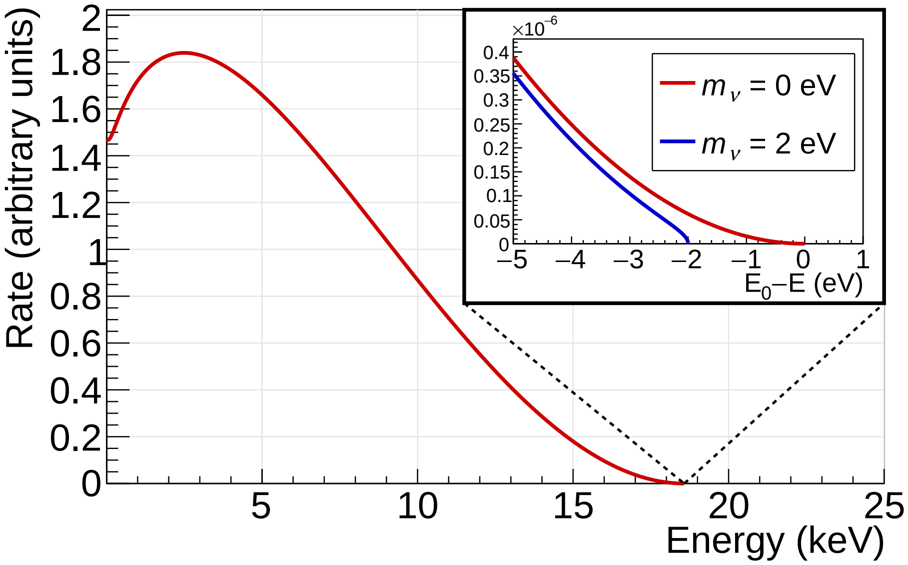

Figure 1.5: Tritium β-decay spectrum. The inset shows the endpoint region ($E_0 = 18.575\,\mathrm{keV}$). Two cases are shown: $m_\nu = 0\,\mathrm{eV}$ (red) and $m_\nu = 2\,\mathrm{eV}$ (blue). A nonzero neutrino mass not only shifts the endpoint energy but also alters the shape of the spectrum near the endpoint. Figure inspired by [74, 76].

Tritium offers a number of advantages compared with other β-decay isotopes. First, tritium β-decay is a super-allowed decay, meaning that M_{nuc} is independent of the β energy [71]. Thus, the decay rate is relatively easy to calculate. Second, tritium has a relatively small endpoint energy of 18.6 keV [74], resulting in a higher fraction of decays near the endpoint compared with other isotopes; this means that more events are acquired per decay that are sensitive to the neutrino mass. Third, the half life of tritium is 12.3 years [74], which is short compared with other popular isotopes like ^{187}Re (4.1×10^{20} years for β^- decay) and ^{163}Ho (4570 years for electron capture) [73]. This allows a smaller amount of tritium to be employed to achieve the same β-decay activity as these other isotopes.

1.5.2 MAC-E Filter Experiments

The best laboratory limits on the neutrino mass come from the Mainz and Troitsk tritium β-decay experiments. Both experiments used magnetic adiabatic collimation with an electrostatic filter, known as a MAC-E filter. This is an integrating high-pass filter that provides excellent energy resolution and high statistics necessary to probe the neutrino mass using tritium β-decay.

Because the sensitivity to the neutrino mass is found near the endpoint of the β-decay spectrum, deducing the shape of the endpoint only requires measuring the highest energy β-particles. If the tritium source and β-detector are connected via magnetic field lines, the simplest method to filter particles would be to place an electrostatic filter between the two. This filter, set at a high negative potential near the endpoint energy, would allow only the highest energy electrons to reach the detector while reflecting low-energy electrons back toward the source. By adjusting the value of the potential used for the filter, it is possible to determine the integrated β-decay spectrum.

However, an electrostatic-filter spectrometer by itself won't provide the necessary energy resolution or the high statistics required to determine the neutrino mass. This is because β-particles in the source which are emitted at large angles relative to the magnetic field will not be properly analyzed by the electrostatic filter, which only blocks electrons based on their longitudinal energy (i.e., energy from motion parallel to the magnetic field). β-particles with energies close to the endpoint and which potentially contain neutrino-mass information will be blocked by the filter if they were emitted in the source with a significant transverse component to their momentum.

Improving the angular acceptance of the filter is thus necessary to attain improved sensitivity. To properly analyze the transverse energy of the β-particle and increase the fraction of analyzed particles, one can use a MAC-E filter [77–79]. The principle behind this technique is that a particle in a smoothly changing magnetic field will conserve its magnetic moment. The magnetic moment of a particle can be written as a function of the magnetic field and the transverse energy of the particle:

$$\mu = \frac{E_\perp}{B}. \tag{1.52}$$

If one adiabatically reduces the magnetic field, the conservation of the magnetic moment requires that the transverse energy must also decrease. Because energy is conserved, any decrease in transverse energy requires an increase in longitudinal energy. Thus, a MAC-E filter works by converting transverse momentum into longitudinal momentum, which can then be properly analyzed by an electrostatic potential. A diagram of a MAC-E filter is shown in Figure 1.6.

The energy resolution of a MAC-E filter depends on the ratio of the minimum to maximum magnetic fields [73]:

$$\frac{\Delta E}{E} = \frac{B_{\mathrm{min}}}{B_{\mathrm{max}}}. \tag{1.53}$$

The maximum magnetic field is applied in the source and/or the detector, while the minimum magnetic field is located near the center of the spectrometer. Because the magnetic flux is conserved, moving from a large to a small magnetic field requires spatially expanding the flux tube. Thus, to achieve a small energy resolution, one needs a large spectrometer vessel to contain the flux tube.

Measuring the neutrino mass with a MAC-E filter follows a fixed procedure. First, one sets the electrostatic retarding potential of the filter near the β-decay endpoint and counts the β-particles that make it through the filter. Next, one repeats this measurement for many other retarding potentials, in order to construct an integrated spectrum near the endpoint. This spectrum is then fit using the calculated spectral form described in section 1.5.1 in order to extract the neutrino mass. Additional details on the fitting method will be given in section 2.3.

The Mainz and Troitsk experiments, although both employing MAC-E filters, used different types of tritium sources. Mainz utilized a solid T_2 source [81], while Troitsk opted for a windowless, gaseous tritium source [82]. However, both experiments had similar sensitivity to the neutrino mass after several years of data-taking. The final limits re-

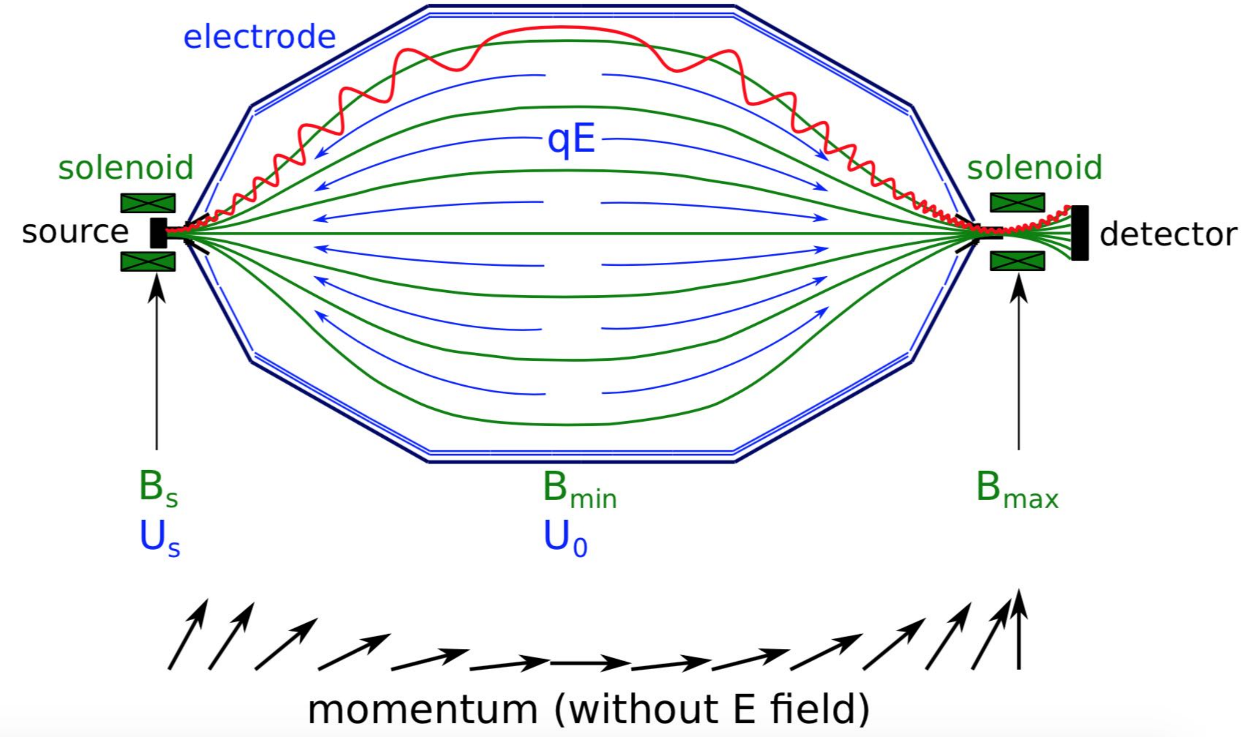

Figure 1.6: Schematic of the MAC-E filter technique. Electrons traveling from the strong source magnetic field B_s to the low magnetic field B_min will conserve their magnetic moment, resulting in their momentum becoming oriented parallel to the magnetic field in the center of the filter. This re-orientation of the electron's momentum allows for enhanced electrostatic filtering by a retarding potential U_0, thus improving the energy resolution and increasing the fraction of transmitted electrons. The central plane in the spectrometer where U_0 reaches its largest value is called the "analyzing plane"". Figure from [80].

ported by the Mainz and Troitsk experiments are $m(\nu_e) < 2.3\,\mathrm{eV/c^2}, (95\,\%\ \mathrm{C.L.})$ [81] and $m(\nu_e) < 2.05\,\mathrm{eV/c^2}, (95\,\%\ \mathrm{C.L.})$ [82], respectively. Combining the results of these two experiments, the PDG states the following limit on the neutrino mass, which is the most stringent direct-detection limit to date:

$$m(\nu_e) < 2\,\mathrm{eV/c^2}. \tag{1.54}$$

The KATRIN experiment, discussed in detail in chapter 2, is the successor to the Mainz and Troitsk experiments. By increasing the intensity of the source and the size of the MAC-E filter, the KATRIN collaboration aims to improve the measured limit on the neutrino mass by an order of magnitude [74].

1.5.3 Other Experiments

Alternative techniques to the MAC-E filter method have emerged due to the challenge of scaling up future experiments. Achieving lower limits than that proposed by KATRIN would be very difficult to achieve using the MAC-E filter technique, since it would require building a larger spectrometer vessel, which would be technically very difficult and prohibitively expensive. Thus, new laboratory-based methods of determining the neutrino mass are being pursued.

Calorimetry and Electron Capture

One alternative method to measure the β-energy spectrum is to use micro-calorimeters [56]. In such an experiment, the decay energy is determined by measuring the change in temperature inside a calorimeter. To achieve an excellent energy resolution and avoid pileup due to multiple decay events, only a small amount of a β-decay isotope can be placed in a small calorimeter (hence a “micro”-calorimeter). In order to get enough statistics to reach sensitivities comparable to MAC-E filter experiments, many thousands of micro-calorimeters are required.

^{187}Re has a very small endpoint energy, close to 2.5 keV [56]. This fact made ^{187}Re a popular β-decay isotope in early calorimeter experiments [83, 84]. The best limit from ^{187}Re β-decay comes from the Milano neutrino mass experiment [84], which found

$$m(\nu_e) < 15\,\mathrm{eV/c^2},\ (90\,\%\ \mathrm{C.L.}). \tag{1.55}$$

However, it was discovered that rhenium exhibited slow thermalization times, which made the isotope non-ideal for a calorimeter experiment [85]. Focus has shifted instead to ^{163}Ho due to its better calorimeter properties. ^{163}Ho undergoes electron capture, and the de-excitation energy spectrum of the daughter ^{163}Dy atom exhibits a similar spectral distortion due to the finite neutrino mass as β^- decay [86].

The Electron Capture in ^{163}Ho (ECHo) experiment plans to use arrays of magnetic metallic calorimeters to measure the decay spectrum [86]. The rise in temperature induced by the electron capture leads to a change in magnetization of the temperature sensor, and the resultant change in magnetic field is measured using a SQUID amplifier. ECHo-1k, consisting of 1 kBq of ^{163}Ho, should be able set a limit of $m(\nu_e) \leq 10\,\mathrm{eV/c^2}$, (90 % C.L.) with one year of data [87].

Another active ^{163}Ho experiment is HOLMES [88, 89]. Here, decay energies are measured using transition edge sensors. These superconducting devices have electrical resistances that are very sensitive to changes in temperature. By measuring the output current from these devices using SQUIDs, the decay energy can be determined. HOLMES is still preparing for data-taking [90].

Cyclotron Radiation

Besides using calorimetric techniques, it is also possible to measure decay energies by detecting the cyclotron radiation of particles in a magnetic field. The cyclotron frequency f of an electron with kinetic energy E_{kin} in a magnetic field with strength B is given by

$$f = \frac{1}{2\pi}\frac{eB}{m_e + E_{\mathrm{kin}}}, \tag{1.56}$$

where m_e and e are the mass and charge, respectively, of the electron [91]. By measuring the frequency of the cyclotron radiation emitted by the electron, the energy of the electron can be determined, assuming sufficient knowledge of the magnetic field.

The Project 8 collaboration has pioneered the technique known as cyclotron radiation emission spectroscopy (CRES) and has succeeded in observing the cyclotron radiation emitted from a single electron [92]. The collaboration is taking a staged approach in building its experimental apparatus, with each stage adding increased complexity and sensitivity to the neutrino mass measurement [91]. Eventual steps for Project 8 include using a larger apparatus in order to increase statistics and using atomic, rather than molecular, tritium gas in order to reduce uncertainties due to the molecular final states.

The calorimeter and CRES methods just described may be able to reach or exceed neutrino mass limits competitive with the KATRIN experiment, although many years of research and development are still required.

Chapter 2

THE KARLSRUHE TRITIUM NEUTRINO EXPERIMENT

The Karlsruhe Tritium Neutrino (KATRIN) experiment will probe the effective electron antineutrino mass using tritium β-decay. This experiment has the goal of achieving a sensitivity which is an order of magnitude smaller than the limit set by its predecessors, the Mainz and Troitsk experiments. However, because β-decay is sensitive to the square of the neutrino mass, KATRIN must increase the precision of the MAC-E filter technique by a factor of 100 in order to reach its goal on the neutrino mass [73]. This ambition requires both improved statistics as well as a better control of systematic errors.

KATRIN is located at the Karlsruhe Institute of Technology (KIT) Campus North in Karlsruhe, Germany. The 70-meter-long experiment is shown in Figure 2.1. The beamline can be conceptually divided into two main parts: the Source and Transport Section (section 2.1) and the Spectrometer and Detector Section (section 2.2). The measurement technique and sensitivity of KATRIN are explained in section 2.3, focusing on the effect of background in reaching the neutrino mass goal.

2.1 Source and Transport Section

The primary purpose of the Source and Transport Section (STS) is to produce and adiabatically guide tritium β-particles. The STS is located within the Tritium Laboratory Karlsruhe (TLK), from which it receives the requisite tritium gas (section 2.1.1). This section consists of four major components: the tritium source (section 2.1.2), two pumping sections (section 2.1.3 and section 2.1.4), and a rear section (section 2.1.5).

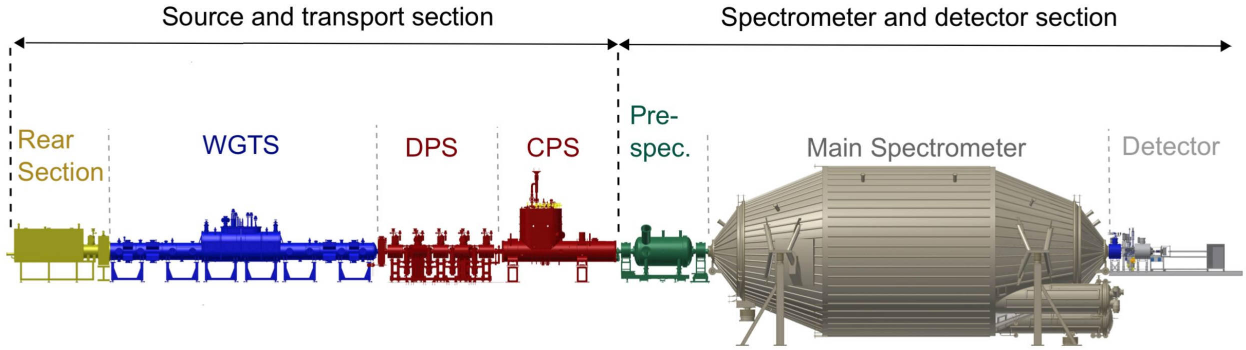

Figure 2.1: The KATRIN beamline. From left to right: the Rear Section, the Windowless Gaseous Tritium Source, the Differential Pumping Section, the Cryogenic Pumping Section, the Pre-Spectrometer, the Main Spectrometer, and the Focal Plane Detector. Figure adapted from [93].

2.1.1 Tritium Laboratory Karlsruhe

Because of the necessary safety requirements regarding handling of tritium, all preparation and processing of the T_2 gas used for the KATRIN experiment must be done within the confines of the TLK. This laboratory has a license for up to 40 g of tritium [74], making it an ideal location for a tritium β-decay experiment.

The tritium must be continually processed via a dedicated loops system [94] in order to remove impurities and ensure the necessary tritium activity in the source [95]. Besides T_2, the gas produced by the TLK will contain other isotopologues (DT, HT, D_2, HD, H_2) [96]. The isotopic composition of the gas is monitored using laser Raman spectroscopy [96].

2.1.2 Windowless Gaseous Tritium Source

Inside the Windowless Gaseous Tritium Source (WGTS), over 10^{11} β-particles are generated per second from tritium decay [93]. A schematic of the WGTS is shown in Figure 2.2. T_2 gas is pumped into the central region of the beam tube (9 cm in diameter) via a sophisticated injection system [93]. Six turbo-molecular pumps (TMPs) located at both ends of the WGTS remove tritium gas from the system in order to limit the tritium flow down the

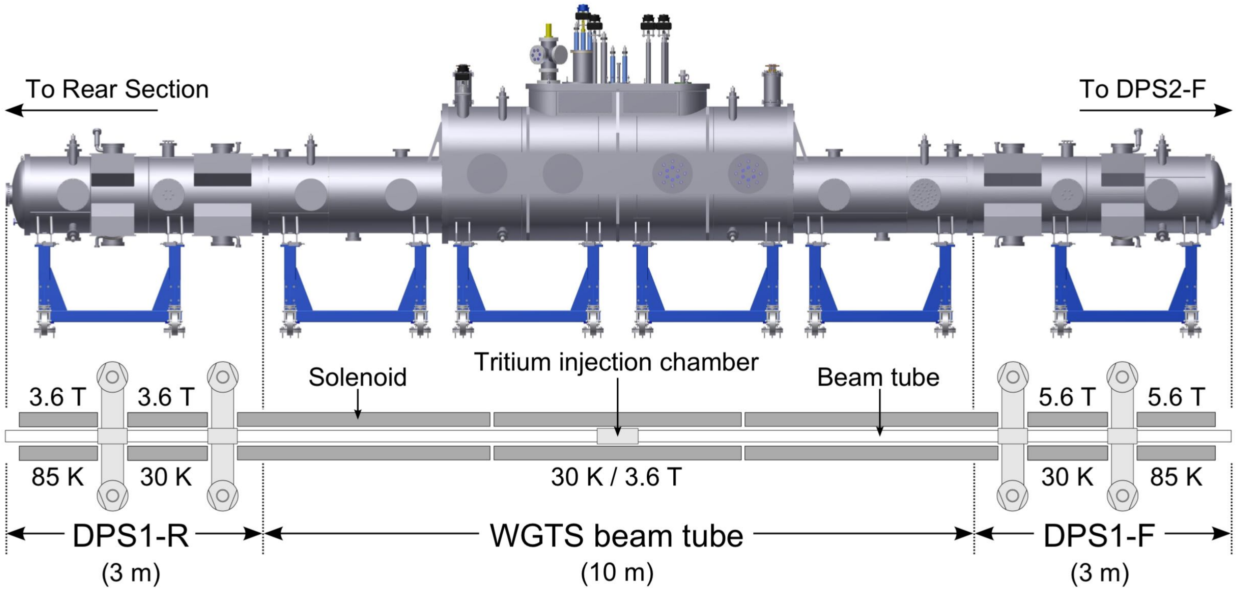

Figure 2.2: The Windowless Gaseous Tritium Source (WGTS). The TMPs in the DPS1-R (rear) and DPS1-F (front) remove tritium gas in order to ensure a well-defined gas density distribution in the beam tube. Figure taken from [34].

beamline and to ensure a well-behaved column density of gas in the source. A series of seven superconducting magnets generate the strong magnetic field inside the source, which guides the β-particles toward both the calibration/monitoring section and the detector [97].

The properties of the tritium gas in the WGTS have important systematic effects on the neutrino mass measurement and must be known with high accuracy and precision. The gas flow and gas dynamics must be carefully modeled to understand the production and transport of electrons [98]. The column density of the source, for instance, directly affects the measured count rate seen by the detector [74]. The beam tube temperature is another important parameter, since it determines the Doppler broadening of the decay spectrum as well as other molecular characteristics of the gas [99]. The temperature stability is ensured using a dual-phase neon system, which keeps the beam tube at 30 K [100]. The design goal for the system is to have temperature fluctuations smaller than 30 mK/h, but commissioning measurements prior to tritium operation have shown a stability that is almost an order of magnitude better than this requirement [99].

2.1.3 Differential Pumping Section

Besides producing and transporting β-particles, the STS must also prevent tritium gas from reaching the spectrometers, as KATRIN has strict background requirements concerning the amount of tritium decays allowed in the Spectrometer and Detector Section. A combination of TMPs, chicanes, and a cryotrap must reduce the tritium pressure by 14 orders of magnitude while transporting the β-particles via superconducting magnets [73, 74]. While initial tritium reduction is handled by the TMPs in the WGTS, significant tritium removal must occur in the aptly named Differential Pumping Section (DPS) and Cryogenic Pumping Section (CPS).

The DPS, shown in Figure 2.3, is connected to the WGTS via a pump port with two TMPs [101]. This section is responsible for removing T_2 via a series of four TMPs [102]. Additionally, to prevent molecular beaming of gas, the five tubes that form this section are placed at a 20° offset relative to each other, forming a chicane [102]. The predicted tritium flow reduction factor (i.e., the ratio of the inlet pressure to the outlet pressure) for the DPS is 2.5×10^4 [102].

Besides reducing T_2, the DPS is also responsible for preventing ions from reaching the Spectrometer and Detector Section (SDS). Ions are produced as a direct result of tritium decay or from ionization of the gas by the β-particles. The background concern from ions will be discussed in section 4.1.1. In order to remove these ions, a dipole electrode has been installed in each of the first four DPS beam tube sections [103]. When put on potential, these electrodes will drift the ions out of the beam tube and remove them via collision with the electrodes. Ring electrodes (discussed in section 4.1.1) are also placed in the DPS and in further downstream components in order to prevent the transport of ions into the spectrometers.

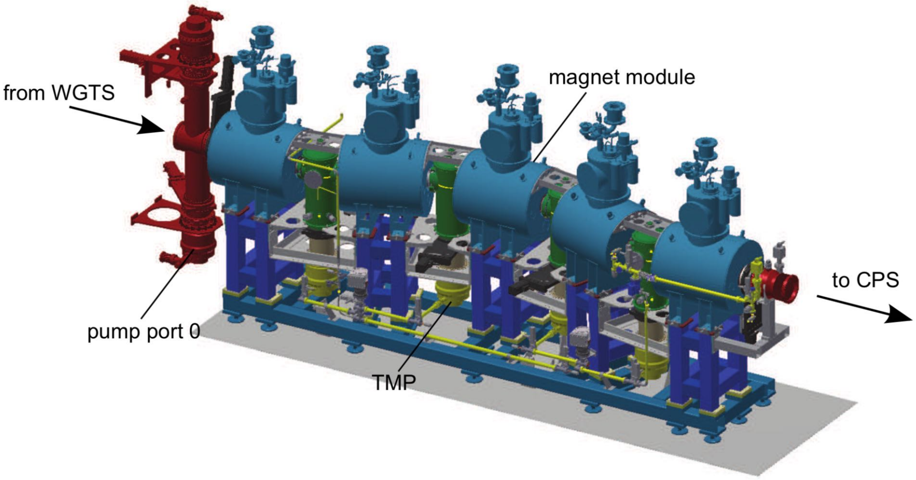

Figure 2.3: The Differential Pumping Section (DPS), containing five magnets arranged in a chicane. Four TMPs are attached to the pump ports between the magnets, while two TMPs are installed at pump port 0. Figure taken from [93].

2.1.4 Cryogenic Pumping Section

The next element in the beamline, the CPS, must further reduce the tritium concentration by seven orders of magnitude [104]. The interior of the CPS is shown in Figure 2.4. Cryogenic pumping is employed via an argon frost layer on a gold-coated surface, which must be kept at 3 K to reach the design efficiency. Liquid helium is used to cool the apparatus [101]. Tritium molecules that impact the tube walls will adhere to the cold argon atoms and thus be removed from the flux tube. A chicane in the beam tube increases the number of molecules that impact the walls. Detailed simulations indicate the CPS should significantly exceed the tritium reduction requirements necessary for KATRIN [105].

Over time, tritium will build up inside the CPS, necessitating a regeneration of the argon frost layer. This process requires warming, pumping, and cooling the system and is scheduled to occur after every two months of operation [74].

A condensed ^{83m}Kr source [106] can be used to calibrate the high voltage system of the spectrometers using mono-energetic electrons [103]. This source is inserted into the beamline

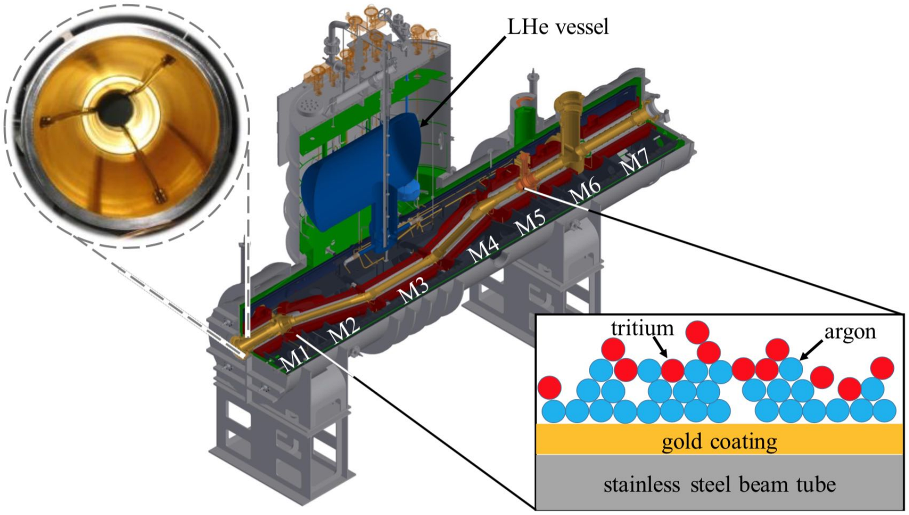

Figure 2.4: The Cryogenic Pumping Section, with seven magnets (M1 through M7). The gold-coated beam tube, cooled with liquid helium, is covered with argon frost to trap tritium. The FBM is inserted at the pump port between magnets M6 and M7 [101]. Figure taken from [108].

at the downstream end of the CPS. Also at this end of the CPS is the Forward Beam Monitor (FBM), which can be used to measure β-particle flux [103]. Normally located at the edge of the magnetic flux tube, but outside of the sensitive volume that connects to the detector, the FBM board is installed on a manipulator arm and can be moved throughout the cross section of the beam tube during special measurements. Besides monitoring the particle flux, the FBM also has sensors to measure the temperature and magnetic field strength [103]. An alternative FBM board with a Faraday cup can also be installed in order to study the ion flux [107].

2.1.5 Rear Section

On the upstream end of the WGTS is the Rear Section (RS), which has several important purposes [109]. First, this system can monitor the T_2 activity in the source by observing the X-rays emitted by β-particles scattering in the RS [103]. Second, the gold-plated rear wall sets the electric potential of the source, which affects the energy scale of the entire experiment. Third, by applying UV illumination, the rear wall will produce photoelectrons, which can neutralize the positive ions produced in the source from β-decay or ionization [103]. These photoelectrons can also be used for studying the transmission of electrons through the entire beamline [103].

An electron gun (e-gun) has recently been installed in the RS and is used to study the transmission of electrons through the beamline. This e-gun was designed to produce electrons with a wide range of energies, radial positions, and starting angles [110]. During early transmission measurements, however, a temporary electron and ion source, called ELIOTT (ELectron impact Ion source to Test the Transport section), was installed in place of the e-gun [103, 108, 111–113].

2.2 Spectrometer and Detector Section

The goal of the Spectrometer and Detector Section (SDS) is to analyze and measure β-particles with energies near the tritium endpoint. A series of two MAC-E-filter spectrometers are available to accomplish this task (section 2.2.1 and section 2.2.2), in combination with an electron detector system (section 2.2.3).

2.2.1 Pre-Spectrometer

The Pre-Spectrometer (PS) is downstream of the CPS and was designed as a pre-filter for the electron beam. The PS is a MAC-E filter operated at a negative potential to block the low-energy component of the β-particle spectrum. This setup reduces the flux of β-particles into the Main Spectrometer (MS) and thus limits the production of background electrons from ionization processes. However, tandem operation with the MS results in the creation of an electron trap between the two spectrometers, which can increase the background rate (see chapter 7).

The exterior of the PS is shown in Figure 2.5a. The vessel has an inner diameter of 1.68 m and a length of 3.38 m; the stainless-steel walls have a thickness of 1 cm [114]. Two

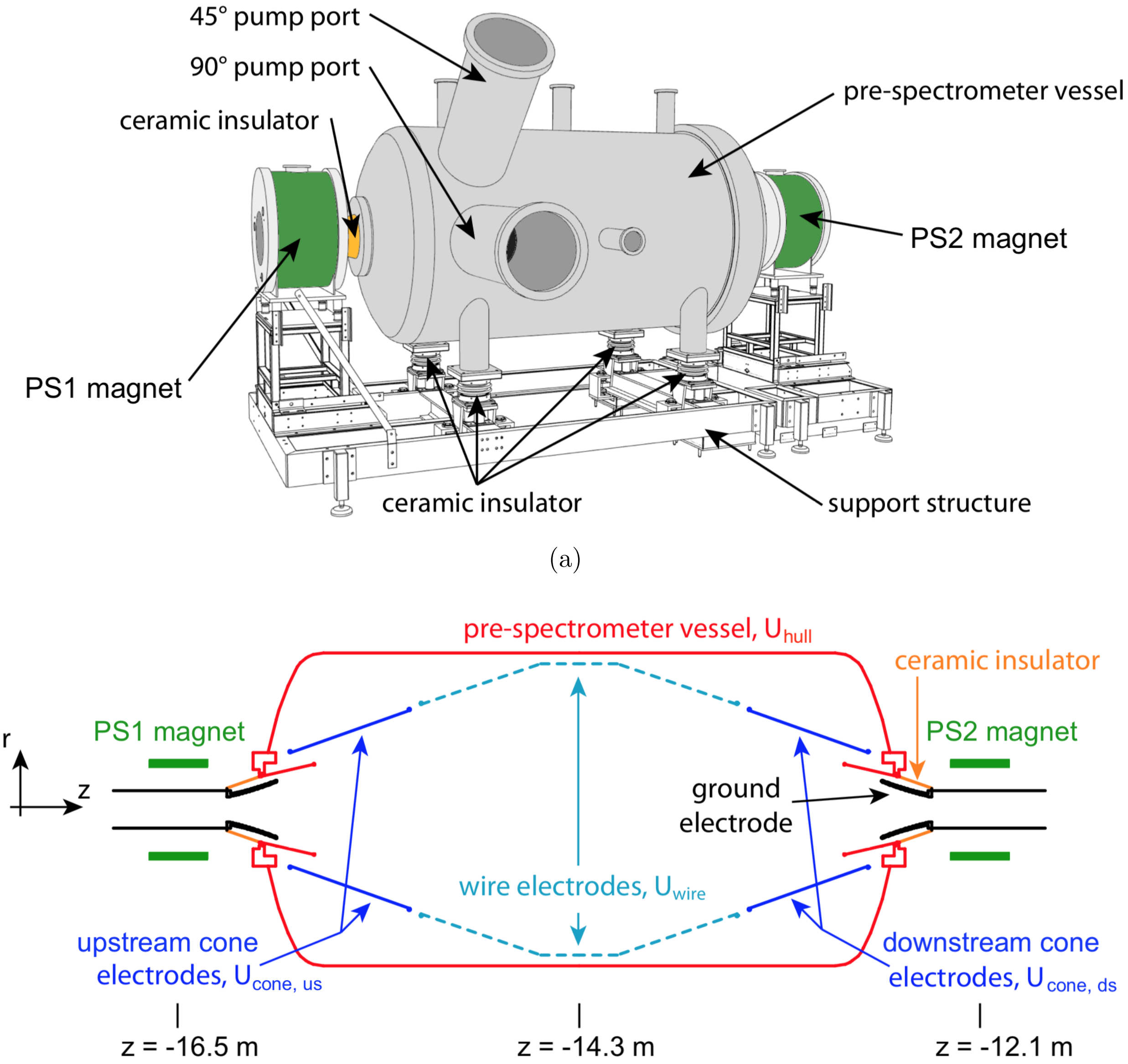

(a)

(b)

Figure 2.5: The (a) exterior and (b) interior of the Pre-Spectrometer (PS). In both figures, the MS is located to the right. The z-coordinates are relative to the center of the MS. Figures adapted from [114].

solenoids, located at the upstream and downstream ends of the vessel (designated as the PS1 and PS2 magnets, respectively) form the guiding magnetic field for passing electrons. Both magnets can be operated up to 4.5 T [97]. In the analyzing plane of the PS, the magnetic field reaches a minimum value close to 0.016 T [115]. Thus, the PS has an energy resolution of 64 eV for 18-keV electrons [116].

The first portion of the KATRIN beamline to be built, the PS was used to test components and techniques that would later be used in the construction of the MS. These include the vacuum and high voltage systems.

Vacuum System

The PS is designed to operate at ultra-high vacuum (UHV) conditions, with a pressure level close to 10^{-11} mbar [117]. Two TMPs are installed at the 90° pump port [115]. However, to reach the required pressure, the PS must be baked-out at 200 °C to remove residual gas, most prominently water, from the inner surfaces of the vessel [115]. The PS has a built-in thermal oil piping system which is used to bake-out the system. A non-evaporable getter (NEG) pump is installed in each of the 45° and 90° pump ports. These pumps work by adsorbing residual gas into the getter material; the activation of the NEG material occurs by baking the pump at 350 °C [115].

A couple of vacuum sensors, installed in the 45° pump port, are available to monitor the pressure inside the vessel [114] (see Table 2.1). The ion extractor gauge (cold-cathode gauge) can measure down to 10^{-12} mbar (10^{-11} mbar) [115]. However, the ion extractor gauge acts as a background source in the PS and is normally turned off during data-taking [114, 115].

High Voltage System

During tandem operation with the MS, the PS vessel is designed to have a retarding energy close to 18.3 keV [74]. This is accomplished by applying static electric potentials to several elements of the PS. A visualization of the interior of the PS is shown in Figure 2.5b. The PS is electrically insulated from the CPS and MS via ceramic connectors, and ground electrodes

Parameter	Sensor Type	KATRIN number	Location/Component
Pressure	Cold cathode	412-RPP-3-1232-0001	PS, 45° pump port
	Ion extractor	412-RPI-3-1221-0001	PS, 45° pump port
	Cold cathode	432-RPP-3-2320-0001	MS, pump port 2
	Ion extractor	432-RPI-3-3110-0001	MS, pump port 3
	Cold cathode	522-RPP-3-1250-0001	FPD UHV
Temperature	Pt1000	527-RTP-6-1285-0001	FPD preamplifier carousel
Voltage	power supply	416-EHV-0-1001-0002	PS hull
	power supply	416-EHV-0-1002-0102	PS IE wire electrodes
	power supply	416-EHV-0-1002-0202	PS IE cone electrodes
	power supply	436-EHV-0-1001-0101	MS hull
	power supply	436-EHV-0-1002-0101	MS IE common
	power supply	525-EHV-0-1050-0001	FPD PAE
	power supply	527-ELV-0-1604-0001	FPD bias

Table 2.1: Slow control sensors in the SDS. The KATRIN number is a unique alphanumeric identifier given to every component in the experiment. Only those sensors relevant to the present work are listed here. The relation between the PS voltages and KATRIN numbers are only valid for the SDS-III measurements.

(fixed to ground potential) are installed at both ends of the vessel [114]. The steel hull is operated at a high voltage $U_{\text{PS, hull}}$.

An inner electrode (IE) system is installed inside the vessel, consisting of a wire electrode in the central region of the spectrometer and solid metal electrodes at both ends of the vessel. Both wire and cone electrodes can be placed on separate offset voltages relative to the vessel voltage ($U_{\text{PS, wire}}$ and $U_{\text{PS, cone}}$, respectively). The purpose of the IE system is two-fold. First, applying a negative potential to the inner electrodes reduces background events by blocking low-energy charged particles originating from the walls from entering the magnetic flux tube. Second, the electrodes enable a fine-tuning of the electric field, which is necessary to set the analyzing potential of the PS [115].

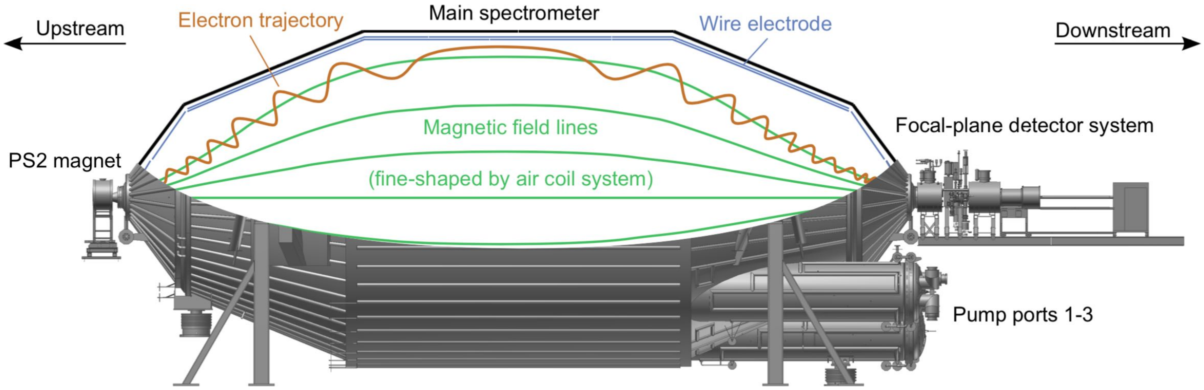

Figure 2.6: Cutaway view of the Main Spectrometer (MS). Figure adapted from [34].

Inter-Spectrometer Beamline Valve

Between the PS and MS is a specially designed valve that allows the two spectrometers to be decoupled during maintenance periods [115, 117]. Because the PS2 solenoid is located between the spectrometers, the valve must reside within the bore of this magnet. This valve also contains the Penning wipers that can be used to mitigate the effect of the inter-spectrometer Penning trap (see section 8.1).

2.2.2 Main Spectrometer

The Main Spectrometer (MS) is the largest component in the KATRIN beamline. Composed of 200 metric tons of low-radioactivity stainless steel, the Main Spectrometer (MS) has a length of 23.2 m and a central diameter of 9.8 m [117]. Its considerable size is necessary to achieve a MAC-E filter energy resolution of 0.93 eV [74]. The vessel will be operated at a voltage near $-18.6\,\mathrm{kV}$ to probe β-particles with energies near the tritium endpoint. A diagram of the MS is shown in Figure 2.6.

The magnetic field inside the vessel is formed primarily by superconducting solenoids located in the PS and detector sections. However, fine-tuning of the magnetic field is accomplished through the use of air-coils that surround the MS vessel [118, 119]. The air-coil

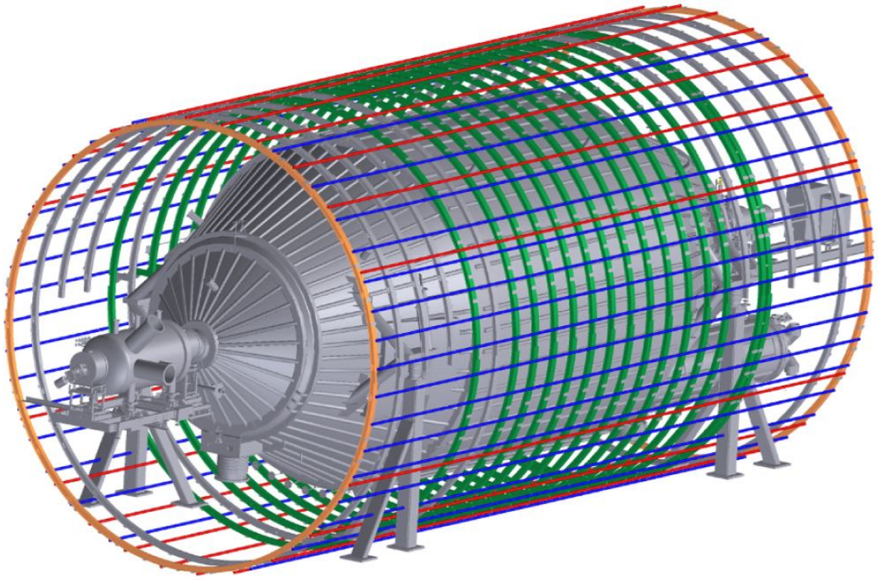

Figure 2.7: The air-coils surrounding the MS, which are used to fine-tune the magnetic field inside the spectrometer. The LFCS consists of 14 coaxial coils, shown in green. The EMCS is composed of 16 loops (10 loops), shown by the blue (red) lines, which cancel the vertical (horizontal) component of the Earth's magnetic field. The vertical and horizontal loop systems each consist of a single current, which connects the loops via the orange circles. The gray rings form part of the aluminum support structure that carries the weight of the air-coils [119]. Figure taken from [118]. Used under the CC BY 3.0 license [120].

system can be seen in Figure 2.7. The Low Field Correction System (LFCS) consists of 14 coils, and different currents and polarities can be applied to each coil [118]. This allows for a wide range of magnetic field configurations inside the vessel [119]. However, the primary purpose of the LFCS is to compensate for the stray fields of the solenoids by constraining the flux tube within the MS [118]. Several additional coils, part of the Earth Magnetic field Compensation System (EMCS), are used to compensate for the Earth's magnetic field [118].

Vacuum System

Maintaining UHV conditions inside the MS, on the level of 10^{-11} mbar, is important to reduce scattering of β-particles with residual gas and to prevent background generation [117]. As with the smaller PS, the MS is baked out at 200 °C using a built-in thermal oil piping system in order to remove residual gas from the inner surface [117]. On the bottom, downstream end of the spectrometer are three large pump ports, each containing a large NEG pump made of 1000 getter strips. All three pump ports have liquid-nitrogen-cooled baffles to prevent radon emanating from the NEG strips from entering the vessel and inducing background (see section 4.1.5).

The second and third pump ports each contain three TMPs, in addition to several vacuum gauges [117]. In pump port 2, there is an inverted magnetron cold-cathode gauge. However, the pressure is primarily measured with an ion extractor gauge located in pump port 3; this pump port also contains a residual gas analyzer (RGA) to measure the gas composition [117].

High Voltage System

The High Voltage (HV) system of the MS is more complex than that of the PS, but follows the same general principle. The hull of the MS is nominally operated at a potential $U_{\text{MS, hull}} \approx -18.5\,\text{keV}$. A two-layer wire IE system covers the interior of the vessel, divided into multiple axial sections [121] (Figure 2.8). Each axial section and layer was designed with the capability to operate at distinct offset voltages; however, due to electrical shorts the entire IE system is usually operated at a single offset voltage $\Delta U_{\text{MS, IE}}$ relative to the hull [34, 122]. Typical values for $\Delta U_{\text{MS, IE}}$ are $\mathcal{O}(-100\,\text{V})$. The IE system blocks background emitted from the hull and allows fine-tuning of the electric field [121]. The background suppression due to the IE system is discussed in section 4.1.4.

Precise electrostatic filtering with the MS requires an extremely stable voltage supply. The KATRIN design report requires that HV variations be smaller than 3 ppm during a two-month measurement, for a voltage of $-18.6\,\text{kV}$ [74]. To achieve this goal, an extensive high voltage concept has been developed that smooths out voltage fluctuations [122]. However, the precision required to measure the small changes in the MS retarding potential is not possible with off-the-shelf products [124]. Combining a custom-built voltage divider with a commercial digital voltmeter allows one to reach the necessary precision. Two voltage dividers, named the K35 [125] and the K65 [126], have been developed; these can handle

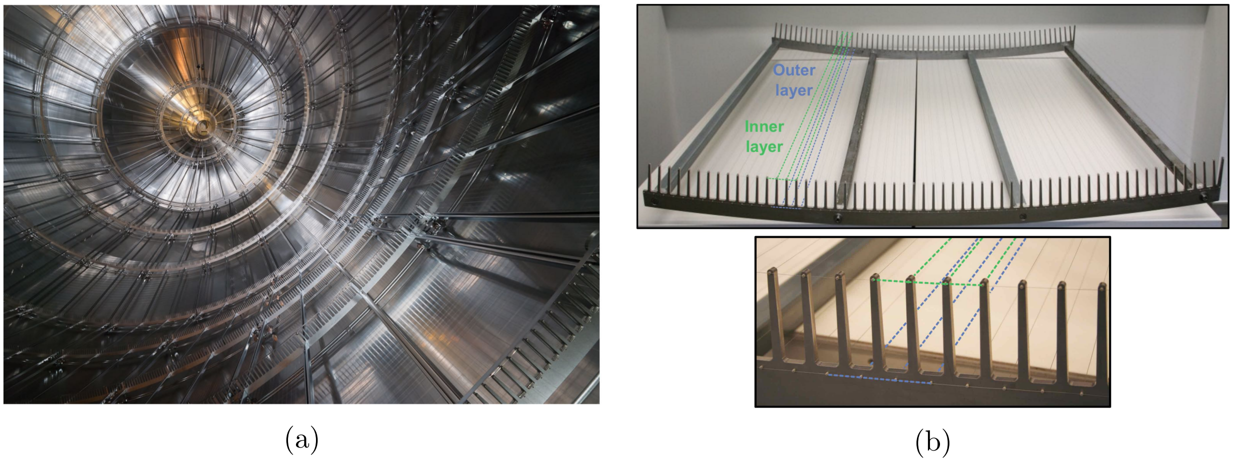

(a)

(b)

Figure 2.8: (a) Inner electrode system inside the MS. Over 23 000 wires are used to create the IE system, installed on 248 steel frames [117]. Photo taken from [123]. (b) A sample frame with wires installed, showing the inner and outer wire layers. Photos taken from [34].

voltages up to 35 kV and 65 kV, respectively. The stability of the K35 was confirmed during measurements with a gaseous $^{83\mathrm{m}}$Kr source in the WGTS [103], which indicated a relative deviation of (-2 ± 5) ppm of the voltage divider scale factor since the last evaluation four years prior [124].

A third MAC-E filter, called the Monitor Spectrometer (MoS), is also used to monitor the voltage stability [127]. The MoS is the former Mainz spectrometer and has been repurposed for use in KATRIN. The same retarding voltage applied to the MS is also applied to the MoS, which is located in a separate beamline. Using an implanted ^{83}Rb/$^{83\mathrm{m}}$Kr source [128], the position of the mono-energetic 17.8 keV electron line is measured over time. This allows long-term drifts of the high voltage system to be monitored [122, 129].

2.2.3 Focal Plane Detector

The final component in the KATRIN beamline is the Focal Plane Detector (FPD) system, which detects β-particles originating from the WGTS with energies above the retarding energy of the MS. The FPD was built and tested at the University of Washington (UW) before

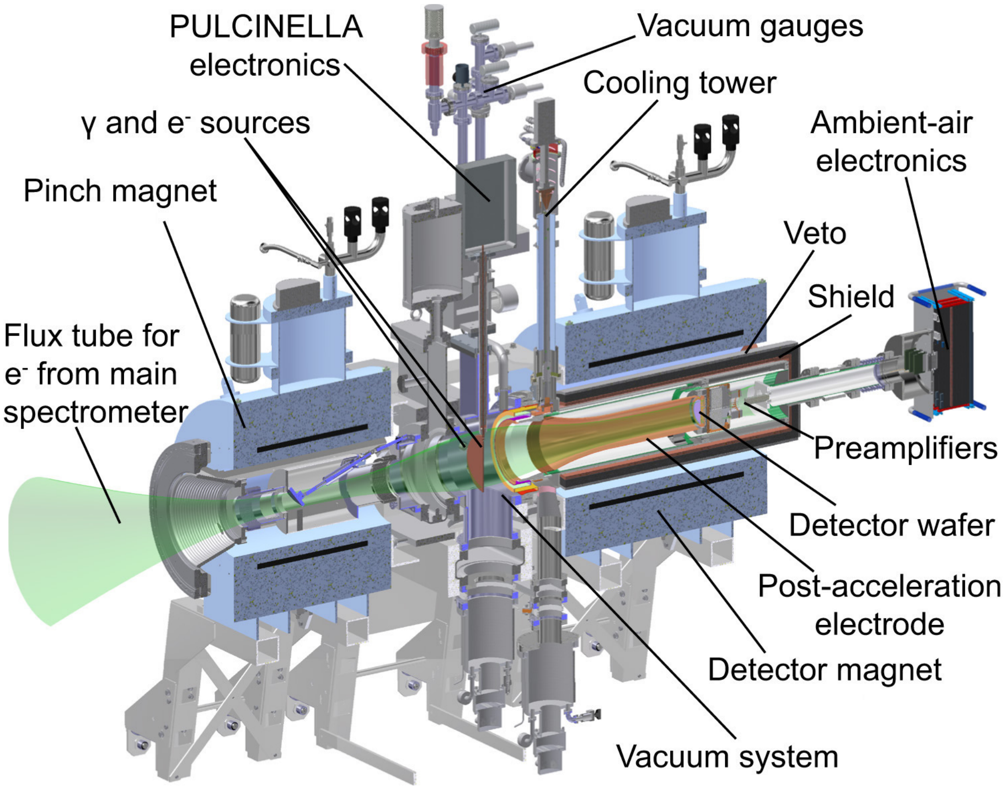

Figure 2.9: A cutaway schematic showing the components of the Focal Plane Detector system. Figure adapted from [130]. Used with permission from Elsevier.

being installed at KIT. Since that time, the detector system has been commissioned [123] and used in numerous data-taking campaigns. A picture of the apparatus is shown in Figure 2.9. A detailed overview of the FPD can be found in [130], from which the following material is mainly summarized.

Hardware

The detector consists of a silicon PIN diode divided into 148 pixels in a dart-board pattern to allow for spatial resolution of the flux tube. A schematic of the detector wafer, manufactured by Canberra Industries, can be seen in Figure 2.10a. The pixels can be radially divided into groups based on ring number: four pixels form the bullseye (ring 0), while the remaining rings (ring 1 through ring 12) consist of 12 pixels each. A bias voltage $U_{\mathrm{bias}} = 120\,\mathrm{V}$ is applied to the wafer during operation. The wafer is attached to a feedthrough flange, which separates the UHV portion of the FPD system (directly connected to the MS) from the high-vacuum section in which initial readout of the detector signals is performed. The wafer is held to the feedthrough flange by a copper ring and six hold-down pins (Figure 2.10b). The signal from each pixel is read out via a spring-loaded pogo pin that connects to one of 24 preamplifier cards through the feedthrough flange.

Two superconducting solenoids constrict the flux tube in the FPD region [97]. The pinch magnet (PCH), located next to the MS, forms the highest magnetic field (B_{max}) in the experiment, up to 6 T, and thus determines the energy resolution of the MS (see section 1.5.2). The detector magnet (DET), with a 3.6-T nominal field, is responsible for focusing the flux tube onto the detector wafer.

Two valves are located between the MS and FPD wafer. A flapper valve, located inside the pinch magnet, can be closed to preserve the integrity of the MS vacuum when the spectrometer and detector system are separated, for instance during baking. During data-taking, a pneumatic gate valve, located between the pinch and detector magnets, can be used to separate the MS and FPD vacuum systems.

A horn-shaped post-acceleration electrode (PAE) is placed in front of the detector wafer. The PAE is normally operated at a positive voltage $U_{\mathrm{PAE}} = 10\,\mathrm{kV}$ to accelerate electrons originating from the MS to higher energies, thus distinguishing them from the low-energy electrons emitted from background processes in the FPD system (see section 3.1). The application of such a voltage requires floating the detector wafer and initial read-out electronics at the same voltage. Optical fibers are used to transport the amplified electronic signals to ground potential, where the signal processing continues.

To avoid overheating of the electronics and reduce electronic noise, the FPD system is cooled with a pulse-tube cooler and thermosiphon [130]. The cooling tower is in thermal contact with the PAE via a ceramic insulator. Heat from the electronics is conducted through the feedthrough flange and PAE to the cooling tower. Cooling the FPD system takes about

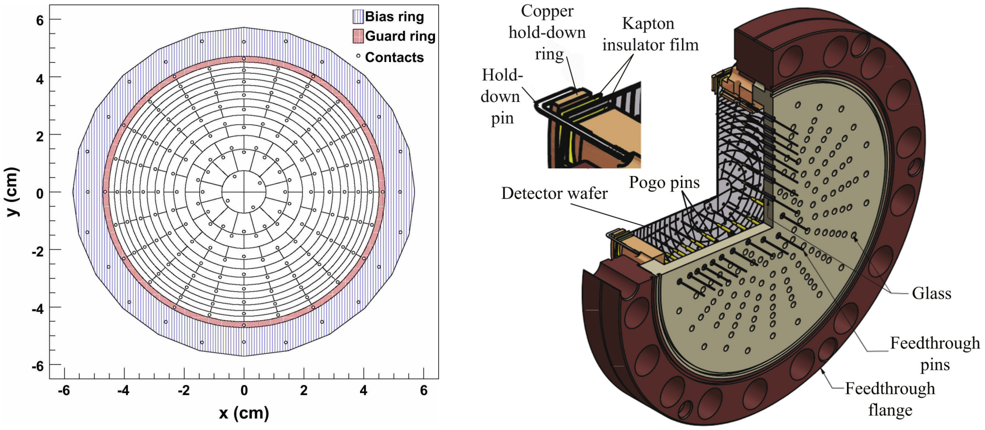

(a) (b)

Figure 2.10: (a) The FPD wafer, consisting of 148 pixels, arranged in dartboard-like pattern with a bullseye (four pixels) and 12 rings (each with 12 pixels). (b) Cutaway view of the feedthrough flange on which the wafer is mounted. The feedthrough pins connect to the preamplifier modules (not shown). Both figures taken from [130]. Used with permission from Elsevier.

two days when starting from room temperature [130]. The temperature stability of the system is monitored with a sensor located on the copper plate (known as the "preamplifier carousel") that separates the detector feedthrough flange and the preamplifier cards. The typical carousel temperature during data-taking has varied between −40 °C and 0 °C (see section 3.2.2).

Electronic Readout, Signal Processing, Data Acquisition, and Software

A diagram of the FPD signal chain is shown in Figure 2.11. The signals from the wafer are first amplified by 24 preamplifier cards located in vacuum. Each card amplifies the signal from six or seven pixels. Signal boards in ambient air (connected to the vacuum chamber via vacuum-tight feedthroughs) provide additional amplification before sending the signals to the ground-potential electronics. Here, signals are processed by first-level-trigger (FLT) cards. The energy and timing information of events is determined by applying two trapezoidal filters,

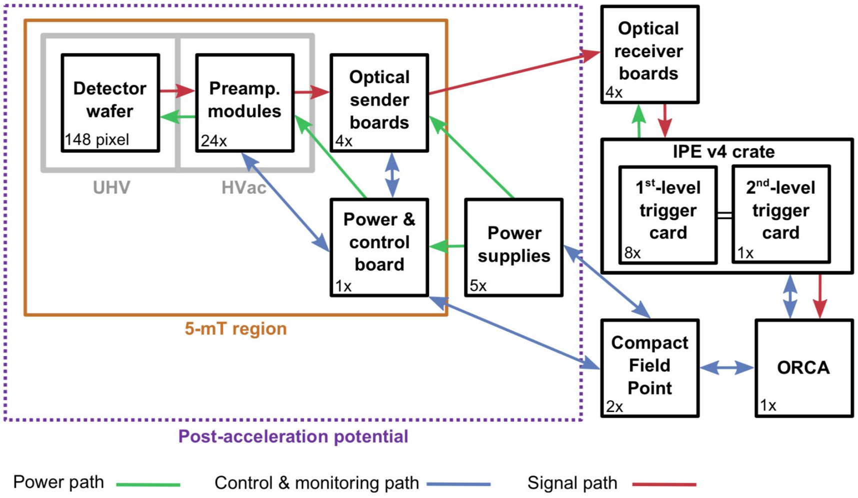

Figure 2.11: Diagram of the electronics readout chain for the FPD system. Figure taken from [34].

defined by a shaping length L and a gap length G [130, 131]. Commissioning measurements have allowed an optimization of the filter settings [130]; the default values are $L = 1.6\,\mu\mathrm{s}$ and $G = 200\,\mathrm{ns}$ [34]. For such values, a timing resolution of 88 ns and an energy resolution of 2.0 keV have been achieved [123]. The energy resolution of the system is discussed in detail in section 3.2.

A second-level-trigger (SLT) card communicates with each of the FLT cards and is connected to the data acquisition (DAQ) computer, from which data runs and settings can be controlled [130]. ORCA (Object-oriented Real-time Control and Acquisition) software handles the DAQ and saves the data to disk [132]. Several data-taking modes are available, with different amounts of saved information. In trace mode, the analog-to-digital converter (ADC) waveform for each event is saved, which is useful for signal and noise analyses. Energy mode, which is the standard operating mode, records the ADC value and timing information for each event. For high data rates, a histogram mode is available in which individual events are not saved but rather their ADC values are stored in a histogram. The ADC value can be converted to an energy value during later analysis by applying a pixel-specific energy

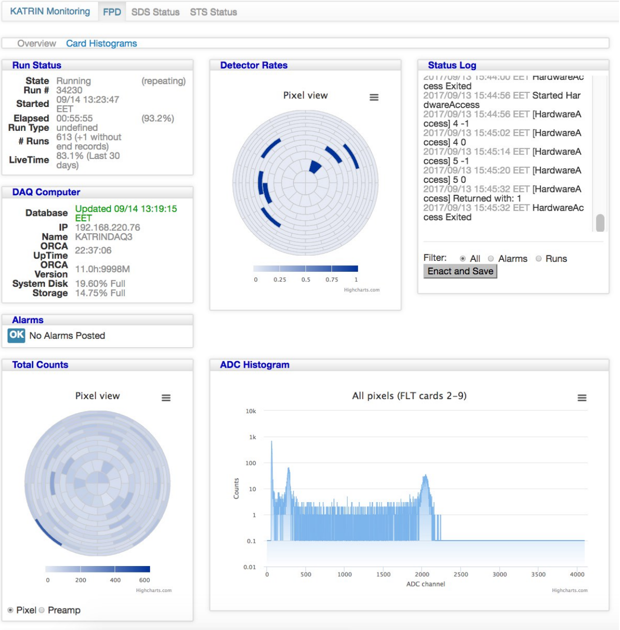

Run Status

State: Running (repeating)
Run #: 34230
Started: 09/14 13:23:47 EET
Elapsed: 00:55:55 (93.2%)
Run Type: undefined
Runs: 613 (+1 without end records)
LiveTime: 83.1% (Last 30 days)

DAQ Computer

Database: Updated 09/14 13:19:15 EET
IP: 192.168.220.76
Name: KATRINDAQ3
ORCA UpTime: 22:37:06
ORCA Version: 11.0h:9998M
System Disk: 19.60% Full
Storage: 14.75% Full

Alarms

OK No Alarms Posted

Status Log

```
2017/09/13 15:44:00 EET HardwareAccess Exited
2017/09/13 15:44:56 EET Started HardwareAccess
2017/09/13 15:44:56 EET [HardwareAccess] 4 -1
2017/09/13 15:45:02 EET [HardwareAccess] 4 0
2017/09/13 15:45:14 EET [HardwareAccess] 5 -1
2017/09/13 15:45:20 EET [HardwareAccess] 5 0
2017/09/13 15:45:32 EET [HardwareAccess] Returned with: 1
2017/09/13 15:45:32 EET HardwareAccess Exited
```

Filter: ● All ○ Alarms ○ Runs
Enact and Save

Figure 2.12: A screenshot of the FPD monitoring website during data-taking.

calibration, which is obtained during dedicated calibration measurements (see below). After completing a data-taking run, the FPD data file is automatically transferred to the KATRIN database server (KDBServer), from which all run files can be accessed for later analysis [76].

During data-taking, on-site operators can monitor the status of the FPD system in real-time through the ORCA interface [130]. Off-site users can check the FPD status in near-time through a monitoring website developed by the author. A screenshot of the website is shown in Figure 2.12. The monitoring webpage developed for the Majorana Demonstrator experiment [68] was used as a template. The ORCA software periodically outputs run details to a database (Apache CouchDB), which the website subsequently reads and displays. The web interface displays run information, ORCA log files, and interactive event histograms.

BEANS (Building Elements for Analysis Sequence) is the primary tool for analyzing KATRIN detector data [76, 133, 134]. This user-friendly C++ code performs energy calibrations, analysis cuts, and data visualization. BEANS forms part of the KASPER framework that includes several other analysis and simulation tools developed by the KATRIN collaboration

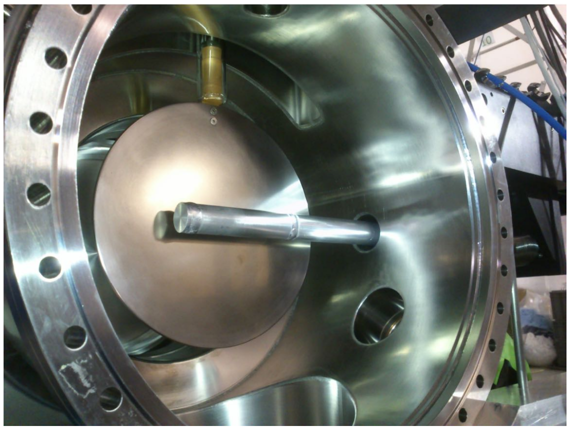

Figure 2.13: Ultra-high vacuum chamber of the FPD system, as viewed from the direction of the detector wafer (the post-acceleration electrode has been detached). The gamma source tube and the electron source disk are visible and can be retracted from the chamber when calibration runs are not being performed. Photo taken from [123, 136].

(details of the Kassiopeia simulation package will be discussed in section 4.2). Although designed to analyze FPD run files, BEANS can also be used to read other types of ORCA run files, such as those produced from the MS muon scintillator panels (see chapter 5), as well as slow control read-out values from numerous KATRIN components. Analysis results from BEANS can be exported into ROOT files [135] for further analysis. A non-exhaustive list of routine analysis tasks include the production of electron energy spectra, rate-trend graphs, and histograms of event rates according to pixel number. In the context of the present work, all FPD runs were initially processed using BEANS.

Energy Calibration

Two calibration systems are available in the FPD system (Figure 2.13). Both sources are retractable and are moved into the beamline upstream of the PAE. A gamma source, consisting of ^{241}Am, is the usual choice for energy calibration. Mono-energetic gammas emitted from the source illuminate the entire wafer. The positions of the 26-keV and 60-keV peaks are used to calibrate the energy for each pixel. However, the interaction of the gammas with the source holder also results in the emission of photoelectrons [123]. In the presence of magnetic fields, these electrons are magnetically guided to a well-defined subset of detector pixels. The ^{241}Am peaks in the energy spectra of the affected pixels are obscured by the scattered electrons [123]. A full calibration of the detector therefore requires taking data with the source located at two distinct and separated radial positions in the flux tube. Measuring the peak width of the 60-keV ^{241}Am source provides an excellent means of determining the detector energy resolution (see section 3.2).

An electron source is also available for calibration purposes. A titanium disk is illuminated with UV light to induce photoelectric emission of electrons from the surface [130, 137]. A voltage can be applied to the disk in order to select the outgoing electron energy. The determination of the electron flux leaving the disk is made using an ammeter, called the Precision Ultra-Low Current Integrating Normalization Electrometer for Low-Level Analysis (PULCINELLA) [137]. The electron disk and PULCINELLA can also be used in a Faraday-cup configuration to measure the flux of charged particles originating from the direction of the MS. Charged particles hitting the disk will induce a charge in the ammeter, which can be read out and converted into a particle rate.

2.3 Sensitivity to the Neutrino Mass

The FPD counts β-particles with energies above the analyzing energy of the MS. By measuring at multiple analyzing energies, an integrated spectrum near the endpoint can be obtained; a simulated result is shown at the top of Figure 2.14. This spectrum is then fit with four parameters: the signal amplitude (A_{sig}), the endpoint energy (E_0), the background rate (A_{bg}), and the squared neutrino mass (m_ν^2) [76]. Because the source strength and background rate differ for each detector pixel, the full data analysis requires fitting each pixel spectrum separately or developing a detailed model to allow for a combined fit [138][1].

---

[1] Also, systematic effects are not uniform across the detector; for example, each pixel must be fit with its own transmission function, and the effects of pile-up and charge sharing at the detector likely differ for each pixel [138].

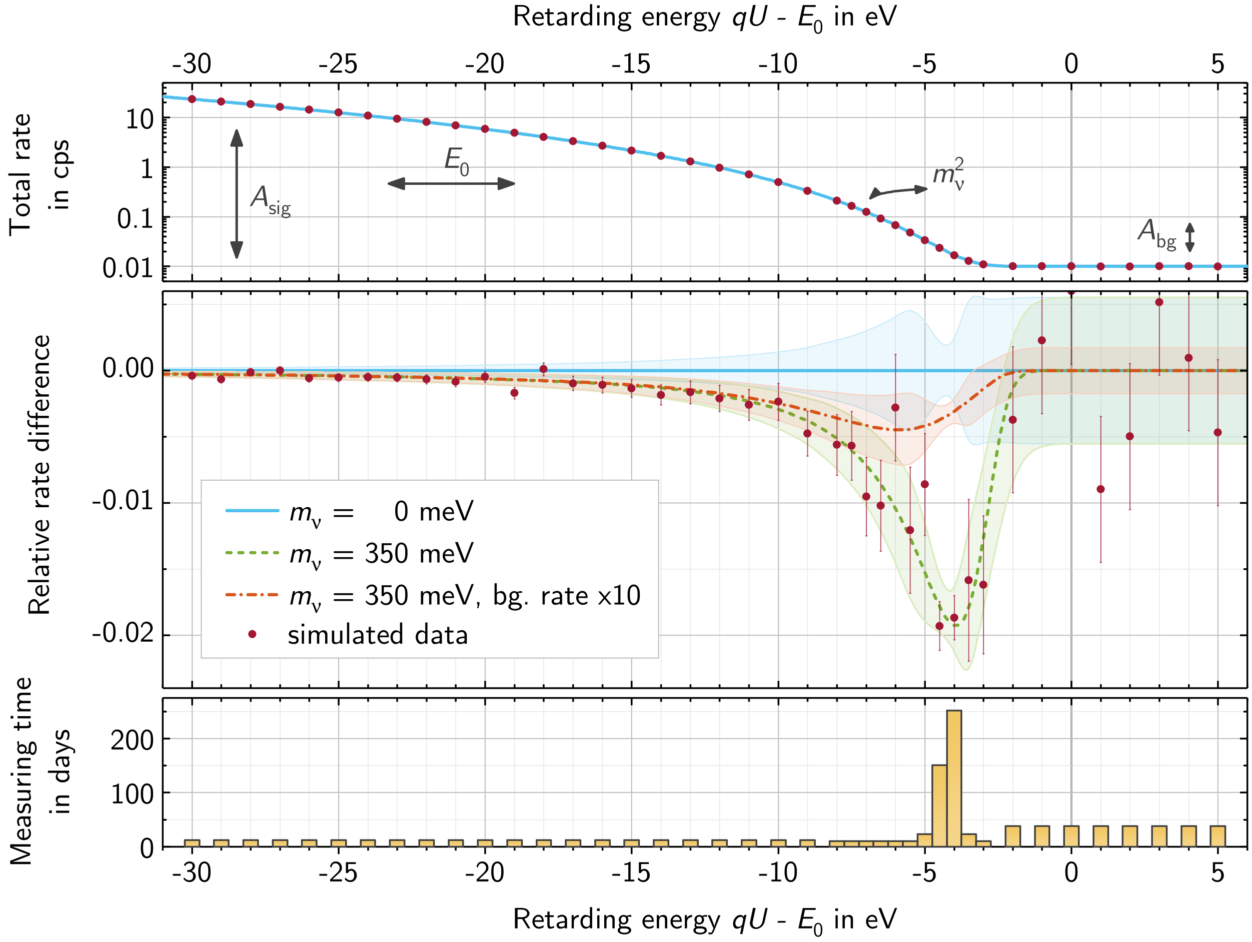

Figure 2.14: Fit of a simulated β-decay spectrum for the neutrino mass analysis. The top figure shows the integrated β-decay spectrum, fitted with four parameters. The middle figure shows the residual between the data (statistical error bars) and the fit, under different neutrino mass and background scenarios. The bottom figure shows the measuring time required at each retarding energy to achieve the shown statistical uncertainties (given by the colored bands in the middle figure). The simulated data assume $m_\nu = 350\,\mathrm{meV}$ and a standard background rate. Figure taken from [75].

First measurements with the entire beamline (designated “First Light”) started in autumn 2016, and first spectroscopic measurements, using gaseous and condensed $^{83\mathrm{m}}$Kr sources, occurred in July 2017 [103]. Low concentrations of tritium gas were injected into the WGTS in May 2018, and the first tritium β-decay integrated spectra were measured over several weeks. Tritium operation is planned to resume in 2019 after remaining commissioning measurements and component maintenance have taken place. Once operational, KATRIN will probe the effective neutrino mass with a sensitivity of 0.2 eV (90 % C.L.) over the course of three beam years (i.e., five calendar years), which is a factor of 10 improvement over the Mainz and Troitsk upper limit [74]. The duration of the experiment is fixed by the goal of acquiring enough data that the statistical and systematic uncertainties on m_ν^2 are roughly equal in magnitude [74].

The above-mentioned sensitivity assumes a Poissonian background rate of 10 mcps (millicounts per second). If the background rate is a factor of 10 larger, but still Poissonian-distributed in time, the sensitivity to the neutrino mass worsens, but only to 0.25 eV (90 % C.L.) [76]. However, if the background rate is a factor of 10 larger and is non-Poissonian, the experimental sensitivity can worsen to 0.33 eV (90 % C.L.) when considering a background model with stored electrons in the MS [139]. Thus, it is paramount to mitigate all background sources, especially those which are non-Poissonian.

Adjusting the measurement-time distribution, as well as extending the measurement interval to smaller retarding potentials, can improve the sensitivity in the face of increased background [76]. If the background rate has a radial dependence (i.e., a higher background for the outermost pixels, which measure portions of the flux tube that are closer to the MS walls) or a volume dependence, increasing the magnetic field in the analyzing plane will reduce this background. However, increasing the magnetic field will also decrease the spectrometer energy resolution, so there is a limit to how much the magnetic field can be adjusted.

Of course, the best scenario is a complete mitigation of the various background sources in order to reach the KATRIN design goal. Each background source, therefore, must be

Campaign	Duration	Components	Backgrounds studied
SDS-I	May–Sept. 2013	MS, FPD	
SDS-IIa	Oct. 2014–Mar. 2015	MS, FPD	cosmic-ray muons
SDS-IIb	June–Sept. 2015	MS, FPD	environmental gammas Secondary electron energy spectrum
SDS-IIIa	Sept.–Dec. 2016	PS, MS, FPD	inter-spectrometer Penning trap
SDS-IIIb	Aug.–Oct. 2017	PS, MS, FPD	inter-spectrometer Penning trap
SDS-IIIc	Dec. 2017–Mar. 2018	PS, MS, FPD	inter-spectrometer Penning trap
STS-IIIa	Sept.–Oct. 2018	entire beamline	

Table 2.2: Measurement campaigns of KATRIN. The listed backgrounds have been limited to those analyzed in detail in the present work. STS-IIIa is given its name due to a commissioning scheme laid out in [140].

properly studied and a background rate (or upper limit) must be assigned to each.

2.4 Background Measurement Campaigns

The MS and FPD system were among the first pieces of the KATRIN beamline to arrive on-site after the PS. Starting with these components, several SDS commissioning campaigns were performed to study background and study other systematic effects of importance for the neutrino mass measurement. A list of these measurement campaigns and their durations appears in Table 2.2. Each campaign consisted of many individual measurements with different electromagnetic configurations and run settings. System maintenance or upgrades usually occurred between commissioning phases. These campaigns provided crucial tests of the functionality of the beamline components, enabled measurement techniques to be investigated, and allowed the study of parameters important for the neutrino-mass analysis. Regarding the latter topic, new insights were gathered that improved the understanding of the background model and prompted further questions to be probed with future measurements. An overview of these backgrounds will be given in the following chapters.

2.4.1 Energy Region of Interest

When a β-particle created in the source reaches the FPD, one expects it to have an energy E_{expected} determined by its initial energy E_{initial} as well as the PAE and detector bias voltages:

$$E_{\text{expected}} = E_{\text{initial}} + (U_{\text{PAE}} + U_{\text{bias}}) \cdot e, \tag{2.1}$$

where e is the elementary positive charge. For the electron to have reached the FPD, it must have surplus energy above the retarding energy of the MS. One can therefore write the initial particle energy as the sum of the retarding energy (determined by the relevant MS voltages) and the surplus energy E_{surplus}:

$$E_{\text{initial}} = -(U_{\text{MS, hull}} + \Delta U_{\text{MS, IE}}) \cdot e + E_{\text{surplus}}. \tag{2.2}$$

Using this formulation, the expected β-particle energy at the detector is

$$E_{\text{expected}} = (-U_{\text{MS, hull}} - \Delta U_{\text{MS, IE}} + U_{\text{PAE}} + U_{\text{bias}}) \cdot e + E_{\text{surplus}}. \tag{2.3}$$

Due to the finite energy resolution of the FPD (see section 3.2), the energy detected by the FPD (E_{detected}) will be smeared out around E_{expected}. This necessitates using an electron region of interest (ROI), or energy window, to count the β-particles and to exclude as many of the background events as possible. A background event is any measured event that is not directly caused by the detection of a signal β-particle by the FPD system. Studying the event rate in the ROI, without any electron sources deployed, allows one to estimate the background rate contributed by the MS and FPD.

The default ROI, which was used from SDS-I through SDS-IIIa [34, 123, 141], is defined to be:

$$E_{\text{expected}} - 3\,\text{keV} < E_{\text{detected}} < E_{\text{expected}} + 2\,\text{keV}. \tag{2.4}$$

Using the nominal voltages ($U_{\text{MS, hull}} + \Delta U_{\text{MS, IE}} = -18.6\,\text{kV}$, $U_{\text{PAE}} = 10\,\text{kV}$, and $U_{\text{bias}} = 120\,\text{V}$), this corresponds to

$$25.7\,\text{keV} < E_{\text{detected}} < 30.7\,\text{keV}, \tag{2.5}$$

where it is assumed that $E_{\mathrm{surplus}} \approx 0\,\mathrm{keV}$. This assumption is warranted since the design KATRIN measurement plan involves measuring down to 30 eV below the endpoint (18.6 keV). This indicates that $E_{\mathrm{surplus}} < 30\,\mathrm{eV}$, which is much smaller than the energy window.

Starting in July 2017, the degradation of the FPD energy resolution (see section 3.2) prompted using an expanded ROI:

$$25.7\,\mathrm{keV} < E_{\mathrm{detected}} < 31.7\,\mathrm{keV}. \tag{2.6}$$

Therefore, later measurements (during SDS-IIIb and SDS-IIIc) used this new energy window for rate calculations. In the rest of this work, any utilized ROI besides those just described will be indicated appropriately.

Chapter 3

FPD BACKGROUND AND ENERGY RESOLUTION

Before discussing background from the spectrometers in detail (chapter 4), it is important to consider the background intrinsic to the detector system (section 3.1). This background rate is directly affected by the FPD energy resolution, which makes it imperative to improve this resolution as much as possible (section 3.2).

3.1 FPD Background

The design for the FPD system specifies an intrinsic background of less than 1 mcps [74]. Simulation and measurements have shown that most of the detector background originates from environmental radioactivity and cosmic-ray muons [130].

To address electrons originating from radioactive decay processes, several preventative measures were taken. First, the apparatus was constructed with materials with low intrinsic radioactivity [123]. Second, shielding was installed where necessary: lead and copper shielding surround the PAE, wafer, and initial readout electronics, and a copper carousel shields the feedthrough flange from the preamplifier electronics [123]. Copper shielding is also installed around the glass feedthroughs to mitigate the effect of the ^{40}K in the glass [130].

Being located above ground, it is not feasible to shield the detector system from cosmic-ray muons. Instead, a muon veto system [142] was developed consisting of several scintillator panels that surround the detector components inside the detector magnet (Figure 3.1). By cutting FPD events that are coincident with events measured in the veto panels, the muon-induced background can be largely mitigated. The veto system hardware has been recently upgraded to achieve better performance [143, 144]. First results with the new system indicate an intrinsic background reduction of about 50 %, although the inclusion of missing scintillator

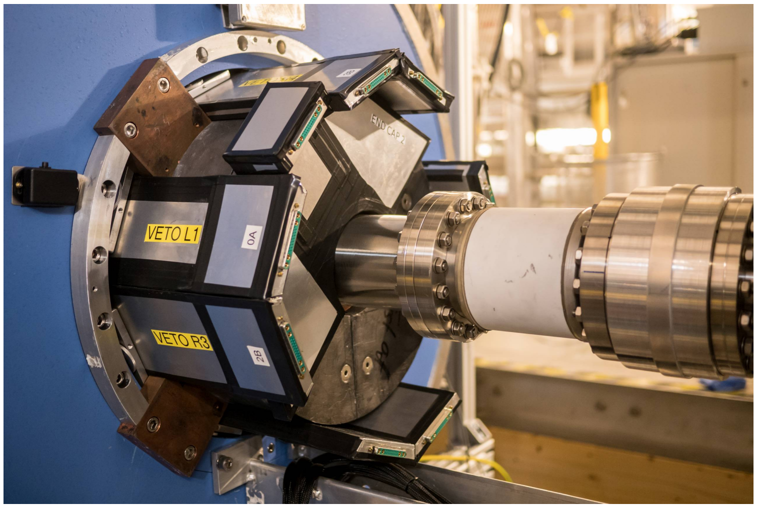

Figure 3.1: View of the partly assembled muon veto system, with a missing semicircular endcap panel and no cabling installed. Underneath the panels, the lead shielding is visible.

panels and optimizing the coincidence cut should give further improvements.

The PAE provides another method to reduce the intrinsic background. By applying a positive potential U_{PAE} to this electrode, β-particles from the MS will be accelerated to higher energies than the intrinsic background spectrum. In this case, the analysis ROI is shifted upward by $e \cdot U_{\mathrm{PAE}}$, thereby reducing the contribution from the low-energy intrinsic FPD background. Although the electrode was designed to operate at potentials up to 30 kV, issues with electrical breakdowns have necessitated running at $U_{\mathrm{PAE}} = 10\,\mathrm{kV}$ [34, 145].

The intrinsic detector background energy spectrum is shown in Figure 3.2. The various spectral features are described in detail elsewhere [123] but are briefly summarized here. The lowest energy events (below about 6 keV) are mainly caused by electronic noise. The peak between 7 keV and 9 keV originates from ^{29}Cu fluorescence of the PAE. Below 125 keV the spectrum is primarily due to fluorescence induced by environmental radioactivity and cosmic-ray muons in the materials surrounding the detector. The rise in the event rate above 125 keV is caused by muons directly passing through the detector wafer. Finally, the peak at 205 keV originates from the overflow bin of each pixel, which is smeared out due

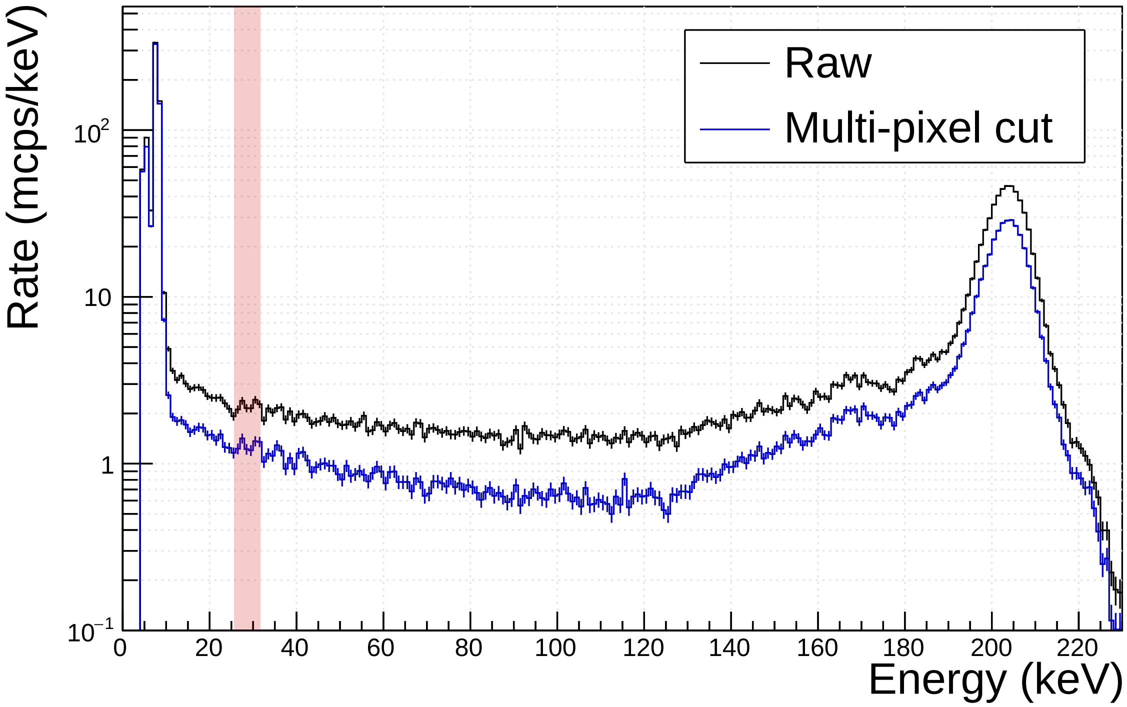

Figure 3.2: Intrinsic FPD background spectrum (black), obtained in July 2018 (FPD runs #41892–41902). The PAE is grounded, and the gate valve between the MS and FPD is closed. No muon veto cut has been applied to the data. The seven pixels associated with preamplifier card #6 are excluded due to noise, but a scaling factor of 148/141 has been applied to the spectrum to compensate for the missing pixels. The background rate is 13.4 mcps in the default ROI (25.7–31.7 keV), indicated by the red box. After the application of the multi-pixel cut (blue), the background rate drops to 7.7 mcps.

to different energy calibrations and electronic read-out characteristics for each pixel. In the default electron ROI (25.7–31.7 keV), the spectrum contributes a background rate of about 13 mcps.

Initial tests with the new muon veto system indicate that a muon-veto cut reduces the intrinsic detector background rate in the ROI by about a factor of 2 [143]. This improved background rate is still larger than the design value (1 mcps), but it is also significantly smaller than the present background contribution from the MS, which will be described in the following chapter. One way to further reduce detector background is by rejecting time-coincident FPD events (also known as "clusters"), since these events likely originate from correlated background processes [123]. This technique is known as the "multi-pixel" cut, and its effectiveness is shown in Figure 3.2.

However, background can also be eliminated by shrinking the energy window used in the neutrino-mass analysis. Measurements during SDS-I and SDS-II utilized a 5-keV ROI, but subsequent deterioration in the detector energy resolution necessitated enlarging this window to 6 keV. Using a smaller ROI thus requires improving the FPD energy resolution.

3.2 Energy Resolution

The energy resolution of the FPD system has dramatically worsened over the last several years. A better energy resolution allows a smaller ROI, thereby reducing the amount of background that contributes to the signal region for the neutrino mass measurement. In this section, an overview of the trend in the energy resolution is presented.

During detector commissioning, a resolution of $\Delta E = (1.40 \pm 0.01)\,\mathrm{keV}$ (full width at half maximum, or FWHM) was achieved using a $^{241}\mathrm{Am}$ calibration source [130]. This value was obtained with a 6.4-µs shaping length for the trapezoidal filter (see section 2.2.3). Since that time, the optimized shaping length has changed to 1.6 µs [146], and only calibration measurements using the latter shaping length will be described here.

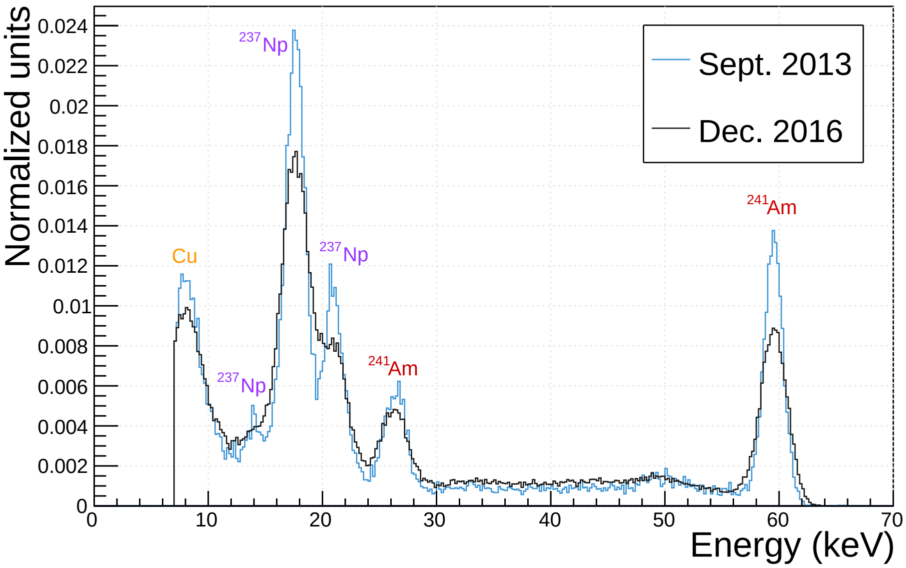

Figure 3.3: Energy spectra for detector pixel 119 from calibration runs with the ^{241}Am source from Sept. 2013 (FPD runs #8000–8001) and Dec. 2016 (FPD runs #32152–32168). Peaks are labelled according to their origin: copper fluorescence, X-rays from ^{237}Np, or γ-rays from ^{241}Am (see [123] for more details). A threshold of 7 keV has been applied to the spectra. The 60-keV peak FWHM increased from 1.9 keV to 2.8 keV.

3.2.1 Calibration Data

Calibration runs provide a reliable and routine method to study the energy resolution. A removable ^{241}Am source (see section 2.2.3) is regularly employed to calibrate the FPD system with gamma rays. Figure 3.3 shows energy spectra for a single detector pixel from two calibration measurements: one from 2013 and the other from 2016. A number of peaks are observed in the energy spectrum; a detailed description of the various spectral components can be found in [123]. The main point of emphasis here is that the spectral peaks have significantly broadened since 2013.

The energy resolution of the detector can be determined by fitting the 60-keV gamma peak in the ^{241}Am spectrum to a Gaussian and finding the FWHM. In Figure 3.4, the FWHM energy resolution is plotted as a function of time. Each data point corresponds to a calibration measurement with the ^{241}Am source, usually consisting of several consecutive runs. The energy resolution was calculated for each detector pixel, and each point in the plot is the average over all pixels.

3.2.2 Temperature Dependence

At the bottom of Figure 3.4, the average temperature of the FPD preamplifier carousel during each calibration measurement is shown. This temperature is measured with a Pt1000 sensor located on the copper carousel that separates the preamplifiers and the feedthrough flange [123] (see Figure 3.13). This is the closest available temperature sensor to the detector wafer when the PAE is on high voltage [145]. During data-taking, the carousel temperature tracks the temperature of the feedthrough flange. The energy resolution of the wafer is correlated with the carousel temperature, a fact which can be easily observed for the SDS-I and SDS-II data.

One expects the energy resolution to be correlated with temperature due to thermal noise in the electronics chain. The electron drift velocity in a material will fluctuate due to random currents induced by the thermal excitations of electrons [147]. Cooling (heating) the system will therefore reduce (increase) these fluctuations.

The energy resolution of a semiconductor detector can be written as

$$\Delta E = E_{\text{ion}} \cdot Q_n, \tag{3.1}$$

where E_{ion} is the ionization energy of the detector and Q_n is the equivalent noise charge (ENC) of the detector readout system [147]. For thermal noise, the square of the ENC is linear with temperature [148]:

$$Q^2_{n,\text{thermal}} \propto T. \tag{3.2}$$

Therefore, one expects $(\Delta E)^2$ to be linear with temperature if thermal noise dominates. A more complete examination of the possible noise sources affecting the FPD energy resolution will be described in the following section.

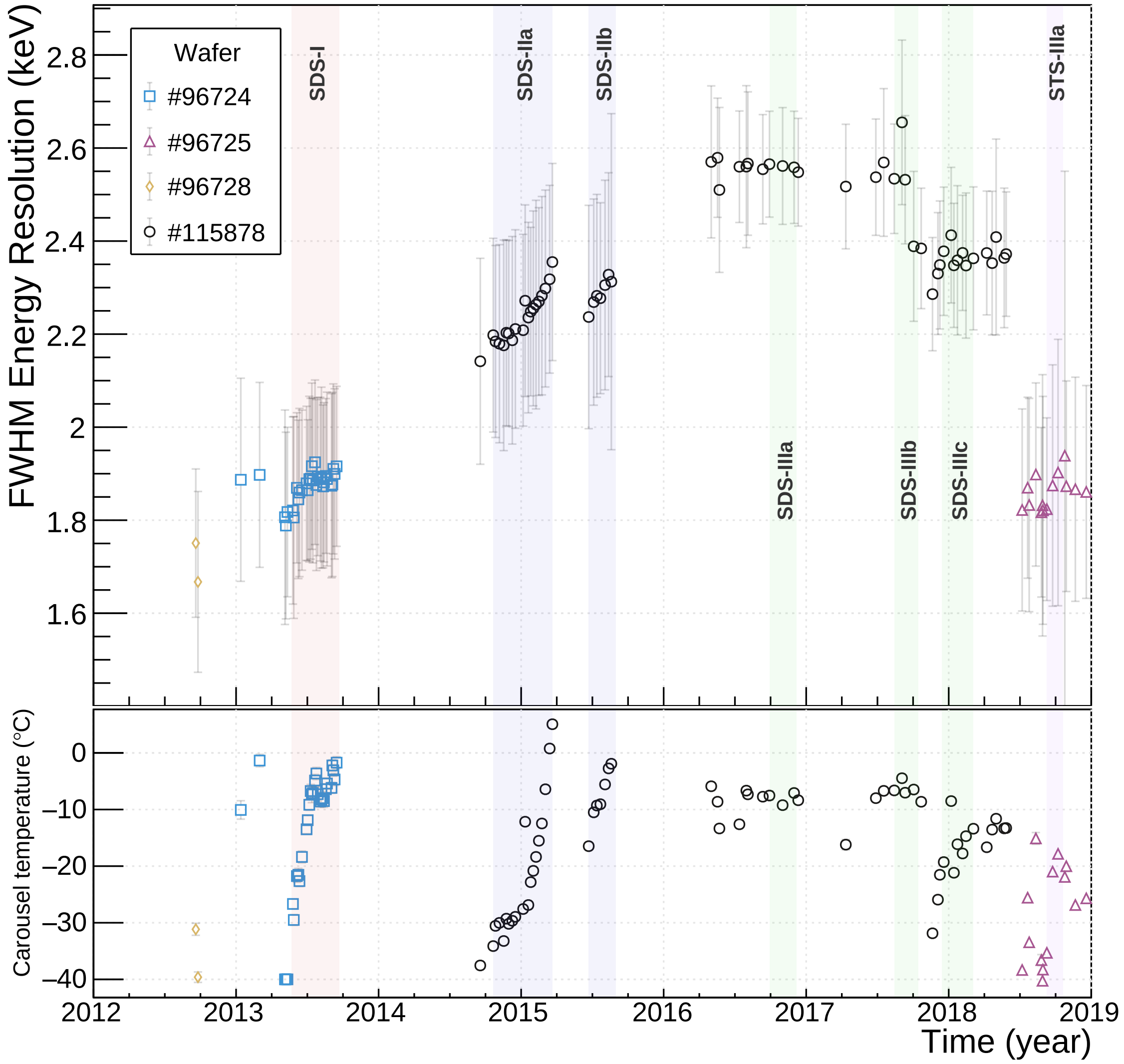

Figure 3.4: FWHM energy resolution (top) and carousel temperature (bottom) plotted as a function of time. The energy resolution is the average over all pixels, and the error bars display the root mean square (RMS) error. Calibration runs are distinguished by which detector wafer was installed in the FPD. The dates of noteworthy measurement campaigns are indicated by the vertical colored bands and associated labels.

Dataset	Wafer	Description	$d(\Delta E)^2/dT$ ($10^{-2}\,\mathrm{keV}^2/°\mathrm{C}$)	$(\Delta E(0\,°\mathrm{C}))^2$ (keV^2)	χ^2/ndf
A	96724	SDS-I (2013)	1.05 ± 0.04	3.67 ± 0.01	28.1/29
B	115878	SDS-II (2014-2015)	1.84 ± 0.05	5.44 ± 0.01	38.4/25
C	115875	Test wafer (2016)	3.42 ± 0.14	8.92 ± 0.05	165.5/110
D	115878	Magnets off (June 2016)	2.66 ± 0.07	7.37 ± 0.01	117.4/86
E	115878	SDS-IIIb (June 2017)	2.43 ± 0.09	6.84 ± 0.02	117.7/109
F	115878	Post-discharge (2017-2018)	1.52 ± 0.12	5.89 ± 0.02	86.4/22
G	96725	Post-tritium (2018)	1.15 ± 0.05	3.71 ± 0.01	170.5/12

Table 3.1: Fit parameters (derived from Figure 3.5) describing the temperature dependence of the FPD energy resolution.

In Figure 3.5, the squared energy resolution is plotted as a function of carousel temperature. A high degree of correlation is observed for each of the plotted datasets, which correspond to different measurement campaigns. Each dataset was fit with a line, and the resultant fit parameters are listed in Table 3.1. The goodness of fit for all datasets is fairly good with the exception of dataset F.

The slope $m = d(\Delta E)^2/dT$ of the line can be used to apply a temperature correction to the energy resolution. If T is the temperature at which an energy resolution ΔE was measured, then the resolution $\Delta E'$ at T' is simply:

$$(\Delta E')^2 = (\Delta E)^2 + m \cdot (T' - T). \tag{3.3}$$

This method was applied to produce the temperature-corrected energy resolution data shown in Figure 3.6; the energy resolution for all points was adjusted to a temperature of 0 °C. The corrected energy resolution remains essentially constant during periods of active data-taking.

3.2.3 Noise Analysis

From the correlation between the carousel temperature and the energy resolution, it is possible to narrow down the source of the resolution degradation. Different noise sources have different dependencies on temperature. The present work is an extension of the analysis described in [146].

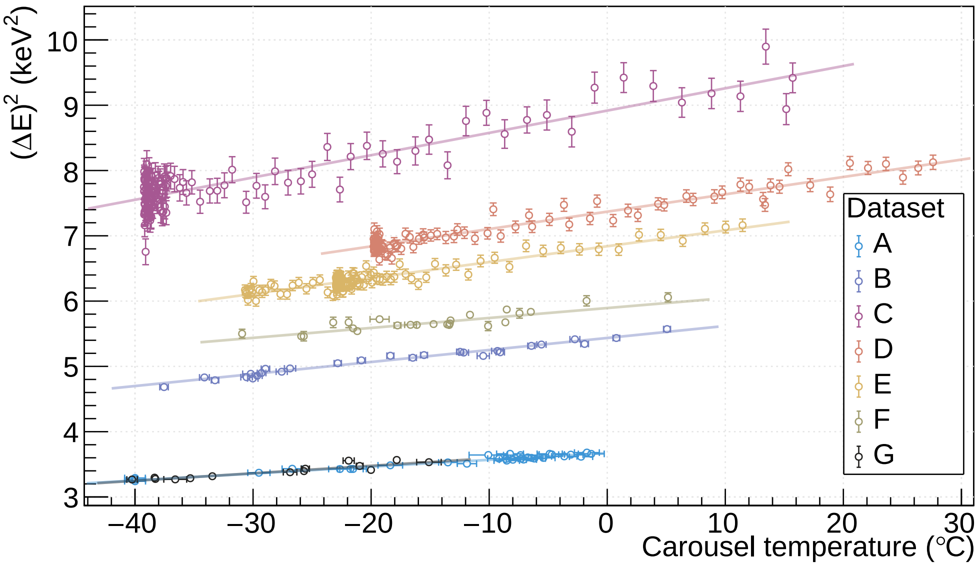

Figure 3.5: Squared energy resolution as a function of carousel temperature. Each dataset is fit to a line. The FWHM energy resolution for each datapoint was computed by combining the energy spectra for all detector pixels and performing a single fit to the 60-keV peak.

The FPD signal processing chain uses a trapezoidal filter, which can be approximately modeled as a CR-RC pulse shaper. The ENC of a CR-RC shaper can be directly calculated [147]:

$$Q_n^2 = \left(\frac{\exp(2)}{8}\right)\left[\left(2eI_d + \frac{4kT}{R_P} + i_{na}^2\right)\cdot\tau + (4kTR_S + e_{na}^2)\cdot\frac{C^2}{\tau} + 4A_fC^2\right], \tag{3.4}$$

where e is the elementary charge, k is the Boltzmann constant, T is the temperature, R_P is the parallel resistance, i_{na}^2 is the current noise of the amplifier, R_S is the series resistance, e_{na}^2 is the voltage noise of the amplifier, C is the total capacitance, τ is the filter time constant, and A_f is the frequency-dependent gain. I_d is the detector bias current and is a function of temperature [147]:

$$I_d(T) = I_0\left(\frac{T}{T_0}\right)^2 \exp\left(-\frac{E_g}{2k}\cdot\frac{T_0 - T}{T_0\cdot T}\right). \tag{3.5}$$

I_0 is the current at temperature T_0 and E_g is the band gap energy. For silicon, $E_g = 1.12\,\mathrm{eV}$ at $T_0 = 300\,\mathrm{K}$ [149].

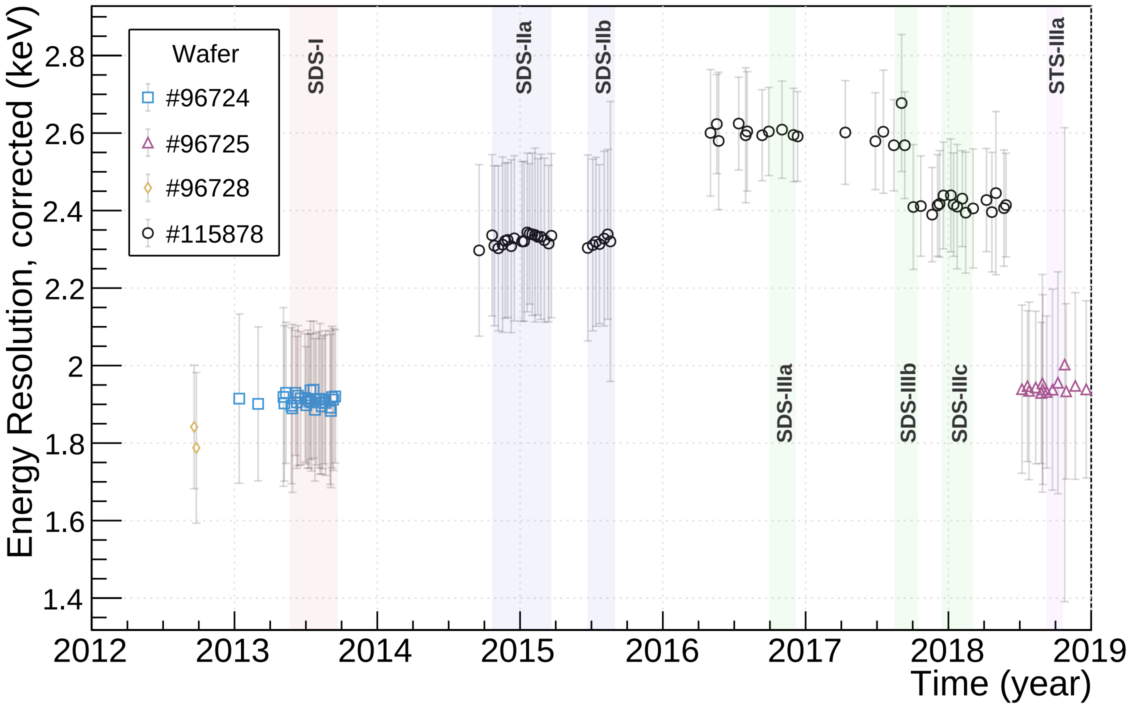

Figure 3.6: FPD energy resolution plotted as a function of time, adjusted to a carousel temperature of 0 °C. The error bars indicate the RMS spread in the resolution across the wafer.

Using the above equations (in addition to Equation 3.1), one can produce an approximate form for the squared energy resolution of the FPD system as a function of temperature:

$$(\Delta E)^2(T) \approx A + B \cdot \left(\frac{T}{T_0}\right) + C \cdot \left(\frac{T}{T_0}\right)^2 \exp\left(-\frac{E_g}{2k}\frac{T_0 - T}{T_0 \cdot T}\right), \tag{3.6}$$

where A, B, and C collect terms which are independent of temperature:

$$A = \left(\frac{\exp(2)E_{\text{ion}}^2}{8}\right)\left(i_{na}^2\tau + \frac{e_{na}^2 C^2}{\tau} + 4A_f C^2\right), \tag{3.7}$$

$$B = \left(\frac{\exp(2)E_{\text{ion}}^2}{8}\right)\left(\frac{4k\tau}{R_P} + \frac{4kR_S C^2}{\tau}\right)T_0, \tag{3.8}$$

$$C = \left(\frac{\exp(2)E_{\text{ion}}^2}{8}\right)(2eI_0)\,. \tag{3.9}$$

From the linear dependence already observed in Figure 3.5, the exponential term in Equation 3.6 cannot contribute significantly ($B \gg C$). Under this conclusion, the temperature derivative of Equation 3.6 is

$$\frac{d(\Delta E)^2}{dT} \approx \frac{B}{T_0}. \tag{3.10}$$

If B is constant, the temperature dependence of the energy resolution should also be constant. However, the temperature dependencies of the datasets in Figure 3.5 are not the same. As can be seen in Figure 3.7, $(\Delta E)^2$ is correlated with the slope ($d(\Delta E)^2/dT$). This indicates that a changing value of B is responsible for the change in energy resolution. Looking at Equation 3.8, B corresponds to thermal (Johnson) noise, coming from either voltage noise (proportional to R_S) or current noise (proportional to $1/R_P$). Therefore, one of these two types of noise is responsible for the energy resolution degradation.

However, an analysis of the FPD noise spectrum indicates the stability of the voltage noise over the SDS measurement campaigns. This argument was first articulated in [146] and will now be briefly explained. Figure 3.8a shows the simulated power spectral density for different types of noise sources in the FPD system. The histograms are derived from data generated with DRIPS, which is a piece of software that simulates the FPD signal readout

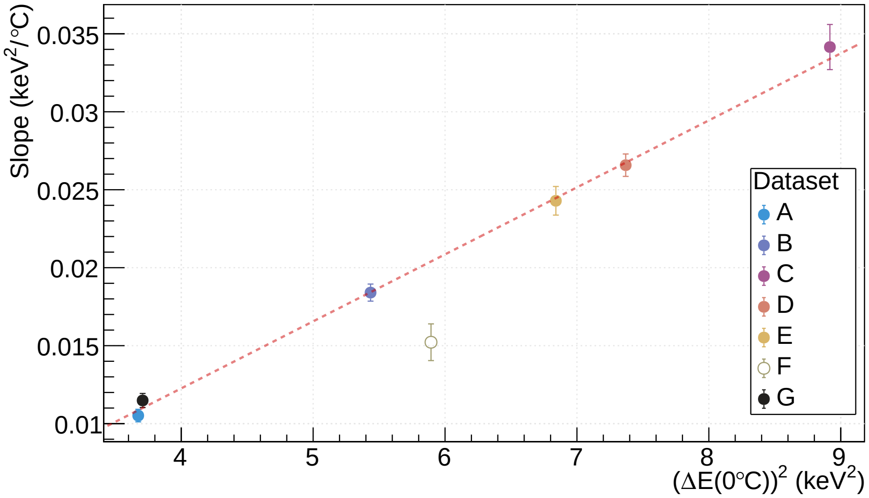

Figure 3.7: Fitted slope values ($d(\Delta E)^2/dT$) from Table 3.1, as a function of the squared energy resolution at $T = 0\,°\mathrm{C}$. The dotted line is a linear fit ($y = mx+b$) to the points, excluding dataset F. The fit gives $m = (4.3 \pm 0.2) \times 10^{-3}$ /°C and $b = (-4.9 \pm 0.8) \times 10^{-3}\,\mathrm{keV}^2/°\mathrm{C}$ with $\chi^2/\mathrm{ndf} = 2.2/4$.

chain [133, 134]. Of relevance for the present analysis are the shape of the distributions. The current noise and flicker noise both peak at low frequencies; in contrast, the voltage noise dominates at high frequencies but flattens out at low frequencies.

In Figure 3.8b, measured power spectral densities sampled from previous years are shown. By comparing the changes in the shapes of the spectra to the simulated noise sources, it is possible to deduce which noise sources have also changed. There is little variability in the measured datasets at high frequencies, which implies that the voltage noise is stable. The relatively large changes in the distributions at low frequencies must be due to current and/or flicker noise. However, as the temperature dependence of the FPD energy resolution has shown, the increase in noise must be primarily due to current or voltage noise. Thus, the temperature analysis and the shape of the noise spectrum isolates current noise as the source of the degraded FPD energy resolution. Additional current noise is generated from a reduced value of the total parallel resistance, R_P, as shown in Equation 3.8.

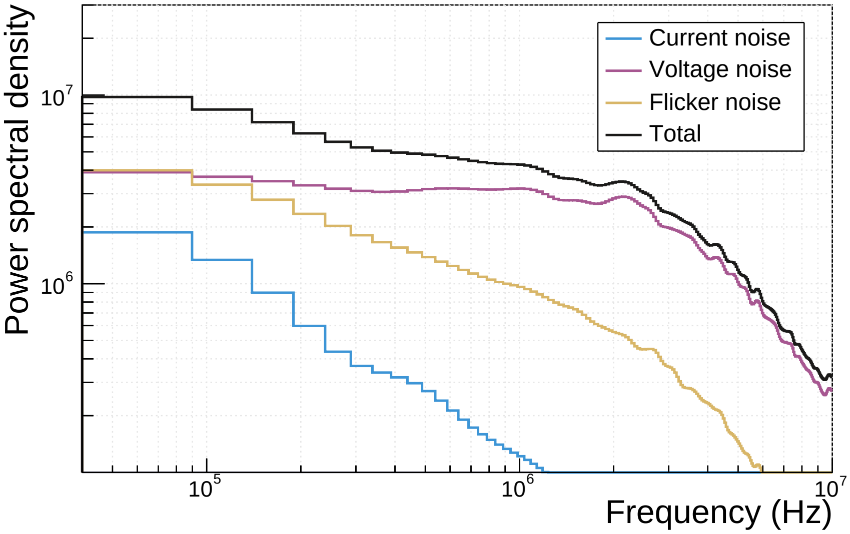

(a)

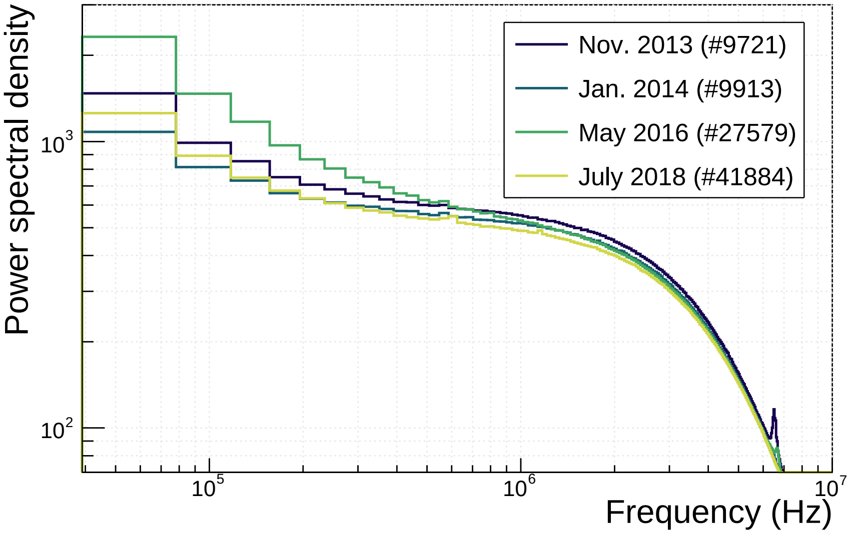

(b)

Figure 3.8: (a) Simulated FPD noise spectra for different noise components. The relative amplitude of each noise source was determined from a fit to the noise spectrum of FPD run #1830, as described in [150]. A shaping length of 6.4 µs was used to generate the data with DRIPS. The histograms were smoothed to reduce fluctuations. (b) Measured FPD noise spectra. The FPD run number for each dataset is shown in the legend. Both figures are based on [146, 150].

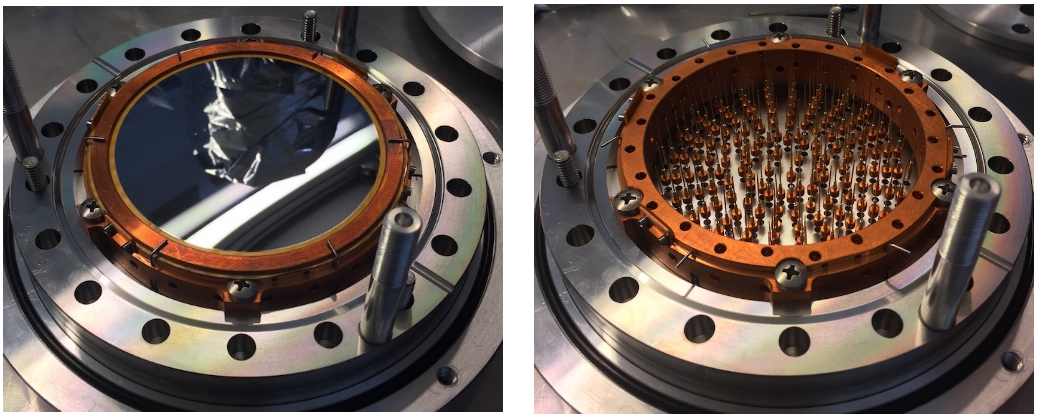

(a) (b)

Figure 3.9: (a) Wafer installed on a feedthrough flange. (b) Flange without wafer installed. The pogo pins that make electrical contact with each pixel are visible. Both photos are taken from the KATRIN ELOG.

A viable source of this noise is excess parallel resistance located near the carousel [146]. This could be caused by surface contamination or degraded insulation. One possibility is decreased inter-pixel resistance on the detector wafer. However, measurements have shown that the inter-pixel resistance is greater than 100 GΩ for wafer #115876 (from the same batch as wafer #115878, which was used for SDS-II and SDS-III); a value less than 1 GΩ is required to explain the data [137]. It is also possible that decreased pin-to-pin resistance on the feedthrough is responsible. This does not seem to be the case, since the pin-to-ground resistance of the feedthrough flange has been measured to be greater than 20 GΩ. Photos of the feedthrough flange with and without a wafer are shown in Figure 3.9.

3.2.4 Changes in the Energy Resolution

The rise in energy resolution seems to occur exclusively during hardware breaks between measurement campaigns. The exception to this fact is during SDS-IIIb, when a large Penning discharge seems to have improved the energy resolution, as described below. In this subsection, possible sources of rise in energy resolution are investigated by observing the effect of several hardware modifications.

Effect of Wafer: SDS-I and SDS-II

A significant rise in the energy resolution occurred between the SDS-I and SDS-II measurements (see Figure 3.6). During this time period, the FPD system underwent significant maintenance: large portions of the FPD system were disassembled, and the detector wafer was also exchanged. The rise in energy resolution was deemed acceptable at that time since all pixels on the new wafer (#115878) worked, in contrast with the previous wafer (#96724) which had two electrically shorted pixels [34]. A pixel-by-pixel comparison of the energy resolution between the two wafers is shown in Figure 3.10. Although a slight radial dependence is evident in the SDS-I data, the effect is much more pronounced in the SDS-II data, where the resolution is noticeably worse for the outermost pixels.

Wafer #115878 came from a newer production batch than wafer #96724 [34]. One could imagine that a change in the wafer manufacturing process caused the resolution degradation.

Effect of Wafer: SDS-II and SDS-IIIa

The detector system was also disassembled between the second and third spectrometer commissioning phases [145]. A different wafer (#115875) was installed and tested, although this new wafer exhibited a degraded energy resolution ($\Delta E = 3.05\,\mathrm{keV}$ at $0\,^{\circ}\mathrm{C}$). The previously installed wafer (#115878) and its flange were kept in a sealed, nitrogen-filled container during the tests with wafer #115875 [145]. It was decided to reinstall wafer #115878; however, after reinstallation, a deterioration in the energy resolution was observed during SDS-IIIa compared with the performance during SDS-II (see Figure 3.10). Because the same wafer was used for the two measurement phases, some component other than the wafer is likely responsible for the resolution degradation.

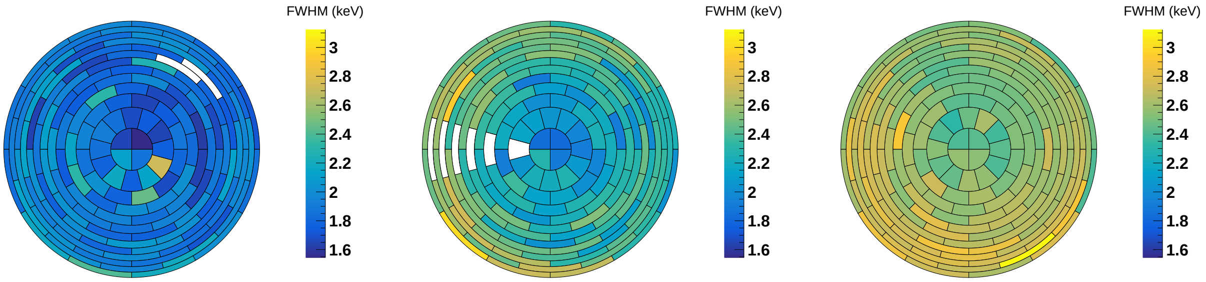

(a) $\overline{\Delta E} = 1.91$ keV (b) $\overline{\Delta E} = 2.32$ keV (c) $\overline{\Delta E} = 2.61$ keV

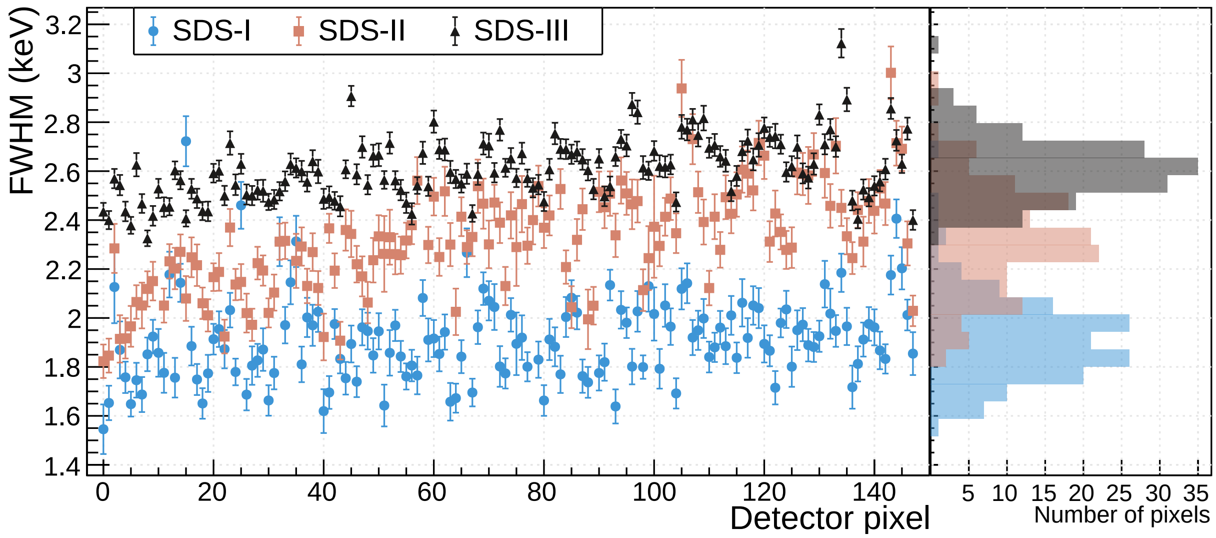

(d)

Figure 3.10: Pixel energy resolution during (a) SDS-I (FPD runs #5449–5450, wafer #96724), (b) SDS-II (FPD runs #25157–25161, wafer #115878), and (c) SDS-III (FPD runs #30165–30188, wafer #115878). The data have been adjusted to a carousel temperature of 0 °C. The white detector pixels in (a) and (b) are excluded from analysis due to electrical shorts affecting two pixels (SDS-I) and a broken preamp card affecting six pixels (SDS-II), respectively. The energy resolutions are displayed together in (d).

Effect of Wafer: SDS-IIIa and SDS-IIIb

Between the first and second parts of SDS-III, another test wafer (#115877) was installed in the detector system, with wafer #115878 temporarily being removed from the system. Wafer #115877 exhibited a similar energy resolution ($\Delta E = 2.65\,\mathrm{keV}$ at $0\,^{\circ}\mathrm{C}$) but was not installed due to an indication of shorted pixels. (A wafer testing device has been developed [137] which allows automated electrical tests of a flange-mounted wafer.) When wafer #115878 was reinstalled, the measured energy resolution appeared to be unchanged from the value observed during SDS-IIIa. This lack of change in resolution is strange because a similar wafer-swapping scenario between SDS-II and SDS-III saw a rise in energy resolution, as described above.

Effect of the Feedthrough Flange

A cooling failure during December 2013 (between SDS-I and SDS-II) resulted in the FPD electronics reaching a temperature close to $100\,^{\circ}\mathrm{C}$. After disassembling the system, an oily residue was observed on the walls of the high vacuum chamber, where the vacuum electronics are installed. The oily residue was also observed on the preamplifier side of the feedthrough flange (Figure 3.11a). This substance is thought to be plasticizer emitted from the cabling during the high-temperature operation. The affected components were cleaned with ethanol.

Two feedthrough flanges are available for mounting wafers to be installed in the FPD system. Wafer #115878, which has been used for measurements during SDS-II and SDS-III, has always been installed on the same feedthrough flange (the “primary” flange). When wafers #115875 and #115877 were temporarily installed in the system, the spare feedthrough flange was used.

Between April 2017 and June 2017, the FPD system was disassembled for maintenance. At this time, a gray residue was noticed on the preamp-facing side of both the primary and the spare flange (Figure 3.11b). Neither ethanol nor citric acid removed the residue, but application of acetone was successful. The preamplifier sides of both flanges were cleaned.

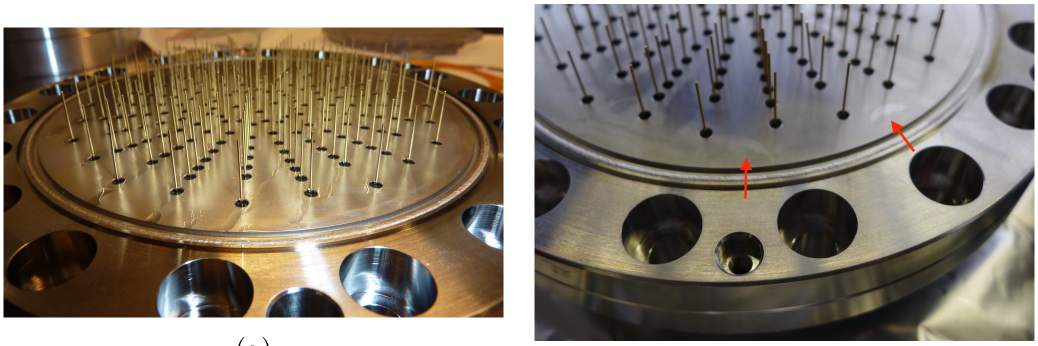

(a)

(b)

Figure 3.11: (a) Preamplifier-facing side of the feedthrough flange with oily substance (likely plasticizer) in April 2014, prior to cleaning. (b) Gray residue on a feedthrough flange in May 2017, prior to cleaning. The arrows point to crescent-shaped regions where the residue has been removed. Photos taken from the KATRIN ELOG.

Additionally, the copper carousel that is situated between the flange and the preamp cards was cleaned with citric acid. After reassembling the system, the energy resolution did not appear to be significantly affected by the cleaning procedure (Figure 3.12). However, it is interesting to note that this maintenance period (between SDS-IIIa and SDS-IIIb) is unique from others in that no rise in energy resolution occurred. The handling of the wafer and other components did not change significantly compared with the previous maintenance phases. Thus, it is possible that the cleaning may have suppressed the typical effect from the maintenance phase, although this idea is purely speculative. It is clear, however, that cleaning the preamplifier side of the feedthrough flange has not proven successful in returning the energy resolution to previously measured values.

Effect of the Electronics

Because the resolution degradation has occurred during periods of maintenance when the FPD system was disassembled and exposed to air, the increase in resolution may be due to changes in the electronics readout chain. For instance, electronics could be damaged or

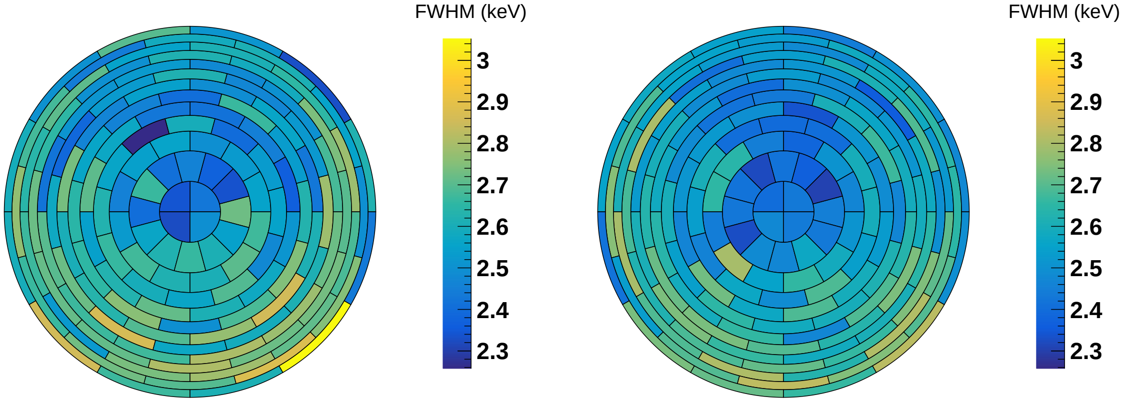

(a) $\overline{\Delta E} = 2.60$ keV (b) $\overline{\Delta E} = 2.57$ keV

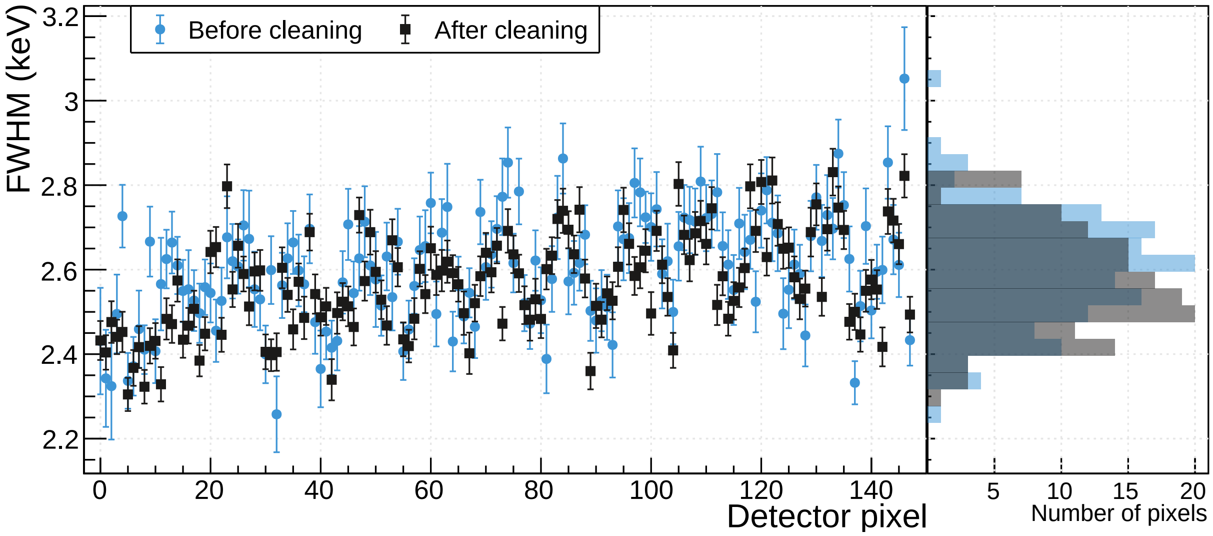

(c)

Figure 3.12: Pixel energy resolution (a) before cleaning the preamplifier side of the feedthrough flange (April 2017, FPD runs #32632–32639) and (b) after cleaning (August 2017, FPD runs #33618–33636). The data have been adjusted to a carousel temperature of 0 °C. The pixel-by-pixel comparison is shown in (c).

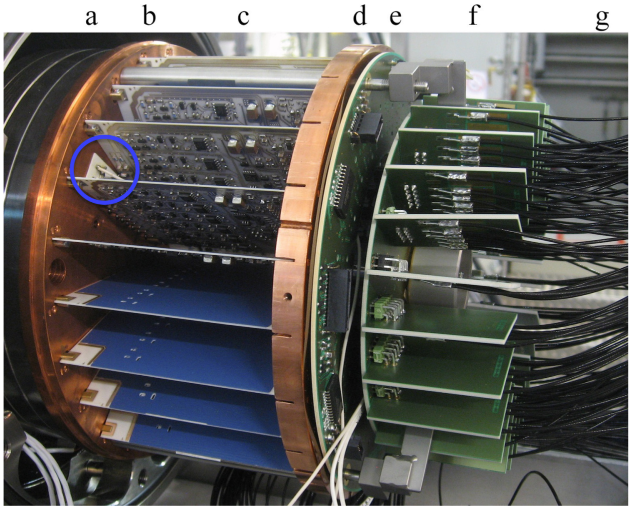

Figure 3.13: The vacuum electronics in the FPD system. Many components have been cleaned or exchanged during the last several years of detector maintenance. (a) Feedthrough flange: exchanged and partly cleaned; (b) copper carousel: cleaned; (c) preamplifier cards: card #14 replaced twice; (d) copper ring: cleaned; (e) power-and-control distribution board: unchanged; (f) cable harness with (g) cabling: replaced. The carousel temperature sensor is circled in blue. Figure adapted from [130]. Used with permission from Elsevier.

improperly connected, or one or more of the components could react with the air.

Several components in the FPD readout chain have been upgraded or replaced over the last several years. A photograph of the vacuum electronics is shown in Figure 3.13, and details about the changes to the system are given in the caption. Preamplifier card #14 was replaced twice due to being physically broken. Other parts were upgraded to improve performance. The new cable harness, for instance, reduced outgassing, and the pressure in the high vacuum chamber improved by about a factor of 100 after its installation. Several ambient-air components in the read-out chain were also switched out, including the power and control board, two optical sender boards, a first-level trigger card, and the bias voltage power supply (see Figure 2.11). However, after all of these replacements, no improvement was observed in the energy resolution. In addition to hardware changes, power supplies and corresponding voltages were varied in an attempt to reduce the resolution, but to no avail.

Between December 2016 and February 2017, the FPD system was turned off, including the vacuum pumps. During this time, the high vacuum chamber reached a pressure close to 100 mbar, which is significantly higher than standard operating conditions (~10^{-6} mbar). However, no change was observed in the energy resolution after the system was brought back into measurement mode. Thus, exposure of the vacuum electronics to air does not seem to affect the energy resolution.

Effect of the Penning Discharge

A very large Penning discharge occurred during the SDS-IIIb commissioning measurements, which resulted in damage to the detector wafer. Details of this event are described in section 8.3.2. Comparing data taken before and after the Penning discharge, a noticeable reduction in detector efficiency was observed for specific pixels. However, the discharge also seems to have improved the energy resolution (Figure 3.14). The decrease is uniform across the entire wafer. This is in contrast with the reduced detector efficiency, which is localized to a specific set of pixels. If the improved energy resolution was caused by the high particle flux during the Penning discharge, it would seem to indicate that source of the degradation is on the wafer-facing side of the feedthrough flange, since it is difficult to imagine how other FPD components could have been affected by the discharge.

Effect of Wafer: After First Tritium

Due to the discharge-induced damage suffered by the wafer, it was decided to replace the wafer used during and prior to First Tritium (#115878). Several wafers were installed and tested in the system. Wafer #115875 exhibited poor energy resolution ($\Delta E = 3.09\,\mathrm{keV}$ at 0 °C); wafer #76040 had extremely high noise levels on the inner pixel rings, making those rings unusable. The outer rings had an average energy resolution of 2.48 keV at 0 °C. These two wafers came from the third and first production batch, respectively.

The final wafer to be tested was wafer #96725, from the second production batch, and it exhibited very good energy resolution (Figure 3.15). In fact, the energy resolution with this wafer is only slightly worse than the excellent energy resolution seen with the system

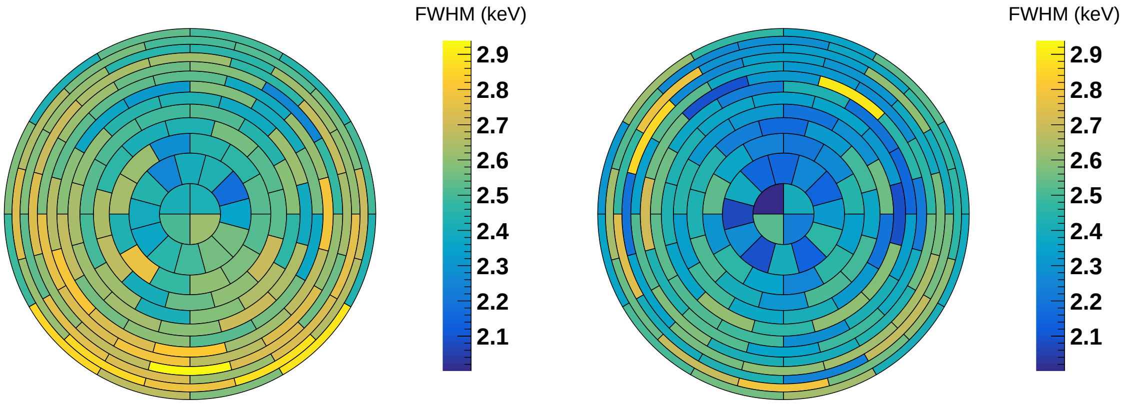

(a) $\overline{\Delta E} = 2.57$ keV

(b) $\overline{\Delta E} = 2.41$ keV

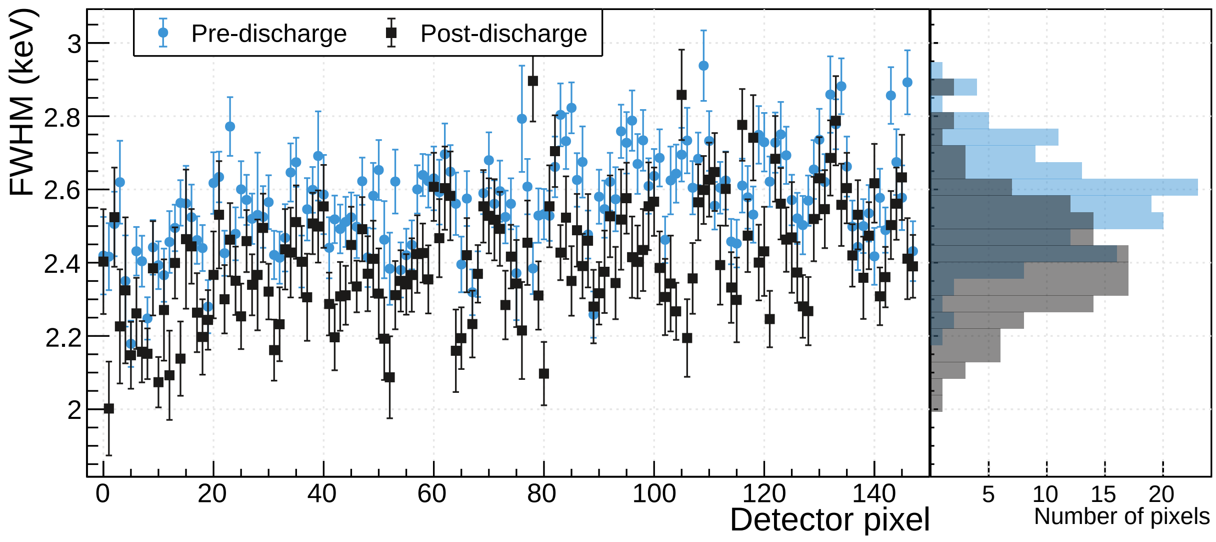

(c)

Figure 3.14: The effect of the Penning discharge on FPD energy resolution. (a) and (b) show the energy resolution before the discharge (FPD runs #34154–34161) and after the discharge (FPD runs #34497–34500), respectively. The data have been adjusted to a carousel temperature of 0 °C. The same values are shown together in (c).

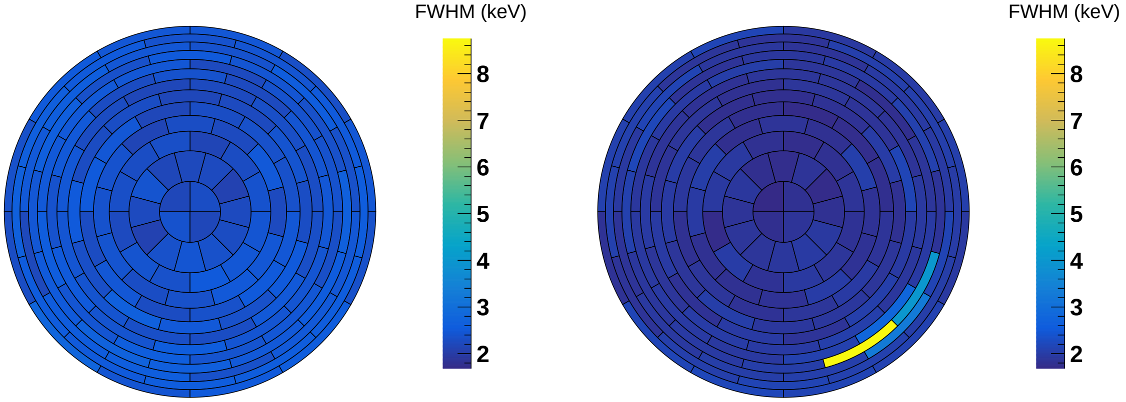

(a) $\overline{\Delta E} = 2.41$ keV (b) $\overline{\Delta E} = 2.00$ keV

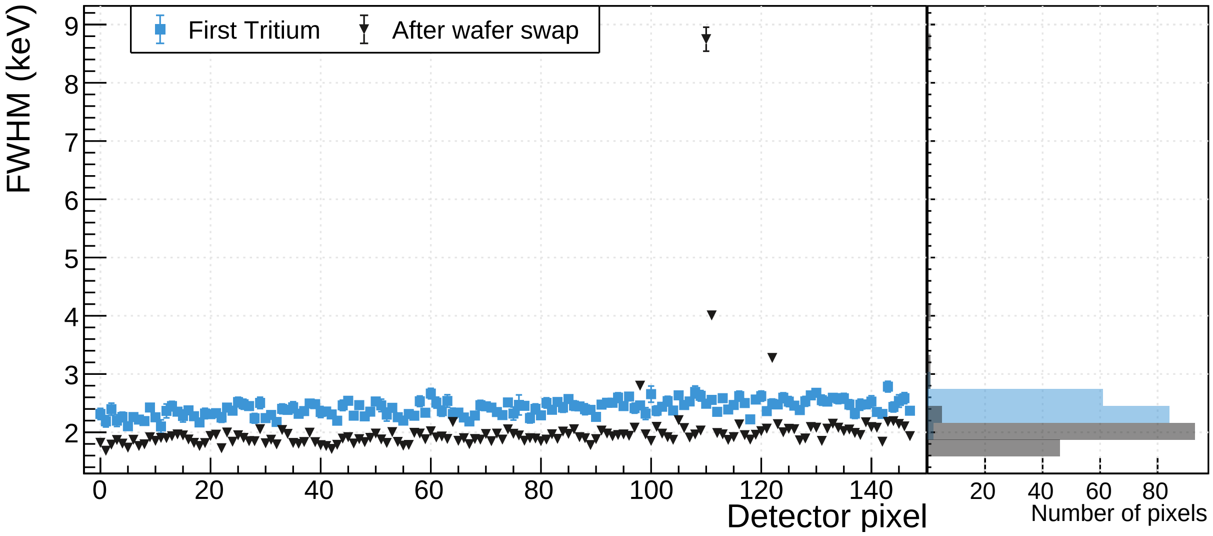

(c)

Figure 3.15: Pixel energy resolution during (a) First Tritium (FPD runs #40425–40430, wafer #115878) and (b) after First Tritium (FPD runs #41267–41272, wafer #96725). Pixel #110 has been excluded from the latter. The data have been adjusted to a carousel temperature of 0 °C. The energy resolutions are compared in (c).

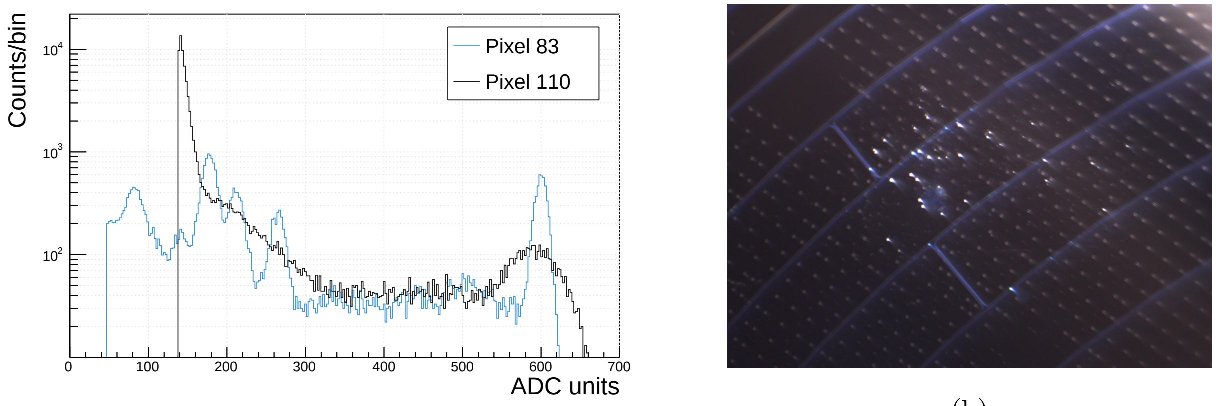

(a)

(b)

Figure 3.16: (a) Comparison of the energy spectra obtained with two different pixels from wafer #96725. Pixel 110 has about four times worse energy resolution than pixel 83. (b) Contamination in the surface of wafer #96725. This affected surface may explain the degraded resolution for pixel 110. Photo taken from the UW KATRIN ELOG.

during SDS-I[1]. However, one pixel (#110) showed very poor energy resolution (~8 keV; see Figure 3.16a), with several neighboring pixels exhibiting a partly degraded energy resolution. This wafer was previously examined under a microscope; at that time, contamination in the surface by dust-like deposits was observed for localized regions of the wafer (Figure 3.16b). This contamination seemed to be part of the wafer and is likely a result of the manufacturing process. The poor energy resolution for pixel #110 and its neighboring pixels may be due to this contamination.

Due to the otherwise excellent wafer performance, wafer #96725 was deemed acceptable as a replacement. This wafer is planned to be used for future commissioning measurements. Care must be taken, however, to incorporate the poor energy resolution of pixel #110 into the data analysis procedure.

---

[1] An even better energy resolution was observed during detector commissioning, but in that case a 6.4 µs shaping length was utilized, rather than a 1.6 µs shaping length.

Batch	Wafer	When in use	ΔE (keV)	Note
1	76040	2018 (test only)	2.5	Many very noisy pixels
2	96724	2013 (SDS-I)	1.9	Pixels #78 and #89 are shorted
	96725	2018 (STS-IIIa)	2.0	Pixel #110 is very noisy
	96728	2012	1.8	Pixels #73 and #74 are shorted
3	115875	2016, 2018 (test only)	3.1	Several noisy pixels
	115877	2017 (test only)	2.7	Mechanically damaged
	115878	2014-2018 (SDS-II, SDS-III)	2.3	Damaged by Penning discharge

Table 3.2: Detector wafers installed and tested in the FPD system at KIT. The listed energy resolutions exclude shorted or very noisy pixels.

3.2.5 Conclusions

Several conclusions can be drawn from the energy resolution measurements. First, the energy resolution is stable during standard detector operation and data-taking. The resolution increase is due to some effect that generally occurs as a result of detector maintenance. Second, temperature is directly correlated with the energy resolution but cannot explain the large increases in energy resolution. An analysis of the temperature dependence indicates that parallel noise is responsible for the rise in energy resolution.

The wafer batch appears to have a large effect on the energy resolution. From the measurements performed so far, it appears as though wafers from the second production batch have significantly better energy resolution than those from the third batch. This information is summarized in Table 3.2.

The energy resolution is on average worse for the outermost pixels. The reason for this radial dependence is not well understood, since noise modeling predicts a larger noise for the innermost pixels [150]. Due to the way the wafer is mounted, there could be stress on the wafer, distributed in a radial manner. However, test measurements several years ago saw no effect on energy resolution due to stress on the wafer [151]. Another possibility is that the inner pixels experience better cooling than the outer pixels [123].

Cleaning or replacing components on the preamplifier-side of the feedthrough flange has not improved the energy resolution. However, the wafer-facing side of the flange has not

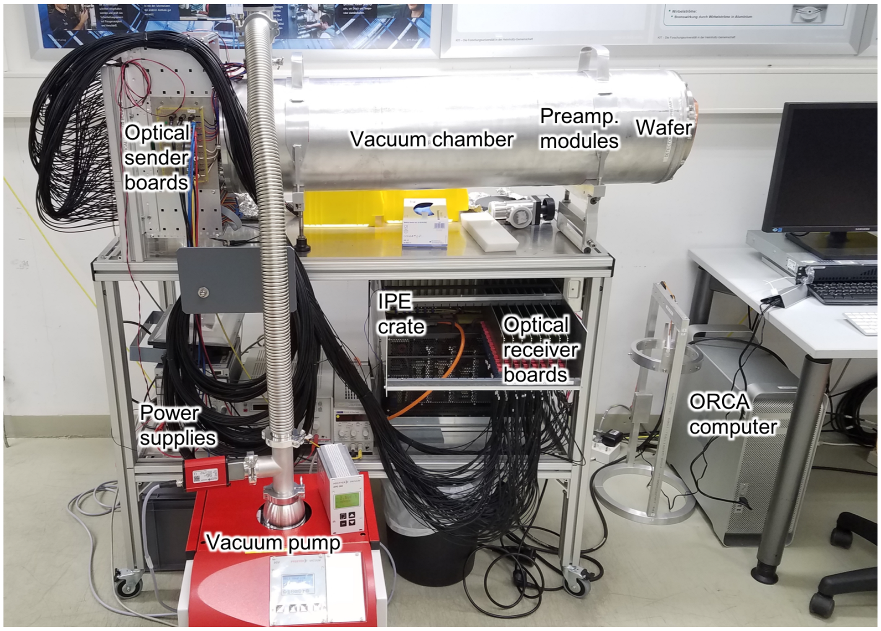

Figure 3.17: Photo of the wafer test stand, as installed underneath the detector platform at the spectrometer hall.

been cleaned during maintenance periods. Exposing the wafer and its mount to a high flux of radiation (from a Penning discharge) did moderately improve the resolution. This could indicate a surface buildup of material, which was subsequently removed by the radiation. From these facts, it seems probable that the increased energy resolution could be partly explained by some surface effect on the wafer-facing side of the feedthrough flange.

A wafer test stand (Figure 3.17) has been built and is now in operation at KIT [152]. This device will enable characterization of detector wafers outside of the FPD, using a duplicate DAQ hardware chain. One important use of the setup will be testing five new wafers recently purchased from the manufacturer. By studying the available wafers and feedthrough flanges, a thorough understanding of the mechanism behind the energy resolution degradation will hopefully be reached.

Chapter 4

SPECTROMETER BACKGROUND AND SECONDARY ELECTRON EMISSION

The backgrounds from the PS and MS have been investigated in detail during several years of commissioning measurements. In this chapter, the various sources of spectrometer background electrons are described (section 4.1), as well as the methods (both passive and active) that have been developed to mitigate these sources. A description of the KASSIOPEIA simulation package is then provided, due to its critical role in studying background processes in KATRIN (section 4.2). Finally, the simulation software is applied to study secondary electron (SE) emission from the spectrometer surface (section 4.3).

4.1 Background Sources

Although the signal electrons have energies close to 18.6 keV before entering the MS, inside the spectrometer their energies are drastically reduced due to the retarding potential. Low-energy electrons that are produced inside the MS have almost identical energies as the signal electrons and cannot be distinguished by the FPD. This is shown in schematically in Figure 4.1.

A wide array of background sources exists in electrostatic spectrometers; a graphical overview is shown in Figure 4.2. The most important background sources will now be described, as well as the developed means of combatting them, ranging from material selection to the design of the apparatus to the applied electromagnetic fields.

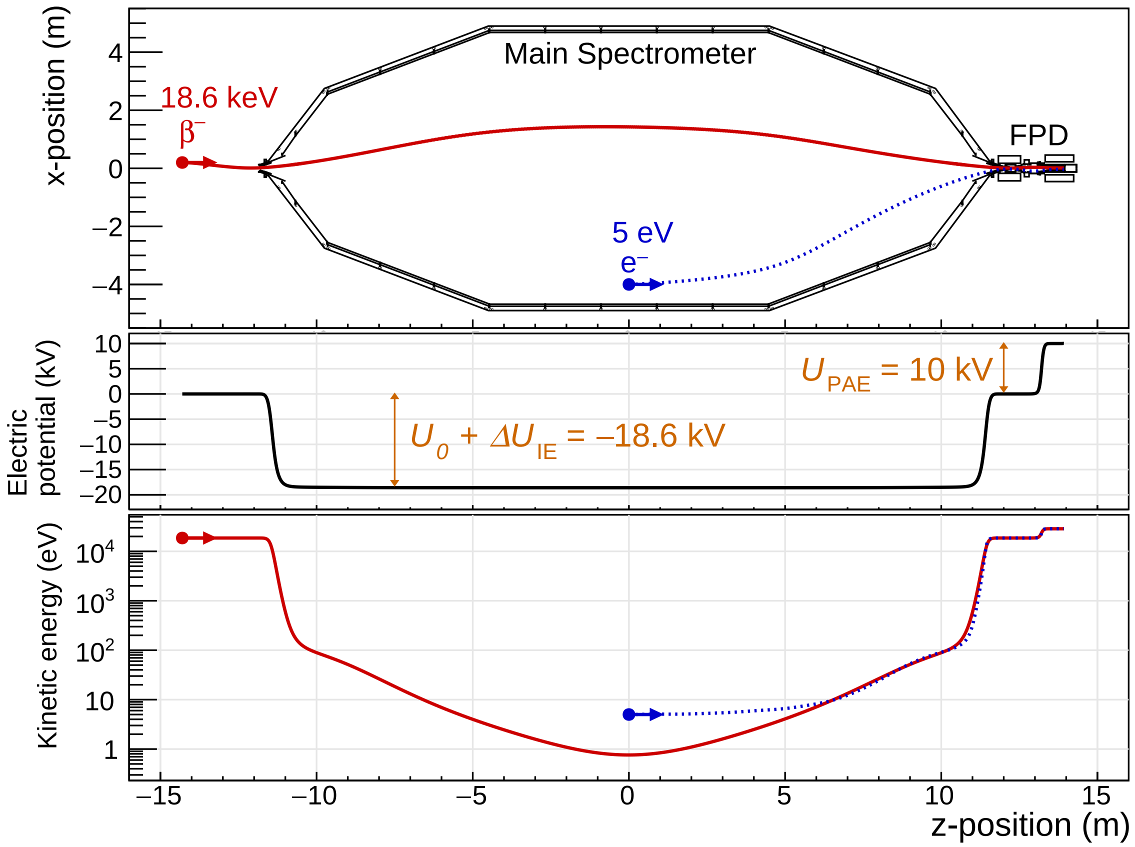

Figure 4.1: Schematic of electron transport inside the MS. The upper plot shows two particle tracks: a through-going β-particle (solid red line) and a secondary electron (SE) produced inside the vessel (dotted blue line). The electrons spiral around the magnetic field lines as they travel, although this motion is too small to be observed here. The middle plot shows the electric potential along the β-particle track, with labels indicating the important voltage contributions. The lower plot shows the energy of the two particles as a function of z-position. Due to the finite energy resolution of the FPD, the two particles cannot be distinguished.

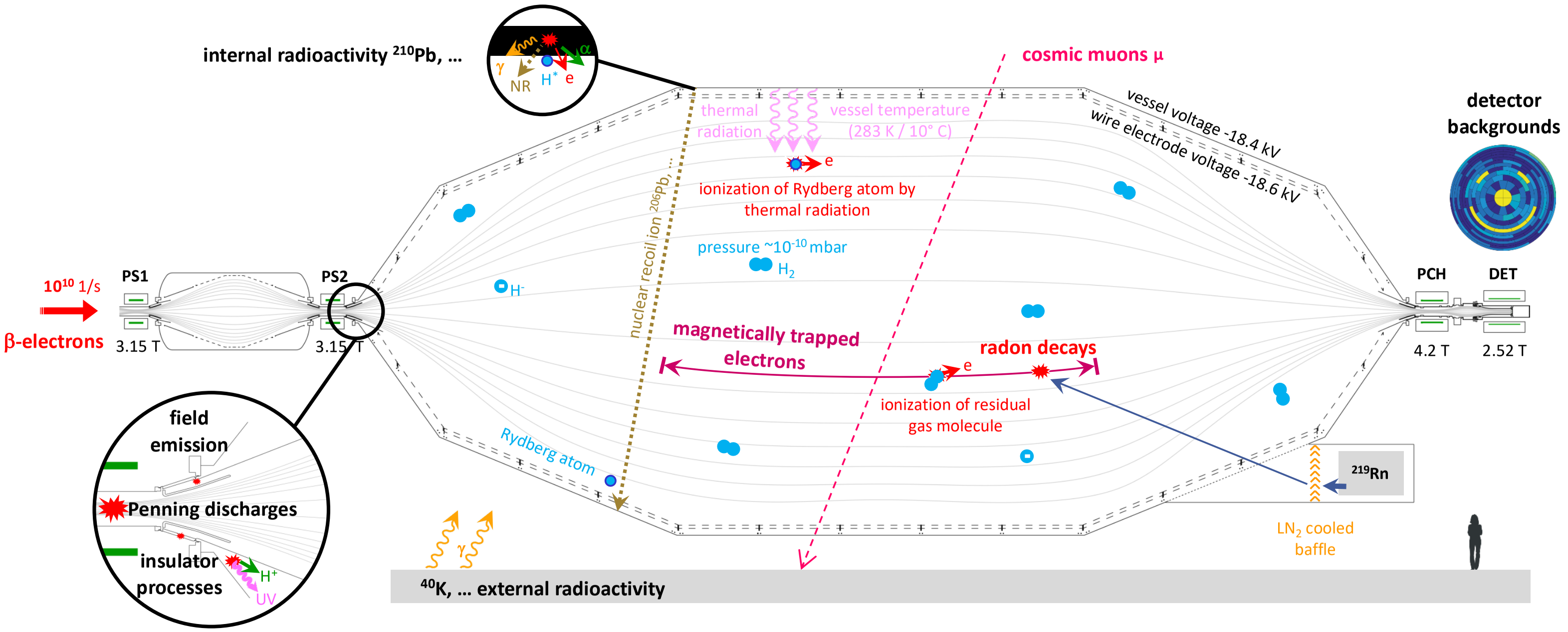

Figure 4.2: Background processes in the MS. Figure courtesy of Florian Fränkle, with adaptations.

4.1.1 Tritium Gas and Ions

A contamination of the MS with tritium gas or ions will spoil the KATRIN measurement because the resultant β particles will create a background spectrum that obscures the spectrum emitted from the WGTS. As discussed in section 2.1, the STS is responsible for reducing the neutral tritium flow entering the PS by 14 orders of magnitude [73] through a combination of turbo-molecular and cryogenic pumping. The background from tritium gas should therefore be mitigated, assuming the pumping sections operate within specifications.

However, over 10^{11} tritium ions per second are produced in the WGTS due to ionization of the tritium gas by β-decay and subsequent collisions [153]. These ions (such as T_3^+) are not removed by pumping since charged particles will follow the magnetic field lines. Alternative methods are therefore required to prevent these ions from entering the MS.

Countermeasure: Blocking Electrodes

An ion blocking/removal concept using a series of electrodes has been developed (Figure 4.3). Ring electrodes, elevated to a small positive voltage (100 V) block the low-energy positive ions while allowing β-particles to pass through [153]. Positive ions, therefore, are trapped in the STS, prevented from traveling downstream by the ring electrodes and upstream by the gas flow in the WGTS [153]. To remove the ions, the dipole electrodes in the DPS are used. A negative voltage (−100 V) applied to one side of the dipole electrode will drift the ions out of the beam tube, where they can be neutralized [153]. Additional details about this ion blocking scheme and its effectiveness can be found in [154].

4.1.2 Ionization from Scattering of β-particles

Ionization of residual gas inside the MS results in low-energy electrons which cannot be distinguished from the signal β-particles. Of particular concern is the ionization caused by β-particles. Because of the analyzing potential of the MS, most β-particles only traverse a small region of the MS near its upstream entrance. Ionization electrons produced at this

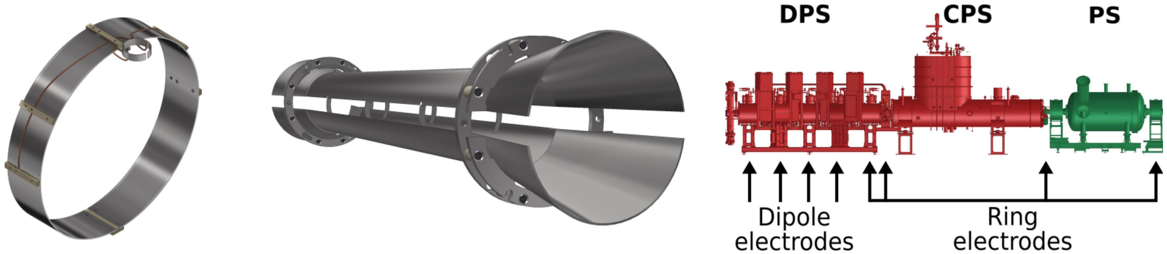

(a) (b) (c)

Figure 4.3: (a) A ring electrode, used to block ions. (b) A dipole electrode, used to drift ions out of the beam tube. (c) Location of electrodes in the transport section and PS. Figures adapted from [153]. Used under the CC BY 3.0 license [120].

location will not be able to reach the detector. However, positive ions produced from the ionization process will be accelerated into the negatively charged MS. These ions can ionize residual gas in regions of the vessel where the resultant electrons can reach the FPD.

As discussed in section 2.2, both spectrometers are designed to operate at UHV conditions. This limits the amount of residual gas available for scattering and ionization. Calculations have indicated that no significant background rate due to β-scattering is expected, as long as a positive blocking electrode is used between the spectrometers [116]. However, this prediction must be substantiated with measurements. During the First Light commissioning campaign, a measurement was performed in which a flux of about 10^8 electrons, produced from UV illumination of the rear wall, entered the MS [103]. These electrons had energies close to 110 eV, which is well below the analyzing energy (18.6 keV) of the MS. These electrons should therefore be reflected at the entrance to the MS and not reach the FPD. Under these conditions, an elevated detector rate was observed, about a factor of four higher than the rate with no electrons [103]. The use of the positive blocking electrode between the spectrometers did significantly reduce this rate increase, but an elevated rate still remained.

This measurement was performed with an electron rate about a hundred times smaller than expected during tritium operation; thus, one naively expects a large background contribution from this scattering. However, certain abnormal conditions during this measurement (e.g., a non-baked MS, low electron energies, electron reflections at the rear wall) increased the background rate, and these will not be present during standard operation [103]. Nonetheless, it is important to have some method available to mitigate this background in case its contribution is larger than predicted.

Countermeasure: Pre-Spectrometer

Because KATRIN is only concerned with measuring β-particle energies close to the endpoint energy, it is permissible to block the portion of the spectrum below about 18.3 keV. By only allowing the highest energy electrons to reach the MS, the amount of scattering-induced ionization drops significantly. This pre-filtering is achieved with the PS, which is designed to operate at a retarding potential as large as $-18.3\,\mathrm{kV}$ [74].

During the First Light measurement discussed above, placing the PS at a small retarding potential ($-300\,\mathrm{V}$) resulted in the background rate returning to its reference value, thereby mitigating the scattering due to the electron beam [103]. Thus, the PS seems to be effective in preventing background from β-induced ionization. Future commissioning measurements will be needed to confirm this result under nominal operating conditions.

4.1.3 Penning Traps

Penning traps are formed in regions of strong electric and magnetic fields and result in the storage of charged particles. These creation conditions can be satisfied in multiple locations along the KATRIN beamline. The build-up of charged particles in such a trap can lead to a Penning discharge, where charges flow between a cathode and an anode [139]. This discharge can lead to an electric breakdown [139]. Although the trapped particles cannot directly reach the detector, messenger particles (such as ions or photons [139]) can escape the trap and ionize residual gas to produce detectable background.

Countermeasure: Electrode Design

The creation of Penning traps and their background generation was noticed during the commissioning of the PS [114, 155]. Trapping conditions were present in the region of the cone electrode, ground electrode, and flange, on both ends of the PS. These traps caused electrical breakdowns as well as extremely high background rates [155]. To prevent the formation of these traps, newly designed "anti-Penning" electrodes were installed between the ground electrodes and cone electrodes. The anti-Penning electrodes are electrically connected to the hull and disrupt the Penning trap storage conditions. Measurements showed the success of this solution, after redesigned ground electrodes were also installed [155]. As a result, similar anti-Penning and ground electrodes were produced for the MS, and no background from Penning traps has been observed in the location of these electrodes [156].

Countermeasure: Sweeping/Static Wire

Placing the PS on high voltage, although reducing the flux of β-particles into the MS, results in the formation of a Penning trap for electrons between the spectrometers. This trap cannot be avoided as long as both spectrometers are placed on negative high voltage, which is the design configuration. A sweeping or static wire can be used to remove electrons in the Penning trap. The nature of this trap, its contribution to the background rate, and testing of the removal mechanism will be discussed in detail in chapter 7 and chapter 8.

4.1.4 Surface Electron Emission

A number of processes result in the emission of electrons from the spectrometer surface [157]. Natural radioactivity, mainly located in the concrete of the spectrometer hall, produces gammas with enough energy to travel through the walls of the MS. These gammas can excite SEs from the surface into the volume of the vessel. Muons produced from cosmic rays also easily penetrate the walls of spectrometers and can induce SEs. The inner surface of the MS provides a large area for electron emission ($690\,\mathrm{m}^2$ for the steel hull and $532\,\mathrm{m}^2$ for the wire electrode system) [117, 158]. The backgrounds induced by cosmic-ray muons and environmental gammas will be discussed in detail in chapter 5 and chapter 6, respectively.

Additionally, strong electric fields near the spectrometer surface can produce electrons. This process, called field emission, lowers the potential barrier for tunneling out of the material [157]. Field emission was measured during SDS-I [123, 157] but was not observed during SDS-II or thereafter [34]. Although not fully understood, this disappearance may be the result of better symmetry of the magnetic field or different bake-out procedures [34].

"True secondary" electrons emitted from the inner surface of the MS have low energies, below about 50 eV [159]. Their energy spectrum will be discussed in detail in section 4.3.2. Because these electrons are low-energy, several shielding methods are available, which are described below.

Countermeasure: Magnetic Shielding

The standard magnetic field in the MS naturally shields the flux tube from low-energy charged particles emitted from the walls. The particles experience a Lorentz force due to the magnetic field and are deflected back into the walls via a circular path. If particles do succeed in escaping the surface (through a process like that shown in Figure 4.4a), they will generally be guided by the magnetic field lines close to the walls and will not reach the sensitive volume of the flux tube [139]. However, the presence of any axial asymmetries in the electric and magnetic fields can cause the electrons to drift to smaller radii and contribute to the background rate [80]. Nonetheless, the magnetic shielding is expected to reduce the background from surface electron emission by about 10^5 [80].

Countermeasure: Electrostatic Shielding

In order to achieve a background rate of 10 mcps from surface electron emission in the MS, a total background reduction of 10^7 is required [80]. Thus, additional mitigation beyond the inherent shielding of the magnetic flux tube must be implemented. This further background reduction is accomplished through electrostatic shielding, in the form of the wire IE system

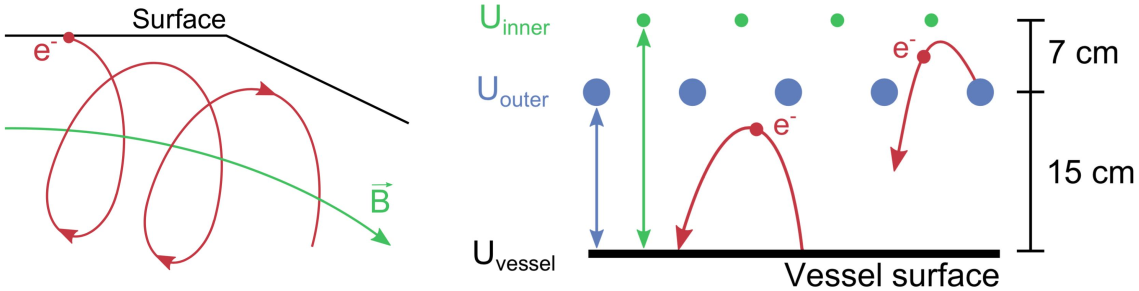

(a)

(b)

Figure 4.4: (a) If the magnetic field is not perfectly parallel to the vessel surface, electrons will not necessarily be deflected back to the surface but can travel along the magnetic flux tube. (b) The principle of the inner electrode system, consisting of two layers of wires, shown by the blue and green circles (the wires are oriented perpendicular to the page). The shielding is effected by setting $U_{\text{inner}} < U_{\text{outer}} < U_{\text{vessel}}$. Electrons emitted from the vessel will be electrically repelled by the offset voltage applied to the wires. Both figures taken from [34].

installed inside the MS [121]. A graphical representation of the two-layer IE is shown in Figure 4.4b. By elevating the IE system to an electric potential more negative than the spectrometer vessel, the wires reflect low-energy emitted electrons back to the vessel surface.

Each of the two layers of the wire electrode was designed to operate at a different voltage. In this way, the innermost wire grid can repel electrons emitted from the outer wire grid. A thinner wire is used for the innermost wire grid so that there is less area from which electrons can be produced and ejected into the volume. Due to electrical shorts caused by baking [117], however, the two wire layers are generally operated at the same voltage [34]. The effectiveness of both the IE system and the magnetic shielding can be ascertained by studying the muon-induced background (chapter 5) and the gamma-induced background (chapter 6).

4.1.5 Stored Particles (Radon)

The excellent energy resolution of a MAC-E-filter requires a low magnetic field in the analyzing plane and strong magnetic fields at both ends of the filter. Low-energy electrons produced upstream of the MS will not be able to bypass the spectrometer potential. However, charged particles that are produced in the low-field region near the analyzing plane can become magnetically trapped in the spectrometer, depending on their initial angle θ relative to the magnetic field. If B_{start} and U_{start} are the values of the magnetic field and electrical potential, respectively, where the electron with energy E_{start} is generated, and B_{max} is the maximum magnetic value at either end of the spectrometer, then the electron will be trapped if

$$\theta > \arcsin\left(\sqrt{\frac{qU_{\text{start}}}{E_{\text{start}}} \cdot \frac{B_{\text{start}}}{B_{\text{max}}}}\right), \tag{4.1}$$

where q is the charge of the electron [34]. This type of trap is known as the magnetic mirror trap or magnetic bottle, since the particle is trapped in the low-field region.

Using $B_{\text{max}} = 4.5\,\text{T}$ (at the PS1 magnet) as well as $B_{\text{start}} = 3.8\,\text{G}$ and $E_{\text{start}} = -18.6\,\text{keV}$ (at the MS analyzing plane), a 10 eV electron is trapped if its initial angle relative to the magnetic field is greater than 23.3°. For an electron with 10 keV, however, the electron is trapped for angles greater than 0.72°. Assuming isotropic creation of electrons inside the MS volume, the majority of high-energy electrons will be magnetically stored [160].

Once magnetically trapped, the electron will undergo several types of motion, as shown in Figure 4.5: axial, cyclotron, and magnetron motion. These three motions will be discussed in detail in the context of particle motion in a Penning trap (section 7.5.1). The cooling of the electron through collisions with residual gas can take minutes or even hours, during which large numbers of SEs can be produced [80].

Radon, primarily in the form of ^{219}Rn and ^{220}Rn, is a particularly concerning creator of stored electrons [162–164]. This background source was first noticed during commissioning measurements with the PS [165]. Emanating from the NEG pumps in the PS and MS, radon can easily travel into the spectrometer volume. With half-lives of less than a minute, ^{219}Rn

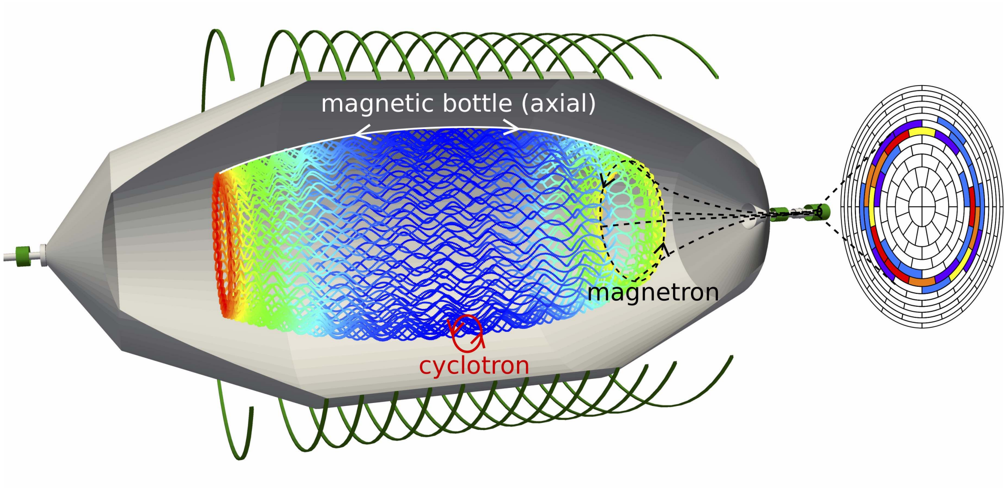

Figure 4.5: A high-energy electron produced in the MS can be magnetically stored for an extended period of time. Collisions with residual gas result in SEs that can reach the detector. A ring-shaped background pattern is visible on the FPD due to the magnetron motion of the stored electron. Figure taken from [161].

and ^{220}Rn cannot be substantially removed by turbo-molecular pumping before undergoing α-decay. Each decay can result in up to 20 electrons being produced from a combination of internal conversion, shake-off, and relaxation processes, with energies up to several hundred keV [166]. The high-energy electrons that are magnetically trapped inside the MS can prduce hundreds or even thousands of SEs via ionization with residual gas [80]. Measurements indicate that radon induces a MS background rate of several hundred mcps, if left unmitigated [34].

To eliminate the background from stored particles, both passive and active methods have been developed. The passive methods prevent the accumulation of electrons in the MS volume, while the active methods remove electrons that are already trapped. These strategies will now be described.

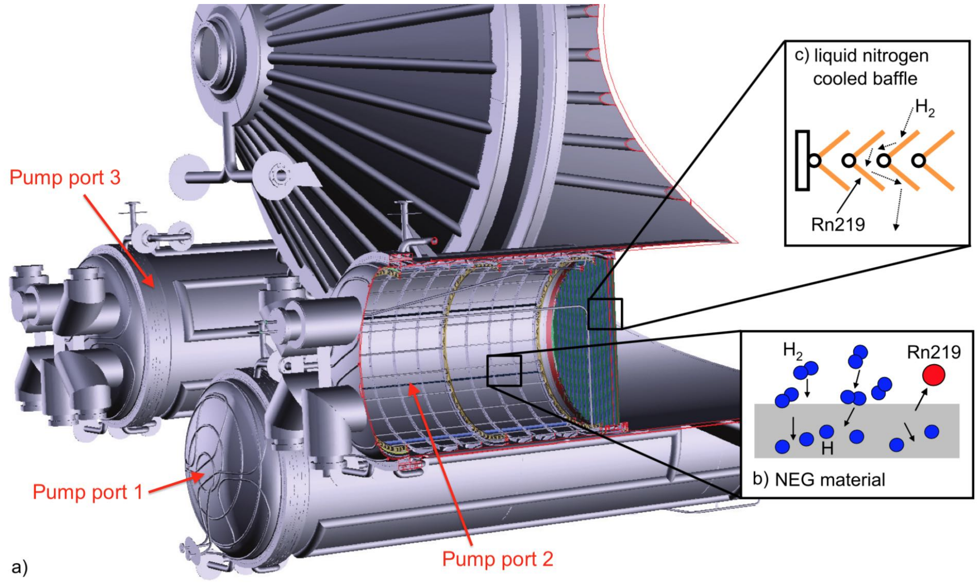

Figure 4.6: (a) Cutaway view of pump port 2 in the MS. (b) The NEG pumps adsorb hydrogen gas but emit radon. (c) Cooled baffles prevent the passage of radon into the MS volume but still allow hydrogen to be pumped. Figure adapted from [115].

Countermeasure: Cryogenic Baffles

The NEG pumps are the primary source of radon inside the MS, which emanates from the getter material [115]. To block the radon flow, baffles were installed between the pump ports and the spectrometer volume (Figure 4.6). These baffles are cooled with liquid nitrogen, causing radon to stick to the surface, while still allowing the passage of hydrogen gas. The installation and use of baffles in the three large pump ports of the MS has almost entirely eliminated the background due to radon decays [115]. The residual background rate will be enumerated in a forthcoming publication [164].

Countermeasure: Electron Cyclotron Resonance

As shown in Figure 4.5, an electron trapped in a magnetic field undergoes cyclotron motion. By providing a radio pulse that coincides with the frequency of the cyclotron motion, it is possible to excite the electron to higher energies [139]. At large enough energies, the electron's cyclotron radius will be too large to fit in the MS, thereby resulting in the electron impacting the walls of the vessel. This method is known as electron cyclotron resonance and has been tested in the PS [139, 167]. Although successful in removing trapped electrons [167], the technical requirements for this method were not implemented in the MS [168].

Countermeasure: Magnetic Pulse

Another method of emptying trapped electrons in the MS is by temporarily reducing the magnetic field [80, 160]. Decreasing the magnetic field removes electrons through several effects. First, lowering the magnetic field widens the magnetic flux tube, thereby connecting magnetic field lines in the spectrometer to the walls of the vessel and allowing trapped electrons to impact the walls and be removed. Second, a smaller magnetic field increases the cyclotron radius for electrons; the expanded radius will cause the trapped electrons to impact the wall. Third, a decreasing magnetic field induces an electric field that results in a radially outward $\mathbf{E} \times \mathbf{B}$ drift for electrons [160]. All of these effects work together to remove trapped electrons. Simulations of the magnetic pulse method indicated that it should be particularly effective in removing high-energy ($>1\,\mathrm{keV}$) electrons [80].

The magnetic pulse method is implemented by temporarily changing the polarity of the MS air-coils [160]. During the SDS-I and SDS-II measurement phases, the magnetic pulse method was shown to be successful in removing stored electrons [160, 168].

Countermeasure: Electric Dipole

A charged particle in perpendicular electric and magnetic fields will experience an $\mathbf{E} \times \mathbf{B}$ drift [169]. This drift can be used to remove stored electrons. In the MS, the electric field required for creating such drifts is produced using the IE system. The eastern and western halves of the MS electrodes can be placed at different voltages, thereby creating a dipole field perpendicular to the axial magnetic field. The effectiveness of the electric dipole method in removing low-energy ($<1\,\mathrm{keV}$) trapped electrons has been shown via simulations [80].

The method has since been extensively tested during the SDS-I and SDS-II measurement campaigns [169].

4.1.6 Rydberg Atoms

Electric dipole and magnetic pulse measurements indicate that the largest remaining background component is not due to stored electrons [160, 169]. All indications point to a novel background source: the ionization of Rydberg atoms. The hypothesized creation mechanism of these atoms follows a chain of nuclear decays, which will now be described [34].

Before its active use, the MS was exposed to ambient air, including ^{222}Rn, over the course of several years [34]. One daughter of this isotope is ^{214}Po, which subsequently α-decays to produce ^{210}Pb [34]. If this latter decay occurs at the spectrometer surface, the ^{210}Pb can become imbedded in the steel. The subsequent α-decay of ^{210}Pb can result in the sputtering of atoms from the surface [170, 171].

The subsequent ejected atoms can end up in highly excited electronic states, known as Rydberg atoms [171]. As neutral particles, such atoms will not be deflected by electric and magnetic fields, but will freely travel into the sensitive volume of the MS. Because they are highly excited, Rydberg atoms are easily ionized, even by thermal radiation. The ionization electrons will then be magnetically guided to the FPD.

Although this background mechanism may seem convoluted, it was validated during SDS-IIIa by artificially exposing the MS to a short-lived lead isotope [172]. A ^{228}Th source was attached to the MS to allow the decay product ^{212}Pb to become implanted on the spectrometer surface. Subsequent measurements saw an elevated background rate in the MS, and the rate exhibited a decay constant consistent with the half-life of ^{212}Pb (10.6 h) [172]. A nearly identical background mechanism is expected for ^{210}Pb, which has a much longer half-life (22.2 years) [172].

To reduce the Rydberg background, several approaches are possible. The obvious course of action is to clean the spectrometer surface in order to remove the buildup of ^{210}Pb atoms. Studies have shown that electropolishing is $\sim$90 % effective in removing the lead, while acid or other chemical techniques are significantly less effective [173]. However, cleaning the interior spectrometer surface would be very challenging with the IE system already installed. A large-scale operation of this sort would significantly delay the progress of the experiment.

A more feasible approach may be removing residual gas from the spectrometer surface, thereby reducing the number of atoms that can be excited into Rydberg states. Baking the MS reduced the background by about 40 % [34, 141] although a background rate of several hundred mcps remains. Exposing the inner spectrometer surface to UV light should remove additional gas from the surface. Measurements with a very strong UV source, however, did not show any long-term reduction in the background rate after illuminating the spectrometer surface [172].

Although certain aspects of the Rydberg model have been validated experimentally, further characterization of this background source is still being pursued. Measurements of energy spectra of the ionization electrons will hopefully illuminate the exact production mechanism of the Rydberg atoms and help determine which atomic elements principally contribute [141].

4.2 **Kassiopeia** ***Simulation Package***

Simulations play a crucial role in studying background processes within the spectrometers. For this reason and for others, the KATRIN experiment has developed its own particle-tracking simulation software, called KASSIOPEIA [174]. Existing software, such as GEANT4, is not well-suited to the setup of KATRIN. Along the intricately designed beamline, the electric and magnetic fields change dramatically in magnitude. KASSIOPEIA allows distinct particle tracking conditions in different geometrical regions, enabling more efficient calculations of electron trajectories and better use of computational resources. The base code is written in the C++ language, but the particular simulation details are set by the user via Extensible Markup Language (XML) configuration files.

A thorough description of the KASSIOPEIA software has been published elsewhere [174]. Here, a brief overview of the structure of the simulation code will be given in the context of the KATRIN experiment; the material is taken primarily from the previously cited reference.

4.2.1 Geometry

The simulation geometry is defined by the placement of volumes and surfaces inside a world volume. Complicated geometries can be formed by the combination of simple shapes, such as cylinders, cones, and frustums. While full 3D models exist for certain KATRIN components (such as the MS [175]), such detailed geometries are not needed for many simulations. Instead, axially symmetric representations of KATRIN components, such as the spectrometers and detector system, have been implemented and are typically used. Since the defined geometry is customizable, it is easy to add new elements to or remove unnecessary components from the simulation as needed.

4.2.2 Structure

Each simulation in KASSIOPEIA is broken into a hierarchy of events, tracks, and steps. A diagram of the simulation algorithm is shown in Figure 4.7. A simulation consists of multiple events. The number of events is preselected by the user in the simulation configuration. Each event is generated by starting a particle at a specified location with an initial energy and an initial direction. This particle is then tracked through the simulation geometry in space and time. Multiple tracks can be produced during a single event; for instance, SEs are created when the primary particle ionizes residual gas.

Each track is further subdivided into steps. In each step, a particle is propagated from one position to another, based on the energy, momentum, and intrinsic properties (e.g., charge) of the particle, as well as the electromagnetic fields at the particle location. After each step, the energy and momentum of the particle are updated accordingly. It is during each step that interactions can occur, such as scattering, that result in changes to the particle's kinematic properties or additional particles to be tracked. Termination of tracks is computed on the step level; terminators are conditions set by the user which will terminate tracks when specified conditions are fulfilled. Common types of terminators include ending a track when

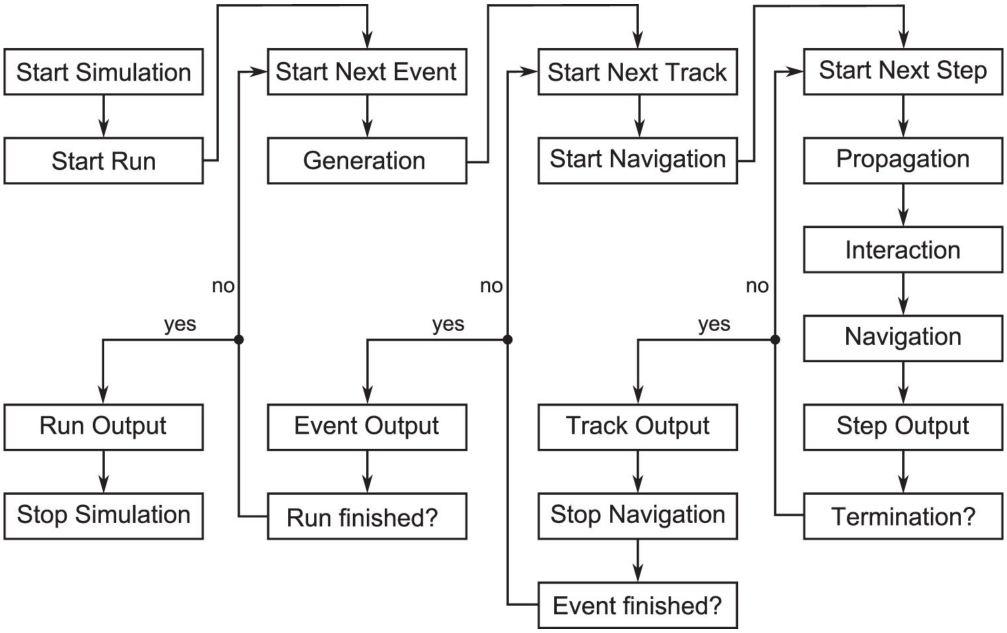

Figure 4.7: Simulation algorithm implemented in Kassiopeia. Figure taken from [174]. Used under the CC BY 3.0 license [120].

the particle enters or leaves a specified volume or surface (such as an electrode or detector), or when some parameter of the particle (e.g., radius or energy) reaches a certain threshold. An event ends once all tracks have been terminated.

The user can determine which parameters (particle position, particle energy, field values, etc.) from the simulation are recorded for later analysis. The initial and final values of these parameters can be recorded on a step-by-step basis and/or on a track-by-track basis.

4.2.3 Field Calculations

KASSIOPEIA calculates electric and magnetic fields separately. The field calculations are performed at the beginning of the simulation and are saved to file; in this way, subsequent simulations with identical electromagnetic conditions can load the file and do not need to recalculate the fields. The electric field is calculated using the boundary element method, which utilizes the electric potentials assigned to geometry elements by the user. The surfaces of these elements are broken into smaller pieces, and the charge densities for each element are computed. The electric potential/field can then be calculated at an arbitrary point by summing the contributions from each boundary element.

The magnetic field calculation is much less computationally intensive than the electric field calculation. For axially symmetric coils, such as the air coils and solenoids in the KATRIN beamline, the magnetic field is calculated using the zonal harmonic expansion method. The currents and positions of the coils in the geometry are used as input to the calculation. Constant magnetic fields, like the Earth's local magnetic field, can also be included.

4.2.4 Propagation

The propagation of a particle is determined by the Lorentz force due to the electric and magnetic fields. The differential equations governing particle motion are numerically integrated using Runge-Kutta integrators. Two types of trajectories are primarily used in Kassiopeia simulations. These are shown in Figure 4.8. The exact trajectory calculates the effect of magnetic and electric forces on the particle at each step. The adiabatic trajectory, on the other hand, doesn't calculate the full motion of the particle. Instead, only the guiding center is tracked–any cyclotron motion is added after the calculation. The adiabatic trajectory is an efficient method when the particle experiences adiabatic motion (i.e., when the electric and magnetic fields do not vary substantially within a cyclotron radius of the particle [174]). The validity of using adiabatic trajectories for simulating electrons in the KATRIN beamline has been previously shown for β-particles produced in the WGTS and tracked to the MS [176].

For each trajectory, the step size must be determined in some way, and several methods are provided. It is common to use a step size based on the cyclotron motion of a particle: the step size is set to the distance travelled by the particle after undergoing a specified fraction of the cyclotron period. This method requires the presence of a magnetic field. Alternatively, a fixed step size can also be used by specifying a distance.

A useful method to determine the acceptability of a certain trajectory is to confirm that

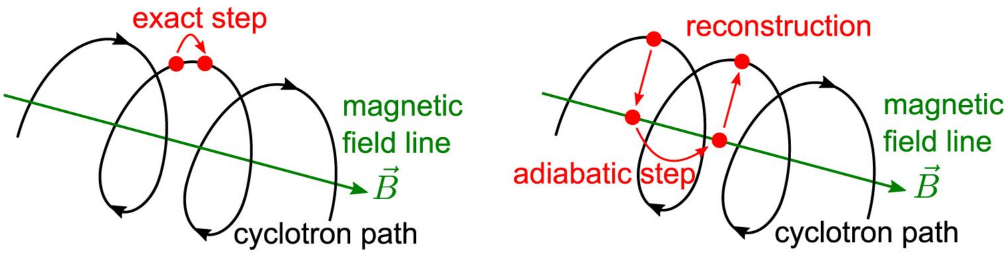

(a) Exact trajectory (b) Adiabatic trajectory

Figure 4.8: Trajectories available in KASSIOPEIA. Figure taken from [174]. Used under the CC BY 3.0 license [120].

energy conservation is being observed over the course of the particle track. The sum of the kinetic and electric potential energies can be compared at the beginning and end of a track. The relative deviation between the initial and final energies is a good measure of the trajectory's accuracy; in practice, values below 10^{-8} generally indicate that a trajectory has sufficient accuracy [172]. This method is employed for the ion-induced background simulations described in section 7.6.1.

4.2.5 Interactions

Space interactions (such as scattering with residual gas or scattering inside the silicon wafer) are available within the simulation software. These are implemented by selecting a particular scattering calculator and by defining the density of the target medium. The density can be set directly or can be computed from the temperature and pressure (using the ideal gas law). The calculator determines which scattering processes and thus which cross sections are to be included. The scattering of electrons on hydrogen gas can be effected in the XML configuration file in the following manner:

```
<ksint_scattering name="scattering_name">
        <calculator_hydrogen elastic="true" excitation="true" ionisation="true"/>
        <density_constant temperature="300." pressure_mbar="1.e-7"/>
</ksint_scattering>
```

In this example, a temperature of 300 K and a pressure of 10^{-7} mbar are used. For hydrogen scattering, cross sections for elastic, excitation, and ionization processes are available. Additional details on the implementation of interactions in Kassiopeia will be described in section 7.4.

4.3 Secondary Electron Emission Characteristics

In this section, characteristics of SE emission from the MS surface are investigated. SE emission as a background source was previously introduced in section 4.1.4. Measurements and simulations were performed which allow the study of both the SE energy spectrum and emission rate.

4.3.1 Asymmetric Magnetic Field

An important method of studying SEs is to use specialized magnetic field configurations. Utilizing the air-coils surrounding the MS vessel, along with the solenoid magnets at the entrance and exit, it is possible to create a variety of magnetic field conditions inside the spectrometer. The standard configuration to be used during neutrino mass data-taking, as discussed in section 4.1.4, is referred to as a "symmetric" configuration since the magnetic field is approximately symmetric across the $z = 0$ plane. An example of this configuration is shown in Figure 4.9a. The symmetric magnetic field naturally shields the flux tube from SEs emitted from the MS hull.

In contrast, an "asymmetric" field configuration does not have this mirror symmetry; rather, the field lines connect the MS surface to the FPD, as shown in Figure 4.9b. With this setting, electrons are naturally guided from the spectrometer surface to the FPD. This setting, therefore, allows a direct measurement of electrons emitted from the spectrometer surface. A full listing of the magnetic field settings described in this thesis can be found in Appendix A.

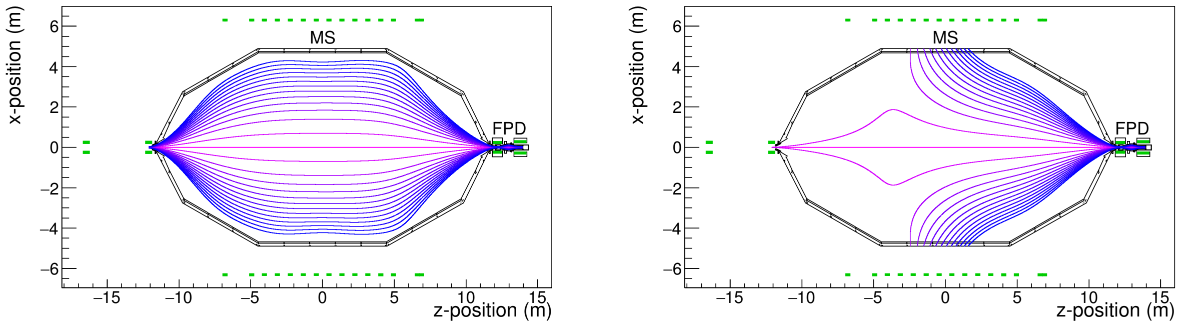

(a) Symmetric (b) Asymmetric

Figure 4.9: The two basic types of magnetic field configurations inside the MS. The displayed magnetic field lines intersect the FPD rings and are produced by the beamline solenoids and air-coils, shown in green.

4.3.2 Energy Spectrum

During SDS-IIb, measurements were performed to study SEs emitted from the MS [177]. The method used to determine the energy spectrum of SEs emitted from the walls of the MS follows a similar procedure to that outlined in [157], where the electron energy spectrum for the MoS was calculated. Utilizing the asymmetric magnetic field configuration shown in Figure 4.9b, the FPD rate was measured as a function of the IE offset voltage. Electrons with energies less than $-e \cdot \Delta U_{\mathrm{IE}}$ are screened and therefore not detected[1]. The voltage scan data are displayed in Figure 4.10, and the measurement settings are listed in Table 4.1.

The electron rate as a function of the IE offset voltage $\Delta U_{\mathrm{IE}} < 0$ can be written as

$$R(\Delta U_{\mathrm{IE}}) = R_0 + \int_{-\Delta U_{\mathrm{IE}}}^{\infty} F(E) \cdot P(E, \Delta U_{\mathrm{IE}}) \cdot \mathrm{d}E, \tag{4.2}$$

where E is the electron energy and F is the energy spectrum of secondaries emitted from

---

[1] In reality, the screening energy for each electron is not exactly equal to $-e \cdot \Delta U_{\mathrm{IE}}$. The electric potential inside the MS has a maximum at $r = 0$ and decreases for larger radii [168, 178]. An electron emitted from the MS surface will explore different radial positions depending on its initial axial position within the asymmetric magnetic field; therefore, different screening voltages will also be experienced. Only by performing detailed tracking simulations with the IE system can the effective screening energy be computed, which is beyond the scope of the present work.

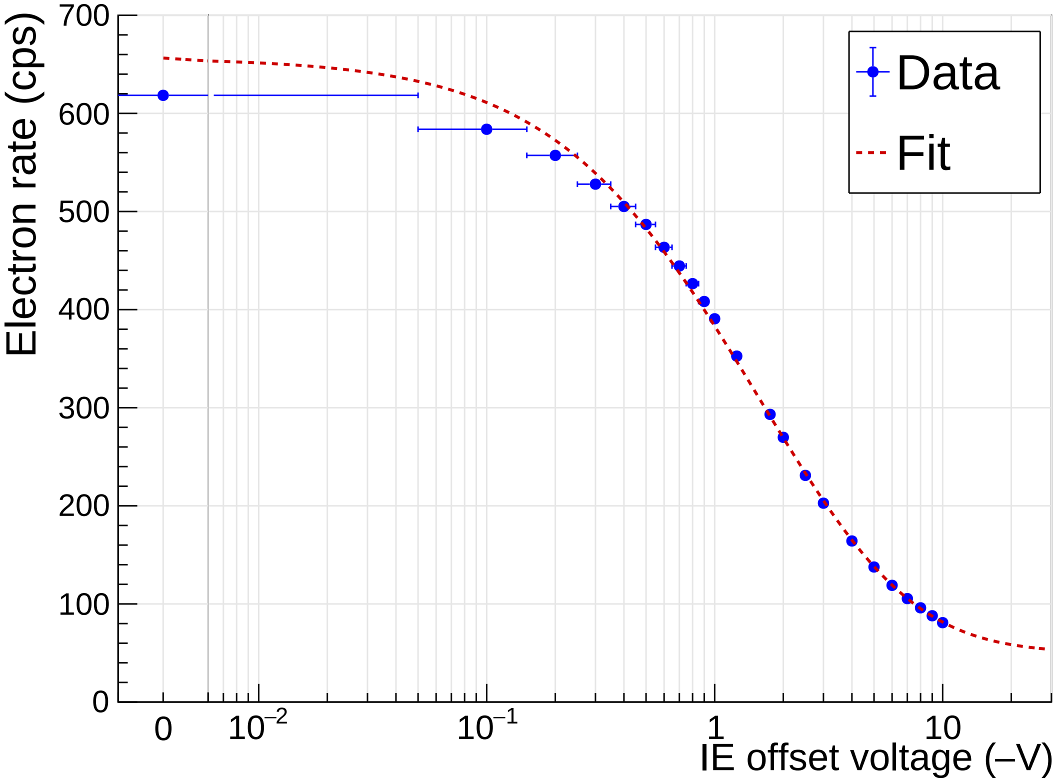

Figure 4.10: The electron rate detected at the FPD as a function of the IE offset voltage. The datapoints are fit using Equation 4.2, with $\chi^2/\text{ndf} = 15.4/20$. The central 16 detector pixels are excluded from the rate calculation. Poisson errors are assumed for the rate, but the error bars are too small to be seen in the plot. The offset voltage was generated using the offset power supplies (model *ISEG EHS 8205 p-K* [34]), which have a voltage accuracy of $10^{-4} \cdot |U_{\text{offset}}| + 0.05\,\text{V}$ [179]. The accuracy is treated as the uncertainty on the voltage and is shown for each datapoint by a horizontal error bar; the uncertainty is assumed to be uncorrelated between datapoints.

Parameter	Value
FPD runs	25637, 25640–25661
Magnetic field	setting C
U_0 (V)	$-18\,600$
ΔU_{IE} (V)	-10 to 0
U_{PAE} (V)	10 000
ROI (keV)	25.7 to 30.7

Table 4.1: Settings used for the IE voltage scan measurements.

the vessel [157]. A constant background rate R_0 is included to account for other background sources. P is the probability for an electron emitted from the MS surface to reach the FPD. A detected electron from the hull must overcome both the offset voltage and the magnetic mirror effect [157]:

$$P(E, \Delta U_{\mathrm{IE}}) = P_{\mathrm{offset}}(E, \Delta U_{\mathrm{IE}}) \cdot P_{\mathrm{mirror}}(E) \tag{4.3}$$

Assuming a cosine angular distribution for the electrons relative to the surface normal (which is a valid approximation for true secondaries [159]), the probability of surmounting the offset voltage is simply [157]:

$$P_{\mathrm{offset}}(E, \Delta U_{\mathrm{IE}}) = \left(1 + \frac{\Delta U_{\mathrm{IE}}}{E}\right). \tag{4.4}$$

The probability to overcome the magnetic mirror effect is not easy to calculate analytically. It relies on the initial properties of the electron (energy, starting angle), as well as the nontrivial magnetic field conditions experienced by the electron on its way to the FPD. Therefore, P_{mirror} was determined from Monte Carlo simulations using KASSIOPEIA. The simulation geometry included a simplified version of the system apparatus, consisting of the MS vessel and the FPD system, and employed the same electromagnetic field configuration used in the IE voltage scan measurements but excluding the IE system. Electrons were produced at the MS walls, uniformly spread over axial positions $-2.438\,\mathrm{m} \leq z \leq 1.575\,\mathrm{m}$, which is the range corresponding to the magnetic field lines that connect to the FPD. The starting angle of electrons relative to the MS walls was sampled from a cosine angular distribution.

The simulation results are shown in Figure 4.11. A fit was applied to the data to construct a functional form for the probability of an electron to overcome the magnetic mirror effect, averaged over the initial angular distribution:

$$P_{\mathrm{mirror}}(E) = c_0 + \frac{c_1}{(E + c_2)^{c_3}} + \frac{c_4}{(E + c_5)^{c_6}} + \frac{c_7}{(E + c_8)^{c_9}}, \tag{4.5}$$

where c_i are fit parameters whose values are given in Table 4.2[2].

---

[2] This particular functional form was chosen not because it is the best choice but because the fit was able to properly converge with this form. Looking at Figure 4.11, a simpler functional form should be able to provide a good fit.

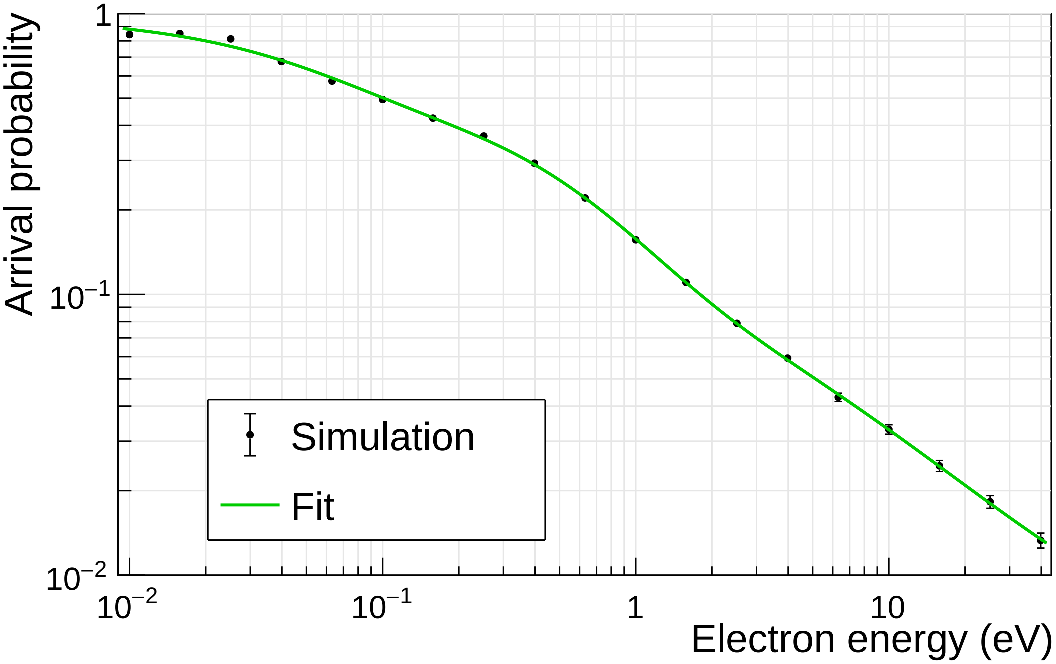

Figure 4.11: The simulated probability P_{mirror} for SEs to overcome the magnetic mirror effect and arrive at the detector for setting C. Only statistical errors are shown. A fit (Equation 4.5) is applied to the data, with $\chi^2/\text{ndf} = 24.1/9$.

Model	Parameter	Value	Unit
P_{mirror}	c_0	0.0038 ± 0.0031	–
	c_1	20.6 ± 8.1	$(\text{eV})^{c_3}$
	c_2	2.21 ± 0.12	eV
	c_3	4.93 ± 0.29	–
	c_4	0.0037 ± 0.0028	$(\text{eV})^{c_6}$
	c_5	0.757 ± 0.043	eV
	c_6	17.2 ± 1.9	–
	c_7	0.31 ± 0.10	$(\text{eV})^{c_9}$
	c_8	2.87 ± 0.87	eV
	c_9	0.92 ± 0.15	–
F	B	$(3.10 \pm 0.13) \times 10^6$	$(\text{eV})^3$
	Φ	6.88 ± 0.13	eV
	R_0	49.79 ± 0.99	cps

Table 4.2: Fit parameters obtained from the arrival probability simulation (Figure 4.11) and the IE voltage scan data (Figure 4.10).

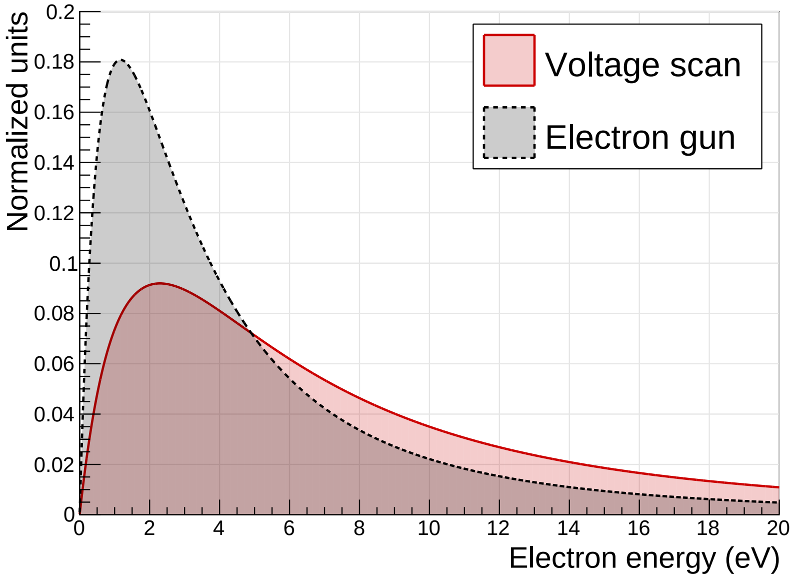

Figure 4.12: SE energy spectra generated from Equation 4.6, using $\Phi = 6.9\,\mathrm{eV}$ (derived from voltage scan measurements) and $\Phi = 3.5\,\mathrm{eV}$ (derived from electron gun measurements). The spectra peak at $E = \frac{1}{3}\Phi$. The spectra have been normalized to unity.

Turning towards the SE energy spectrum, a theory-based form can be found in [180–182]:

$$F(E) = B \cdot \frac{E}{(E+\Phi)^4}, \tag{4.6}$$

where B is a normalization factor and Φ is the work function.

The voltage scan measurement data were fit to Equation 4.2, as can be seen in Figure 4.10. By fitting to data, the parameters in $F(E)$, as well as R_0, were fixed, and their values are given in Table 4.2[3]. The derived energy spectrum is plotted in Figure 4.12. The fit indicates that $\Phi = (6.9 \pm 0.1)\,\mathrm{eV}$ for the MS surface, excluding systematic errors[4]. This number is twice

---

[3] The covariance matrix computed from the fit for P_{mirror} was not used in the fit of Equation 4.2.

[4] This result assumes that the energy spectrum takes the form given by Equation 4.6, that electrons are emitted according to a cosine angular distribution, and that the screening voltage is exactly equal to ΔU_{IE}. However, it is difficult to estimate the effect of each of these assumptions on the computed value of Φ without significant effort. The reader should consider the listed value of Φ to have large systematic errors.

as large as the result obtained from transmission measurements with a photoelectron source ("electron gun") in the MS [110]. In that case, Φ varied between 3.39 eV and 3.65 eV [168]. The energy spectrum with $\Phi = 3.5\,\mathrm{eV}$ is plotted for comparison in Figure 4.12[5].

It is not clear why there is such a large discrepancy in the derived value of the spectrometer work function determined from the two methods. The electron gun measurements were performed with an unbaked spectrometer during SDS-IIa, while the voltage scan data were collected during SDS-IIb with a baked spectrometer. There are indications that cleaned, type 316L steel (which is nearly identical by composition to the type 316LN steel used in fabricating the MS hull [183]) has a work function of ∼5.0 eV [184]. However, the value derived from the voltage scan measurements is significantly larger.

As will be shown in chapter 5, simulations of muon-induced SEs match measurement data when their energy is sampled from a spectrum with a work function of 3.5 eV. Therefore, this smaller value of Φ is assumed in the remainder of this thesis for simulating background.

4.3.3 Emission Rate

In this section, the electron rate emitted from the MS surface was investigated for different measurement campaigns. For these measurements, the MS was on high voltage (−18.6 keV) and the IE system was electrically shorted to the MS hull. The measurements spanned the time from SDS-I through STS-IIIa. An identical energy ROI of 25.7–30.7 keV was used for each measurement. The comparison between measurement campaigns is made difficult by the fact that different asymmetric magnetic fields were used during the various SDS campaigns. This necessitates converting the measured total rates to a rate per unit area of the MS surface in order to compare results. Visualizations of each magnetic field configuration and the utilized magnet settings can be found in Appendix A.

Only pixel rings which measured a well-defined region of the MS hull were included in the analysis; this selection was determined by magnetic field line simulations with KASSIOPEIA.

---

[5] An attempt was also made to fit the data in Figure 4.10 assuming a work function of 3.5 eV, but a very poor fit result was obtained. Further investigation was not attempted.

Misalignments of the flux tube or collisions with the flapper valve [123] also result in pixels being excluded from analysis. Additionally, during and after the SDS-III measurements, the lower right portion of the wafer must be excluded due to an elevated rate from the MS hull caused by accidental ^{228}Th contamination [185]. Visualizations of the detector rate before and after the pixel cuts can be found for each asymmetric magnetic field setting in Appendix B.

In order to reconstruct the electron emission rate at the MS surface from the rate measured at the FPD, the electron transport probability from the surface to the detector must be known. The average probability was calculated for each magnetic field setting using Kassiopeia simulations. Electrons were started at the MS hull, uniformly spread across the surface scanned by the asymmetric magnetic field. Their energies were sampled from Equation 4.6 with $\Phi = 3.5\,\mathrm{eV}$.

True SEs are produced isotropically inside the steel; electrons emitted from the surface, therefore, follow a cosine angular distribution [159, 181, 186]. This type of distribution was used to generate the starting angle of electrons in the simulation:

$$\frac{dn}{d\Omega}(\theta) \propto \cos\theta \Rightarrow \frac{dn}{d\theta}(\theta) \propto \cos\theta \sin\theta. \tag{4.7}$$

Here, dn is the number of emitted particles emitted in the solid angle $d\Omega$, and θ is the angle between the particle momentum and the surface normal [187, 188].

The average detection probability at the FPD for each magnetic field setting is listed in Table 4.3. The detection efficiency of the FPD ($95.0 \pm 2.8\,\%$) is included in the calculation [130]; however, the effect of backscattering from the detector surface is ignored [189]. The detection probabilities vary between 6 % and 16 % for the different magnetic field settings. Besides total probabilities, probabilities for each pixel ring were also calculated. The rates and probabilities for each pixel ring are shown in Figure 4.13 for the case of magnetic field setting A. Similar plots for the other magnetic field settings can be found in Appendix B.

Let S be the rate emitted from the MS per unit area. This parameter can be calculated

Magnetic field	Detector rings	Detection probability (%)
A	6–12	15.0 ± 0.5
B	2–11	13.0 ± 0.4
C	2–12	8.4 ± 0.3
D	3–12	10.6 ± 0.3
E	1–12	15.7 ± 0.5
F	1–12	9.1 ± 0.3
G	1–11	14.7 ± 0.4
H	1–11	15.9 ± 0.5
I	3–12	6.6 ± 0.2
J	2–10	13.7 ± 0.4

Table 4.3: Average probability for SEs emitted from the MS surface (within the region spanned by the listed detector rings) to be detected by the FPD. Detailed information on each magnetic field setting can be found in Appendix A.

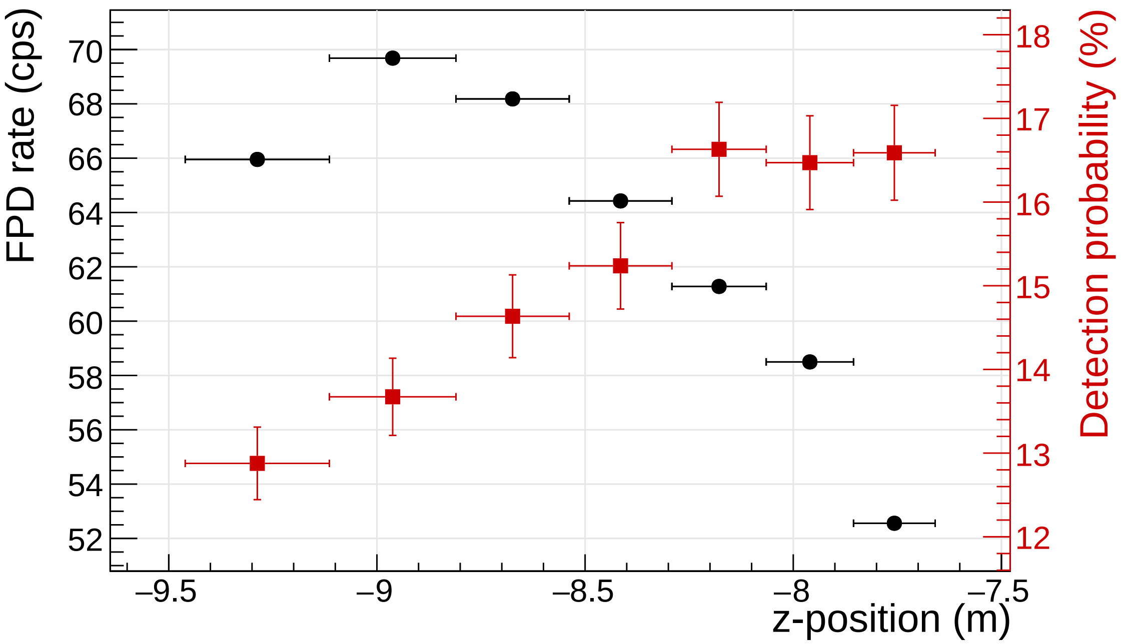

Figure 4.13: The FPD rate as a function of axial position for magnetic field setting A. Each datapoint corresponds to a detector pixel ring. The FPD rate has been corrected for missing/excluded pixels. Also shown is the electron detection probability for each pixel ring, as determined from simulation.

using the following formula:

$$S = \frac{1}{A} \sum_{r=r_{\min}}^{r_{\max}} \frac{R_r}{P_r}, \tag{4.8}$$

where R_r and P_r are the FPD rate and arrival probability, respectively, for detector pixel ring r. $r_{\min}$ and $r_{\max}$ are the minimum and maximum detector rings included in the analysis. A is the surface area of the MS measured by the included detector pixel rings. The values of S for each magnetic field setting are listed in Table 4.4. Besides the rate emitted from the entire surface, it is also possible to find the rate for each pixel ring:

$$S_r = \frac{R_r}{A_r \cdot P_r}, \tag{4.9}$$

The values of S_r are plotted in Figure 4.14 for each magnetic field setting; the ring number has been converted to the axial position on the MS surface.

Also shown in the same table are the values of S calculated using the single event rate at the FPD. Single events are defined to be FPD events that are at least 0.2 ms away from preceding or following events [34, 188]. Events within 0.2 ms of other events are known as cluster events. Cluster events can be localized on the detector wafer (i.e., events on the same pixel or on neighboring pixels) or spread across the wafer, depending on the background creation mechanism; the spatial distribution of cluster events was not considered in the present analysis. Certain background processes (such as the decay of radon in the spectrometer volume or the sputtering of atoms from the spectrometer surface) are known to produce large event multiplicities [34, 170, 177]. As will be shown in the following chapters, SE emission induced by cosmic-ray muons and environmental gamma radiation predominantly results in single electron events.

Considering the total event rate, several observations can be made. First, baking seems to have a small effect on the electron rate originating from the walls. The MS was baked between SDS-IIa and SDS-IIb. After the bake-out, the background measured in the MS for the symmetric magnetic field setting dropped by 40 % [34, 141]. However, the asymmetric measurement results presented here show only a modest decrease of about 15 %. The MS was again baked between SDS-IIIa and SDS-IIIb, but this time no significant change in the

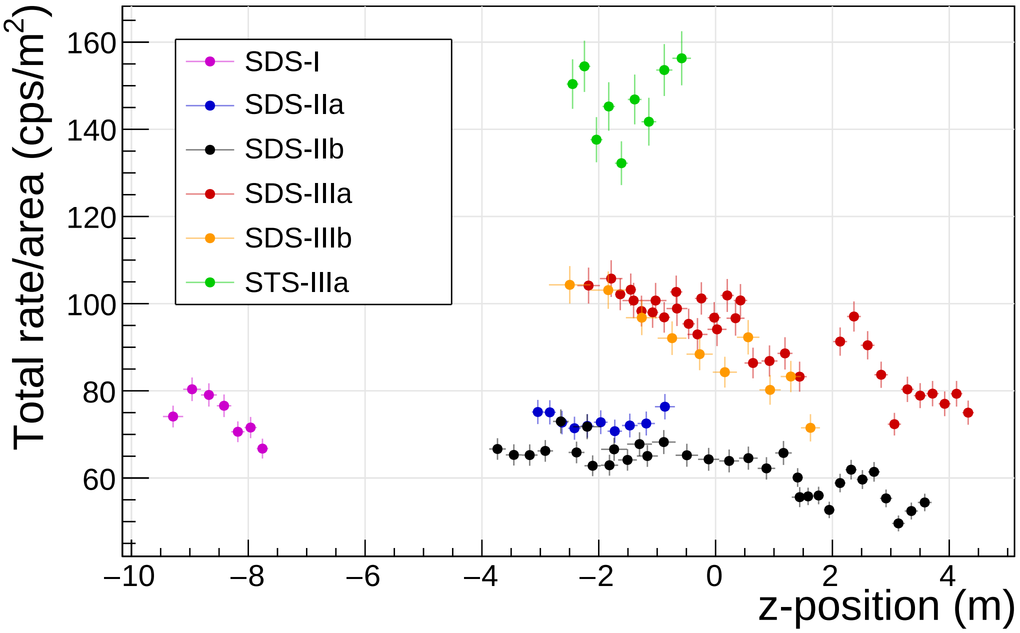

(a) All electron events

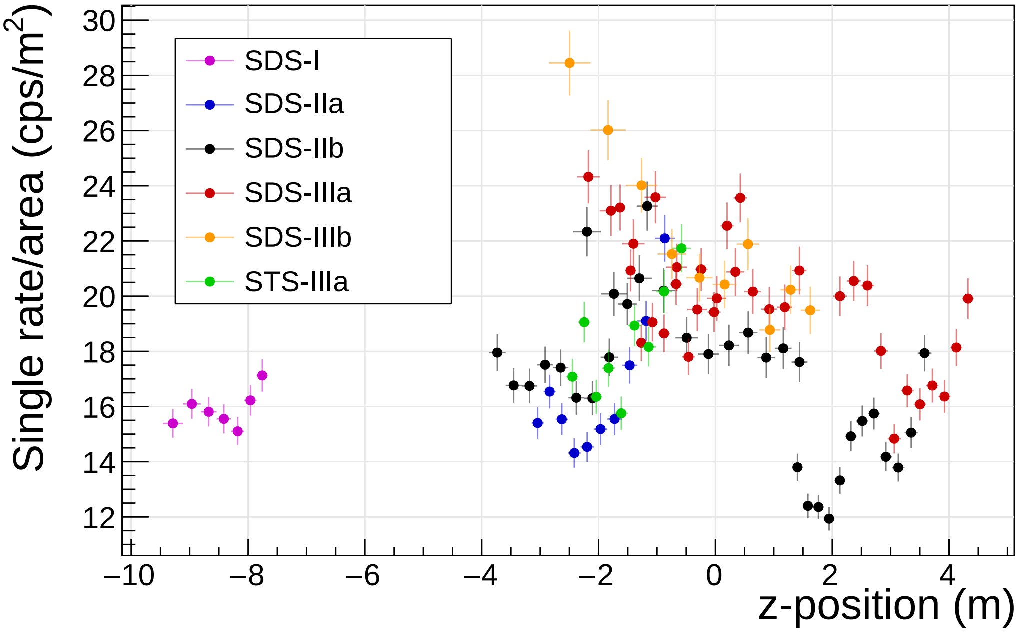

(b) Single electron events

Figure 4.14: The SE emission rate per unit area in the MS. Each datapoint corresponds to a detector pixel ring.

Campaign	MS status	Magnetic field	S (total events) (cps/m^2)	S (single events) (cps/m^2)	FPD runs
SDS-I	baked	A	74.5 ± 1.0	15.9 ± 0.2	7111–7133
SDS-IIa	unbaked	B	73.2 ± 0.9	16.9 ± 0.2	21831–21899 (every 4th run)
SDS-IIb	baked	C	65.6 ± 0.8	19.3 ± 0.2	25135
		D	65.6 ± 0.8	18.2 ± 0.2	25854–25863
		E	56.4 ± 0.6	14.4 ± 0.2	25864–25870
SDS-IIIa	unbaked*	F	95.9 ± 1.1	21.4 ± 0.3	32683–32708
		G	82.6 ± 0.9	18.0 ± 0.2	32709–32715
		H	99.7 ± 1.1	20.5 ± 0.2	32716–32717
SDS-IIIb	baked*	I	91.9 ± 1.3	22.9 ± 0.3	33977
STS-IIIa	baked*	J	147.0 ± 1.9	18.5 ± 0.2	43695

Table 4.4: SE emission rate for different magnetic field configurations. The measurements marked with an asterisk were taken after the MS was contaminated with ^{228}Th and therefore some caution is needed to compare with older results.

surface electron rate was observed after baking. Second, the contamination of the MS surface with ^{228}Th has led to a significant increase in the total event rate, even after excluding the detector pixels that scan the affected surface region of the MS (see Figure B.1). The rate during STS-IIIa is elevated compared with the SDS-III rates; the origin of this increase is not understood and warrants future investigation.

Turning toward the single electron event rate, essentially no change is observed across the various measurement phases. The average single event rate is 16.5 cps/m^2. This result indicates that, if single electron events primarily originate from SE emission (i.e., cosmic-ray muons and environmental gamma radiation), changes in vacuum or surface conditions inside the MS do not affect the SE emission rate.

4.4 Statistical Analysis of Small Background Signals

In the following chapters, the background contribution due to cosmic-ray muons, environmental gammas, and the inter-spectrometer Penning trap will be determined using the unified approach of G. J. Feldman and R. D. Cousins [190], which is briefly explained below. Let

$\mu > 0$ be the mean rate contribution from a particular background source that is Gaussian-distributed. Suppose the measured mean is x, with a standard deviation σ. If $x \gg 0$, determining a two-sided confidence interval on μ is straightforward [191]:

$$\mu = x \pm (1.645 \cdot \sigma) \ (90\,\% \ \text{C.L.}) \tag{4.10}$$

Here, an interval corresponding to a 90 % confidence level is used, but other confidence levels can be used by changing the numerical constant appropriately.

However, if x is close to zero, an upper limit, rather than a two-sided interval, should be used since μ is constrained to be non-negative. Conveniently, Feldman and Cousins developed a frequentist approach that smoothly unifies these two cases [190]. This unified approach allows the value of x itself to determine whether an upper limit or an interval is appropriate, depending on the desired confidence level. For instance, if one would like to quote a result at 90 % C.L., an upper limit rather than a two-sided interval is used if $x < 1.3\sigma$ [190]. The exact value of the upper limit (or range of the confidence interval) has been calculated by Feldman and Cousins and can be accessed via a look-up table [190]. The use of this prescription, therefore, is a robust and straightforward way to determine, first, whether a two-sided interval or upper limit is to be used and, second, the range of the interval or the value of the limit.

Chapter 5

MUON-INDUCED BACKGROUND IN THE MAIN SPECTROMETER

Located on the Earth's surface, the KATRIN beamline is exposed to atmospheric muons. These muons are generated from interactions of cosmic-ray particles high in the Earth's atmosphere. Due to the large size of the MS, a substantial rate of muons is expected to pass through the vessel. Electrons will be emitted from the steel walls of the vessel due to the passage of muons. Muons were responsible for a significant amount of background electrons observed with the Mainz spectrometer [81]. Electrostatic and magnetic shielding has been implemented in the MS to prevent these SEs from reaching the detector (see section 4.1.4), but the effectiveness of the shielding must be tested experimentally.

In this chapter, the effect of cosmic-ray muons on the MS background rate is investigated using coincidence and correlation measurements with a muon detector system. The chapter content is mostly copied or derived from a recently published paper [188].

5.1 Simulation of the Muon Flux

To estimate the flux of muons passing through the MS, a simulation was performed with the Geant4 toolkit [192–194]. It has been discovered that several errors were made in the previous KATRIN simulations of the muon flux, which have propagated through multiple theses [157, 195–198].

The muon flux at sea level is 189 $\mu/\mathrm{m}^2\,\mathrm{s}^{-1}$ [199]. The angular distribution of the flux f roughly follows a $\cos^2\theta$ distribution, where θ is the angle between the muon's momentum and the normal of the Earth's surface [42, 200–202]. Due to solid angle effects, however, the generation of muons in the simulation requires using a $\cos^2\theta \cdot \sin\theta$ distribution:

$$\frac{df}{d\Omega}(\theta) \propto \cos^2\theta \Rightarrow \frac{df}{d\theta}(\theta) \propto \cos^2\theta \sin\theta, \tag{5.1}$$

where $d\Omega$ is the solid angle. Failing to include this effect, as was done in a previous calculation [157], results in a ~10 % lower muon flux through the MS.

The only geometry included in the simulation was the inner volume of the MS. Particles were started in a 400 m × 400 m plane located 7 m above the spectrometer axis, with starting angles given by Equation 5.1. Instead of using muons, "geantinos" were used, which "are virtual particles for simulation which do not interact with materials and undertake transportation processes only" [203]. This was done to avoid particle interactions and speed up the simulation. "Hits" were recorded when the particle entered or left the spectrometer volume. The flux through the MS was normalized by assuming a rate of 189 $\mu/\mathrm{m}^2\,\mathrm{s}^{-1}$ through the starting plane (see above). A total of 10^8 particles were simulated, resulting in 2.98×10^5 hits. This corresponds to a total flux through the MS of $(45\,031 \pm 83)\,\mu/\mathrm{s}$.

5.2 Muon Detector System

The muon detector system consists of 8 large modules and 1 small module surrounding the MS (Figure 5.1 and Figure 5.2). Each module is made of BICRON BC-412 plastic scintillator that was previously used in the KARMEN experiment [204]. The large panels have an area of $2.05\,\mathrm{m}^2$, while the small panel has an area of $0.3\,\mathrm{m}^2$. Muons that pass through the scintillator stimulate the emission of photons, which are collected by PMTs located on the ends of the modules. The signals from the modules are collected by a dedicated muon DAQ system which has been synchronized with the FPD DAQ computer; the timing accuracy is 50 ns. Muon module events are saved in a separate but similar data stream as FPD events. Additional details about the design, assembly, and commissioning of the muon detector system can be found elsewhere [80, 188, 197].

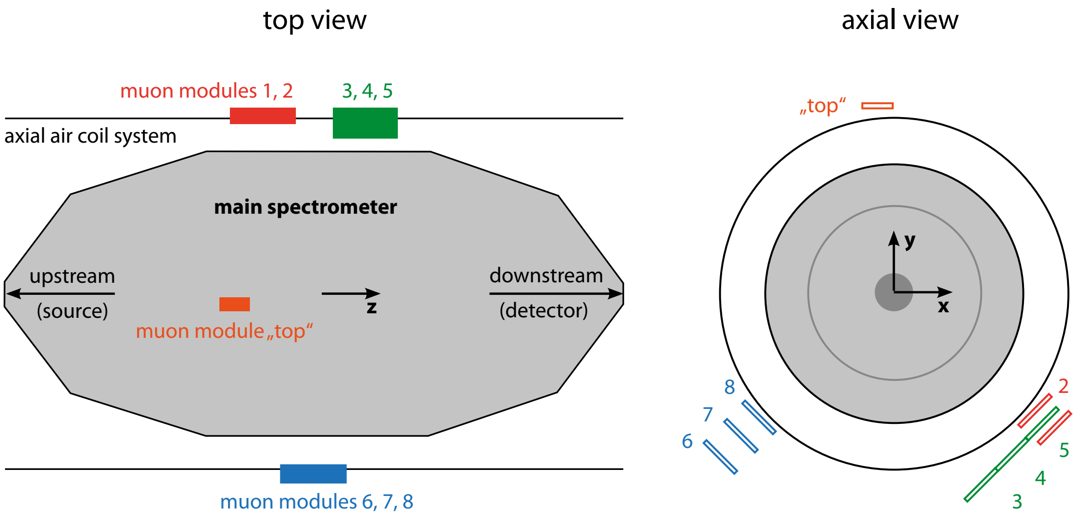

Figure 5.1: Diagram of the muon detector modules within the spectrometer hall. Figure taken from [188].

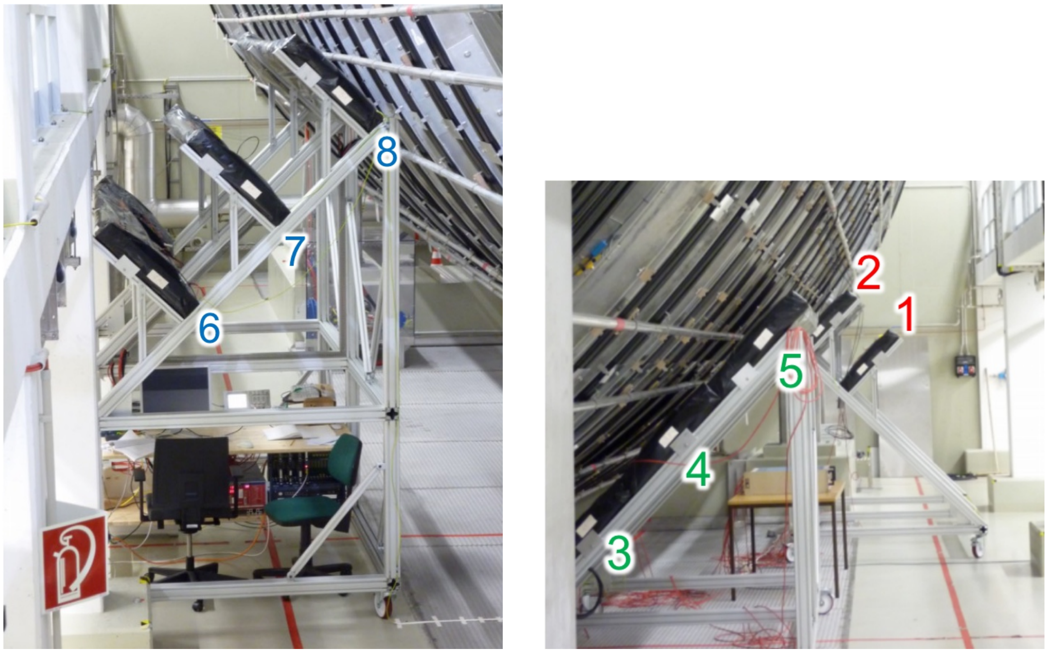

Figure 5.2: Muon modules installed next to the MS in the spectrometer hall. Photos adapted from [205].

Setting	1	2	3
Run duration (s)	1500	5000	5000
Number of runs	111	111	110
Live time (days)	1.93	6.42	6.37
Magnetic field	setting B (asym.)	setting K (sym.)	setting K (sym.)
U_{MS} (kV)	-18.6	-18.6	-18.5
ΔU_{IE} (V)	-5	-5	-100
U_{PAE} (kV)	4	4	4
ROI (keV)	19.7 to 24.7	19.7 to 24.7	19.7 to 24.7

Table 5.1: Long-term measurements with the muon modules and FPD system during SDS-IIa.

5.2.1 Measurements

Previous measurements with the muon detector system at the MS did not find definitive evidence of FPD event correlation or coincidence with muon module events [157, 198]. A new, two-week long measurement campaign was therefore performed during SDS-IIa, in which both the muon system and FPD detector system were running in parallel. A run script was used to cycle through three different run settings, which are listed in Table 5.1.

Run setting #1 utilized an asymmetric magnetic field (setting B; see Appendix A) with field lines that intersected the MS hull near its axial center, close to the axial positions of the muon modules. In this way, some fraction of muon events that induce electrons from the MS surface will be detected by one or more of the muon modules. Run settings #2 and #3 used a symmetric magnetic field (setting K) but differed in terms of the electrostatic shielding. This symmetric magnetic field setting is a proxy for the conditions that will be in place during neutrino mass measurements.

Although the modules are wrapped in permalloy foil to allow them to be placed near the MS magnetic field, the event rate in modules 1 and 2 nevertheless exhibited a large magnetic field dependency. These two modules are excluded from the analyses described in the rest of this chapter.

5.3 Validation of Muon-Induced Background Mechanism

Using FPD events that were coincident with those from the muon detectors, the time distribution for SEs emitted from the MS surface was determined (section 5.3.1). The measured data were then compared to a simulated distribution in order to verify the model of muon-induced events (section 5.3.2). Finally, in section 5.3.3 the results of the electron-muon coincidence analysis under nominal magnetic field conditions are discussed.

5.3.1 Coincidence Analysis

A straightforward method to study the muon-induced background is to perform a coincidence analysis on muon and electron events. If muons passing through the MS vessel are responsible for creating electrons that reach the FPD system, one expects an excess of electron events in the time window following a muon event. (This is only true for the asymmetric magnetic field configuration; for the symmetric configuration, electrons can be trapped in the MS for long durations.) The timing difference between muon and electron events allows the determination of the electron flight time, which can be compared with simulation. Muon-coincident electron events were previously observed with the MoS [157]. The analysis described in the present work is the first time that muon coincidence was definitively seen in the MS.

In terms of event selection for a coincidence study with the FPD, it is desirable that all selected muons travel through the walls of the MS in order to have a chance of producing detectable electrons. Out of the available muon modules, modules 6, 7 and 8 are best suited to fulfill this condition (see Figure 5.1). The position and orientation of these modules relative to the MS is such that a muon that creates a signal in all three modules is geometrically constrained to have passed through the MS. (The deflection from the Lorentz force is negligible.) Thus, only three-module muon events are used in the coincidence study, where such an event has concurrent signals within a 200-ns window. This time window was chosen to account for the 50-ns timing resolution of the muon modules.

In order to study events originating from the walls, only events from the outer 132 pixels

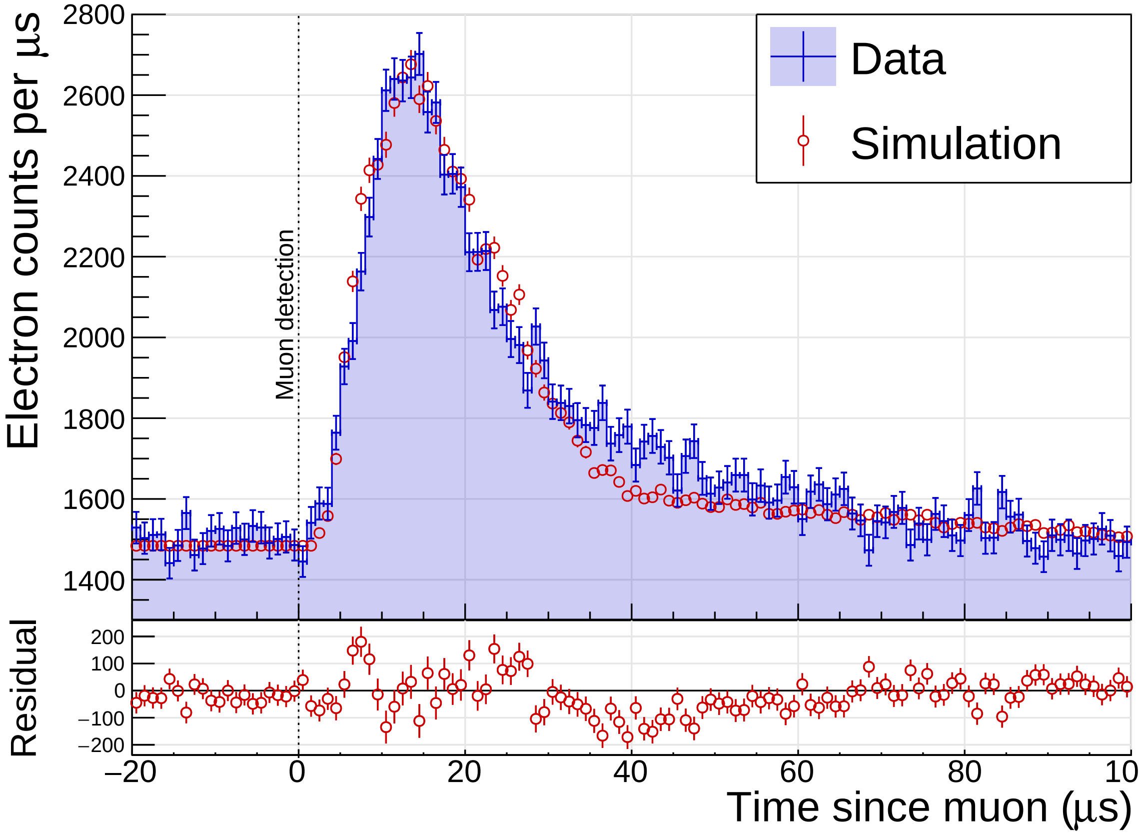

Figure 5.3: The distribution of the time differences between electron and muon events collected with field setting #1 (blue points and fill). On the x-axis, $t = 0\,\mu\text{s}$ corresponds to the detection of a three-module muon event. Overlaid is the simulated time distribution (red markers) produced with Kassiopeia. The simulated distribution is scaled to minimize the χ^2/ndf (248.0/99 for $t > 0\,\mu\text{s}$) with the offset from zero being fixed by the average electron counts prior to muon detection ($-100\,\mu\text{s} < t < 0\,\mu\text{s}$). The error bars are purely statistical. At the bottom of the figure, the residual (Simulation − Data) is displayed.

of the detector were included in the analysis, since these pixels directly measure events from a well-defined section of the MS surface. For each electron event, the time difference between the electron event and the most recent muon event was tabulated, and the distribution of these time differences is shown in Figure 5.3 for the case of setting #1. An excess above the random-coincidence level is clearly visible, indicating the presence of muon-coincident electron events. The distribution peaks at time differences of about 15 µs.

5.3.2 Comparison with Simulation

To confirm that the time structure of the coincidence peak is consistent with the production of muon-induced electrons, Monte Carlo simulations were performed using KASSIOPEIA. The simulation geometry included a simplified version of the system apparatus, consisting of the MS vessel and the FPD system, and employed the same electromagnetic field configuration used in setting #1, excluding the IE system. Over 10^5 electrons were produced at the MS walls, uniformly spread over axial positions $-3.14\,\mathrm{m} \leq z \leq -0.27\,\mathrm{m}$, which is the range corresponding to the magnetic field lines that connect to the FPD (pixel rings 2–12). The initial energy and emission angle of the electrons were sampled from the same distributions discussed in section 4.3.3.

The flight times for the simulated electrons that reached the FPD are shown in Figure 5.3. The simulation replicates the essential features of the measured distribution of electron events. However, at longer times ($t > 15\,\mu\mathrm{s}$) the simulation tends to underestimate the number of events. The simulation excludes any effects from IE system, which were placed at an offset voltage ($\Delta U_{\mathrm{IE}} = -5\,\mathrm{V}$) during the measurement. This voltage is large enough to block a significant fraction of events from the vessel walls. However, SEs are also emitted from the IE system and its holding structure (in the same way as from the walls), and these secondaries are not electrically shielded. The combined effect of the blocked electrons from the walls and the additional events from the wire electrodes may explain the slight differences between the distributions. Overall, however, the good agreement between measurement and simulation validates the proposed SE energy spectrum and confirms KATRIN's basic model

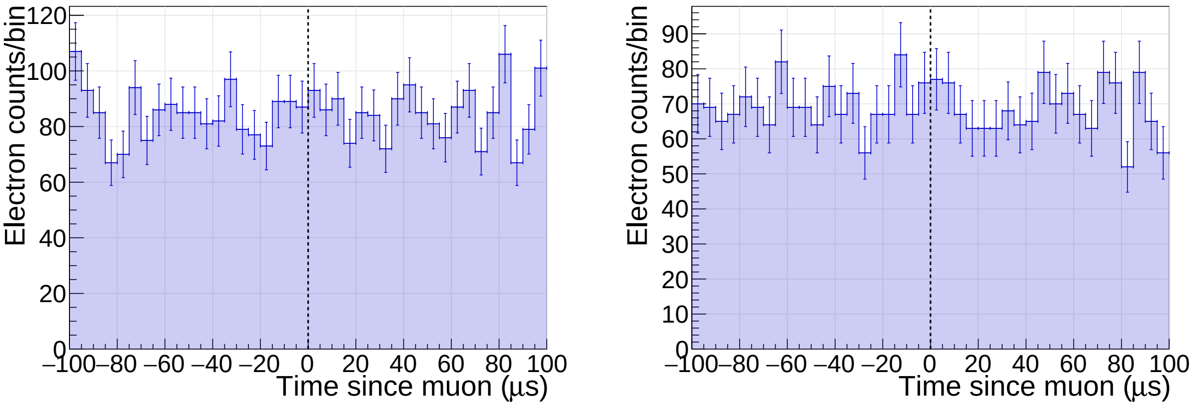

(a) Setting #2

(b) Setting #3

Figure 5.4: The distribution of the time differences between electron and muon events under symmetric magnetic field settings. The black dashed line indicates $t = 0\,\mu\mathrm{s}$, the detection of a muon event.

of background production due to muons.

5.3.3 Coincidence Under Nominal Conditions

The time distributions of muon-coincident electron events under setting #2 and setting #3 are displayed in Figure 5.4. No corresponding increase in the number of electron events following the three-module muon signals is observed.

One can attempt to set an upper limit on the muon-induced background rate by counting the excess number of events for $t > 0$ compared with $t < 0$, and then scaling the result appropriately to consider all muon events that pass through the MS, not just those that pass through modules 6, 7, and 8. However, this approach is vulnerable to systematic uncertainties. First, it is challenging to accurately extrapolate the coincidence rate for a particular region of the MS surface to the entire vessel without understanding the efficiency of electron transport as a function of the initial location on the MS surface. This requires significant particle-tracking simulations beyond the scope of the present work. A second difficulty is the possible time-dependent behavior of the secondaries. Electrons can be magnetically trapped in the symmetric magnetic field of setting #2 and setting #3 for up to several minutes [80]; thus, muon-induced secondaries and any additional electrons produced in the trap can reach the FPD well beyond the 100 µs interval applied in the coincidence study.

To test the statistical sensitivity of using the coincidence data to set an upper limit, a naive extrapolation to the entire MS was performed; the resulting upper limit on the muon-induced rate is comparable to the value derived from the correlation study (see section 5.4.3). Because the uncertainties for the coincidence approach are difficult to calculate, this method was not developed further.

5.4 Correlation Analysis

If the MS background rate is partly muon-induced, the measured electron rate should correlate with the muon flux as a function of time. Let us assume that the total measured electron rate $R_{\mathrm{FPD}}(t)$ is composed of two components:

1. A muon-induced rate $R_{\mathrm{FPD},\mu}(t)$, which is proportional to the muon rate $R_\mu(t)$ summed over all modules.
2. A constant rate $R_{\mathrm{FPD,other}}$ caused by other background sources.

In this case, one can write

$$R_{\mathrm{FPD}}(t) = K \cdot R_\mu(t) + R_{\mathrm{FPD,other}}, \tag{5.2}$$

where K is a proportionality constant. If one divides this equation by the average FPD rate $\overline{R_{\mathrm{FPD}}}$, one gets

$$\frac{R_{\mathrm{FPD}}(t)}{\overline{R_{\mathrm{FPD}}}} = K \cdot \frac{\overline{R_\mu}}{\overline{R_{\mathrm{FPD}}}} \cdot \frac{R_\mu(t)}{\overline{R_\mu}} + \frac{R_{\mathrm{FPD,other}}}{\overline{R_{\mathrm{FPD}}}}. \tag{5.3}$$

If one defines $m \equiv K \cdot (\overline{R_\mu}/\overline{R_{\mathrm{FPD}}})$, where $\overline{R_\mu}$ is the average muon module rate, then Equation 5.3 can be rewritten as

$$\frac{R_{\mathrm{FPD}}(t)}{\overline{R_{\mathrm{FPD}}}} = m \cdot \frac{R_\mu(t)}{\overline{R_\mu}} + (1 - m). \tag{5.4}$$

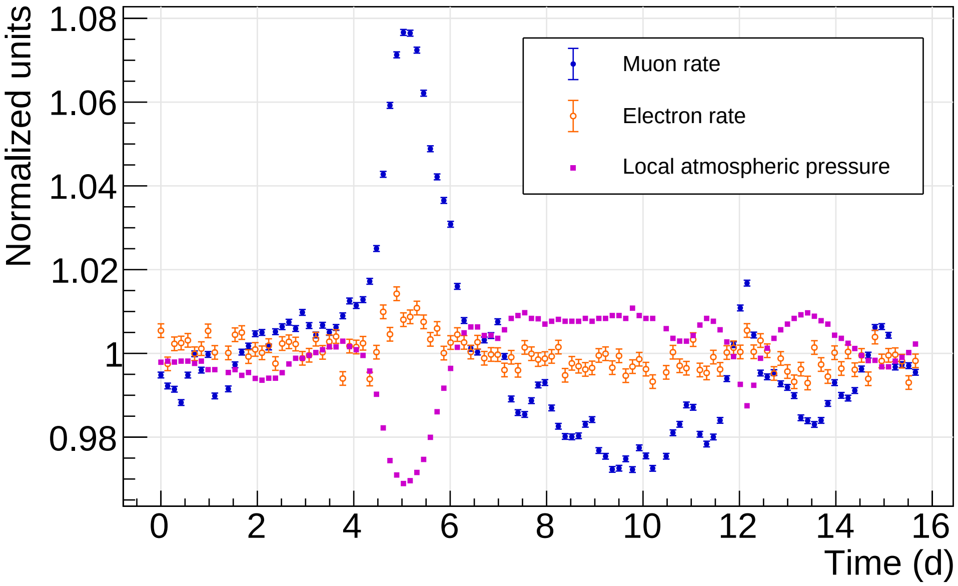

Figure 5.5: The normalized muon and electron rates as a function of time under setting #1. Each datapoint corresponds to the average value during an FPD run. The pressure was measured by a weather station housed in the spectrometer hall (located at ground level), which correlates with the atmospheric pressure.

From this equation, one can see that the normalized FPD rate ($R_{\text{FPD}}(t)/\overline{R_{\text{FPD}}}$) is proportional to the normalized muon module rate ($R_\mu(t)/\overline{R_\mu}$). Therefore, the value of m indicates the fraction of the total FPD rate that is muon-induced, and can be obtained from the slope if one plots the normalized FPD rate as a function of the normalized muon module rate and fits to Equation 5.4.

The first iteration of the correlation analysis described in this chapter was developed in a previous work [206], and the results were also used to study the Rydberg background [34, 177]. However, the correlation analysis presented here contains several updates, including the use of additional measurement runs.

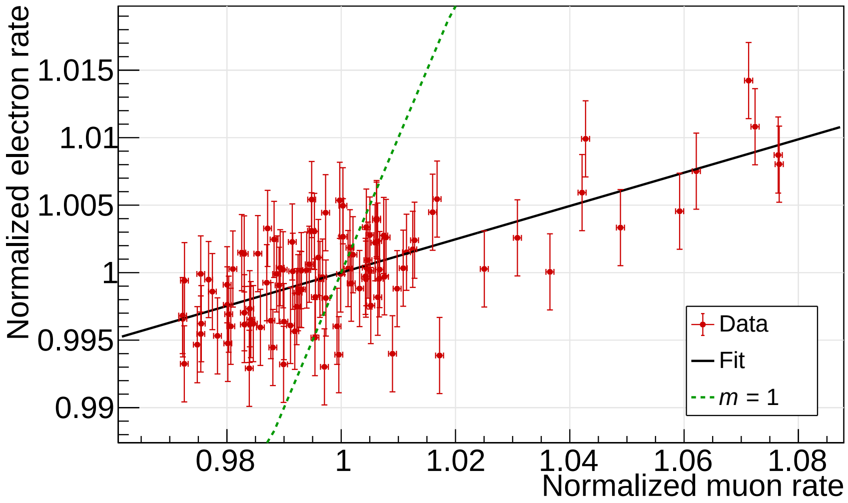

Figure 5.6: The normalized electron rate as a function of the normalized muon rate under setting #1. A fit, given by the solid black line, indicates a slope of $m = 0.123 \pm 0.012$ with a correlation coefficient of $r = 0.70 \pm 0.06$. If muons were responsible for the entire electron rate, then one would find $m = 1$ (indicated by the dashed green line).

5.4.1 Asymmetric Magnetic Field

The normalized muon and electron rates as functions of time for setting #1 are displayed in Figure 5.5. A large increase in the muon rate is visible near day 5, caused by a low-pressure weather system that passed over the experiment. The reduced atmospheric pressure indicates a decreased air density (and therefore a larger mean free path) that results in more muons reaching the Earth's surface [207].

The normalized electron rate as a function of the normalized muon rate is shown in Figure 5.6. A fit to the points indicates a slope of $m = 0.123 \pm 0.012$, with a Pearson correlation coefficient of $r = 0.70 \pm 0.06$. A strong correlation is therefore observed between the muon and electron rates, but only a relatively small number of electron events ($12.3 \pm 1.2\,\%$) are caused by muons. A further analysis of the setting #1 correlation results, which is based on differentiating between single and cluster electron events, can be found in the published paper [188].

5.4.2 Electron Production Rate

One can use the value of m obtained from the asymmetric magnetic field measurements to determine another quantity: the electron production rate from cosmic-ray muons passing through the MS [195]. This quantity, denoted by α, can be computed by taking the ratio of the electron emission rate from the inner MS surface and the muon rate through the same surface:

$$\alpha = \frac{m \cdot N_{\mathrm{FPD}} \cdot C}{N_\mu}. \tag{5.5}$$

The numerator of Equation 5.5 indicates the number of muon-induced electrons emitted from the MS surface for setting #1, but without any electrostatic shielding (i.e., $\Delta U_{\mathrm{IE}} = 0\,\mathrm{V}$). The FPD rate measured in this configuration is $N_{\mathrm{FPD}} = 790\,\mathrm{cps}$; this measurement is described in another work [34]. The rate measured at the FPD must be corrected to account for the electron transport probability from the spectrometer surface and the detector efficiency (see section 4.3.3); the correction factor C is found to be 8.0. Finally, to get the muon-induced rate from the surface, one must multiply by $m = 0.123$. The denominator N_μ indicates the number of muons that pass through the same region of the spectrometer surface. The Geant4 simulation described in section 5.1 was used to calculate this value, and one finds that $N_\mu = 13.3\,\mathrm{kcps}$.

Inserting the aforementioned values into Equation 5.5, the result is $\alpha = 0.058$. Inverting this number, one electron is produced for every ∼17 muon crossings of the spectrometer surface.

5.4.3 Correlation Under Nominal Conditions

The correlation analysis was repeated for setting #2 and setting #3, which utilized symmetric magnetic fields; the results are given in Table 5.2. No significant correlation was observed for either of these two settings. This indicates that the magnetic shielding inside the MS is effective at preventing muon-induced electrons emitted from the vessel surface from reaching the FPD.

Setting	Avg. FPD rate (cps)	Avg. muon rate (cps)	Correlation	Slope m
1	252.726 ± 0.068	1413.14 ± 0.09	0.70 ± 0.06	0.123 ± 0.012
2	0.8259 ± 0.0015	1421.15 ± 0.05	-0.02 ± 0.10	-0.013 ± 0.079
3	0.6639 ± 0.0014	1420.69 ± 0.05	0.12 ± 0.08	0.118 ± 0.093

Table 5.2: Summary of the muon-electron correlation analysis. The errors on the FPD rates (listed here and shown in Figure 5.6 and Figure 5.7) are the RMS errors.

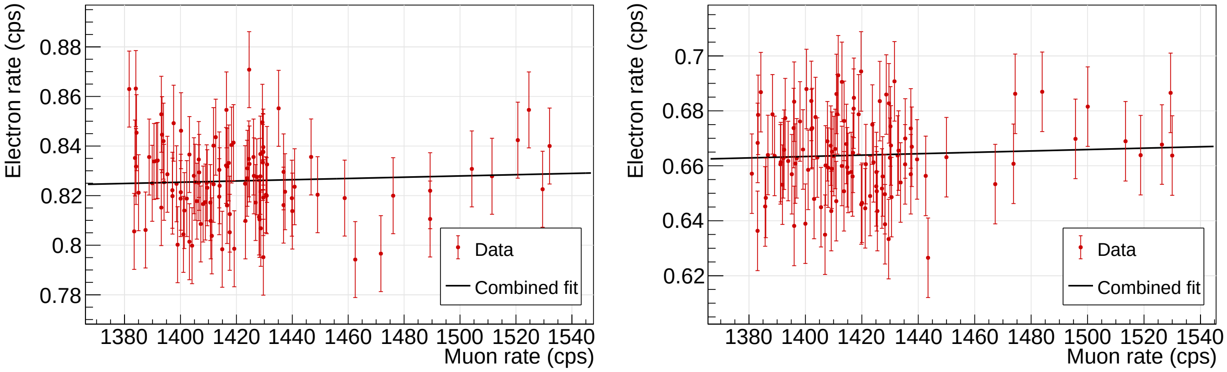

(a) Setting #2

(b) Setting #3

Figure 5.7: Electron rate as a function of muon rate for symmetric magnetic field settings. A simultaneous linear fit of both datasets (black line) finds a slope $K = (2.5 \pm 3.2) \times 10^{-5}$, indicating $m = 0.044 \pm 0.054$ for setting #2 and $m = 0.054 \pm 0.068$ for setting #3.

To determine the residual contribution from muons on the MS background, a combined fit was performed for settings #2 and #3 (Figure 5.7). The rationale for doing a combined fit is to increase the available statistics. Setting #3, with its substantial electrostatic shielding, is closest to the standard KATRIN measurement setting. Setting #2 has significantly less shielding from the IE system and muons are more likely to produce background with this setting. Incorporating the setting #2 data into the analysis with setting #3 should, in principle, increase the fitted value of m. However, as the analysis is statistics-limited, the fitted value of m for setting #3 decreases for the combined fit: $m = 0.054 \pm 0.068$ (compared with $m = 0.118 \pm 0.093$ when only using setting #3).

Following the unified approach (see section 4.4), the upper limit on the muon-induced fraction is

$$m < 0.166 \quad (90\,\%\ \text{C.L.}). \tag{5.6}$$

The average background rate under setting #3 is 0.692 cps, after applying a corrective factor (148/142) to account for six excluded detector pixels. Thus, Equation 5.6 indicates that cosmic-ray muons contribute less than 0.115 cps to the total MS background rate under nominal conditions.

Chapter 6

GAMMA-INDUCED BACKGROUND IN THE MAIN SPECTROMETER

When passing through the MS steel, environmental gamma radiation can produce SEs. As discussed in chapter 4, of particular concern is the generation of low-energy (true secondary) electrons. Due to imperfections in the magnetic and electrostatic shielding, SEs emitted from the surfaces may have a small probability to enter the sensitive magnetic flux tube that connects to the FPD. The validity of this background-generating mechanism from gammas has been confirmed from measurements with the Mainz spectrometer [208] and the PS [209]. Because of the increased size of the spectrometer, there is the potential for a significant background contribution from gamma-induced surface electrons in the MS.

In this chapter, the effect of environmental gamma radiation on the MS background rate is investigated through a combination of simulation and measurement data, and the effectiveness of the shielding in the MS is demonstrated. The content of this chapter is copied from a paper in preparation for publication [158]. The expected gamma flux in the spectrometer hall, as derived from simulations, is discussed in section 6.1. In section 6.2, the simulation results are compared to background measurements under conditions of gamma enhancement and suppression. The contribution of environmental gamma radiation to the KATRIN background rate is derived in section 6.3. A single/cluster event analysis using the measurements described in this chapter can be found in another thesis [177].

Isotope	Wall concrete	Floor concrete	MS steel
^{40}K	409 ± 22	61 ± 3	$< (3 \times 10^{-6})$
^{238}U	23 ± 5	6.0 ± 0.7	$(5.0 \pm 2.5) \times 10^{-2}$
^{232}Th	18 ± 1	3.3 ± 0.3	$< (1.2 \times 10^{-3})$
^{235}U	1.7 ± 0.5	0.6 ± 0.1	
^{60}Co			$(1.8 \pm 0.3) \times 10^{-3}$

Table 6.1: Specific activities (in units of Bq/kg) determined from radioassay measurements for materials in the KATRIN spectrometer hall. The activity of the wall concrete was only measured for the basement walls; for the upper walls, the same distribution of activities was assumed. The steel activities were measured at the Oroville Low Background Facility [210].

6.1 Environmental Gamma Radiation in the Spectrometer Hall

6.1.1 Radioactivity Measurements

The MS was constructed using low-radioactivity materials in order to limit background production from environmental gammas. The central cylindrical portion of the MS vessel was built from 32 mm-thick sheet metal, composed of type 316LN stainless steel [74]. A sample of this metal, from the same batch used for the MS vessel, was measured for radioisotopes; the results of this study are given in Table 6.1. However, the primary source of gammas in the KATRIN spectrometer hall is not the vessel itself but rather the intrinsic radioactivity of the concrete used to construct the walls and floors.

The walls of the spectrometer hall are made of standard concrete. To reduce the effect of ambient gamma radiation, the floors were built using a low-activity concrete due to their close proximity to the MS. During construction of the hall, samples from every load of low-activity concrete were monitored with a NaI detector to ensure the activity fell within specifications. Additionally, the gamma spectra of several samples of the concrete were measured at KIT using a shielded high-purity germanium (HPGe) detector. The concrete activities shown in Table 6.1 were derived from these measurements. ^{40}K was found to be the largest contributor to the activity in the concrete, followed by the ^{238}U and ^{232}Th decay chains.

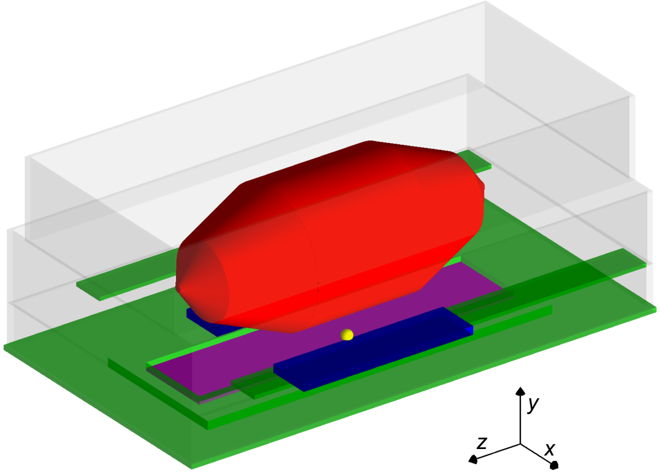

Figure 6.1: The GEANT4 simulation geometry, consisting of the steel MS (red), the concrete walls (gray) and floors (green), and, optionally, water tanks (blue) and basin water (purple). The yellow sphere indicates the position of the optional ^{60}Co source. The coordinate axes for the experiment are also shown, where the z-direction (x-direction) corresponds to due north (west). For orientation, the FPD is located north of the spectrometer.

6.1.2 Simulation of the Gamma Flux

To better understand the background due to environmental gamma radiation, simulations of the gamma flux in the MS were performed with the GEANT4 simulation toolkit [192–194], version 10.4.p02. A simplified reproduction of the KATRIN spectrometer hall was implemented; the geometry included the steel MS vessel and the concrete walls and floors (Figure 6.1). Radioactive isotopes were uniformly created in the walls, floors, and steel with the relative production rates determined from the radioassay measurements given in Table 6.1. The effect of ^{222}Rn in the air was also included, assuming an activity of $49 \pm 15\,\mathrm{Bq/m^3}$, which is the average indoor radon level in Germany [211]. The decays of the isotopes and any subsequent daughters were handled by the GEANT4 Radioactive Decay Module, and secular equilibrium was assumed. This module has recently been updated by the GEANT4 collaboration to include newer versions of the Evaluated Nuclear Structure Data File (ENSDF) datasets [212] and to better ensure energy conservation for decays [194]. Available physics

Component	MS rate (gammas/s)	Percentage
Concrete walls	$(2.06 \pm 0.08) \times 10^6$	80.2 %
Concrete floors	$(4.1 \pm 0.2) \times 10^5$	15.8 %
Air	$(9.0 \pm 2.7) \times 10^4$	3.5 %
Steel hull	$(1.1 \pm 0.5) \times 10^4$	0.4 %
Total	$(2.56 \pm 0.09) \times 10^6$	

Table 6.2: Sources of gamma radiation in the simulated spectrometer hall. For each component, the computed gamma flux at the inner surface of the MS is listed. The errors are purely systematic and indicate the uncertainty of the component activities.

processes were set by the `Shielding_EMZ` physics list, which uses the most accurate electromagnetic physics models and is well-suited for shielding simulations [213].

The gamma fluxes determined from simulation are listed in Table 6.2 for each geometrical component. As expected, the concrete walls are the primary contributor to the gamma flux inside the MS, followed by the concrete floors. The gammas originating from the steel vessel and the air, combined together, make up less than 4 % of the rate inside the MS.

Gamma spectra were measured at various locations in the spectrometer hall using a HPGe detector. One of these spectra, collected for the detector facing the western wall in the basement of the hall, is shown in Figure 6.2. The dominant contributor to the gamma spectrum is the 1461 keV line from the decay of ^{40}K [214]. To compare with the measurement, a very simple germanium detector was implemented in the GEANT4 simulation. The simulated spectrum (see Figure 6.2) qualitatively replicates the important features of the measured gamma spectrum. Overall, the simulation is able to adequately approximate the spectrum of environmental gammas in the spectrometer hall.

6.2 Background Measurements

During SDS-IIb, measurements were performed to study the gamma-induced background. As described in the following subsections, the electron rate was measured by the FPD for several configurations that modified the flux of environmental gammas at the MS. The voltage

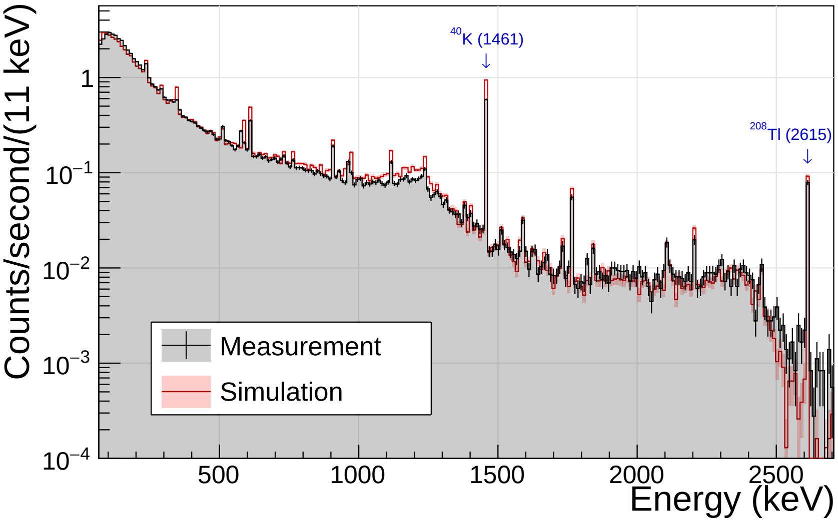

Figure 6.2: The energy spectrum measured by a HPGe detector in the spectrometer hall (grey), and the simulated spectrum for energy deposited in a germanium crystal by gammas originating from a 0.6 m by 0.6 m region of the concrete wall (red). The simulated spectrum has been normalized to the measured spectrum, with a normalization factor of 5.7. Prominent lines from ^{208}Tl (^{232}Th decay chain) and ^{40}K are labeled for reference.

settings used for these measurements are given in Table 6.3. Due to a broken preamplifier module in the detector readout, six FPD pixels (each located in a different pixel ring) were not functional. The rate for each detector pixel ring with a missing pixel is linearly scaled by a corrective factor of $\frac{12}{11}$.

6.2.1 Enhancement of Gamma Flux

To increase the gamma-induced background, a ^{60}Co source with a total activity of 53.3 ± 2.7 MBq was positioned in the vicinity of the MS. Details of this source are shown in Figure 6.3. Measurements were completed with the source partially outside its lead shielding ("open" configuration) and completely inside its lead shielding ("closed" configuration). The decay of ^{60}Co primarily results in the cascade emission of two gammas at 1173 keV and 1332 keV [215].

Measurements of the electron rate with the FPD system were performed with the source

Component	Voltage	Value/range (V)
MS hull	U_0	$-18\,500$ to $-18\,600$
MS inner electrode	ΔU_{IE}	0 to -100
Post-acceleration electrode	U_{PAE}	$10\,000$
Bias ring of detector wafer	U_{bias}	120

Table 6.3: The voltage settings used during the gamma-induced background measurements.

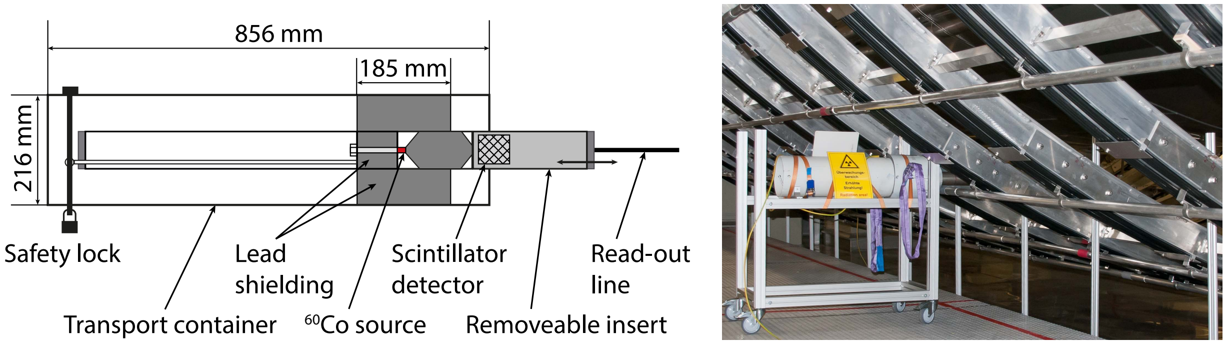

(a)

(b)

Figure 6.3: The ^{60}Co source used to increase the gamma radiation at the MS. (a) Schematic of the source (in the "closed" configuration). When the safety lock is removed, the source can be moved to the right, outside of the transport container with its lead shielding. (b) Photo of the source installed next to the air-coils, beneath the MS vessel. Both figures are taken from [158].

Magnetic field	U_0 (kV)	ΔU_{IE} (V)	Source	Rate (cps)	ΔRate (cps)
setting C (asym.)	-18.5	0	open	871.9 ± 0.7	231.7 ± 0.9
			closed	640.2 ± 0.6	
setting C (asym.)	-18.5	-100	open	95.6 ± 0.2	26.8 ± 0.3
			closed	68.8 ± 0.2	
setting L (sym.)	-18.5	-100	open	0.566 ± 0.004	0.005 ± 0.006
			closed	0.561 ± 0.005	

Table 6.4: Results from the FPD measurements with the ^{60}Co source. For the asymmetric magnetic field measurements, the rates exclude the inner 16 detector pixels. All rates are scaled to correct for the broken preamplifier module (but not for the inner 16 detector pixels), and the errors on the rates are statistical.

located at different locations near the MS. However, extended measurements with the "closed" configuration were only performed at one position: the ^{60}Co source located under the west side of the MS, approximately equidistant from the ends of the vessel (see Figure 6.1). Therefore, only results from this position are presented here.

The FPD rate was measured for several magnetic-field and electrostatic shielding configurations; the rates can be found in Table 6.4. The effect of the ^{60}Co source can clearly be seen in the bottom-right portion of the detector wafer in the left and center panels of Figure 6.4 (asymmetric magnetic field), but is absent in the right panel (symmetric magnetic field).

The measurements with the ^{60}Co source demonstrate the effectiveness of the shielding inside the MS against gamma radiation. The background rate due to the ^{60}Co source under an asymmetric magnetic configuration dropped from 231.7 ± 0.9 cps to 26.8 ± 0.3 cps with the addition of electrostatic shielding (changing ΔU_{IE} from 0 V to -100 V). A further reduction in the rate by at least three orders of magnitude occurred when switching to the symmetric magnetic configuration (0.005 ± 0.006 cps). Though a large number of ^{60}Co-induced SEs were emitted from the MS surface, no significant rate effect was observed with the nominal magnetic field setting.

A simulation of the gamma flux from the ^{60}Co source was performed using the geometry

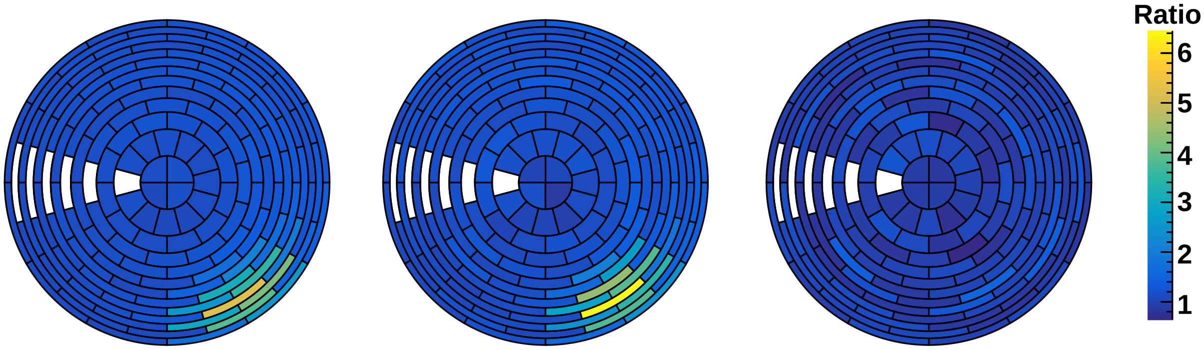

Figure 6.4: The ratio of the electron rate with the open ^{60}Co source to the rate with the closed source, for each detector pixel, for three cases: with no magnetic shielding and no electrostatic shielding (left panel), with no magnetic shielding but with electrostatic shielding (center panel), and with both magnetic shielding and electrostatic shielding (right panel). The detector is being viewed from the FPD end of the beamline. The six white pixels were excluded due to a broken preamplifier module. The total FPD rate with the closed source is 683.3 cps (73.7 cps) (0.540 cps) for the left (center) (right) panel.

Rate (10^6 gammas/s)	^{60}Co	Water
G_0	2.8 ± 0.1	2.564 ± 0.090
G_1	20.9 ± 0.9	2.411 ± 0.088
$G_1 - G_0$	18.2 ± 0.9	-0.153 ± 0.002

Table 6.5: Gamma rates through the interior of the MS as determined from simulations. G_0 is either the rate with the closed ^{60}Co source (second column) or with no water shielding (third column). Similarly, G_1 is either the rate with the open ^{60}Co source or with water shielding. The rate includes all crossings (ingoing and outgoing) of the inner surface. The errors include both statistical and systematic uncertainties, although the latter only includes the uncertainty on the activity of the gamma sources (see Table 6.1). Other systematic effects, such as the accuracy of the included GEANT4 physics processes and the correctness of the simulation geometry, were not calculated.

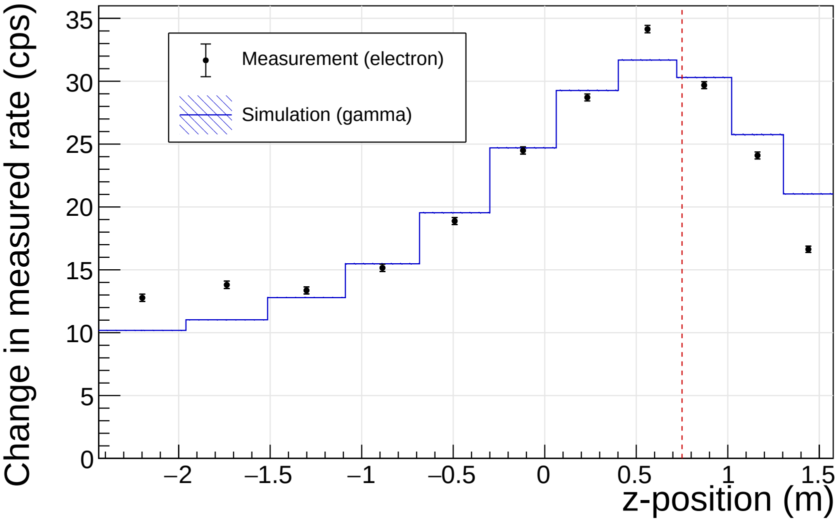

Figure 6.5: The excess FPD rate measured with magnetic field setting C with the ^{60}Co source, as a function of the axial position z. Each bin corresponds to a detector pixel ring which images a specific axial region of the MS surface. Also shown is the simulated gamma rate induced by the source at the inner surface of the MS, which has been scaled to match the total measured rate. The location of the ^{60}Co source in the simulation geometry is marked by the dashed line.

described in section 6.1.2. Table 6.5 shows the simulated rates for gammas traversing the inner surface of the MS vessel. The presence of the ^{60}Co source increases the gamma flux through the entire MS surface by about a factor of 8. The change in rate due to the open ^{60}Co source is plotted as a function of axial position along the MS in Figure 6.5. The distributions for the measured electron rate (asymmetric field setting) and the simulated gamma rate exhibit nearly identical shapes and peak at the same axial position.

6.2.2 Suppression of Gamma Flux

In an effort to reduce the gamma flux originating from the bottom floor of the spectrometer hall, water shielding was temporarily added below the MS. The basin beneath the MS (24.1 m long by 5.6 m wide) was filled with water to a depth of 20 cm. Additionally, a total of four flexible water tanks (each approximately 6.5 m long by 3.2 m wide by 0.6 m high) were

Figure 6.6: Two of the four flexible water tanks placed beneath the MS during the gamma suppression measurements. Photo taken from [158].

installed next to the basin to increase the shielded area. The water tanks can be seen in Figure 6.6.

The background rates for measurements with and without water shielding are shown in Table 6.6. Two asymmetric field settings, with field lines intersecting different regions of the MS surface, were implemented; similar reductions in the electron rate due to the water shielding were found for both ($\sim$0.4 %). For the symmetric magnetic field setting, the shielding had no significant effect on the electron rate.

To investigate the effect of the shielding on the gamma flux, water was added to the simulation geometry using the dimensions cited above (see Figure 6.1). The simulated rates are shown in Table 6.5. The addition of water shielding reduced the gamma rate inside the MS by about 7 %. The change in rate due to the water shielding is plotted as a function of axial position along the MS in Figure 6.7. The simulated gamma rate is mostly flat across the measured range and roughly matches the measured electron rate distribution (which is statistics-limited).

Magnetic field	U_0 (kV)	ΔU_{IE} (V)	Shielding	Rate (cps)	ΔRate (cps)
setting D (asym.)	-18.6	0	no water	620.1 ± 0.1	-2.3 ± 0.2
			water	617.8 ± 0.1	
setting E (asym.)	-18.6	0	no water	653.7 ± 0.2	-2.8 ± 0.2
			water	650.9 ± 0.1	
setting M (sym.)	-18.5	-100	no water	0.469 ± 0.003	0.001 ± 0.004
	-18.6	-100	water	0.469 ± 0.003	

Table 6.6: Results from the FPD measurements with(out) the water shielding. Setting D (setting E) images $-3.9\,\mathrm{m} < z < -1.0\,\mathrm{m}$ ($1.3\,\mathrm{m} < z < 3.7\,\mathrm{m}$). For the asymmetric magnetic field measurements, the rates exclude the inner 28 pixels (setting D) or inner 4 pixels (setting E). All rates are scaled to correct for the broken preamplifier module, and the errors on the rates are statistical.

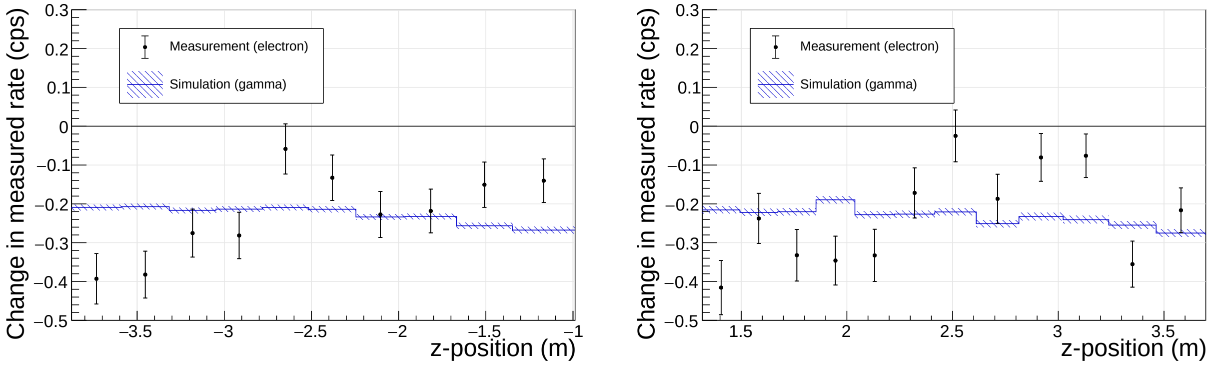

(a) Setting D

(b) Setting E

Figure 6.7: The reduction in the electron rate at the inner surface of the MS, caused by the water shielding, for two asymmetric magnetic field settings. The region shielded by the water tanks is roughly $-6.5\,\mathrm{m} < z < 6.5\,\mathrm{m}$. The simulated decrease in the gamma rate is also shown in each figure, normalized to the measured rate.

6.3 Gamma-Induced Background Contribution

By combining the asymmetric magnetic field measurements and simulation results, it is possible to compute two quantities of interest: the SE yield for gamma radiation traversing the inner surface of the MS, and the fraction of SEs caused by environmental gamma radiation. The symmetric field measurements provide a way to determine the gamma-induced background contribution under standard operating conditions in future neutrino mass measurements.

The relevant values used to calculate these quantities are listed in Table 6.7. Three different rates are to be distinguished: the measured FPD electron rate (R), the calculated gamma-induced MS electron emission rate (S), and the calculated gamma rate through the MS (G). Without the ^{60}Co source or water shielding, the values of R, S, and G can be distinguished as follows:

$$\begin{aligned} R &= R_{\text{env}} + R_{\text{other}}, \\ S &= S_{\text{env}} + S_{\text{other}}, \\ G &= G_{\text{env}}, \end{aligned} \tag{6.1}$$

where "env" indicates the contribution from environmental gamma emitters (e.g., concrete) and "other" indicates the contribution from other backgrounds (e.g., cosmic-ray muons).

The change in rate due to the ^{60}Co source is defined to be

$$\Delta R_{\text{cobalt}} = R_{\text{open}} - R_{\text{closed}}, \tag{6.2}$$

while for water shielding the change in rate is

$$\Delta R_{\text{shielding}} = R_{\text{water}} - R_{\text{no water}}. \tag{6.3}$$

Identical formulations hold for ΔS and ΔG.

6.3.1 Secondary Electron Yield

The yield Y is the gamma-induced electron rate divided by the gamma rate through the same surface. This can be computed from the effect of the ^{60}Co source or water shielding

	^{60}Co source	^{60}Co source	Water shielding	Water shielding
Magnetic field	setting C	setting C	setting D	setting E
z-range (m)	-2.44 to 1.58	-2.44 to 1.58	-3.88 to -0.99	1.32 to 3.70
ΔU_{IE} (V)	0	-100	0	0
R (cps)	640.2 ± 0.6	68.8 ± 0.2	620.1 ± 0.1	653.7 ± 0.2
ΔR (cps)	231.7 ± 0.9	26.8 ± 0.3	-2.3 ± 0.2	-2.8 ± 0.2
G (10^5 gammas/s)	4.5 ± 0.2	4.5 ± 0.2	3.3 ± 0.1	2.7 ± 0.1
ΔG (10^5 gammas/s)	86 ± 4	86 ± 4	-0.257 ± 0.004	-0.209 ± 0.003
P_{arrival} (%)	8.8 ± 0.1	–	11.2 ± 0.1	16.6 ± 0.1
Y (10^{-4} e$^-$/gamma)	3.1 ± 0.2	–	7.9 ± 0.7	8.0 ± 0.6
$f_{\text{env}}(10^{-2})$	1.9 ± 0.1	2.1 ± 0.1	4.6 ± 0.4	5.5 ± 0.5

Table 6.7: Values used in the calculation of the SE yield (Y) and fraction of secondaries induced by environmental gamma radiation (f_{env}). See the text for details about each listed parameter.

according to the following equation:

$$Y = \frac{\Delta S}{\Delta G}. \tag{6.4}$$

ΔS can be computed from ΔR after including electron transport and detection efficiencies:

$$\Delta S = \frac{\Delta R}{\epsilon \cdot P_{\text{arrival}}}, \tag{6.5}$$

where $\epsilon = 0.950 \pm 0.028$ is the FPD detection efficiency [130] and P_{arrival} is the average arrival probability for electrons. Because of the magnetic mirror effect, electrons emitted from the MS surface have a small probability to reach the FPD, which depends on their initial energy and emission angle relative to the magnetic field direction. P_{arrival} was calculated using KASSIOPEIA, following the same procedure outlined in section 4.3.3.

Using the ^{60}Co measurement, one finds $Y = 3 \times 10^{-4}\,\mathrm{e}^-/\gamma$. However, the yields derived from the water-shielding measurements give values that are consistent with each other but are a factor of 2.6 larger than the ^{60}Co result (see Table 6.7). This difference is likely the result of an incorrect value for ΔG obtained from simulations; the tension can be alleviated by decreasing the simulated effect of the ^{60}Co source or by increasing the simulated effect of the water shielding.

6.3.2 Fraction of Secondary Electrons Induced by Gammas

The fraction of SEs emitted from the MS surface which are caused by environmental gamma radiation can be computed in the following manner:

$$f_{\mathrm{env}} = \frac{S_{\mathrm{env}}}{S} \approx \frac{R_{\mathrm{env}}}{R}. \tag{6.6}$$

Assuming that R_{env} is proportional to the flux of gammas in the MS, the following relation applies:

$$R_{\mathrm{env}} \approx \frac{\Delta R}{\Delta G} G_{\mathrm{env}} \tag{6.7}$$

The gamma-induced fraction can thus be obtained by combining Equation 6.6 and Equation 6.7:

$$f_{\mathrm{env}} \approx \frac{G_{\mathrm{env}}}{\Delta G}\frac{\Delta R}{R} \tag{6.8}$$

Table 6.7 shows the values of f_{env} calculated from the ^{60}Co measurements under the two electrostatic shielding conditions, as well as from the gamma suppression measurements with water shielding. The results indicate that less than 6 % of SEs emitted from the MS surface are induced by environmental gammas. However, the values from the ^{60}Co and water shielding measurements differ by a factor of 2.5. The scale of this discrepancy is equivalent to the difference in the electron yields between the two types of measurements, as discussed in the previous section.

6.3.3 Gamma-Induced Background Rate under Standard Conditions

Similar to the asymmetric field measurements, it is possible to use Equation 6.7 to determine the effects of environmental gamma radiation under symmetric field conditions. Applying the measured and simulated rates listed in Table 6.8, one finds that $R_{\mathrm{env}} = 0.7 \pm 0.9\,\mathrm{mcps}$, which is consistent with zero. Assuming the rate is Gaussian, one can follow the unified approach [190] and set an upper limit on the gamma-induced background rate, obtaining $R_{\mathrm{env}} \leq 2.2\,\mathrm{mcps}$ (90 % C.L.).

	^{60}Co source	Water shielding
ΔG ($10^5\,\gamma$/s)	182 ± 9	-1.53 ± 0.02
G_{env} ($10^5\,\gamma$/s)	25.6 ± 0.9	25.6 ± 0.9
ΔR (mcps)	5 ± 6	0.8 ± 4.5
R_{env} (mcps)	0.7 ± 0.9	-13 ± 75
Upper limit (90 % C.L.) on R_{env} (mcps)	5.6	110

Table 6.8: Background rate R_{env} induced by environmental gamma radiation under standard conditions (symmetric magnetic field and $\Delta U_{\text{IE}} = -100\,\text{V}$). The relevant values used to calculate this rate are also listed. A corrective factor of 2.6 was applied to the upper limit on R_{env} for the ^{60}Co source.

However, one must account for the discrepancy in the results between the ^{60}Co source and water shielding measurements, as mentioned in the previous sections. A conservative approach is to allow for the possibility that the simulation overestimates the flux of gammas through the MS from the ^{60}Co source by a factor of 2.6. In this case, one finds

$$R_{\text{env}} \leq 5.6\,\text{mcps (90\,\% C.L.)} \tag{6.9}$$

Given a nominal rate of 561 mcps, this result indicates that less than ~1 % of the MS background rate can be attributed to environmental gamma radiation.

A similar procedure was followed with respect to the water shielding data, giving a limit of $R_{\text{env}} \leq 110\,\text{mcps}$ (90 % C.L.). Here, a corrective factor of $(2.6)^{-1}$ (which accounts for the possibility that the simulation underestimates the effect of the water shielding) was not applied, in order to obtain a conservative result. Only a weak limit is obtained in this case due to the small value of ΔG and the large uncertainty on ΔR.

Chapter 7

SIMULATIONS WITH THE INTER-SPECTROMETER PENNING TRAP

In this chapter, the Penning trap formed between the two KATRIN spectrometers is described in detail. First, the formation of Penning traps is briefly discussed (section 7.1) before turning to the details of the inter-spectrometer trap and its background production (section 7.2). Using updated simulation models, the motion of electrons in the Penning trap is presented (section 7.5). Additionally, the role of ionization of residual gas on the background produced from the Penning trap background is investigated via simulation (section 7.6). The simulation analyses required expanding the Kassiopeia code (section 7.3), most importantly to allow the inclusion of ion interactions (section 7.4).

7.1 Formation Conditions

Penning traps are formed in regions of strong electric and magnetic fields. Consider a simple cylindrical geometry, like that shown on the upper left side of Figure 7.1. The cylindrical tube is grounded, while at the ends of the cylinder are two cathodes, placed at $-2\,\mathrm{kV}$. This setup confines electrons along the axis of the cylinder (the axial direction) if they have energies below $2\,\mathrm{keV}$. Confinement along the radial direction will occur if a magnetic field is applied in the axial direction. The magnetic field induces a Lorentz force on the electrons, which causes them to undergo cyclotron motion and prevents them from reaching larger radii. Thus, this configuration of electric and magnetic fields creates a three-dimensional trap for low-energy electrons. The stronger the fields, the more energy is required by the electrons to escape the trap. Because the cathodes are directly placed at the axial ends of the trap, this type of Penning trap is known as a “cathode-to-cathode” trap.

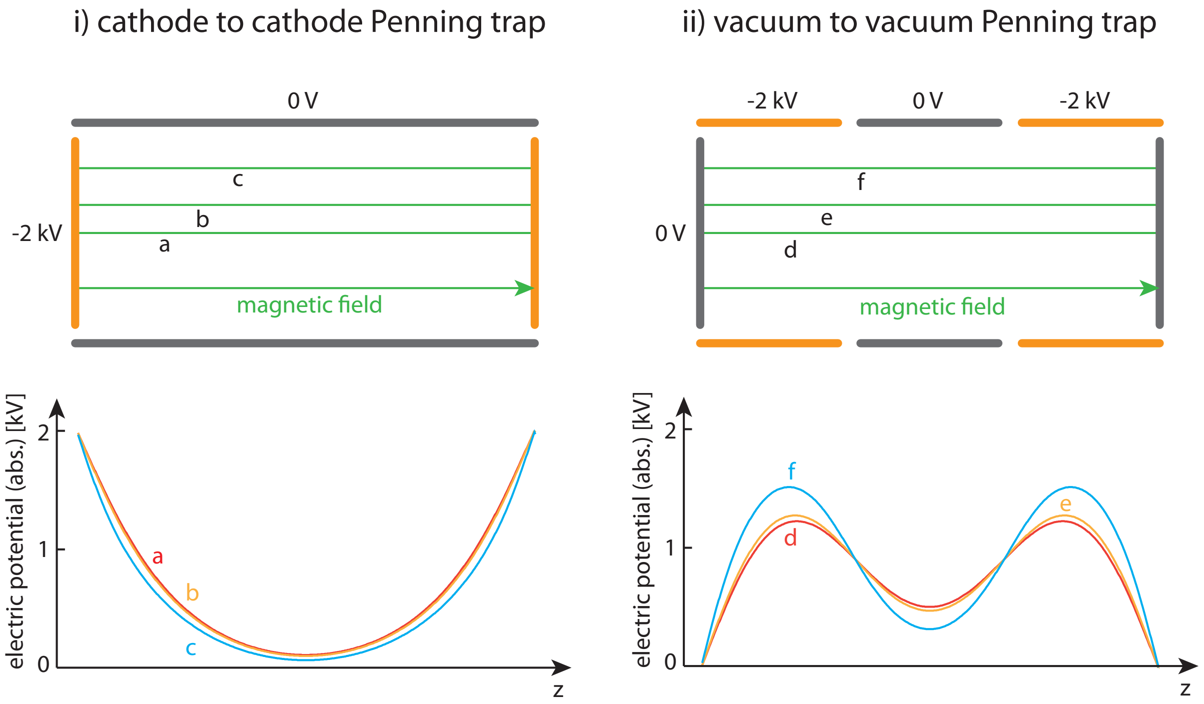

Figure 7.1: Types of Penning traps, shown for the case of a cylindrical geometry. In the cathode-to-cathode Penning trap (left figure), the magnetic field lines directly connect to the cathodes, which provides a direct filling mechanism. In contrast, the vacuum-to-vacuum trap (right figure) has a trapping region for electrons that is not connected to the cathodes by the magnetic field lines. Figure courtesy of Florian Fränkle, with adaptions from the version found in [155] with ©SISSA Medialab Srl. Reproduced by permission of IOP Publishing. All rights reserved.

A slightly more complex type of Penning trap is a "vacuum-to-vacuum" trap. An example with cylindrical geometry is shown on the right side of Figure 7.1, Here, electrons are also trapped due to the presence of cathodes, but the cathodes are located along the sides of the cylinder, separated by a grounded surface, with the flat ends of the cylinder also grounded. In this configuration, the trapping potential reaches its largest magnitude in the axial regions surrounded by the cathodes, but for a magnetically confined electron the trap edge is located in the vacuum and not directly at the cathode surface.

7.2 Inter-Spectrometer Trap

The Penning trap between the spectrometers was already considered in the initial design of the KATRIN experiment [74, 216]. Since that time, a series of simulation and experimental tests have been performed in order to quantify the trap conditions, estimate background production, and devise methods for the removal of stored electrons. Initial simulations of the Penning trap were undertaken by K. Essig [217]. However, the design of the KATRIN beamline has since been updated with new anti-Penning electrodes, re-designed ground electrodes, and a different magnet setup [218]. The present work is a study of the Penning trap properties under the geometry and electromagnetic fields planned for the neutrino mass measurements.

7.2.1 Electromagnetic Conditions

The inter-spectrometer Penning trap is a vacuum-to-vacuum trap. During standard KATRIN operation, the MS is operated at a large negative potential to fulfill its role as the primary MAC-E filter. The PS is placed at a slightly smaller negative potential to act as a pre-filter for the flux of β-particles originating from the WGTS. This creates a trapping region between the spectrometers. Low-energy electrons are axially confined by the potentials of the PS and MS. Due to the presence of the PS2 solenoid, the magnetic field inside the beamline has a local maximum in the region of the valve connecting the two spectrometers. This strong magnetic field prevents low-energy electrons from escaping in the radial direction.

This Penning trap cannot be avoided if both spectrometers are operated on high voltage. Figure 7.2 shows the electromagnetic conditions between the spectrometers

7.2.2 Filling the Trap

β-particles with an energy greater than the retarding energy of the PS will travel through the valve connecting the two spectrometers. Particles will make either one or two passes through the valve, depending on whether they are reflected by the retarding potential of the MS. If a β-particle scatters on residual gas in the region of the Penning trap, it can lose enough energy to be trapped by the electrostatic potentials.

An electron in the trap cannot escape unless the retarding potential of one of the spectrometers is reduced or the electron is provided additional energy (such as through a scattering process) to overcome the retarding potential. However, trapped electrons immediately begin losing energy upon being confined in the trap. The primary energy-loss mechanisms are synchrotron emission and scattering [218]. Trapped electrons can ionize residual gas and produce additional electrons in the trap. The threshold to ionize residual gas is 15.4 eV for H_2 [218]. Depending on the electrostatic potential where an ionization electron is produced, the electron can have enough energy to produce further ionizations. Ionization electrons produced in the center of the trap will have very small energies ($\sim$eV), while those produced near the trap edges, where the electric potential has a larger magnitude, can have keV-scale energies. Through these scattering and ionization processes, more and more electrons will fill the trap over time. Simulations performed by F. Glück show that a self-sustained avalanche of electrons in the Penning trap is possible, with a single 18 keV electron in the trap producing 10^8 ionizations [218]. This buildup of electrons, known as a *Penning discharge* [114, 155], can be a large and dangerous source of background particles, as described below.

7.2.3 Background Generation

Collisions between residual gas and trapped electrons produce positively charged ions. These ions will be accelerated into the negatively charged MS. Inside the spectrometer there is a

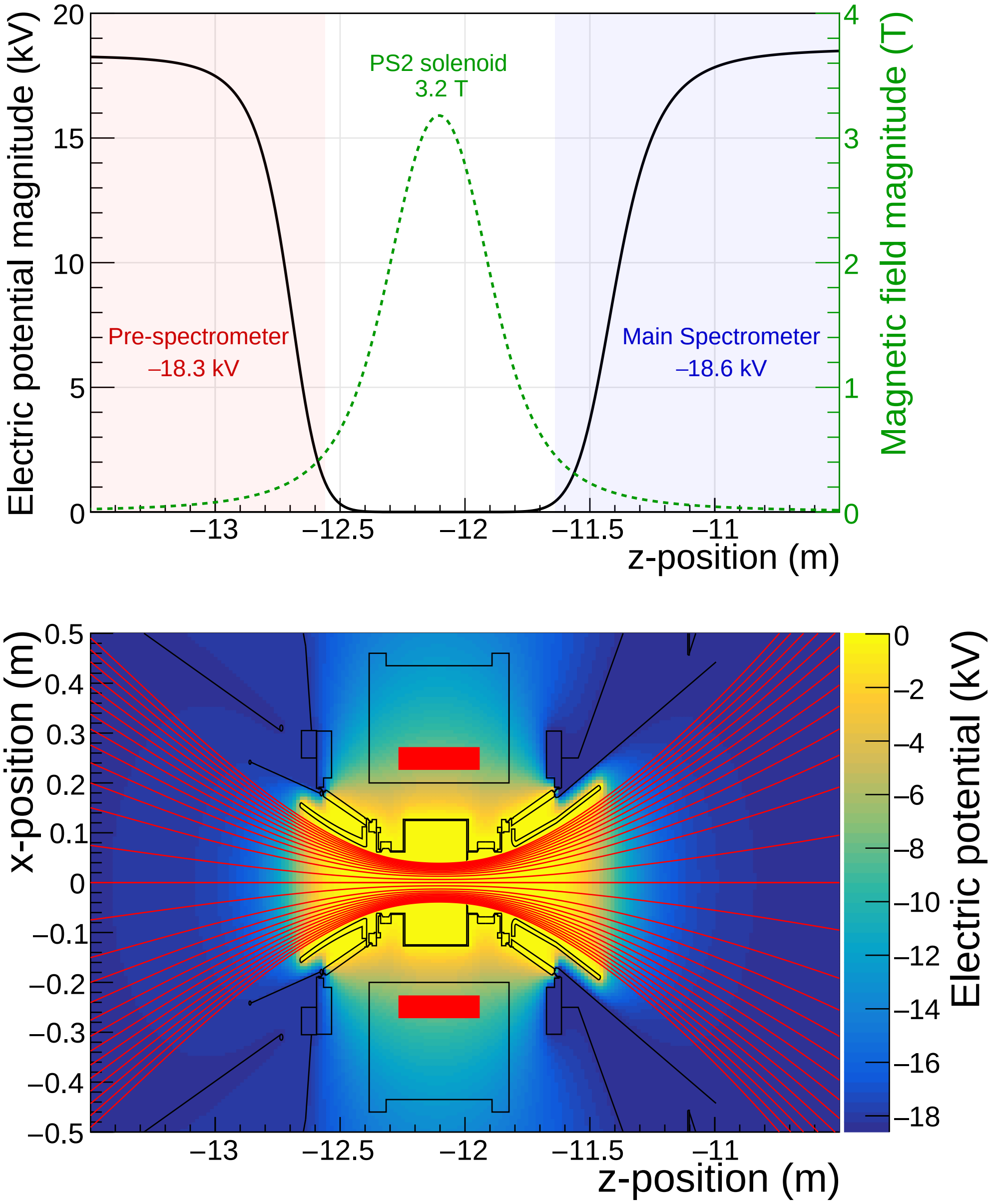

Figure 7.2: (*Top*): One-dimensional view of the electromagnetic conditions in the inter-spectrometer region, along the spectrometer axis. In black (green) is the magnitude of the electric potential (magnetic field). (*Bottom*): Cross-sectional view of the electromagnetic conditions in the inter-spectrometer region. The color scale indicates the electric potential; the value of the potential is only correct inside the beam-tube elements (i.e., inside the spectrometers and the connecting valve). The red lines are magnetic field lines that intersect the FPD. The position of the PS2 solenoid is marked by the red rectangles.

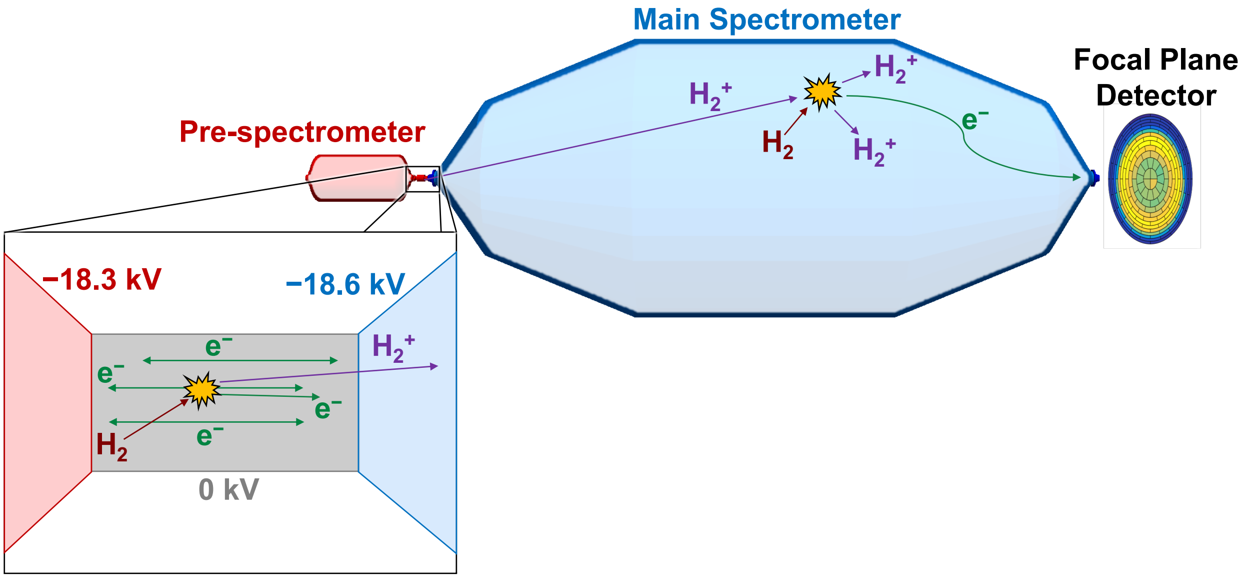

Figure 7.3: Diagram of background production from the Penning trap. The ionization of residual gas in the Penning trap leads to the creation of positive ions, which are accelerated into the MS and create ionization electrons which reach the FPD.

non-negligible probability for the positive ions to ionize residual gas, thus producing ionization electrons that will be magnetically guided to the detector. These electrons cannot be distinguished from the signal β-particles. In summary, more electrons in the Penning trap will lead to more positive ions entering the MS, which will cause more background events through ionization processes. A diagram of this background production mechanism is shown in Figure 7.3.

Background can also be generated by the high-energy positive ions when they impact the surface of the MS. After being accelerated by the negative potential of the MS, the positive ions will not follow an adiabatic trajectory but will rather follow approximately straight lines upon entering the MS. The impact of ions will lead to the emission of electrons from the surface. However, the effect of these electrons is mitigated by the electrostatic and magnetic shielding of the spectrometer.

Another possible background-generating mechanism comes from the production of UV light within the Penning trap [139]. Photons emitted during an ionization process are not bound by the trap but can enter the MS and ionize residual gas, thus producing background electrons.

7.2.4 Mitigation Strategies

In order to use the PS as a pre-filter in conjunction with the MS, an effective and reliable approach is needed to prevent background generation from the Penning trap. Four basic strategies are available:

1. Preventing electrons from being trapped.
2. Removing trapped electrons.
3. Preventing the creation of positive ions from the trap.
4. Preventing scattering of ions with residual gas in the MS.

Ensuring a very low residual gas pressure inside the beamline will address strategies #1, #3, and #4. However, if the Penning trap still produces background at the lowest achievable pressure inside the spectrometers, a way to implement strategy #2 is required. The emptying of stored electrons can be performed electromagnetically or mechanically.

Electromagnetic Removal of Electrons

Although applying an electric dipole field is an effective method to remove stored electrons inside the MS, it is not a practical solution for electrons in the Penning trap. Previous studies indicated that a dipole potential applied to the PS IE system on the order of 20 kV is required to significantly affect the storage conditions in the trap [218].

Removing stored electrons by a magnetic pulse method showed better promise [219, 220], but this technique requires an additional magnetic coil to cancel out the field of the PS2 magnet. Such a coil would be difficult to realize due to space and design constraints in the inter-spectrometer valve region.

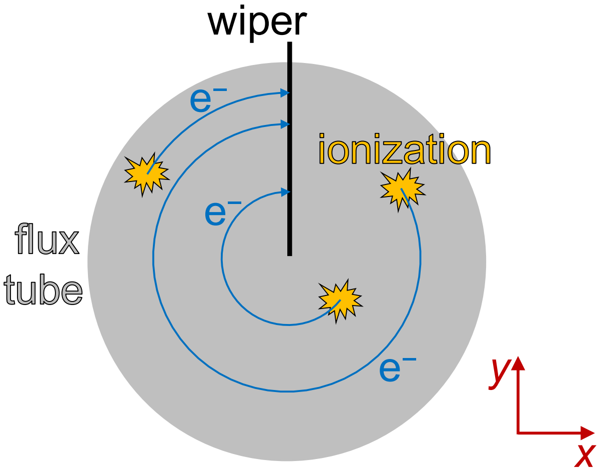

Figure 7.4: Schematic of mechanical means of emptying the Penning trap. Trapped electrons will undergo magnetron motion in the xy-plane (shown) and axial motion along the z-axis (not shown). The azimuthal motion results in the electrons eventually impacting the metal rod (wiper) and being removed. Drawing based on Figure 6.12 from [220].

Mechanical Removal of Electrons

Another method of removing trapped electrons is by mechanical means. By inserting a metal rod into the Penning trap, trapped electrons will impact the rod and be removed from the trap. Trapped electrons will undergo a magnetron drift and thus move azimuthally in the trap until they hit the metal rod (Figure 7.4). Two modes of operation are possible: a rod that is periodically inserted and removed (a Penning "wiper"), and a static mode, where the metal rod is continuously positioned in the flux tube. The static mode is not preferred since the rod would shadow a portion of the detector pixels and reduce the number of pixels that could be used for the neutrino mass measurement. However, if the trap fills quickly, periodic operation of the wiper may not be effective in preventing a Penning discharge; in this case, static operation of the wiper is required.

The mechanical method of emptying the Penning trap was first tested at Mainz [218, 221]. A Penning trap was created using the Mainz spectrometer and a disk-shaped electrode (a vacuum-to-cathode trap). A UV light source was available to excite electrons from the negatively charged electrode in order to fill the trap. A sweeping wire, made of copper and electrically grounded, was periodically swept through the trapping region to remove electrons. Measurements with this setup showed the effectiveness of the Penning wiper, although optimized settings for the wiper movement were required to prevent large bursts of background.

Based on the work at Mainz, further tests were performed with the PS at KIT [219, 220]. Because the MS was unavailable, a vacuum-to-vacuum trap was created using the PS and an electrode in the shape of a conical frustum. With this setup, both operation with a sweeping wire and with a static rod proved effective in removing trapped electrons. Due to the benefit of not shadowing the detector, it was decided to pursue a moving metal rod as the method to empty the Penning trap in the actual KATRIN setup. The installed Penning wiper device will be described in section 8.1.

7.3 Extensions to Kassiopeia

The Kassiopeia software package, previously described in section 4.2, was employed in the present work to study the inter-spectrometer trap. Before describing the new simulations of the Penning trap, however, it is helpful to discuss the extensions to Kassiopeia that made these simulations possible.

7.3.1 Particle Identification

In order to generate a particle in Kassiopeia, the particle type must be selected by the user. Previously, the only method to select a particle was by providing a particle identification (PID) number. Kassiopeia uses the Monte Carlo particle numbering scheme developed by the PDG [14]. Each particle and/or state has its own unique PID. Although this numbering scheme is used by Geant4, it does not meet KATRIN's needs since ions and molecules are not encapsulated in the design. This is because the PDG scheme was designed for particle physics applications, and thus the focus is primarily toward high-energy physics rather than

Particle Type	**Composition**	**PID range**
Atoms and homonuclear molecules (99000-99199)	Hydrogen	99000-99029
	Deuterium	99030-99059
	Tritium	99060-99089
	Helium	99090-99109
	Other	99110-99199
Heteronuclear molecules (99200 upwards)	H,D,T	99200-99229
	He-H,D,T	99230-99249
	Other T	99250-99269
	Other	99270 upwards

Table 7.1: Ranges for particle ID numbers based on constituent atoms. A division is made between homonuclear molecules (containing only identical nuclei) and heteronuclear molecules (containing different nuclei) [223].

atomic or molecular physics [222].

Expanded Numbering Scheme

To rectify this shortcoming, a molecular and ion numbering scheme was developed specifically for Kassiopeia. An overview of the numbering scheme can be found in Table 7.1. The scheme was designed to specifically handle the molecules and ions that are important for KATRIN. Thus, there is a focus on hydrogen isotopes as well as other gases present inside the beamline.

The PDG recommends that users with their own particle states begin the PIDs with 99 [72]. This advice was followed, and subsequent divisions of PID ranges were made to sort particles based on type and composition. Ample room was provided to allow for additional molecules and ions to be added in the future. A detailed listing of the PID scheme developed for Kassiopeia is found in Table 7.2 and Table 7.3. Simple particles, such as the electron and proton, retain their PDG numbers.

Composition	**Particle**	**String ID**	**PID**
Simple	Ghost	`"ghost"`	0
	Electron	`"e-"`	11
	Positron	`"e+"`	-11
	Muon	`"mu-"`	13
	Anti-muon	`"mu+"`	-13
	Proton (H^+)	`"p+"`	2212
	Anti-proton	`"p-"`	-2212
	Neutron	`"n"`	2112
Hydrogen	H	`"H"`	99001
	H_2	`"H_2"`	99002
	H^* (Rydberg)	`"H^*"`	99010
	H_2^+	`"H_2^+"`	99012
	H_3^+	`"H_3^+"`	99013
	H^-	`"H^-"`	99021
Deuterium	D	`"D"`	99031
	D_2	`"D_2"`	99032
	D^+	`"D^+"`	99041
	D_2^+	`"D_2^+"`	99042
	D_3^+	`"D_3^+"`	99043
	D^-	`"D^-"`	99051
Tritium	T (triplet state)	`"T"`	99061
	T_2	`"T_2"`	99062
	T^+	`"T^+"`	99071
	T_2^+	`"T_2^+"`	99072
	T_3^+	`"T_3^+"`	99073
	T_4^+	`"T_4^+"`	99074
	T_5^+	`"T_5^+"`	99075
	T^-	`"T^-"`	99081

Table 7.2: Identification scheme for particles in KASSIOPEIA. The particles indicated in grey have not yet been implemented in the code.

Composition	**Particle**	**String ID**	**PID**
Helium	^{3}He	`"^3He"`	99090
	$^{3}He^{+}$	`"^3He^+"`	99091
	$^{3}He^{++}$	`"^3He^{++}"`	99092
	^{4}He	`"^4He"`	99100
	$^{4}He^{+}$	`"^4He^+"`	99101
Other atoms and homonuclear molecules	N_2	`"N_2"`	99110
	N_2^{+}	`"N_2^+"`	99111
	O_2	`"O_2"`	99120
	O_2^{+}	`"O_2^+"`	99121
	Ar	`"Ar"`	99130
	Kr	`"Kr"`	99140
H,D,T molecules	HD	`"HD"`	99200
	HT	`"HT"`	99201
	DT	`"DT"`	99202
	HD^{+}	`"HD^+"`	99210
	HT^{+}	`"HT^+"`	99211
	DT^{+}	`"DT^+"`	99212
	HD^{-}	`"HD^-"`	99220
	HT^{-}	`"HT^-"`	99221
	DT^{-}	`"DT^-"`	99222
He-H,D,T molecules	$^{3}HeH^{+}$	`"^3HeH^+"`	99230
	$^{3}HeD^{+}$	`"^3HeD^+"`	99231
	$^{3}HeT^{+}$	`"^3HeT^+"`	99232
Other T molecules	OT_2	`"OT_2"`	99250
Other heteronuclear molecules	H_2O	`"H_2O"`	99270
	H_2O^{+}	`"H_2O^+"`	99271
	CO	`"CO"`	99280
	CO^{+}	`"CO^+"`	99281
	CO_2	`"CO_2"`	99290
	CO_2^{+}	`"CO_2^+"`	99291

Table 7.3: Identification scheme for particles in Kassiopeia. Only $^{4}He^{+}$ has thus far been implemented in the code.

String ID

In order to generate a specific particle, the unique PID must be found via a look-up table. This situation is not very convenient for KASSIOPEIA users since the PIDs by themselves are quite cryptic. To circumvent the need for a look-up table and enable more intelligible user code, parseable string identifiers were developed for each particle (see Table 7.2 and Table 7.3). The human-readable string corresponds to either the symbolic name (for basic particles) or the chemical formula (for ions and other molecules).

In KASSIOPEIA it is now possible to use the particle string ID to select which particles to generate. Each particle has a primary string identifier; however, alternate string identifiers are also provided for each particle to handle differences in string input. As an example, the primary string identifier for H_3^+ is `"H_3^+"`, but `"H3^+"` and `"H3+"` are also acceptable. This capability is also useful because some particles can be described using different but equally valid names. For instance, the proton can be written as both p^+ and H^+; thus both `"p^+"` and `"H^+"` are valid string inputs when generating a proton.

As an illustration, here are two XML code snippets used to generate a proton via the KASSIOPEIA configuration file. The first uses the PID:

```
<ksgen_generator_composite name="generator_name" pid=2212>
```

The second uses the string identifier:

```
<ksgen_generator_composite name="generator_name" string_id="p+">
```

In conformity with previous iterations of the code, if neither `pid` nor `string_id` is set, KASSIOPEIA will by default make the generated particle an electron. If both `pid` and `string_id` are set, the `pid` value will override the `string_id` value. To avoid confusion on the part of the user, then, only one type of identifier should be set in the configuration file.

7.3.2 Magnetron Terminator

When simulating the motion of charged particles in a Penning trap, one important parameter is the magnetron frequency (see section 7.5.1). This frequency can be determined from the time needed for a particle to complete an entire magnetron period. A terminator that ends a particle track after completing a full magnetron period is, therefore, a useful tool. A "magnetron terminator" was previously developed and used in KASSIOPEIA [80]. This terminator kept track of the azimuthal angle traversed by the particle, and terminated the track after an integer number of magnetron periods were completed. However, during later upgrades to the KASSIOPEIA framework, the magnetron terminator was not retained due to disuse.

In the context of the present thesis, the magnetron terminator code was reintroduced into the KASSIOPEIA software. A new method of terminating the particle was adopted: instead of selecting an integer number of magnetron periods, the user selects an angle $\phi_{\max}$. If the particle transits an azimuthal angle greater than $\phi_{\max}$, the particle will be terminated. By default, $\phi_{\max} = 360°$ (one full magnetron period). This modification allows the user to only simulate a portion of the magnetron period of a particle (which may be necessary due to limited computational resources) and then extrapolate the result to determine the magnetron frequency. Here is an example implementation of the magnetron terminator with $\phi_{\max} = 20°$:

```
<ksterm_magnetron name="term_magnetron" max_phi="20"/>
```

7.4 Ion Scattering

The framework for electron scattering with residual gas is already included in KASSIOPEIA. Scatterings on hydrogen, tritium, and argon are available in the code [174]. However, in order to study the background generated from the Penning trap, it was necessary to extend the interaction framework in order to include the scattering of ions on residual gas.

7.4.1 Interaction Probability

A detailed description of the implementation of scattering interactions in KASSIOPEIA is given in [174]. The probability for a particle with velocity v to scatter in a time duration Δt is

$$P(\Delta t) = 1 - \exp\left(-\frac{v\Delta t}{\lambda}\right), \tag{7.1}$$

where λ is the mean free path. λ can be written in terms of the number density n of the target gas and the cross section σ for the interaction:

$$\lambda = \frac{1}{n\sigma}. \tag{7.2}$$

For a particular Kassiopeia simulation, the number density is determined from input values (pressure and temperature, or density) set in the configuration XML file. The cross section is calculated using hard-coded formulas that depend on the properties of the incident particle (i.e., isotope and energy) and the composition of the target gas. Details of the implementation of the cross sections for ion scattering are discussed in the following sections.

For a simulation step of duration Δt_{step}, there is a probability $0 < P(\Delta t_{\text{step}}) < 1$ for scattering to occur. To stochastically determine if scattering will occur during a particular simulation step, one randomly selects a probability P_{rand} between 0 and 1. If $P_{\text{rand}} \leq P(\Delta t_{\text{step}})$, then a scattering interaction takes place; if $P_{\text{rand}} > P(\Delta t_{\text{step}})$, then a scattering interaction does not take place.

Using the definition (which is derived from rewriting Equation 7.1)

$$\Delta t_{\text{rand}} = -\ln(1 - P_{\text{rand}}) \cdot \frac{\lambda}{v}, \tag{7.3}$$

the condition for scattering can be equivalently stated in the following way. If $\Delta t_{\text{rand}} \leq \Delta t_{\text{step}}$, scattering occurs, while no scattering occurs if $\Delta t_{\text{rand}} > \Delta t_{\text{step}}$. This is the method used in Kassiopeia for determining whether an interaction occurs. The kinematic properties of the incident particle are then adjusted to account for the interaction event, and any secondary particles are likewise created.

The ionization process is a three-body interaction, consisting of the projectile ion, the recoil ion (the ionized target atom), and the ionization electron [224]. To simulate the interaction, it is necessary to know the energy and momentum of the final state of each particle. The following prescriptions are enacted in the code.

Projectile ion: The energy of the outgoing projectile ion E_{out} is calculated assuming energy conservation:

$$E_{\text{out}} = E_{\text{in}} - E_{\text{e}} - B, \tag{7.4}$$

where E_{in} is the energy of the incoming projectile, E_{e} is the electron energy, and B is the binding energy of the target gas. No angular deflection is applied to the outgoing projectile ion.

Recoil ion: The ionized residual gas particle is ignored in the simulation, due to a lack of available data on its final-state properties. This approach is justified since there is evidence in the literature that the vast majority of recoil ions have a much lower energy than the projectile ion [225, 226]. As will be shown in the following sections, the ionization cross section increases with the ion energy, at least for the energy range of interest for KATRIN.

Ionization electron: The energy and emission angle of the electrons are sampled from distributions obtained from fits to cross-section data. These distributions are described in the following sections.

7.4.2 Ionization of H_2 by H^+, H_2^+, and H_3^+

For a baked spectrometer, hydrogen is the largest component of the residual gas [117]. In this case, hydrogen ions are likely to be formed by electron scattering in the inter-spectrometer Penning trap. When accelerated inside the MS, a fraction of these ions will scatter on hydrogen gas. Thus, the most important scattering processes to include in KASSIOPEIA (in the context of the present thesis) are hydrogen ions scattering on neutral hydrogen molecules. Because the creation of detectable background is of primary interest, only ionization cross sections have so far been implemented in the code. However, elastic and excitation interactions are non-negligible at the ion energies of interest and so likely also play an important role [227]; future effort should be made to include the cross sections for these processes as

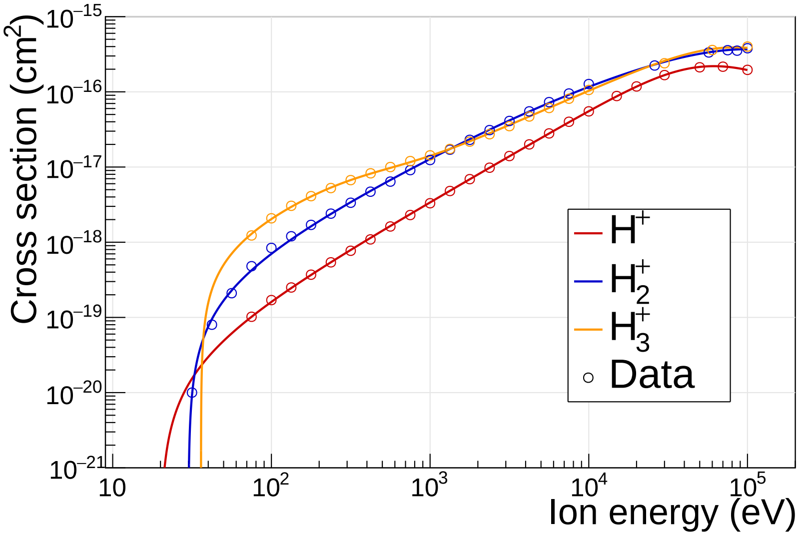

Figure 7.5: Cross sections for ionization of H_2 by different ion species. The solid lines indicate the cross sections implemented in KASSIOPEIA, which follow analytic forms taken from [228]. The markers are measured values from [227, 229].

well [228][1].

A new interaction calculator (KSIntCalculatorIon) was created to handle ion scattering. An example usage of this calculator for the case of scattering on H_2 is

```
<ksint_scattering name="scattering_name">
        <calculator_ion gas="H_2"/>
        <density_constant temperature="300." pressure_mbar="1.e-7"/>
</ksint_scattering>
```

The details of the implementation of this calculator are described below.

Total Ionization Cross Section

The total ionization cross section determines the probability for an ionization interaction to take place. Analytic forms for the total ionization cross section as a function of ion energy for H^+, H_2^+, and H_3^+ on H_2 [228] were incorporated into the code. These are plotted in Figure 7.5

---

[1] Some model for the energy and momentum distributions of the interaction products would also be needed.

	Implemented		Measured		
Reaction	E_{min}	E_{max}	E_{min}	E_{max}	Reference
$H^+ + H_2 \rightarrow e^-$	20	10^5	75	10^5	[228]
$H_2^+ + H_2 \rightarrow e^-$	30	10^5	31.6	10^5	[228]
$H_3^+ + H_2 \rightarrow e^-$	36	10^5	75	10^5	[228]
$H^+ + H_2O \rightarrow e^-$	100	5×10^6	7×10^3	4×10^6	[230]

Table 7.4: Energy ranges (in units of eV) for ionization cross sections. The implemented ranges are used by KASSIOPEIA, while the measured ranges are those for which experimental values are available.

in addition to the experimental data [227] on which the functions are based. It can be observed that the cross sections generally increase for larger ion energies. The implemented energy ranges for the ionization reactions are given in Table 7.4. The lower bound for the energy range is derived from the analytic function, while the upper bound is determined by the availability of experimental data [228]. For scattering on H_2, the experimental data only exist up to ion energies of 10^5 eV, but this is adequate for KATRIN since the maximum energy of positive ions in the experiment is roughly 18.6 keV. Therefore, the implemented cross sections on H_2 should be valid for all expected energies of hydrogen ions in KATRIN.

During neutrino-mass operation, deuterium and tritium ions will also be generated in the beamline. However, cross sections for these ions are not readily available in the literature. To account for interactions of deuterium and tritium ions on H_2, identical cross sections were implemented as for protium scattering. Experimental evidence indicates that ionizations of helium by H^+ and D^+ are not markedly different [231]; thus, the use of identical ionization cross sections should be a reasonable approximation.

Electron Energy Distribution

The energy of the ionization electron resulting from the scattering interaction is sampled from an energy distribution. This distribution is simply the differential cross section for the ionization of H_2 by H^+, which is taken from the literature [232, 233]. Identical formulae for

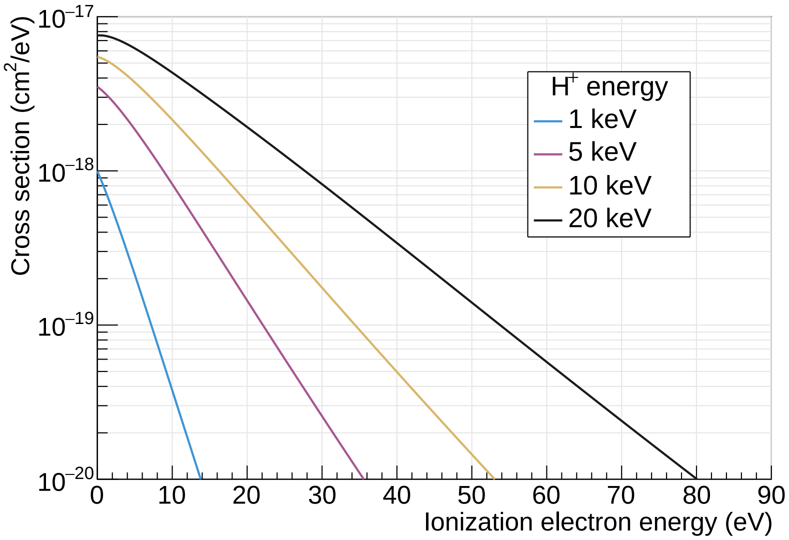

Figure 7.6: Electron energy distributions (differential cross sections) for ionization of H_2 by H^+. Each line indicates a different initial energy for the H^+ ion. The values are calculated using Equation 41 from [233].

the energy distribution were applied to the ionization of H_2 by H_2^+ and H_3^+; different electron energy distributions are obtained for each ion species since the analytic formula depends on the mass of the projectile ion.

The electron energy distributions for several projectile energies are shown in Figure 7.6 for the case of H^+ scattering on H_2. As expected, higher SE energies are possible for higher projectile energies. However, electron energies on the order of a few eV are favored no matter the projectile energy.

Electron Angular Distribution

Measured datasets for the angular distribution of ionization electrons exist in the literature [234]. However, no parameterization of the distribution is provided. A functional form using datasets from an older experimental apparatus is provided in [235], but this formula does not provide a good fit to the newer and more reliable data in [234]. Therefore, an analytic expression was obtained by fitting the lowest-energy (20-keV) projectile ion dataset

Parameter	Fit value	
	H_2	H_2O
p_0	$(1.64 \pm 0.13) \times 10^{-18}\,\mathrm{cm^2/sr}$	$(8.0 \pm 0.4) \times 10^{-19}\,\mathrm{cm^2/(eV \cdot sr)}$
p_1	$(2.93 \pm 0.06) \times 10^{-16}\,\mathrm{cm^2/sr}$	$(5.8 \pm 0.9) \times 10^{-18}\,\mathrm{cm^2/(eV \cdot sr)}$
p_2	$(3.88 \pm 0.06) \times 10^{9}$ degrees	$(1.5 \pm 7.4) \times 10^{2}$ degrees
p_3	0.747 ± 0.001	2.17 ± 0.98
p_4	$(2.81 \pm 0.03) \times 10^{6}$	$(3 \pm 25) \times 10^{1}$

Table 7.5: Fit parameters for the electron angular distribution (Equation 7.5) for the ionization of H_2 and H_2O by H^+.

from [234]. The data were fit [135, 236] using the functional form:

$$\sigma(\theta) = p_0 + \frac{p_1 - p_0}{\left[1 + \left(\frac{\theta}{p_2}\right)^{p_3}\right]^{p_4}}, \tag{7.5}$$

where σ is the differential cross section (with units of $\mathrm{cm^2/sr}$) and θ is the outgoing electron polar angle in degrees. The values of p_i are given in Table 7.5. The angular distribution data and fit are shown in Figure 7.7.

Equation 7.5 was applied in the code for all ion energies. The rationale for this prescription is the following. In KATRIN, positive ions have a maximum energy of 18.6 keV, and the probability to ionize residual gas increases exponentially at higher energies; therefore, the application of the 20-keV data to all ion energies is a reasonable approach. Nevertheless, angular distributions for lower ion energies (down to 5 keV; see [237]) share the same characteristic as the 20-keV measurement: a significant preference for smaller angles.

The outgoing angle of the electron is written in terms of spherical coordinates, with the z-axis defined by the momentum vector of the projectile ion. The polar angle is sampled from Equation 7.5, while the azimuthal angle is randomly sampled from a uniform distribution between 0° and 360°.

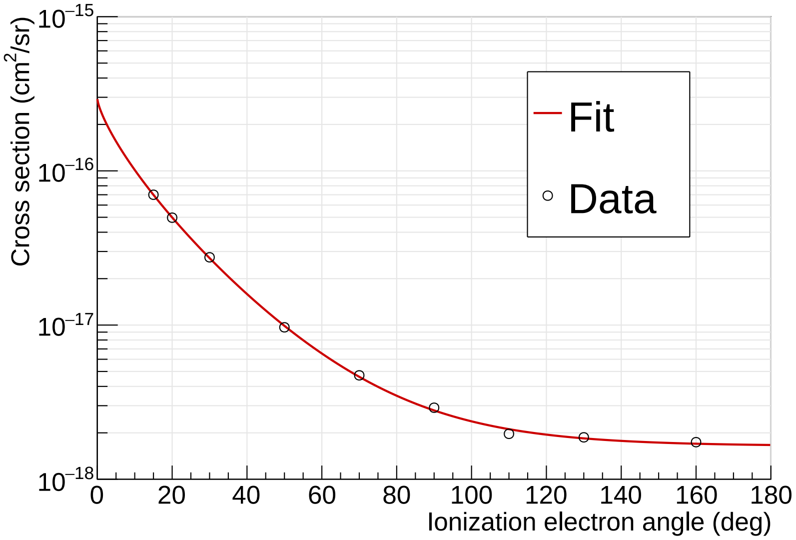

Figure 7.7: Electron angular distribution (differential cross section) for ionization of H_2 by 20-keV H^+ ions. The angle is relative to the momentum of the projectile ion. The data points (taken from [234]) were fit using Equation 7.5.

7.4.3 Ionization of H_2O by H^+

With an unbaked spectrometer (such as was present during SDS-IIIa), water vapor is the dominant residual gas species [117] . To simulate ionization under this condition, scattering on H_2O was added to the code to understand the ion-blocking efficiency of the PS; this work was initially performed in the context of the master thesis of W.-J. Baek [172]. Therefore, only a brief overview of the implementation is described here.

Total Ionization Cross Section

The total cross section for the ionization of H_2O by H^+ was implemented using an analytic expression from the literature [230]. This cross section is shown in Figure 7.8a. A subset of the data used to determine the analytic expression is also displayed for comparison.

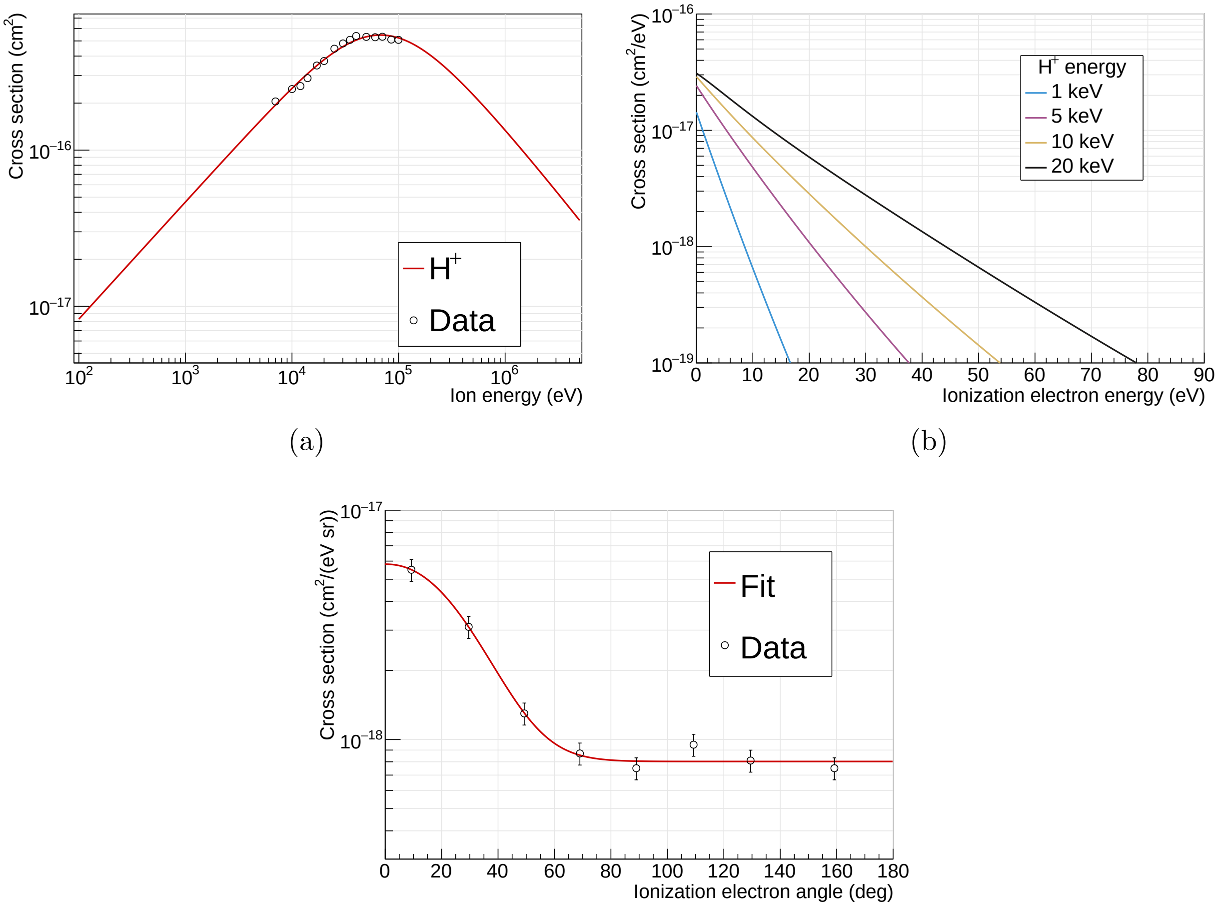

(a) (b) (c)

Figure 7.8: Cross sections for ionization of H_2O by H^+. (a) Total ionization cross section; generated from Equation 1 from [230]. Measured data points were manually extracted from a plot in [230]. (b) Electron energy distributions (differential cross sections). Each line indicates a different initial energy for the H^+ ion. The values are calculated using Equation 41 from [233]. (c) Electron angle distribution (doubly differential cross section) for 15-keV H^+ ions producing 10-eV electrons. The angle is relative to the momentum of the projectile ion. The data points (manually extracted from a plot in [238]) were fit using Equation 7.5.

Electron Energy Distribution

The electron energy distribution is determined using an analytic expression for the differential cross section found in the literature [233]. Compared with the implementation described in [172], further corrections to the code were made to account for the ionization of electrons in all orbitals of H_2O [233]. The electron energy distribution for several ion energies is shown in Figure 7.8b.

Electron Angular Distribution

Isotropic emission of electrons was assumed in [172]; however, the implementation of an analytic form for the angular distribution was enacted in the context of the present thesis. This functional form was determined by fitting the doubly differential cross section for 15-keV H^+ ions producing 10-eV electrons [238]. The data were fit [135, 236] using Equation 7.5, where σ has units of $\mathrm{cm}^2/(\mathrm{eV} \cdot \mathrm{sr})$. The data and fit are displayed in Figure 7.8c, and the fit parameters are given in Table 7.5. The functional form was applied in the code for all ion and SE energies.

7.5 Electron Motion in the Penning Trap

In this section, the motion of electrons in the inter-spectrometer Penning trap is simulated using Kassiopeia. Studies of electron motion in the Penning trap formed by the PS test setup [219] were performed by J. Behrens [220]. The present work is a replication and extension of the previous results using the current beamline geometry as well as the nominal electric potential and magnetic field settings. A visualization of the motion of an electron in the inter-spectrometer Penning trap is shown in Figure 7.9.

7.5.1 Types of Motion

The motion of a trapped particle in a Penning trap can be broken down into three components, each with its own characteristic frequency [218, 220]. These are the cyclotron, axial,

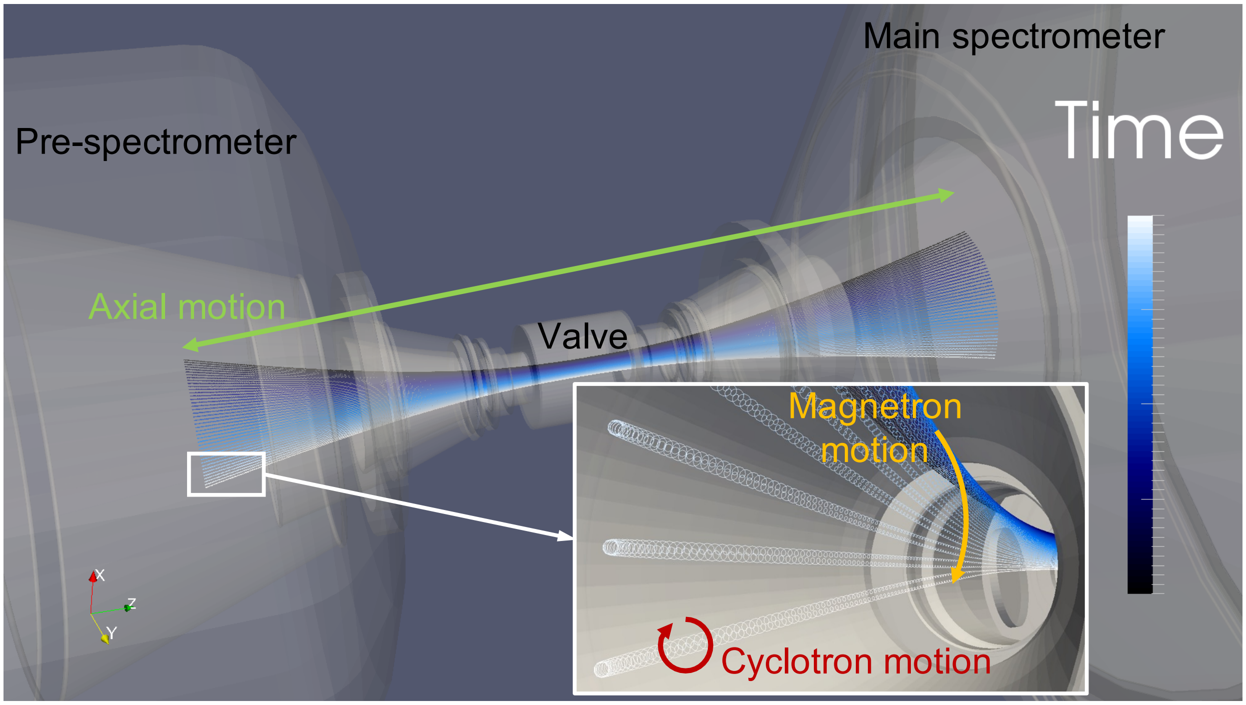

Figure 7.9: A view of electron motion in the inter-spectrometer Penning trap. The track coloring indicates the time since the start of the simulation. The axial, magnetron, and cyclotron motions are visible and labelled. The figure was generated with ParaView [239].

and magnetron motions, which are briefly described below.

Cyclotron Motion

A particle with charge q and mass m traveling with a velocity $\mathbf{v}$ in a magnetic field $\mathbf{B}$ will experience a Lorentz force:

$$\mathbf{F} = q\mathbf{v} \times \mathbf{B} \tag{7.6}$$

If the magnetic field is uniform, the effect of this force is a circular, or cyclotron, motion in the azimuthal direction (where the axial direction is defined by the magnetic field). The frequency of this motion, called the cyclotron frequency, can be written as

$$f_{\text{cyclotron}} = \frac{qB\sin\theta}{2\pi m\gamma}, \tag{7.7}$$

where θ is the angle between the velocity of the particle and the magnetic field, and γ is the relativistic Lorentz factor. For an electron in the 3.2-T magnetic field between the spectrometers, the maximum cyclotron frequency is about 9×10^{10} Hz. The cyclotron motion is the fastest of all movements within the Penning trap.

Axial Motion

The electrostatic trap is responsible for the second type of motion, called the axial motion. Electrons will oscillate in the potential well formed by the two cathodes of the Penning trap. The oscillation frequency is termed the axial frequency, since the motion is along the axial direction. The geometry of the trap and the energy of the electron dictate the value of the axial frequency. For the inter-spectrometer trap, one can estimate the axial frequency by assuming an electron in a square well:

$$f_{\text{axial}} = \frac{v_{\|}}{2\Delta z} = \frac{c}{\Delta z}\sqrt{\frac{E_{\|}}{2m}}, \tag{7.8}$$

where c is the speed of light, Δz is the axial trap length, and $v_{\|}$ and $E_{\|}$ are the momentum and energy, respectively, parallel to the axial magnetic field. For an electron with $E_{\|} = 1\,\text{keV}$

and $\Delta z = 1\,\mathrm{m}$, the axial frequency is $\sim 9 \times 10^6\,\mathrm{Hz}$. This result is an upper limit, since in reality the trapped electron will slow down near the trap edges.

Magnetron Motion

The slowest type of motion in a Penning trap is the magnetron motion. The cause of this motion is twofold:

1. The misalignment between the electric and magnetic fields, resulting in an $\mathbf{E} \times \mathbf{B}$ drift.
2. The curvature of the magnetic field, resulting in a ∇B drift [71, 218].

The magnetron velocity can be written as the sum of these two components [218, 220]:

$$\mathbf{v}_{\text{magnetron}} = \mathbf{v}_{\mathbf{E}\times\mathbf{B}} + \mathbf{v}_{\nabla B} = \left[\frac{\mathbf{E}\times\mathbf{B}}{B^2}\right] + \left[\frac{m_e}{eB^3}(v_\parallel + \frac{1}{2}v_\perp)\cdot\mathbf{B}\times\nabla B\right], \tag{7.9}$$

where $v_\parallel$ ($v_\perp$) is the particle velocity parallel (perpendicular) to the magnetic field, and relativistic effects have been ignored. Due to the large electric fields in the region of the Penning trap, the $\mathbf{E} \times \mathbf{B}$ drift is the dominant contributor [220].

The magnetron motion is directed in the azimuthal direction, like the cyclotron motion, but the motion of the former occurs at a much lower frequency. A rough calculation indicates $\mathcal{O}(f_{\text{magnetron}}) = 10^4\,\mathrm{Hz}$ [219, 220].

Therefore, one finds that the frequencies of motion in a Penning trap are organized in the following manner:

$$f_{\text{magnetron}} < f_{\text{axial}} < f_{\text{cyclotron}}. \tag{7.10}$$

In Figure 7.10, the total combined effect of the aforementioned motions in a Penning trap is displayed.

7.5.2 Simulation Results

Cyclotron Frequency

The cyclotron frequency for an electron in the Penning trap is shown in Figure 7.11. This frequency is automatically calculated in Kassiopeia for each step in the simulation. As

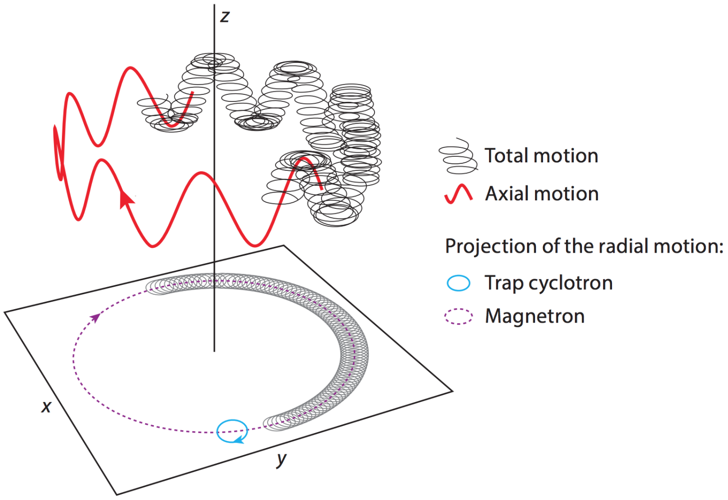

Figure 7.10: Total motion of a charged particle in a Penning trap, consisting of a slow azimuthal motion (magnetron motion), a faster axial motion, and a very fast azimuthal motion (cyclotron motion). Figure taken from [240], with small modifications. Republished with permission of Annual Reviews, Inc.; permission conveyed through Copyright Clearance Center, Inc.

expected, this frequency is proportional to the magnetic field strength (see Figure 7.2).

Axial Frequency and Trap Length

The axial frequency of an electron in the Penning trap, as a function of energy, is shown in Figure 7.12a. The axial frequency is calculated from the simulation output using the following formula:

$$f_{\text{axial}} = \frac{1}{2 \cdot |t(z_{\text{max}}) - t(z_{\text{min}})|}, \tag{7.11}$$

where $t(z_{\text{max}})$ is the time when the electron reaches the maximum z-position and $t(z_{\text{min}})$ is the time when the electron reaches the minimum z-position.

For low energies, the frequency increases as the kinetic energy of the electron increases. This makes sense if one considers the motion of an electron in a flat potential well of fixed width. Increasing the electron energy will result in the electron having a smaller period of motion. At high energies, however, the axial frequency decreases with the initial kinetic

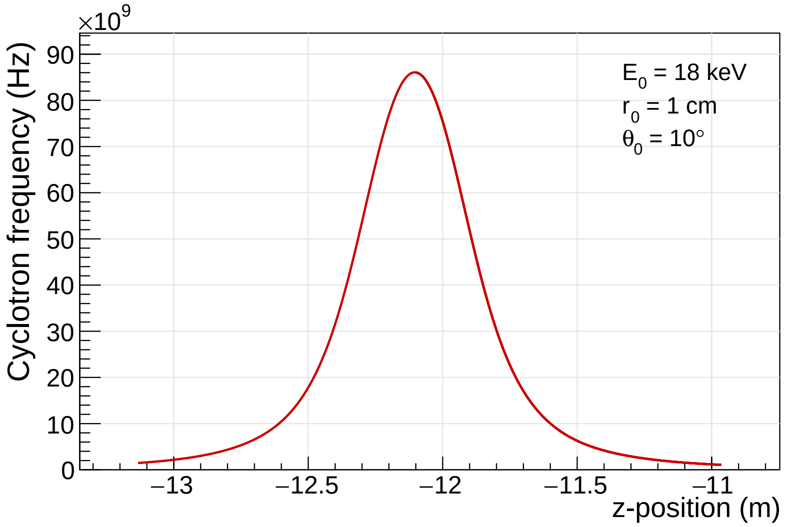

Figure 7.11: Cyclotron frequency of an electron in the Penning trap, as a function of axial position. The initial conditions for the electron are listed in the figures, where E_0 is the initial energy, r_0 is the initial radius, and θ_0 is the initial polar angle to $\mathbf{z}$.

energy of the electron. In reality, the Penning trap is not a flat well; at high energies, the electrons explore the edges of the trap and travel significantly into the PS and MS. This can be seen in the size of the axial trap length ($\Delta z = z_{\mathrm{max}} - z_{\mathrm{min}}$), which is shown in Figure 7.12b. A larger trap length implies a longer travel time for a single period and thus a reduction in the axial frequency.

The axial frequency as a function of polar angle is shown in Figure 7.13a, for an electron with an initial position on the trap edge. At small angles, the frequency decreases as the polar angle increases since there is less momentum in the direction parallel to the trap axis; the electron thus travels more slowly in the axial direction. Between 20° and 30°, there is a kink in the distribution and the axial frequency begins to increase for larger polar angles. This change is caused by the magnetic mirror effect. For large initial pitch angles, the electron is reflected by the strong magnetic field in the center of the Penning trap. The electron is trapped by the magnetic field of the PS2 and the electric field of the MS, which is a smaller confining region (Figure 7.13b). Therefore, the electron will have a larger axial frequency.

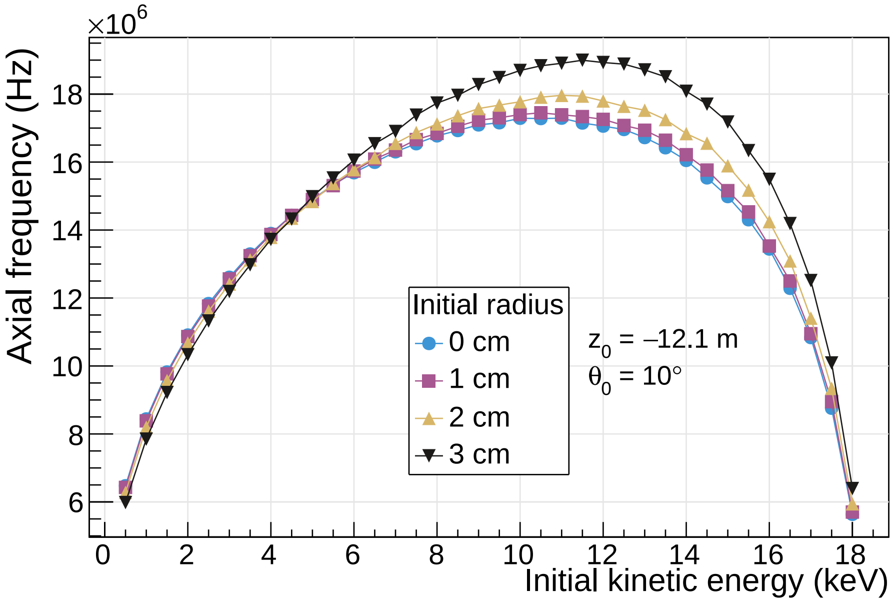

(a)

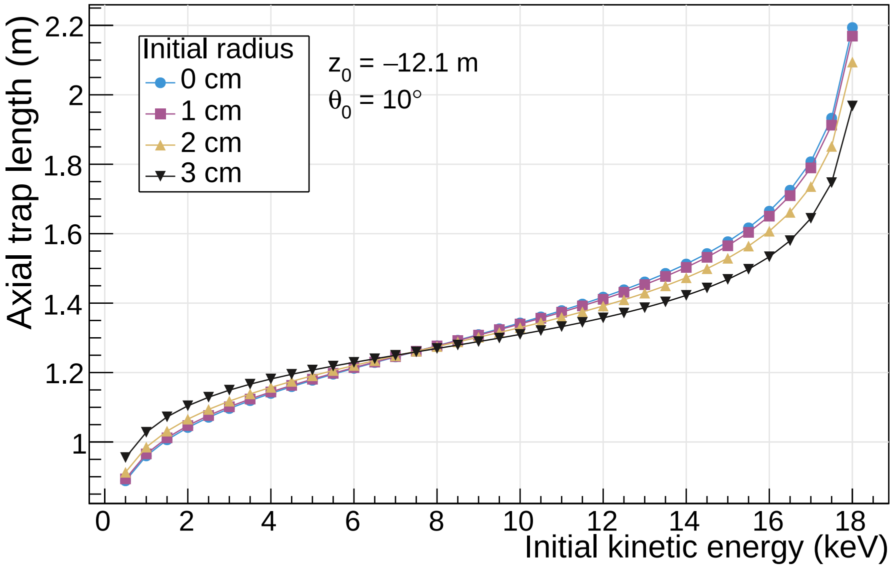

(b)

Figure 7.12: (a) Axial frequency of electrons in the Penning trap and (b) the axial trap length as a function of the initial kinetic energy. Initial conditions for the electrons are listed in the figures, where z_0 is the initial z-position and θ_0 is the initial polar angle to $\mathbf{z}$.

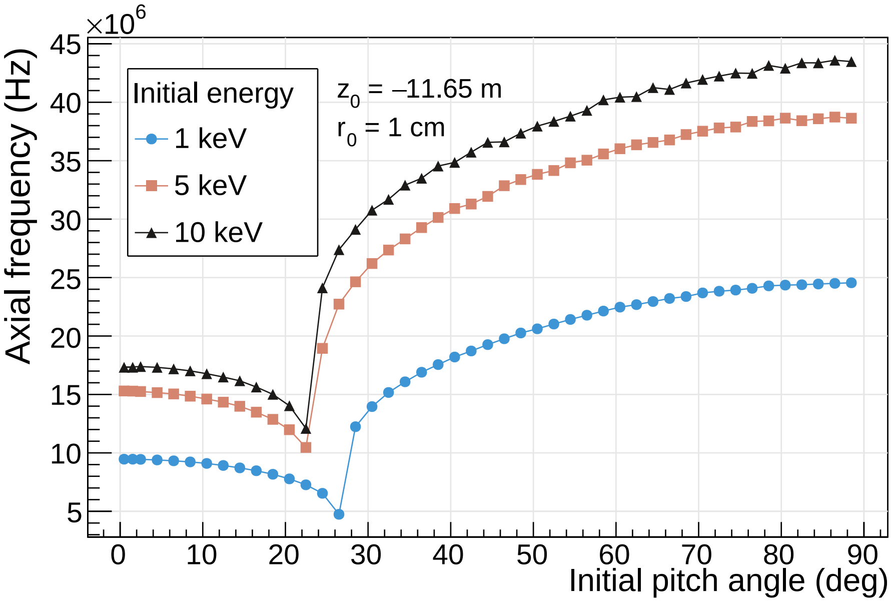

(a)

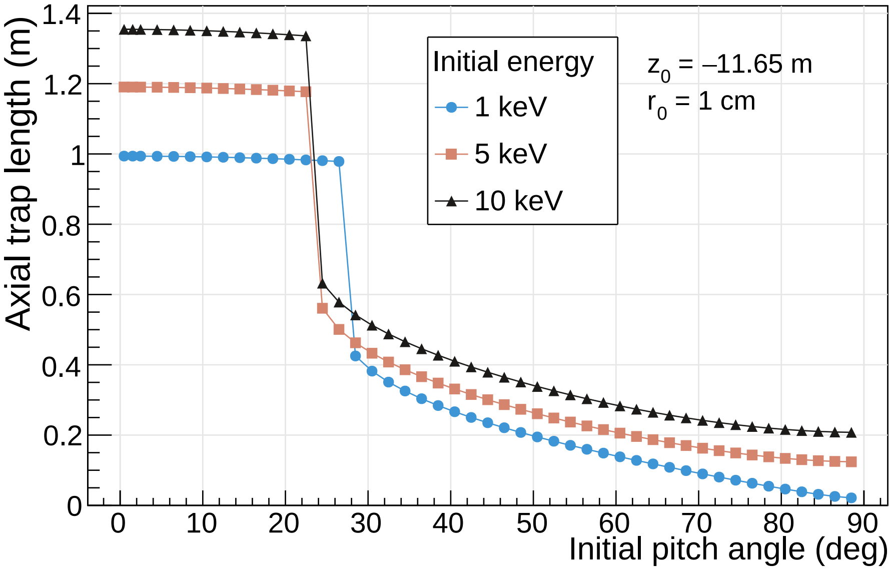

(b)

Figure 7.13: (a) Axial frequency of electrons in the Penning trap and (b) the axial trap length as a function of the initial pitch angle. Initial conditions for the electrons are listed in the figures, where z_0 is the initial z-position and r_0 is the initial radius.

Magnetron Frequency

The magnetron frequency of an electron in the Penning trap is an important parameter for understanding the effectiveness of removing stored electrons via mechanical means. The Penning wiper relies on the magnetron drift of stored particles to ensure that all electrons are emptied from the trap. If the magnetron frequency is very low, the wiper may not be in the flux tube long enough to empty all trapped electrons.

The magnetron terminator (see section 7.3.2) is employed in the calculation of the magnetron frequency. Using $\phi_{\max} = 20°$, the duration Δt of the simulation was recorded, which allows one to calculate the magnetron frequency:

$$f_{\text{magnetron}} = \frac{360°}{\phi_{\max}} \frac{1}{\Delta t}. \tag{7.12}$$

The magnetron frequency is plotted as a function of the electron's initial kinetic energy in Figure 7.14a. The frequency increases up to about 6 keV before decreasing and reaching a minimum close to 13 keV, after which point the frequency increases again. This behavior can be understood by looking at the azimuthal $\mathbf{E} \times \mathbf{B}$ drift velocity of a trapped electron in different regions of the trap (Figure 7.15a). Most of the $\mathbf{E} \times \mathbf{B}$ drift occurs at the edges of the trap, where the electric fields are highest. It can be seen that the value of the $\mathbf{E} \times \mathbf{B}$ drift changes sign at a specific axial positions. Depending on its initial energy, the electron will spend more or less time in different regions of the trap and will thus experience either a net positive or net negative $\mathbf{E} \times \mathbf{B}$ drift. For a specific energy (∼13 keV), the total $\mathbf{E} \times \mathbf{B}$ sums to zero.

The magnetron frequency increases for larger radii in the trap (see Figure 7.14a). This is due to the higher electric fields close to the electrodes, which results in a larger $\mathbf{E} \times \mathbf{B}$ drift in the azimuthal direction (Figure 7.15b) [220]. Figure 7.14b displays the magnetron frequency as a function of the electron's initial pitch angle. As was the case for the axial frequency (see Figure 7.13a), there is a kink in the distribution between 20° and 30°, above which the magnetron frequency begins to increase. Electrons with large polar angles are reflected by the strong magnetic field at the trap center; therefore, these electrons are trapped in a

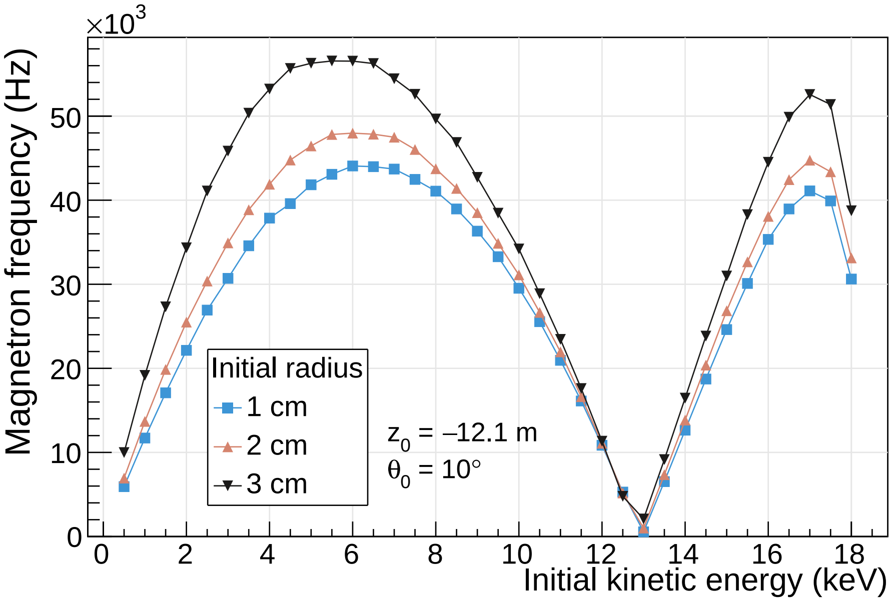

(a)

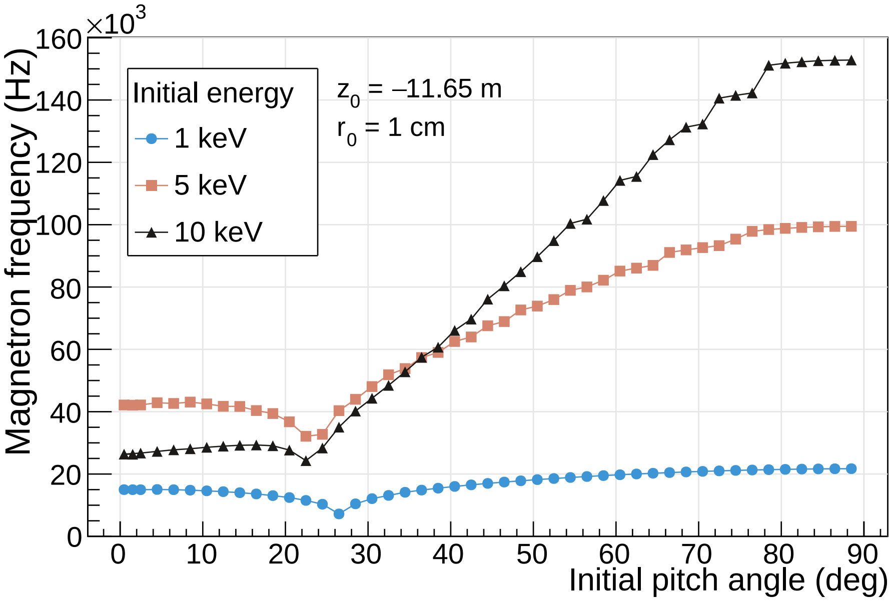

(b)

Figure 7.14: Magnetron frequency of electrons in the Penning trap as a function of (a) the initial kinetic energy and (b) the initial pitch angle. Initial conditions for the electrons are listed in the figures, where z_0 is the initial z-position, θ_0 is the initial polar angle to $\mathbf{z}$, and r_0 is the initial radius.

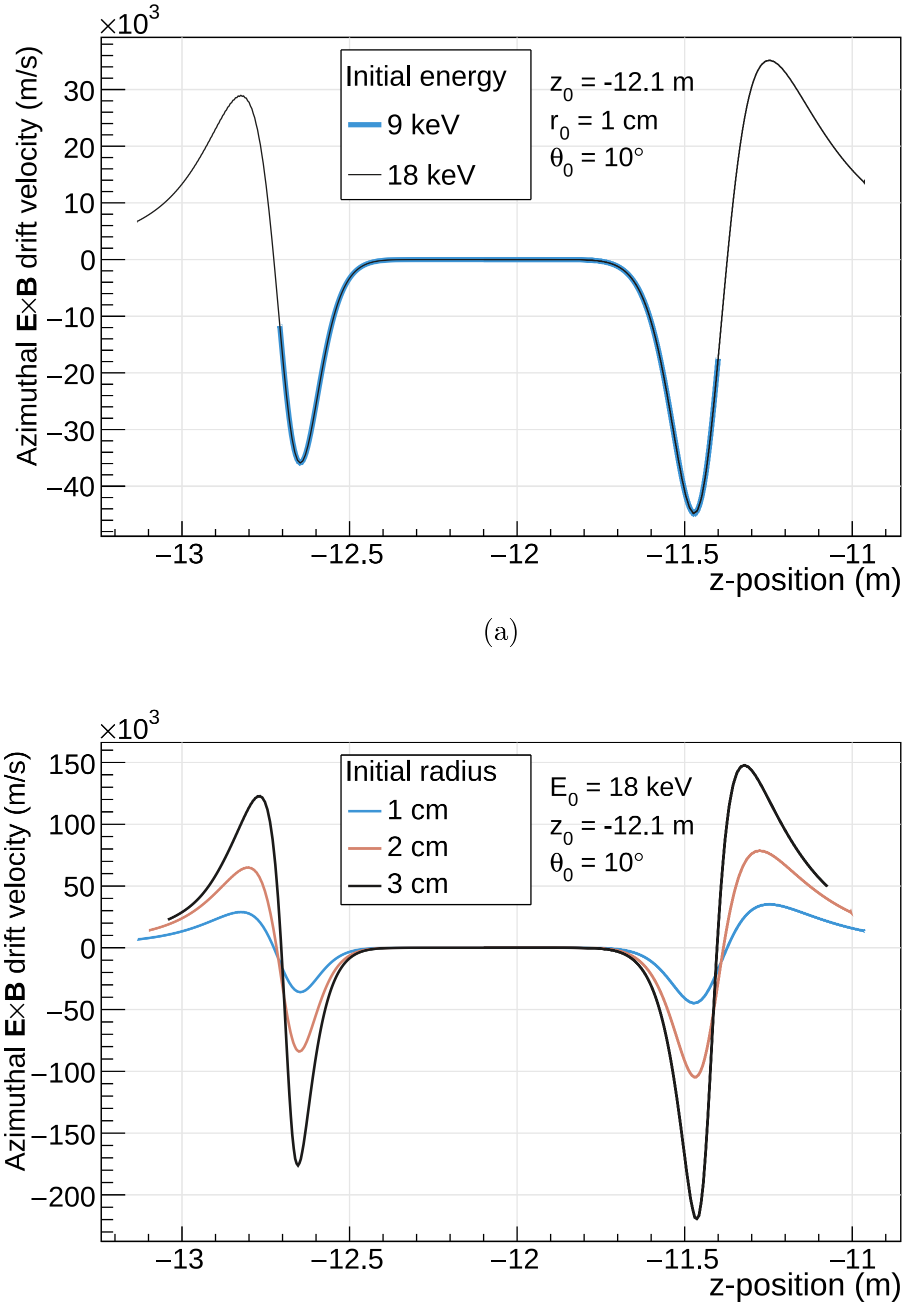

(a)

(b)

Figure 7.15: Azimuthal $\mathbf{E} \times \mathbf{B}$ drift velocity as a function of position for electrons in the Penning trap. (a) Effect of initial energy. (b) Effect of initial radius. Initial conditions for the electrons are listed in the figures, where E_0 is the initial energy, z_0 is the initial z-position, θ_0 is the initial polar angle to $\mathbf{z}$, and r_0 is the initial radius.

smaller region, closer to one of the spectrometers. Because this region is where the $\mathbf{E} \times \mathbf{B}$ drift velocity is large, these electrons will have a higher magnetron frequency.

From Figure 7.14a, it can be seen that the magnetron frequency is greater than 1 kHz for all electron energies, except near 0 keV and 13 keV. Due to energy loss processes (i.e., synchrotron emission and scattering [218, 220]), it is not expected that stored electrons will remain at 13 keV for long durations. Thus, a full magnetron period will generally take less than 1 ms. During its operation, the Penning wiper is designed to remain in the flux tube for $\gtrsim 1\,\mathrm{s}$. Essentially all electrons should therefore be removed from the trap when the Penning wiper is activated.

7.6 Ion-Induced Background from the Penning Trap

After upgrading the KASSIOPEIA software to handle ion scattering (see section 7.4), it became possible to simulate the background generated from positive ions produced in the Penning trap. From these simulations, one can analyze the distribution of ionization electrons as well as the effect of ion initial properties.

7.6.1 Simulation Configuration

For the following simulations, an electromagnetic configuration similar to that planned for neutrino mass measurements was desired. Therefore, the simulations replicated the settings used during the long-term SDS-IIIc measurement (which will be discussed in section 8.4). Both spectrometers were placed at their nominal voltages, and a symmetric magnetic field (setting P) was generated with a 6 G field in the analyzing plane.

H_2^+ ions were generated uniformly within a disk in the xy-plane, in the axial center of the PS2 magnet. This is shown in Figure 7.16. The initial angles of the ions were sampled from an isotropic distribution, but only in the $+z$ direction. All initial parameters for the simulation are listed in Table 7.6. A pressure of 10^{-4} mbar for H_2 was implemented in the interaction calculator, in order to generate a large number of ionization events with limited computational expense. In order to speed up the simulations, ions and ionization electrons

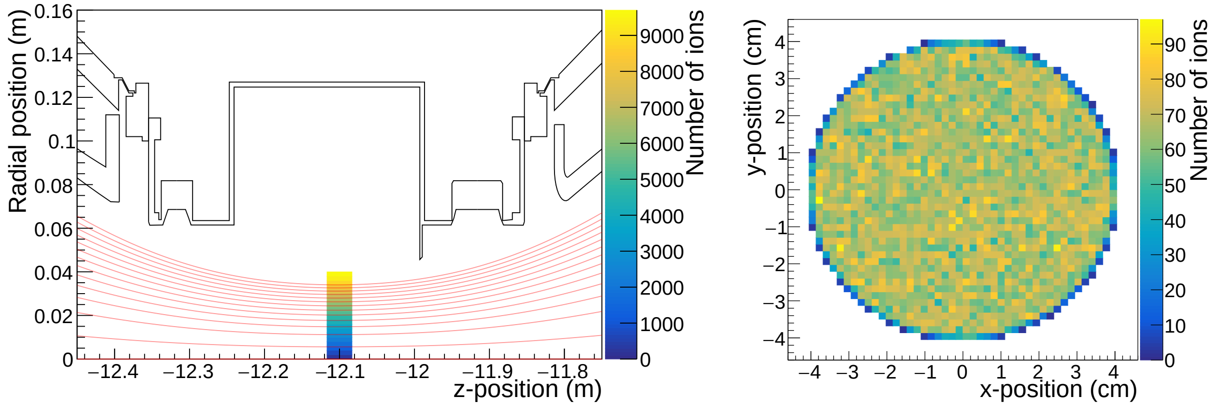

(a) (b)

Figure 7.16: Distribution of simulated ions within the region of the Penning trap. (a) Axial and radial distribution of ions. All ions were generated at $z = -12.10\,\mathrm{m}$ with $r < 4\,\mathrm{cm}$. The red lines are the magnetic field lines that connect to the sensitive area of the FPD. (b) Distribution of ions within the xy-plane.

were terminated if they neared the electrodes of the MS and FPD. Particles that changed direction (i.e., that were magnetically trapped) were also terminated[2].

A non-standard particle trajectory was employed in the simulation of positive ions. The rationale for this is the following. Employing an adiabatic trajectory in KASSIOPEIA is ideal for simulating electrons under standard operating conditions. The adiabatic approximation requires that the electric and magnetic fields do not change significantly within a cyclotron radius [174]:

$$r_{\mathrm{cyclotron}} = \frac{v_{\perp}}{2\pi f_{\mathrm{cyclotron}}} = \frac{m v_{\perp} \gamma}{qB}, \tag{7.13}$$

Due to its large mass, an ion will have a large cyclotron radius compared with that of an electron. Because an ion produced in the Penning trap will experience a large electric field gradient as it travels into the MS [220], the ion will be accelerated by the electric fields and

---

[2] Trapped electrons can eventually reach the detector after scattering or emitting synchrotron radiation [80]. However, such electrons are ignored in the present analysis due to the computational expense required to track them until they reach the detector.

Parameter	Initial value/range
Axial position, z	$-12.10\,\mathrm{m}$
Radial position, r	$0\,\mathrm{cm}$ to $4\,\mathrm{cm}$
Azimuthal position, α	0° to 360°
Polar angle of momentum vector, θ	0° to 90°
Azimuthal angle of momentum vector, ϕ	0° to 360°
Energy, E	$5\,\mathrm{eV}$ to $100\,\mathrm{eV}$

Table 7.6: Generator settings used for positive ion simulations.

will not follow the magnetic field lines. Solely using an adiabatic trajectory, therefore, will not provide accurate tracking for ions [172]. However, only employing a fixed track length is not ideal either, since one must balance simulation accuracy with the computational expense of using smaller step sizes. A dual trajectory scheme was therefore utilized: a fixed-length trajectory (step size of 1 mm), in conjunction with a cyclotron step size ($\Delta t = 0.01/f_{\mathrm{cyclotron}}$). For each step, the smaller of the two step sizes is used.

In total, 10^5 positive ions were simulated, resulting in 5.7×10^4 ionization electrons, although many of these electrons were created outside of the magnetic flux tube (Figure 7.18a). 1.5×10^4 electrons reached the sensitive area of the detector. Conservation of energy for each particle track was checked (see section 4.2.4). The average energy deviation for ion tracks was $2.5 \times 10^{-8}\,\mathrm{eV}$, while for detected electrons (all electrons) the average deviation was $2.0 \times 10^{-9}\,\mathrm{eV}$ ($3.0 \times 10^{-8}\,\mathrm{eV}$). Therefore, the employed trajectory method is sufficiently accurate. An example ion track that produces a detected electron is shown in Figure 7.17.

7.6.2 Ionization Electrons

The distribution of initial positions of ionization electrons that reach detector is shown in Figure 7.18b. A couple of conclusions can be drawn from this figure. First, only electrons produced within the magnetic flux tube will reach the detector. This makes sense because the ionization electrons will adiabatically follow the magnetic field lines, unlike the positive ions. Second, the majority of detected electrons originate from the upstream end of the MS

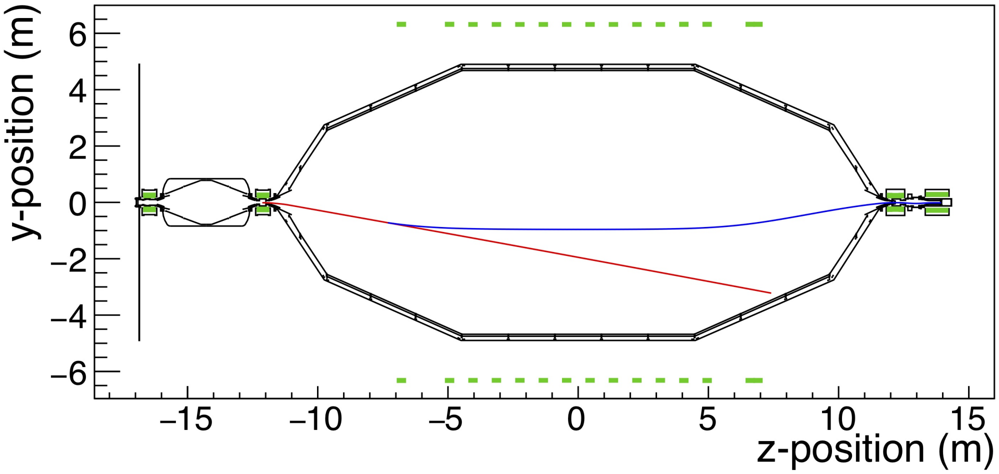

Figure 7.17: Example of a simulated ionization event with KASSIOPEIA. A positive ion (red) produces an ionization electron (blue) which reaches the FPD. The locations of the solenoids and the LFCS are indicated in green.

due to the large number of ion tracks in this region.

The distribution of electron events at the FPD is shown in Figure 7.19. The electron events are uniformly distributed across the wafer. Because the ions were uniformly generated in the Penning trap region, the uniformity observed in Figure 7.19 suggests that the distribution of positive ions in the Penning trap determines the distribution of events at the FPD. This correlation can be observed in Figure 7.20, which shows the distribution of detector events as a function of the ion initial radius in the Penning trap and the electron radius at the detector. As the ion initial radius increases, the minimum detector radius for SEs also increases.

7.6.3 Effect of Initial Conditions

One can look for the effect of particle initial properties (energy, angle, radius) on the detector event distribution and electron arrival probability. Performing this analysis is useful not only for studying the background from positive ions, but also for checking that the simulation re-

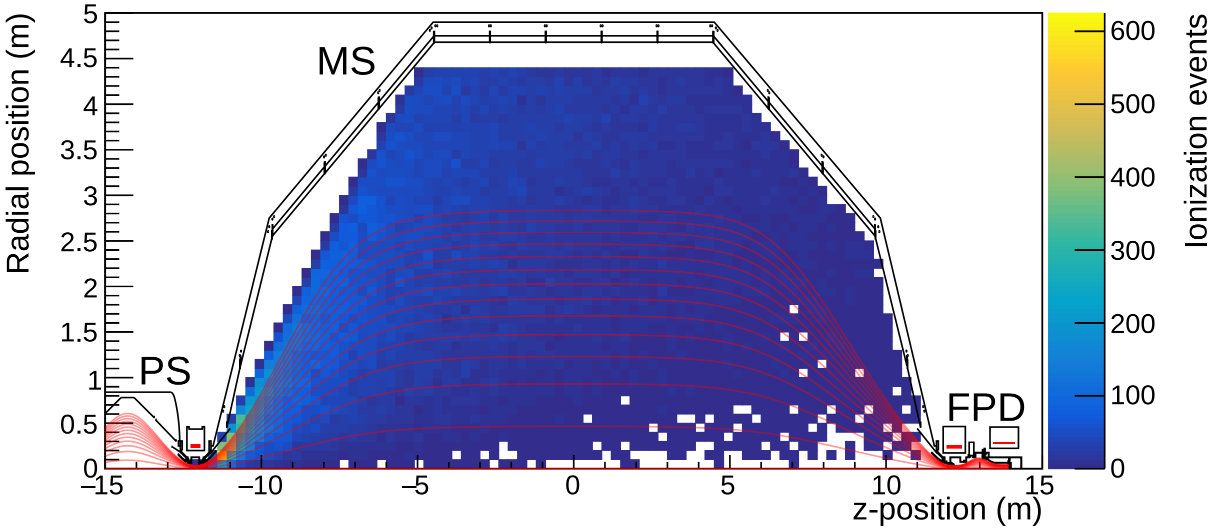

(a) All ionization electrons

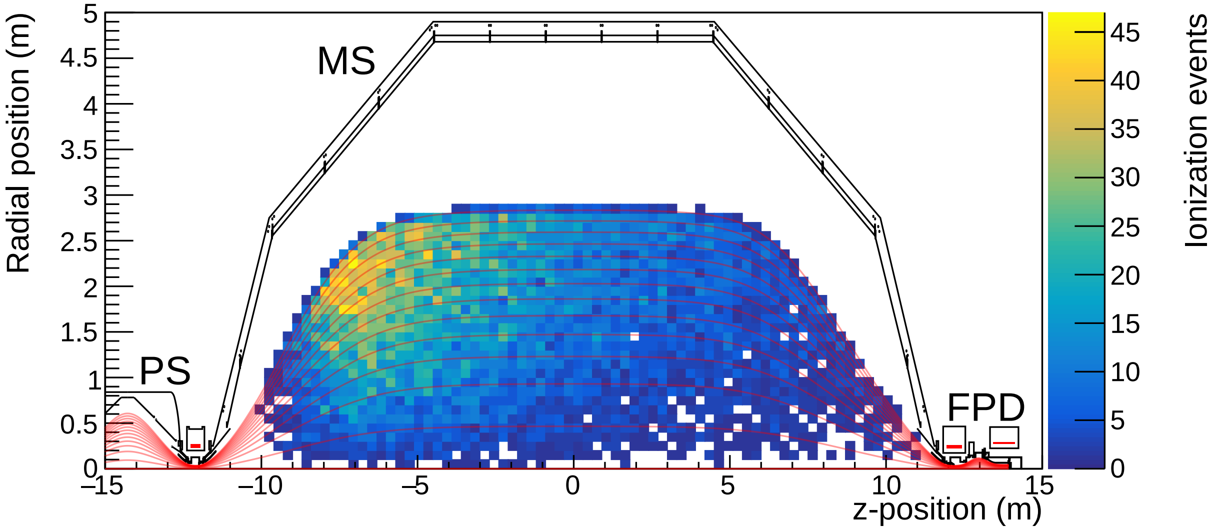

(b) Detected ionization electrons

Figure 7.18: Ionization electrons produced from positive ions from the Penning trap. The red lines are the magnetic field lines that connect to the sensitive area of the FPD.

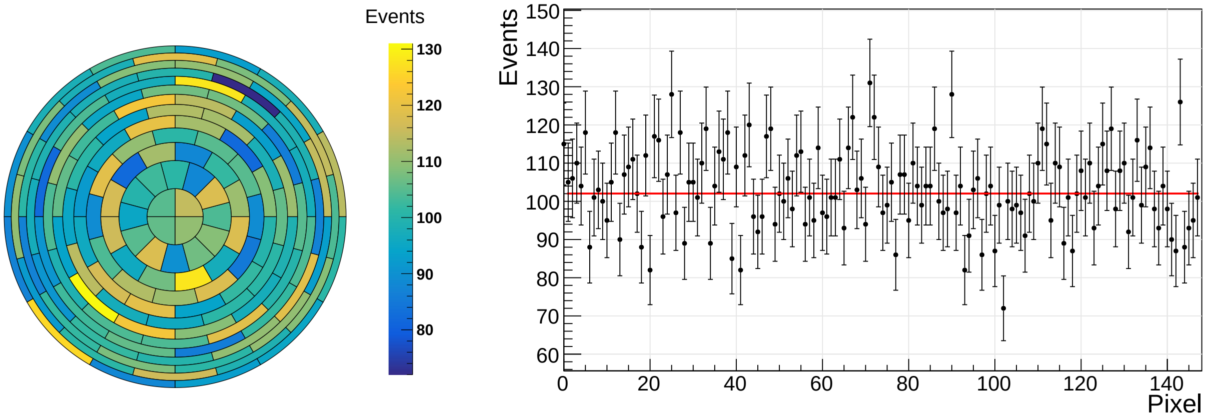

(a) (b)

Figure 7.19: FPD events caused by positive ions from the Penning trap. (a) Pixel distribution of electron events at the detector wafer. (b) Fit of the pixel distribution, with χ^2/ndf = 161.3/147.

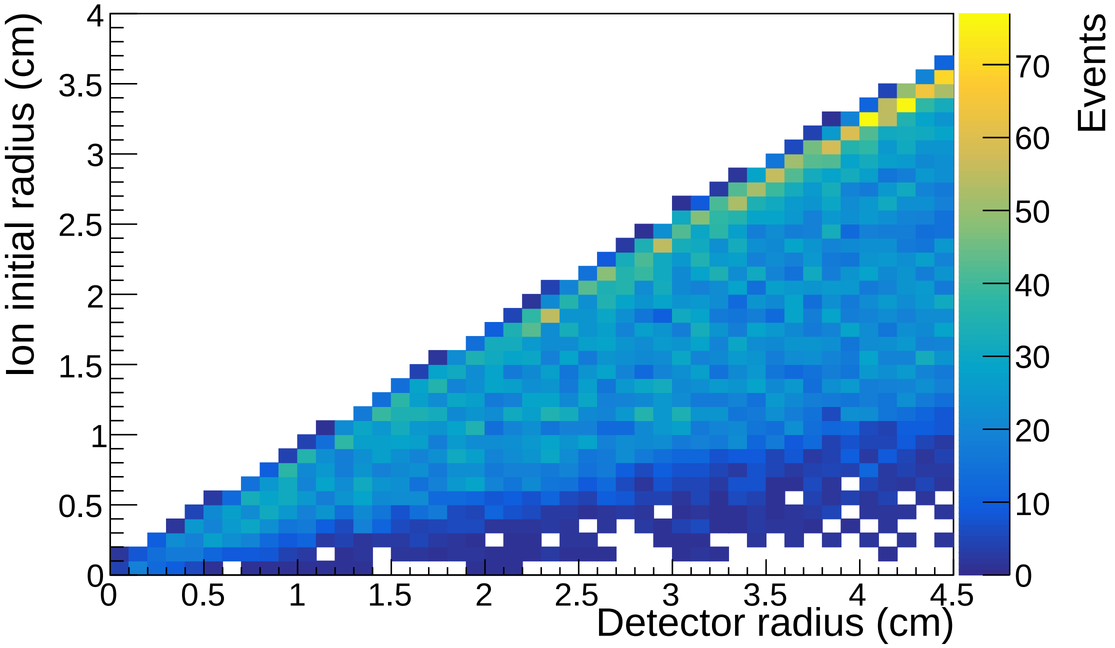

Figure 7.20: Correlation between the radius of an ionization electron at the detector and the projectile ion's initial radius in the Penning trap.

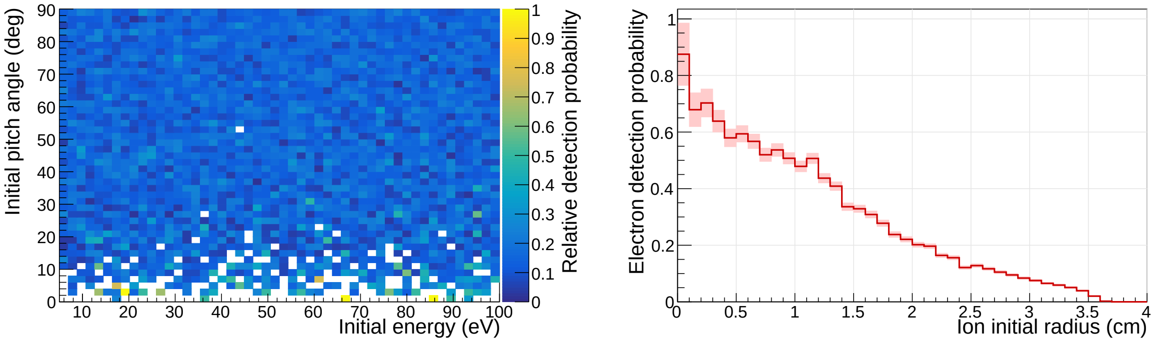

(a) (b)

Figure 7.21: Probability for electron detection at the FPD, based on initial ion properties. (a) Effect of ion initial energy and initial angle. (b) Effect of ion initial radius.

sults agree with expectations. The effect of the ion energy and angle is shown in Figure 7.21a, with regard to the probability of the SE to reach the detector. The distribution is flat with respect to the ion energy and angle, and this result makes sense. Ions are accelerated into the MS in a non-adiabatic manner, without following the magnetic field lines. Thus, the initial energy and momentum of the ion are negligible compared with the acceleration induced by the MS electric field.

The initial radius of the ion within the trap, however, does have a major effect of the detection probability of SEs, as can be seen in Figure 7.21b. Ions created at outer radii are less likely to produce electrons that reach the detector because these ions spend less time in the magnetic flux tube that connects to the detector; therefore, fewer ionization interactions will occur where the resultant electrons can reach the detector.

The initial properties of the ionization electrons, which are determined by the scattering cross-sections (see section 7.4), also affect the detection probability. The effects of the initial angle and initial energy of the electron are shown in Figure 7.22. As expected, electrons with a small pitch angle are more likely to reach the FPD, since they are less likely to be magnetically trapped. Electrons with higher energies also have a higher probability of

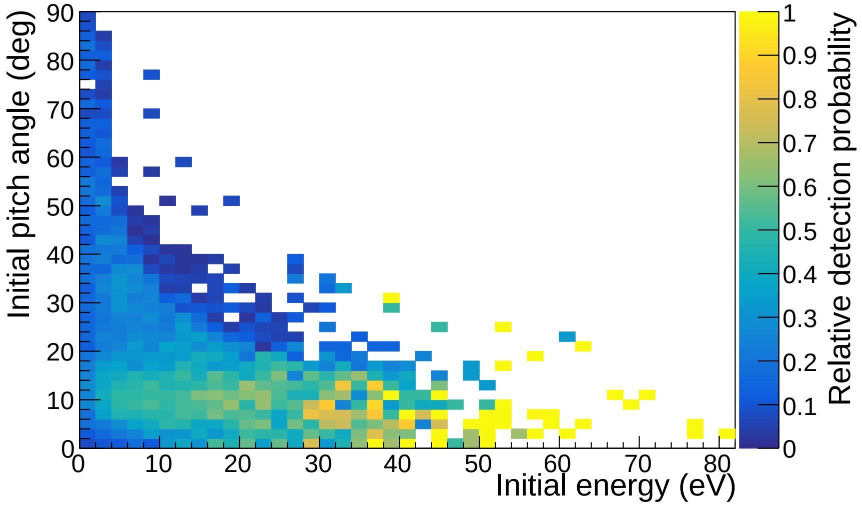

Figure 7.22: Probability for electron detection at the FPD, based on the electron initial energy and initial angle.

reaching the detector; their energies allow them to overcome the electric field in the analyzing plane, if the electrons were created at the upstream end of the MS.

7.6.4 Magnetron Drift

One expects an ion leaving the Penning trap and entering the MS to undergo a magnetron drift due to a $\mathbf{E} \times \mathbf{B}$ force experienced at the axial edge of the trap (see section 7.5.2). The effect of the magnetron drift can be observed by looking at the azimuthal position of the electron at the detector, relative to the initial azimuthal position of the parent ion. This is shown in Figure 7.23. The majority of electrons are detected at a position at least 20° away from where the ion was generated. Ions generated at larger radii experience larger $\mathbf{E} \times \mathbf{B}$ drifts due to the increased electric fields near the electrodes. This latter effect was already observed for electrons in the Penning trap (see Figure 7.15b).

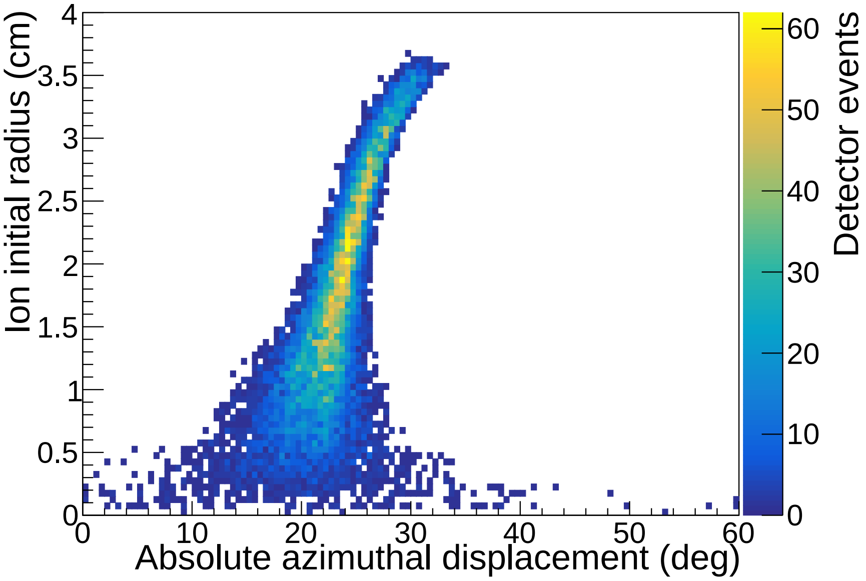

Figure 7.23: Azimuthal displacement of the detected electron relative to the initial ion's position in the Penning trap. This shift is a result of magnetron motion of the positive ions as they enter the MS.

7.6.5 Future Work

In this chapter, ions were generated in the Penning trap at a fixed axial position and uniformly within a specified radius. However, the real distribution of ions within the Penning trap is more complicated and depends heavily on the electron distribution, both in terms of energy and starting position. Future studies should take into account the distribution of trapped electrons, whether originating from PS background processes or from scattering of β-particles within the trapping region.

Ideally, a multistage tracking procedure should be implemented, which takes into account synchrotron emission and elastic/inelastic scattering processes:

1. Tracking of β-particles (or other background particles) through the Penning trap region.
2. Energy, position, and angular distributions of trapped β-particles or ionization electrons.

3. Tracking of trapped electrons in the Penning trap region.
4. Energy, position, and angular distributions of positive ions generated within the trap.
5. Tracking of ions into the MS.
6. Energy, position, and angular distributions of ionization electrons in the MS.
7. Tracking of ionization electrons to the FPD.

Chapter 8

MEASUREMENTS WITH THE INTER-SPECTROMETER PENNING TRAP

This chapter presents measurements of the inter-spectrometer Penning trap obtained during the SDS-III commissioning campaign. First, the Penning wiper apparatus is described (section 8.1), before turning to the initial measurements with the wiper (section 8.2). Next, additional measurements with the Penning trap which were performed under improved vacuum conditions are detailed (section 8.3). Finally, the contribution of the Penning trap to the total background rate is determined from long-term measurements (section 8.4).

The most important parameter for understanding how the Penning trap produces background, aside from the electromagnetic settings of the spectrometers, is the pressure P inside the beamline. For the remainder of this thesis, values for P_{MS} were measured using the ion extractor gauge in pump port 3 of the MS, while those for P_{PS} were measured using the cold cathode gauge in the 45° pump port of the PS. However, the readings from these gauges only provide approximate pressure values. This is because the gauges are located in ports that are at least partly removed from the central volume of either spectrometer, and because it has not been verified that the calibration of these gauges was correct during the Penning trap measurements described below. Nonetheless, the pressure gauges give a sense of the relative changes in pressure within the PS and MS.

8.1 Penning Wiper Apparatus

A detailed paper on the Penning wiper hardware is in preparation [241]. Here, only basic details of the device will be given that are relevant for this thesis. The Penning wiper apparatus was built at the University of Münster. It is installed in the beamline valve

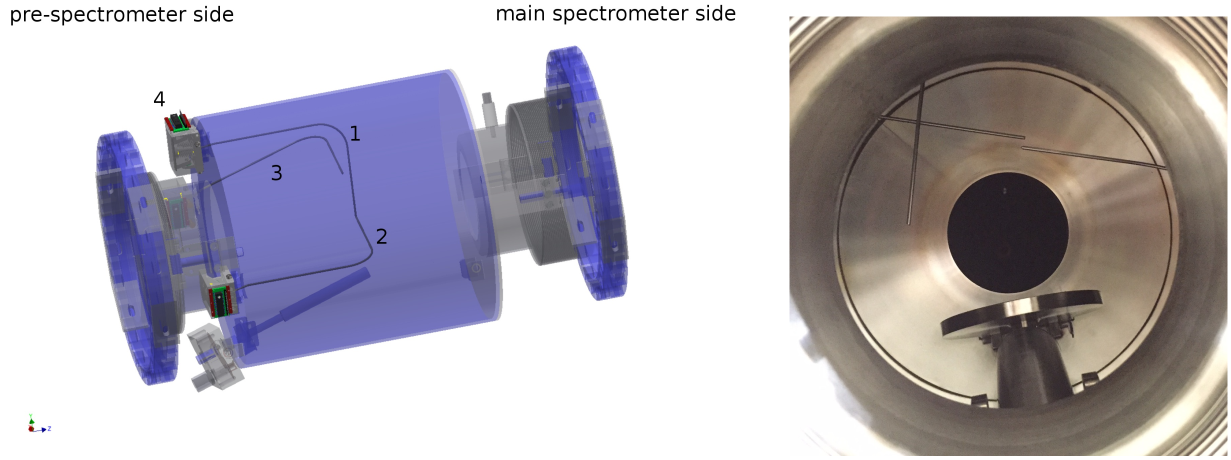

(a)

(b)

Figure 8.1: (a) Drawing of the inter-spectrometer valve with the Penning wipers (1, 2, 3) installed. One of the wiper controllers (4) is labeled. Figure taken from [241]. (b) Photo of the Penning wipers as installed in the PS-MS flapper valve. The valve is being viewed from the PS side. Three Penning wipers are installed. Photo adapted from the KATRIN ELOG.

connecting the two spectrometers (Figure 8.1a). The device consists of three metal rods ("wipers") that can be moved in and out of the flux tube. Due to the placement of the wiper in a high magnetic-field region, a standard motor cannot be used to operate the wipers. Instead, pressurized air is used to actuate one of three muscles that moves a Penning wiper. The choice of having three wipers is a practical one; the vacuum bellows for each wiper is rated for a large though limited number of wiper movements, after which the wiper should no longer be used. The three wipers are identical but are placed at different locations and orientations in the valve (Figure 8.1b). For the measurements described in this thesis, only a single wiper was used at a time.

The operation of each Penning wiper is controlled with the ORCA software that handles run operation and data-taking at the FPD platform. The adjustable parameters of the wiper motion (frequency of operation, duration of time within the flux tube, etc.) can be controlled via run scripts. The movement of each Penning wiper into the flux tube results in the generation of an output signal that is routed to the DAQ system. The wiper signal is saved in the FPD event data stream and is easily accessible for later analysis. To protect the detector system, the detector safety script was adjusted to automatically engage the Penning wipers if the measured rate became too high (due to a Penning discharge).

8.2 Poor Vacuum Conditions (SDS-IIIa)

The first measurements of the PS-MS Penning trap occurred during the SDS-IIIa commissioning phase of KATRIN. This time period marked the first time both spectrometers were operated simultaneously at high voltage, and, correspondingly, the first time that the Penning wipers could be tested in situ. The spectrometers were not baked prior to these measurements; therefore, $P_{\mathrm{MS}} = 2 \times 10^{-9}\,\mathrm{mbar}$. The beamline magnetic field was operated at 20 % of the maximum value due to issues with one of the DPS magnets [108]. However, to simulate the large magnetic field in the Penning trap region that will be in effect during neutrino mass measurements, some of the measurements were taken with the PS1 and PS2 magnets ramped to 80 % of their maximum values.

Due to several other important measurements occurring during this timeframe (including beam-tube alignment [108] and ion transport studies [154]), only a few days of Penning trap measurements were possible. With the MS operating at nominal voltage (−18.6 kV), it was decided to ramp up the PS voltage in stages and observe when the Penning trap would begin to contribute to the background rate. Penning discharges were observed at $U_{\mathrm{PS}} = -1.6\,\mathrm{kV}$ with the PS magnets at 80 % of their maximum values. The Penning wiper generally proved effective at mitigating the background and stopping discharges, but regular operation of the wiper could not prevent discharges from occurring.

This behavior can be seen in Figure 8.2, which shows the FPD electron rate as a function of time during one of the measurement runs. Over the course of about 12 minutes, there were eight Penning discharges with rates exceeding 10 kcps. For each of these discharges, the Penning wiper was activated to empty the trap. Although successful in lowering the background rate, the wiper was only sometimes effective at preventing the discharge from

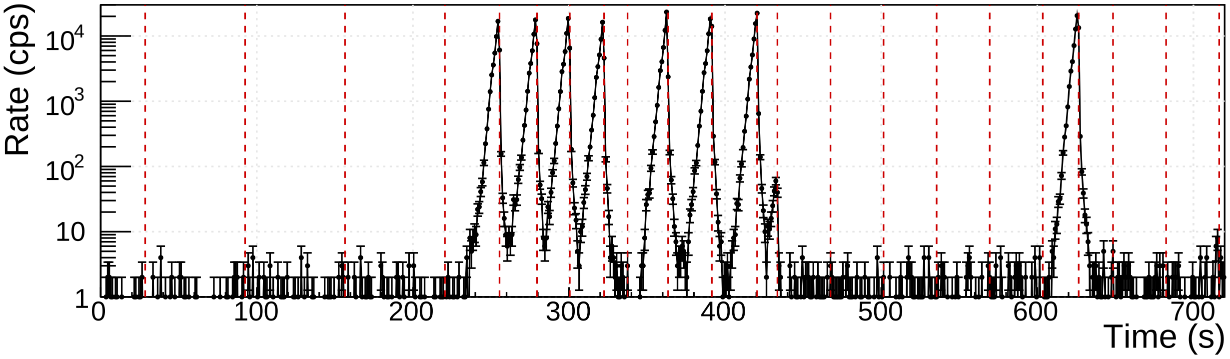

Figure 8.2: The FPD rate in the electron ROI during run #32373. The dashed red lines indicate when the Penning wiper was activated; for each activation, the wiper remained in the beam tube for about four seconds. The wiper was activated at regular intervals (every 60 or 30 seconds) and was also activated when the total rate exceeded 10 kcps.

immediately reigniting.

It was not possible to ramp the PS to high voltages ($U_{\mathrm{PS}} \lesssim -2\,\mathrm{kV}$) without experiencing uncontrollable Penning discharges. Regular operation of the Penning wipers proved ineffective at reducing the background rate. Only by using the Penning wiper in its static configuration (i.e., permanently placing it in the beam tube) could the PS be ramped to its design voltage without Penning discharges occurring.

8.2.1 Spectral Analysis

The FPD energy spectra and pixel rate distributions obtained during measurements with an active Penning trap exhibited interesting characteristics that merited further study. By analyzing these features, one can better understand the mechanism of background generation from the Penning trap.

The upper part of Figure 8.3 shows the energy spectrum obtained during one of the Penning trap measurements (run settings are found in Table 8.1). In addition to the expected peak in the electron ROI (25.7–30.7 keV), there is also a peak centered at ~16.5 keV. A similar peak has been observed in other background measurements [123] and seems to be

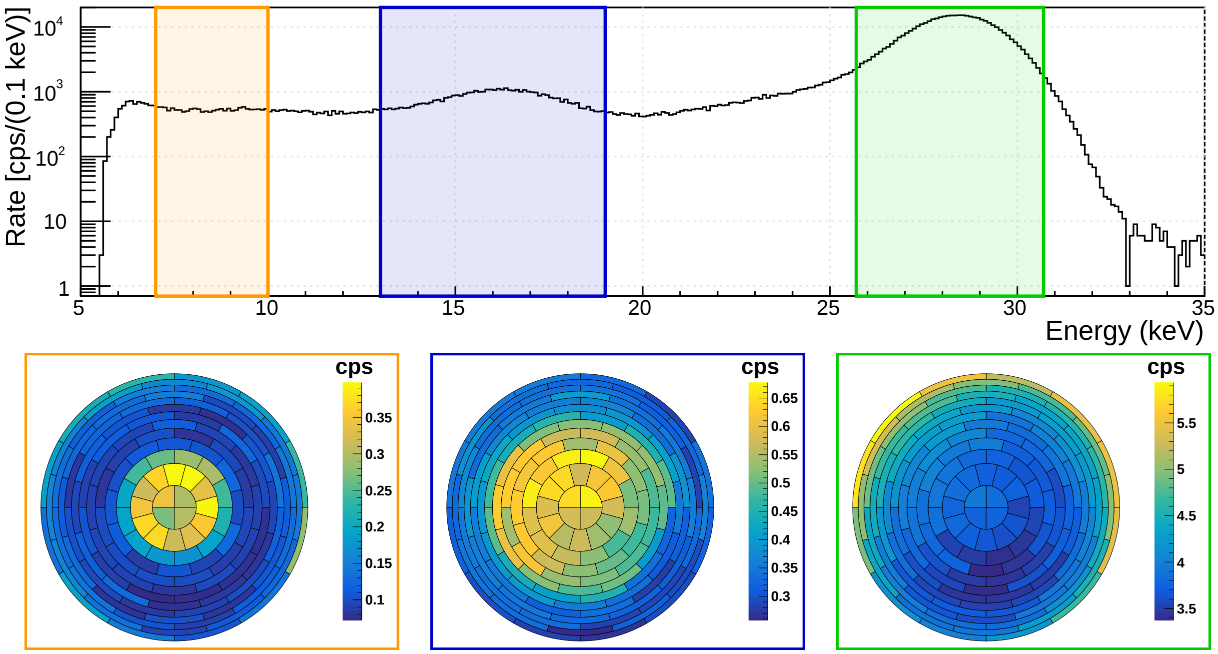

(a) Low-energy: 7–10 keV (b) Ion: 13–19 keV (c) Electron: 25.7–30.7 keV

Figure 8.3: FPD energy spectrum obtained during SDS-IIIa measurements with an active Penning trap (run #32373). Below, pixel rate distributions are shown for three different energy ROIs: (a) low-energy, (b) ion, and (c) electron.

	PS magnets 80%
Run numbers	32373
Magnetic field	setting N
P_{MS} (mbar)	5×10^{-10}
$U_{\mathrm{PS,\ hull}}$ (kV)	-1.6
$U_{\mathrm{PS,\ wire}}$ (kV)	-0.4
$U_{\mathrm{PS,\ cone}}$ (kV)	-0.3
$U_{\mathrm{MS,\ hull}}$ (kV)	-18.5
$U_{\mathrm{MS,\ IE}}$ (kV)	-0.1

Table 8.1: Analyzed run from the SDS-IIIa Penning trap measurements. Details on the magnetic field setting can be found in Appendix A.

caused by negative ions. To study this peak, an ion ROI was defined for 13–19 keV. A third energy regime was also studied, between 7 keV and 10 keV, which is just above the detector noise threshold.

The detector pixel rate distributions for each energy ROI, displayed at the bottom of Figure 8.3, are quite distinct; this indicates that different production mechanisms dominate each energy range. Understanding these distributions provides insight into the background production from the Penning trap.

Electron ROI

The pixel distribution of events in the electron peak (Figure 8.3c) is similar to that observed during other MS background measurements. An example MS background measurement without an active Penning trap is shown in Figure 8.4. For both plots, the top-bottom asymmetry in the rate can likely be explained by a misalignment of the magnetic flux tube relative to the MS vessel walls [141]. The similarity in pixel distributions implies that the background generation mechanism from the Penning trap is volume-dependent, like the remaining MS background (which is primarily caused by Rydberg atoms; see section 4.1.6). The ionization of residual gas inside the MS is a volume-dependent process. Because the flux-tube volume measured by each pixel ring increases for larger radii [34], the volume-dependent background rate will increase in a correlated manner. Therefore, the pixel distribution of events in the electron ROI provides a confirmation that the Penning trap produces background through the ionization of residual gas.

Ion ROI

The peak at 16.5 keV is most likely caused by negative hydrogen ions (H^-) [123]. These ions were previously observed coming from the spectrometer walls when studying field emission from the MS vessel. The ions were thought to be generated from field emission electrons interacting with hydrogen atoms on the vessel surface. Although the anions have energies

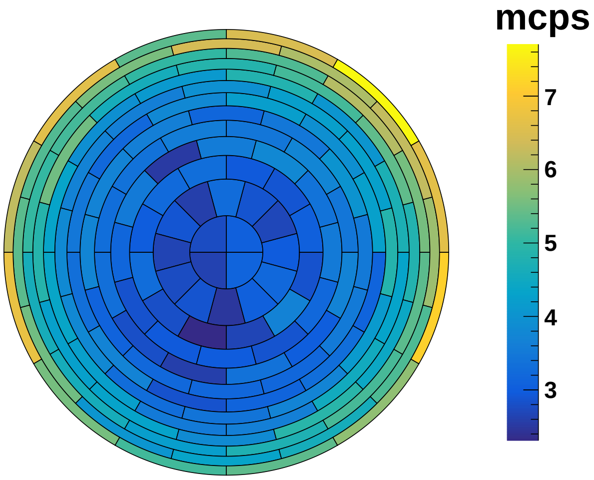

Figure 8.4: MS background rate in the electron ROI, measured without an active Penning trap during SDS-IIIa (FPD runs #32099–32101).

similar to the electrons in the MS, they are detected at the FPD with reduced energy due to dead-layer effects.

The ion peak has also been observed in standard MS background measurements, although the generation mechanism in this case is not understood [141]. The pixel rate distribution (Figure 8.3b) indicates that the hydrogen anions are primarily produced at smaller radii in the MS. This indicates some type of production in the volume of the MS.

Low-Energy ROI

To understand the low-energy region, it is useful to see the energy spectrum across different detector pixel rings. This is shown in Figure 8.5. A couple of features are apparent. First, there is a small peak at 10 keV in the outer pixel rings. The probable cause of this peak is somewhere in the detector section, since the energy corresponds to the PAE voltage of 10 kV. After a large Penning discharge, the detector rate was measured after the gate valve to the main spectrometer was closed. A large peak ("afterglow") at 10 kV was observed in the detector section which persisted for over an hour. This could be caused by a buildup

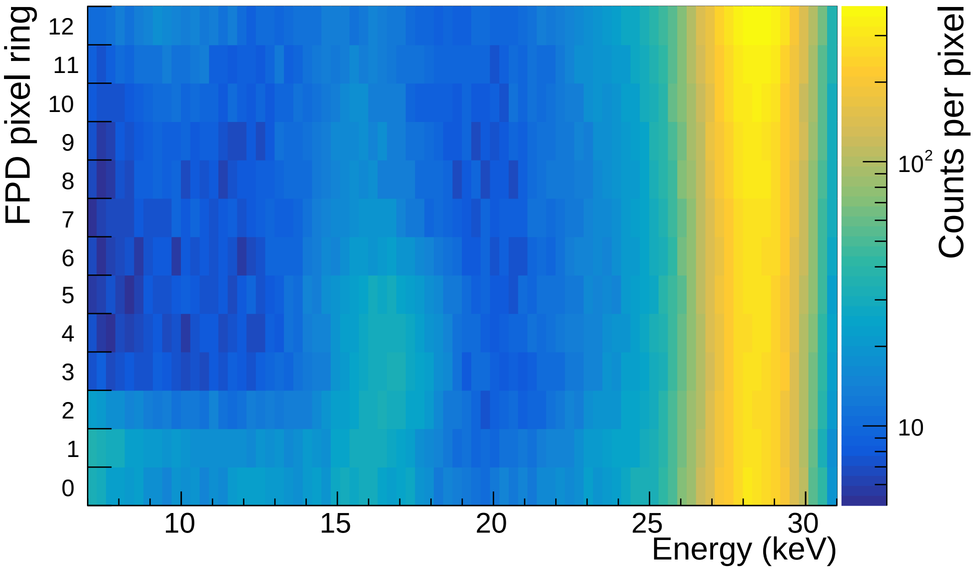

Figure 8.5: 2D energy spectrum obtained during measurements with an active Penning trap (FPD run #32373). The pixel ring number increases with the detector radius.

of positive ions in the FPD system between the PCH magnet and the PAE. Positive ions are generated in the Penning trap, and some fraction will enter the FPD system. These ions have a chance to scatter and become trapped by the positive potential of the PAE and the magnetic mirror generated by the PCH magnet (for large pitch angles). Through the ionization of residual gas (or by impacting the walls of the FPD system), the stored positive ions can produce electrons that will reach the detector with an energy of 10 keV.

Second, below 10 keV the rate is mostly concentrated in the innermost pixel rings (ring < 3). It is difficult to determine the source of these low-energy events. If the events are electrons, they must be generated downstream of the PAE. Or these events could be negative ions, generated upstream of the PAE and experiencing the same dead-layer detector effects as the 16.5 keV peak events. Another possibility is the worsening of the detector energy resolution, which would result in a widened noise distribution and lead to noise events entering the low-energy ROI. However, it is puzzling why any of these scenarios would only affect the

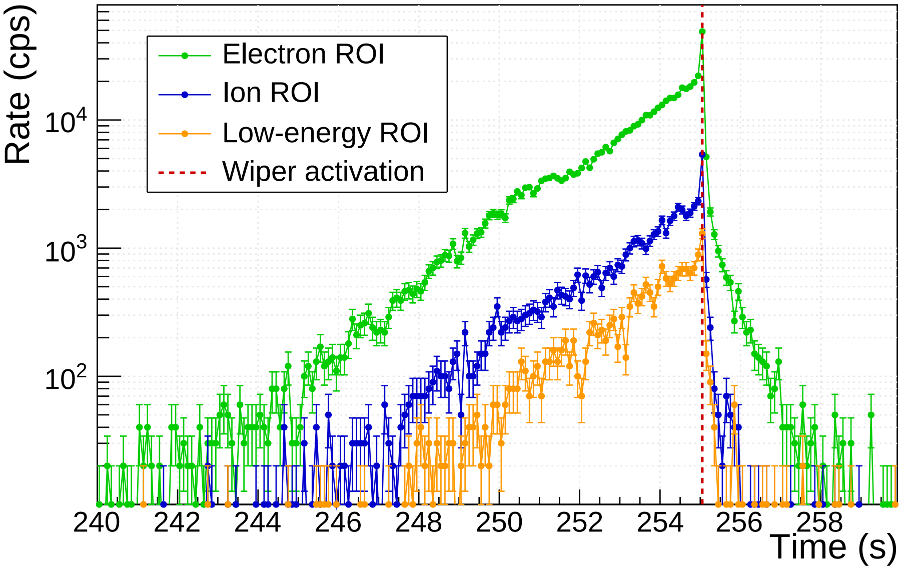

Figure 8.6: FPD rate measured for each ROI during a Penning discharge (run #32373). The Penning wiper activation time is indicated by the dashed line.

central detector pixels. Further investigation is required to understand the low-energy pixel distribution.

Correlation between ROIs

Figure 8.6 shows the detector rate at a function of time for all three ROIs during one of the Penning discharge events. The rates appear to be highly correlated, with increases in all three ROIs as the Penning discharge develops. When the Penning wiper is activated, the rates in all three regions simultaneously decrease. The mechanisms that are responsible for the ion and low-energy events must happen on short timescales. This seems to disfavor stored particles in the MS as a cause of these events.

Another feature that is visible in the figure for all ROIs is a rate increase when the Penning wiper is inserted into the trapping region. This effect may be caused by a tiny amount of residual gas being emitted into the Penning trap region, thereby feeding the trap through ionization. The gas may originate from metal bellows through which the Penning wiper is moved. This hypothesis can be tested in the future by looking for a pixel-dependence in the rate spike that changes for each of the three Penning wipers (since the bellows for each wiper are azimuthally separated).

8.3 Improved Vacuum Conditions (SDS-IIIb)

Penning trap measurements resumed during SDS-IIIb. Prior to these measurements, both spectrometers were baked[1], which significantly improved the vacuum conditions inside the beamline ($P_{\mathrm{MS}} = 10^{-11}\,\mathrm{mbar}$) [242]. To study the background from the Penning trap, once again the PS hull voltage was ramped in stages while the MS remained at its nominal voltage settings. Under the low-pressure conditions, it was possible to reach $U_{\mathrm{PS,hull}} = -18\,\mathrm{kV}$ without observing the severe and rapid onset of Penning discharges that was observed during SDS-IIIa.

8.3.1 Pressure Dependence of the Background Rate

The improved vacuum conditions during SDS-IIIb allowed one to achieve nominal operating voltages for the PS and MS without Penning discharges. To study the pressure dependence of the Penning trap background, dedicated measurements were performed with an artificially elevated pressure. Argon gas was injected into the MS via a small port (Pump Port 100) on the upper, downstream end of the vessel. Argon gas was chosen since it is easily pumped by the TMPs inside the spectrometers. However, to prevent the gas from being pumped away during the measurements at elevated pressure, the valves connecting the TMPs to the PS and MS vessels were closed. In this way, it was possible to create a stable pressure environment at which to perform background measurements.

The pressure effect can be seen in Figure 8.7. Two different sets of measurements were performed (Table 8.2). For each set, the background rate was measured as a function of the

---

[1] However, issues with the PS heating system resulted in the PS NEG pumps not being activated during the bake-out [242].

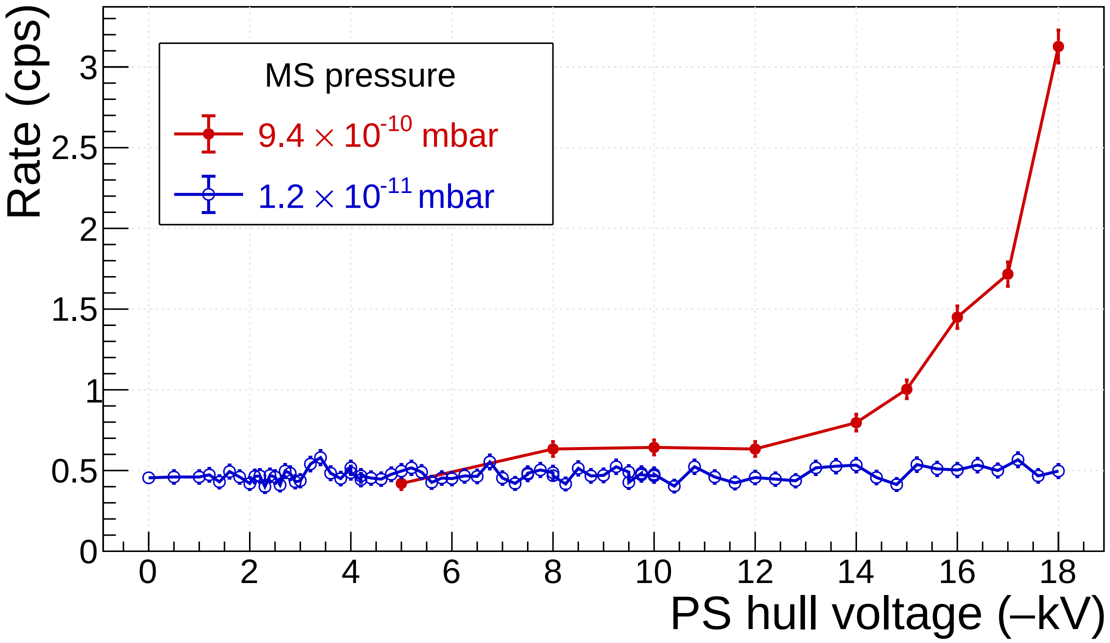

Figure 8.7: The effect of pressure and the PS voltage on the background rate. Each point corresponds to a single FPD run (see Table 8.2). The contribution of the Penning trap becomes noticeable at high pressures and large PS voltages.

	Low pressure	High pressure
FPD runs	34090–34113, 34132–34150, 34177, 34179–34187, 34204–34226	34278–34286
Magnetic field	setting O	setting O
P_{MS} (mbar)	1.2×10^{-11}	9.4×10^{-10}
P_{PS} (mbar)	1.6×10^{-10}	4.9×10^{-10}
$U_{\mathrm{PS,\ hull}}$ (kV)	variable	variable
$U_{\mathrm{PS,\ wire}}$ (kV)	-0.4	-0.4
$U_{\mathrm{PS,\ cone}}$ (kV)	-0.3	-0.3
$U_{\mathrm{MS,\ hull}}$ (kV)	-18.5	-18.5
$U_{\mathrm{MS,\ IE}}$ (kV)	-0.1	-0.1

Table 8.2: Settings for studying the pressure-dependence of the Penning trap background rate (see Figure 8.7). All runs lasted 5 minutes, except run #34090 (10 minutes) and run #34150 (30 minutes).

PS hull voltage. The first set of measurements was performed with $P_{\mathrm{MS}} = 1.2 \times 10^{-11}$ mbar, and the rate was measured to be approximately independent of the PS voltage. For the second measurement set, which occurred at pressure ~80 times higher, a clear increase in rate is observed at higher voltages.

It is obvious from Figure 8.7 that vacuum pressure plays a dominant role in determining the background contribution from the Penning trap. This makes sense from a conceptual point of view. Vacuum pressure affects three processes in the background production chain:

1. Filling the Penning trap with electrons through scattering with residual gas
2. Production of positive ions through collisions of trapped electrons with residual gas
3. Ionization of residual gas in the MS from positive ions emitted from the Penning trap

Therefore, one expects the background rate to be very sensitive to the pressure.

8.3.2 Wafer Damage Due to Large Penning Discharge

A very large Penning discharge occurred on September 21, 2017, during the SDS-IIIb commissioning measurements. To obtain high rates for tests of new DAQ software, the Penning trap between the spectrometers was allowed to produce large background rates through an elevated vacuum pressure ($P_{\mathrm{MS}} = 4 \times 10^{-9}$ mbar) generated by the injection of argon gas. However, a count rate of over 5×10^{7} cps was accidentally reached at the detector, which resulted in the automatic shutdown of the FPD system and the closing of the gate valve between the MS and FPD.

This high rate appears to have damaged the wafer, likely through radiation damage. In particular, the electron ROI peak position shifted downwards for certain pixels; this can be seen in Figure 8.8. The effect is generally worse for pixels at larger radii but is also significant for the pixel ring surrounding the bullseye. As a result of the damage due to the Penning discharge, the detector wafer was eventually replaced (see section 3.2.4).

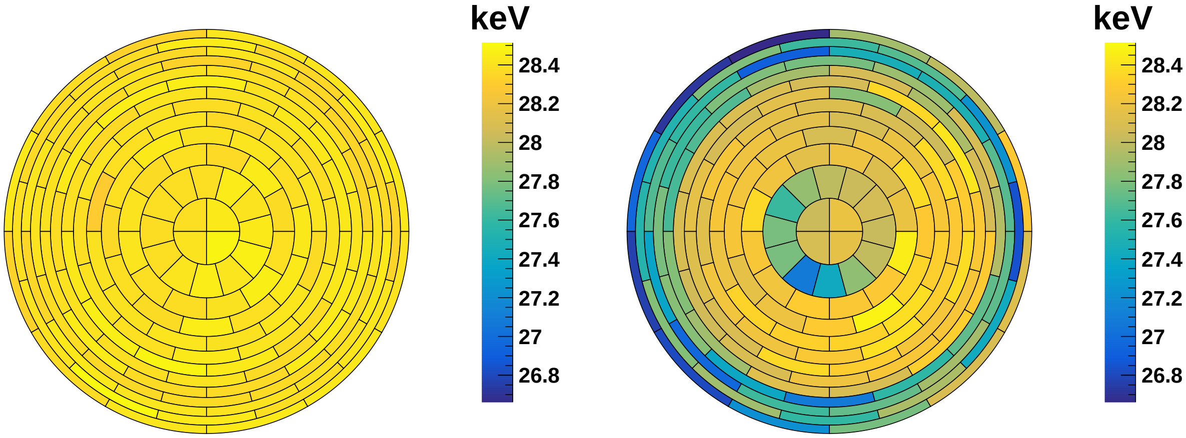

(a) Sept. 12, 2017 (Before the large discharge) (b) Oct. 11, 2017 (After the large discharge)

Figure 8.8: The electron peak position (a) before and (b) after the large Penning discharge on Sept. 21, 2017. The former (latter) was measured using FPD runs #34162–34164 (runs #34567–34568). The expected peak position is 28.7 keV. The lower the peak position, the more damaged is the corresponding pixel.

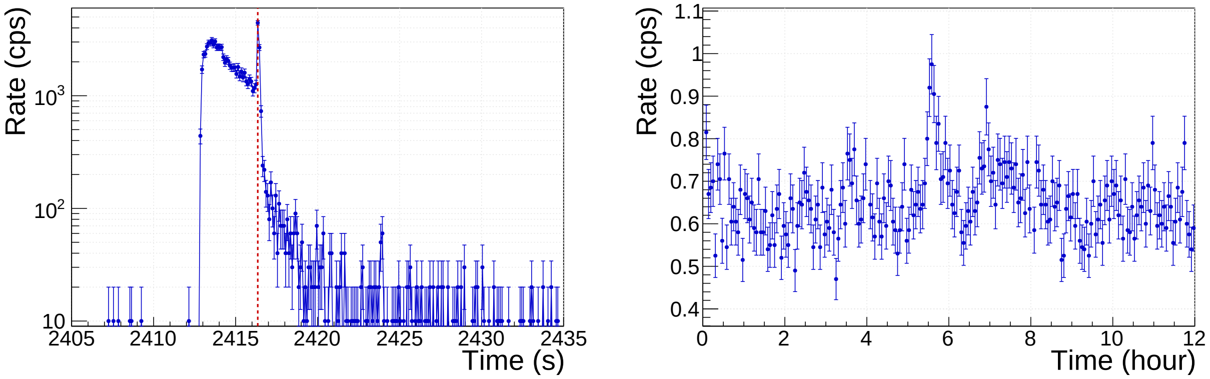

(a) (b)

Figure 8.9: FPD rates in the electron ROI with both spectrometers on high voltage. (a) Penning discharge during run #34265. The red dashed line indicates the activation of the Penning wiper. (b) Large rate fluctuations during runs #34266–34268, presumably caused by the Penning trap.

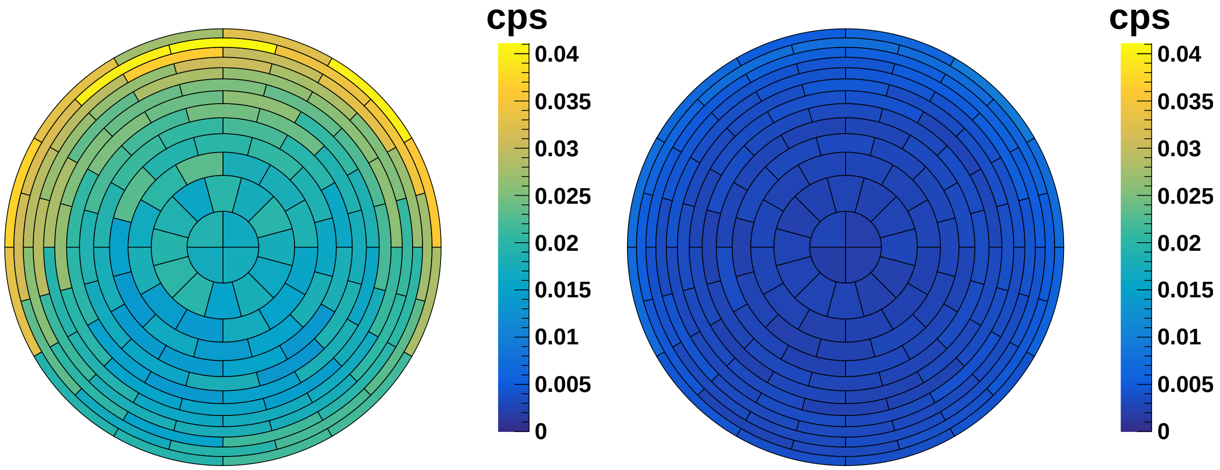

(a) Gauge ON (b) Gauge OFF

Figure 8.10: FPD pixel rate distributions for measurements with the PS extractor gauge on/off. Settings and rates for these measurements are found in Table 8.3.

8.3.3 Minimizing the Background Rate

Although improved pressure conditions allowed the spectrometers to be used in tandem, occasional Penning discharges were still observed during long-term measurements, in addition to rate instabilities/spikes. Examples of these phenomena can be seen in Figure 8.9. While the Penning wiper was effective at stopping the discharges, further measurements were performed to see if discharges could be prevented entirely. It was discovered that two hardware components in the PS affected the filling rate of the Penning trap: the ion extractor pressure gauge and the IE system.

PS Extractor Gauge

Figure 8.10 shows the pixel rate distribution observed at an elevated pressure ($P_{\mathrm{MS}} = 9 \times 10^{-10}$ mbar) with the PS ion extractor vacuum gauge on, and with the gauge off. The rate dropped by about a factor of six after turning the gauge off (Table 8.3).

The PS ion extractor vacuum gauge has a direct line of sight into the PS vessel through

	Gauge ON	Gauge OFF
FPD runs	34288–34289	34303–34312
Magnetic field	setting O	setting O
P_{MS} (mbar)	9.3×10^{-10}	9.4×10^{-10}
P_{PS} (mbar)	4.9×10^{-10}	4.9×10^{-10}
$U_{\text{PS, hull}}$ (kV)	-18.0	-18.0
$U_{\text{PS, wire}}$ (kV)	-0.4	-0.4
$U_{\text{PS, cone}}$ (kV)	-0.3	-0.3
$U_{\text{MS, hull}}$ (kV)	-18.5	-18.5
$U_{\text{MS, IE}}$ (kV)	-0.1	-0.1
ROI (keV)	25.7 to 31.7	25.7 to 31.7
ROI rate (cps)	3.19 ± 0.02	0.548 ± 0.004

Table 8.3: Measurements to study the effect of PS extractor gauge on the background rate.

the 45° pump port (see Figure 2.5). The effect of this device on the background rate was previously observed in commissioning measurements with the PS [114, 115]. The ion extractor gauge is a type of hot-cathode gauge [115], which operates by emitting electrons from a hot cathode and using the ionization of residual gas to measure the vacuum pressure [243].

However, some unknown fraction of the electrons (or electron-induced secondary particles) emitted from the cathode are able to travel into the magnetic flux tube of the PS vessel and create background. The background electrons produced in the PS cannot overcome the retarding potential of the MS; however, they can become trapped or create ionization electrons within the Penning trap. Thus, the ion extractor gauge increases the fill rate of electrons within the trap. To prevent this filling mechanism, the vacuum gauge was turned off during all subsequent Penning trap measurements.

PS Cone Electrode Voltage

One way of preventing electrons produced within the PS from reaching the Penning trap is by adjusting the voltages applied to the IE system. By properly setting the relative values of the wire and cone electrode voltages (discussed in section 2.2.1), it is possible to reduce the filling rate of the Penning trap.

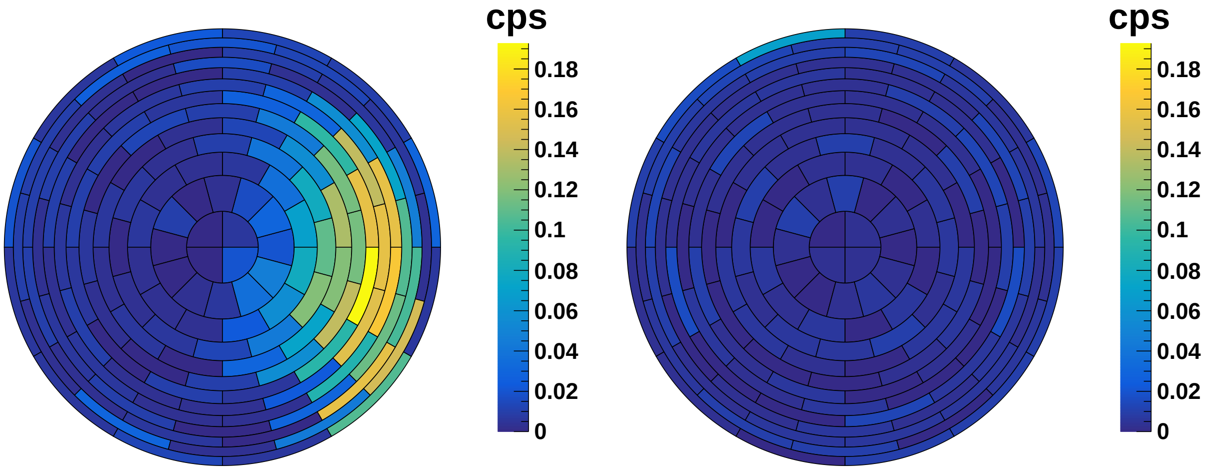

(a) $U_{\text{PS, cone}} = -300\,\text{V}$, $U_{\text{PS, wire}} = -400\,\text{V}$ (b) $U_{\text{PS, cone}} = -400\,\text{V}$, $U_{\text{PS, wire}} = -400\,\text{V}$

Figure 8.11: Pixel rate distribution plots for measurements of the PS background, with the inner electrodes at different voltages.

To study electron production in the PS, a special voltage configuration was used along with a modified ROI (Table 8.4). The voltage of the MS hull was lowered from $-18.5\,\text{kV}$ to $-18.0\,\text{kV}$ in order to directly observe PS background electrons with the FPD. Figure 8.11 shows the detector pixel rate distribution for measurements with two different PS electrode settings. If the wire electrode has a more negative potential than the cone electrodes, a high rate is observed. The rate is highest on the west side of the PS vessel (this rate distribution is not understood). However, if the cone electrodes are placed at the same voltage as the wire electrodes, the rate excess disappears.

This observation can be explained in terms of the ability of the cone electrode to block electrons. When the wire electrode is at a more negative potential, electrons originating from the region of the wire electrode will not be blocked by the cone electrode but can travel through the Penning trap region. The reconfigured inner electrode settings, with both electrodes at the same potential, was used for future Penning trap background measurements.

	Equal voltages	Unequal voltages
FPD runs	34425	34424
Magnetic field	setting O	setting O
P_{MS} (mbar)	1.4×10^{-11}	1.3×10^{-11}
P_{PS} (mbar)	1.8×10^{-10}	1.8×10^{-10}
$U_{\mathrm{PS,\ hull}}$ (kV)	-18.0	-18.0
$U_{\mathrm{PS,\ wire}}$ (kV)	-0.4	-0.4
$U_{\mathrm{PS,\ cone}}$ (kV)	-0.3	-0.4
$U_{\mathrm{MS,\ hull}}$ (kV)	-18.0	-18.0
$U_{\mathrm{MS,\ IE}}$ (kV)	-0.1	-0.1
ROI (keV)	25.5 to 31.5	25.5 to 31.5
ROI rate (cps)	4.8 ± 0.1	0.83 ± 0.05

Table 8.4: Measurements to study the effect of the PS inner electrode voltages on the background rate.

Total Rate Improvement

Table 8.5 lists background measurements taken before and after the modifications to the PS extractor gauge and IE voltages. Excluding periods of rate spikes or Penning discharges that occurred for earlier measurements, the modifications to the PS resulted in a 20 % decrease in the MS background rate. This result shows that electrons produced within the PS can fill the inter-spectrometer trap but that it is possible to limit their production and prevent them from reaching the trapping region. In this way, the contribution of the Penning trap to the background rate can be diminished.

8.4 Background Contribution under Nominal Conditions (SDS-IIIc)

To determine the residual contribution of the Penning trap to the total MS background rate, a long-term (two-week) measurement was performed during SDS-IIIc with both spectrometers on high voltage. The electromagnetic settings (Table 8.6) were chosen to mimic the planned settings for neutrino-mass data-taking. Instead of the 3.8 G magnetic field (setting O) in the MS analyzing plane that was used for previous measurements, a 6.0 G magnetic field (setting P) was generated by the LFCS (see Appendix A for details on the magnetic field settings).

	Before modifications	After modifications
FPD runs	34259–34264	34415–34420
Total duration (h)	24	24
Magnetic field	setting O	setting O
PS extractor gauge	On	Off
P_{MS} (mbar)	1.3×10^{-11}	1.4×10^{-11}
P_{PS} (mbar)	1.7×10^{-10}	1.8×10^{-10}
$U_{\text{PS, hull}}$ (kV)	-18.0	-18.0
$U_{\text{PS, wire}}$ (kV)	-0.4	-0.4
$U_{\text{PS, cone}}$ (kV)	-0.3	-0.4
$U_{\text{MS, hull}}$ (kV)	-18.5	-18.5
$U_{\text{MS, IE}}$ (kV)	-0.1	-0.1
ROI (keV)	25.7 to 31.7	25.7 to 31.7
ROI rate (mcps)	583 ± 3	468 ± 2

Table 8.5: Measurements of the MS background rate before and after PS hardware modifications.

A larger magnetic field results in a smaller magnetic flux tube volume and therefore partly mitigates any volume-dependent background (see section 2.3). A detailed investigation of the background during this long-term measurement has already been performed elsewhere [141]. The average background rate was (287.7 ± 0.5) mcps.

Immediately after this long measurement, a shorter measurement was performed with identical settings except that the PS was grounded. The measured rate for this latter measurement was (4.1 ± 1.4) mcps less than the former measurement (see Table 8.6). This rate difference corresponds to the effect of the Penning trap on the background rate, assuming no other systematic effects or non-Poissonian contributions to the rate. There are indications, however, of rate instabilities during these measurements [141], implying that the difference in rate between the two measurements may not be due to the Penning trap, but rather to some unknown process.

Nonetheless, a conservative estimate can be made on the background contribution from the Penning trap. Assuming that the contribution increases linearly over time, the measured difference of (4.1 ± 1.4) mcps between the two measurements indicates a contribution of

	PS on	PS off
FPD runs	35023–35110	35112–35123
Duration (d)	14.7	1.9
Magnetic field	setting P	setting P
P_{MS} (mbar)	9.2×10^{-12}	9.3×10^{-12}
P_{PS} (mbar)	4.3×10^{-11}	4.1×10^{-11}
$U_{\mathrm{PS,\ hull}}$ (kV)	-17.9	0
$U_{\mathrm{PS,\ wire}}$ (kV)	-0.4	0
$U_{\mathrm{PS,\ cone}}$ (kV)	-0.4	0
$U_{\mathrm{MS,\ hull}}$ (kV)	-18.4	-18.4
$U_{\mathrm{MS,\ IE}}$ (kV)	-0.2	-0.2
ROI (keV)	25.7 to 31.7	25.7 to 31.7
ROI rate (mcps)	287.7 ± 0.5	283.6 ± 1.3

Table 8.6: Settings and rates for the long-term SDS-IIIc measurements.

(8.1 ± 2.8) mcps at the end of the measurement interval. As the measurement with the Penning trap lasted 14.7 days, the contribution at the end of one week is (3.9 ± 1.3) mcps. The upper limit (90% C.L.) on the contribution of the Penning trap after one week is therefore 6.1 mcps, which corresponds to 2.1 % of the total measured background rate. At present, the Penning trap is not a dominant contributor to the spectrometer background rate.

During future tritium measurements, the high rate of electrons through the Penning trap region may cause additional filling of the trap and lead to increased background production. Care should be taken, therefore, to ensure that this filling mechanism is under control during neutrino-mass data-taking. If the background from the Penning trap increases over time or exhibits non-Poissonian behavior, the sensitivity of KATRIN to the neutrino mass could be significantly worsened (see section 2.3). However, the evidence collected thus far indicates that excellent vacuum conditions greatly mitigate any background contribution from the inter-spectrometer Penning trap.

Chapter 9

SUMMARY AND CONCLUSIONS

The mass of the neutrino is one of the major outstanding questions in contemporary physics. The determination of the neutrino mass scale provides the promise of insight into physics beyond the Standard Model. The KATRIN experiment aims to measure the neutrino mass with an unprecedented precision by measuring the tritium β-decay energy spectrum near the endpoint. The experiment uses a windowless gaseous tritium source and a MAC-E filter spectrometer to reach its goal; both of these tools were utilized by previous experiments. However, technical advances by KATRIN have led to the development of a high-luminosity source and a massive 24-m long, 10-m wide spectrometer that will enable an order of magnitude better sensitivity to the neutrino mass than previous tritium-based measurements.

The FPD system is responsible for detecting the β-particles that pass through the MS. The energy resolution of the detector, which determines the background contribution of the FPD system, shows large changes over time. A temperature and noise analysis indicates that the detector wafer is the primary cause of these variations, with each wafer manufacturing batch showing distinct intrinsic energy resolutions. With this knowledge, future upgrades to the FPD system can ensure that the best wafer is used for data-taking.

The large size of the spectrometer enables an excellent sensitivity to the β-particle energy, but it also comes with the prospect of increased background. SEs emitted from the spectrometer walls are a known source of background for prior MAC-E filter experiments. Approximately 45 000 cosmic-ray muons travel through the MS every second, and a muon detector system was previously constructed to quantify the effect of these particles on the background rate. In this work, a coincidence analysis between muon and FPD events allowed a validation of the background generation mechanism from muons. However, the contribution of muons to the spectrometer background rate is consistent with zero; an upper limit of 115 mcps (90 % C.L.) was determined from correlation measurements with the same muon detector system.

Environmental gamma radiation, primarily originating from the concrete surrounding the spectrometer, is another source of SEs. Simulations performed with GEANT4 found that over 10^6 gammas/s pass through the spectrometer. These simulations were compared with measurements that significantly increased or decreased the expected number of gammas passing through the MS. A combined analysis of the simulation and measurement data allowed the rate contribution of environmental gammas to be determined; gammas are responsible for less than 6 mcps (90 % C.L.) of the total background rate. Therefore, one can conclude from the gamma and muon analyses that the electric and magnetic shielding of the spectrometer is effective at blocking SEs generated at the spectrometer surface.

The use of tandem spectrometers is a technique unique to KATRIN and inherently comes with a background challenge. A Penning trap for electrons is formed by the electric retarding potentials of the spectrometers and the guiding magnetic field. Measurements show that the trap can produce large background rates that endanger the sensitivity of KATRIN. Simulations were performed to quantify the motion of electrons in the trap and to understand the background mechanism from positive ions and ionization electrons inside the MS.

Over the course of several measurement campaigns, the background rate due to the active inter-spectrometer Penning trap was studied in detail. Settings in the PS were modified to reduce the fill rate of the trap. However, it was discovered that pressure is the crucial parameter determining the volatility of the Penning trap. Operating at low pressures (on the order of 10^{-11} mbar) effectively eliminates the background contribution from the Penning trap and enables the spectrometers to be used at their design voltages. Long-term measurements found an upper limit on the residual background rate of 6 mcps/week (90 % C.L.) due to the Penning trap.

When combined with studies of other background sources, the work in this thesis enables a total background model for KATRIN to be developed. This background model is required in the analysis of tritium data in order to reach the best possible sensitivity to the neutrino mass.

BIBLIOGRAPHY

[1] L. M. Brown. "The idea of the neutrino." *Phys. Today*, 31(9):23–28, 1978. URL `http://dx.doi.org/10.1063/1.2995181`. 1, 2

[2] E. Fermi. "Versuch einer Theorie der β-Strahlen. I." *Z. Phys.*, 88(3–4):161–177, 1934. URL `http://dx.doi.org/10.1007/BF01351864`. 2

[3] F. L. Wilson. "Fermi's Theory of Beta Decay." *Am. J. Phys.*, 36(12):1150–1160, 1968. URL `http://dx.doi.org/10.1119/1.1974382`. 2

[4] H. Bethe and R. Peierls. "The "Neutrino"." *Nature*, 133:532, 1934. URL `http://dx.doi.org/10.1038/133532a0`. 3

[5] K. S. McFarland. "Neutrino Interactions." In *Neutrinos in particle physics, astrophysics and cosmology. Proceedings, 61st Scottish Universities Summer School in Physics, SUSSP61, St. Andrews, UK, August 8-23, 2006*, pages 65–90. 2008. URL `https://arxiv.org/abs/0804.3899`. 3

[6] D. Lindley. "Landmarks–Detecting the Elusive Neutrino." *Phys. Rev. Focus*, 19:13, 2007. URL `http://dx.doi.org/10.1103/PhysRevFocus.19.13`. 3

[7] F. Reines and C. L. Cowan. "Detection of the Free Neutrino." *Phys. Rev.*, 92:830–831, 1953. URL `http://dx.doi.org/10.1103/PhysRev.92.830`. 3

[8] C. L. Cowan et al. "Detection of the Free Neutrino: a Confirmation." *Science*, 124(3212):103–104, 1956. ISSN 0036-8075. URL `http://dx.doi.org/10.1126/science.124.3212.103`. 3

[9] F. Reines and C. L. Cowan. "The Neutrino." *Nature*, 178(4531):446–449, 1956. URL `http://dx.doi.org/10.1038/178446a0`. 3

[10] G. Danby et al. "Observation of High-Energy Neutrino Reactions and the Existence of Two Kinds of Neutrinos." *Phys. Rev. Lett.*, 9:36–44, 1962. URL `http://dx.doi.org/10.1103/PhysRevLett.9.36`. 4

[11] M. L. Perl et al. "Evidence for Anomalous Lepton Production in $e^+ - e^-$ Annihilation." *Phys. Rev. Lett.*, 35:1489–1492, 1975. URL `http://dx.doi.org/10.1103/PhysRevLett.35.1489`. 4

[12] K. Kodama et al. “Observation of tau neutrino interactions.” *Phys. Lett. B*, 504(3):218–224, 2001. ISSN 0370-2693. URL `http://dx.doi.org/10.1016/S0370-2693(01)00307-0`. 4

[13] —. “Final tau-neutrino results from the DONuT experiment.” *Phys. Rev. D*, 78:052002, 2008. URL `http://dx.doi.org/10.1103/PhysRevD.78.052002`. 5

[14] C. Patrignani et al. (Particle Data Group). “Review of Particle Physics.” *Chinese Phys. C*, 40(10):100001, 2016. URL `http://dx.doi.org/10.1088/1674-1137/40/10/100001`. 5, 8, 12, 21, 154

[15] S. Mele. “The Measurement of the Number of Light Neutrino Species at LEP.” *Adv. Ser. Direct. High Energy Phys.*, 23:89–106, 2015. URL `http://dx.doi.org/10.1142/9789814644150_0004`. 5

[16] S. Schael et al. “Precision electroweak measurements on the Z resonance.” *Phys. Rept.*, 427:257–454, 2006. URL `http://dx.doi.org/10.1016/j.physrep.2005.12.006`. 5

[17] Planck Collaboration. “Planck 2013 results. XVI. Cosmological parameters.” *Astronomy & Astrophysics*, 571:A16, 2014. URL `http://dx.doi.org/10.1051/0004-6361/201321591`. 5, 19

[18] N. Aghanim et al. “Planck 2018 results. VI. Cosmological parameters.” 2018. URL `https://arxiv.org/abs/1807.06209`. 5, 19, 20

[19] S. Mertens et al. “Sensitivity of Next-Generation Tritium Beta-Decay Experiments for keV-Scale Sterile Neutrinos.” *J. Cosmol. Astropart. Phys.*, 1502(02):020, 2015. URL `http://dx.doi.org/10.1088/1475-7516/2015/02/020`. 6

[20] A. Esmaili and O. L. G. Peres. “KATRIN Sensitivity to Sterile Neutrino Mass in the Shadow of Lightest Neutrino Mass.” *Phys. Rev.*, D85:117301, 2012. URL `http://dx.doi.org/10.1103/PhysRevD.85.117301`. 6

[21] J. P. Ellis. “TikZ-Feynman: Feynman diagrams with TikZ.” *Comput. Phys. Commun.*, 210:103–123, 2017. ISSN 0010-4655. URL `http://dx.doi.org/10.1016/j.cpc.2016.08.019`. 7

[22] G. B. Lubkin. “Nobel Prizes: to Glashow, Salam and Weinberg for Physics. . . .” *Phys. Today*, 32(12):17, 1979. URL `http://dx.doi.org/10.1063/1.2995309`. 6

[23] S. L. Glashow. “Partial Symmetries of Weak Interactions.” *Nucl. Phys.*, 22:579–588, 1961. URL `http://dx.doi.org/10.1016/0029-5582(61)90469-2`.

[24] S. Weinberg. “A Model of Leptons.” *Phys. Rev. Lett.*, 19:1264–1266, 1967. URL `http://dx.doi.org/10.1103/PhysRevLett.19.1264`.

[25] A. Salam. "Weak and Electromagnetic Interactions." *Conf. Proc.*, C680519:367–377, 1968. 6

[26] M. Goldhaber, L. Grodzins, and A. W. Sunyar. "Helicity of Neutrinos." *Phys. Rev.*, 109:1015–1017, 1958. URL `http://dx.doi.org/10.1103/PhysRev.109.1015`. 6

[27] H. Murayama. "The origin of neutrino mass." *Phys. World*, 15(5):35, 2002. URL `http://dx.doi.org/10.1088/2058-7058/15/5/36`. 6, 7, 16, 17

[28] J. C. Palathingal. "Helicity of Antineutrinos Emitted by Nuclei." *Phys. Rev. Lett.*, 24:524–526, 1970. URL `http://dx.doi.org/10.1103/PhysRevLett.24.524`. 7

[29] Borexino Collaboration. "Neutrinos from the primary proton-proton fusion process in the Sun." *Nature*, 512(7515):383–386, 2014. URL `http://dx.doi.org/10.1038/nature13702`. 8

[30] B. Cleveland et al. "Measurement of the Solar Electron Neutrino Flux with the Homestake Chlorine Detector." *Astrophys. J.*, 496(1):505, 1998. URL `http://dx.doi.org/10.1086/305343`. 8

[31] J. N. Bahcall, M. H. Pinsonneault, and G. J. Wasserburg. "Solar models with helium and heavy-element diffusion." *Rev. Mod. Phys.*, 67:781–808, 1995. URL `http://dx.doi.org/10.1103/RevModPhys.67.781`. 8

[32] C. Giunti and C. W. Kim. "Quantum mechanics of neutrino oscillations." *Found. Phys. Lett.*, 14(3):213–229, 2001. ISSN 1572-9524. URL `http://dx.doi.org/10.1023/A:1012230026160`. 9, 10, 11

[33] D. Casper. "Neutrino Oscillations." URL `http://www.ps.uci.edu/~superk/oscillation.html`. [Online; accessed 25-July-2017]. 9

[34] F. Harms. "Characterization and Minimization of Background Processes in the KATRIN Main Spectrometer." Ph.D. thesis, Karlsruher Institut für Technologie, 2015. URL `http://dx.doi.org/10.5445/IR/1000050027`. 9, 11, 35, 43, 45, 46, 50, 57, 60, 73, 92, 93, 94, 95, 98, 99, 106, 113, 126, 128, 194, 234, 236

[35] Wikipedia. "Neutrino oscillation — Wikipedia, The Free Encyclopedia.", 2017. URL `https://en.wikipedia.org/w/index.php?title=Neutrino_oscillation&oldid=792034944`. [Online; accessed 25-August-2017]. 12

[36] B. Pontecorvo. "Neutrino Experiments and the Problem of Conservation of Leptonic Charge." *Sov. Phys. JETP*, 26:984–988, 1968. URL `http://www.jetp.ac.ru/cgi-bin/e/index/e/26/5/p984?a=list`. [Zh. Eksp. Teor. Fiz.53,1717(1967)]. 11

[37] Z. Maki, M. Nakagawa, and S. Sakata. "Remarks on the Unified Model of Elementary Particles." *Prog. Theor. Phys.*, 28(5):870–880, 1962. URL `http://dx.doi.org/10.1143/PTP.28.870`. 11

[38] Y. Fukuda et al. "Evidence for Oscillation of Atmospheric Neutrinos." *Phys. Rev. Lett.*, 81:1562–1567, 1998. URL `http://dx.doi.org/10.1103/PhysRevLett.81.1562`. 13

[39] —. "Measurement of a small atmospheric ν_μ/ν_e ratio." *Phys. Lett. B*, 433(1):9–18, 1998. ISSN 0370-2693. URL `http://dx.doi.org/10.1016/S0370-2693(98)00476-6`. 13

[40] A. Bellerive et al. "The Sudbury Neutrino Observatory." *Nucl. Phys. B*, 908:30–51, 2016. ISSN 0550-3213. URL `http://dx.doi.org/10.1016/j.nuclphysb.2016.04.035`. 13, 14

[41] Aharmim, B. et al. (SNO Collaboration). "Combined analysis of all three phases of solar neutrino data from the Sudbury Neutrino Observatory." *Phys. Rev. C*, 88:025501, 2013. URL `http://dx.doi.org/10.1103/PhysRevC.88.025501`. 13, 14

[42] M. Tanabashi et al. "Review of Particle Physics." *Phys. Rev. D*, 98:030001, 2018. URL `http://dx.doi.org/10.1103/PhysRevD.98.030001`. 14, 15, 16, 18, 117

[43] A. M. Serenelli et al. "New Solar Composition: The Problem with Solar Models Revisited." *Astrophys. J. Lett.*, 705(2):L123, 2009. URL `http://dx.doi.org/10.1088/0004-637X/705/2/L123`. 14

[44] B. Aharmim et al. "An Independent Measurement of the Total Active B-8 Solar Neutrino Flux Using an Array of He-3 Proportional Counters at the Sudbury Neutrino Observatory." *Phys. Rev. Lett.*, 101:111301, 2008. URL `http://dx.doi.org/10.1103/PhysRevLett.101.111301`. 14

[45] K. Eguchi et al. "First Results from KamLAND: Evidence for Reactor Antineutrino Disappearance." *Phys. Rev. Lett.*, 90:021802, 2003. URL `http://dx.doi.org/10.1103/PhysRevLett.90.021802`. 15

[46] M. H. Ahn et al. "Indications of Neutrino Oscillation in a 250 km Long-Baseline Experiment." *Phys. Rev. Lett.*, 90:041801, 2003. URL `http://dx.doi.org/10.1103/PhysRevLett.90.041801`. 15

[47] D. G. Michael et al. "Observation of Muon Neutrino Disappearance with the MINOS Detectors in the NuMI Neutrino Beam." *Phys. Rev. Lett.*, 97:191801, 2006. URL `http://dx.doi.org/10.1103/PhysRevLett.97.191801`. 15

[48] F. P. An et al. "Observation of electron-antineutrino disappearance at Daya Bay." *Phys. Rev. Lett.*, 108:171803, 2012. URL `http://dx.doi.org/10.1103/PhysRevLett.108.171803`. 15

[49] P. Adamson et al. "First Measurement of Electron Neutrino Appearance in NOvA." *Phys. Rev. Lett.*, 116:151806, 2016. URL `http://dx.doi.org/10.1103/PhysRevLett.116.151806`. 15

[50] K. Abe et al. "Measurements of neutrino oscillation in appearance and disappearance channels by the T2K experiment with 6.6×10^{20} protons on target." *Phys. Rev. D*, 91:072010, 2015. URL `http://dx.doi.org/10.1103/PhysRevD.91.072010`. 15

[51] R. Acciarri et al. " Long-Baseline Neutrino Facility (LBNF) and Deep Underground Neutrino Experiment (DUNE) Conceptual Design Report Volume 2: The Physics Program for DUNE at LBNF." 2015. URL `https://arxiv.org/abs/1512.06148`. 15

[52] E. Siegal. "The Little Bit of Dark Matter We Know.", 2013. URL `http://scienceblogs.com/startswithabang/2013/09/18/the-little-bit-of-dark-matter-we-know/`. [Online; accessed 27-July-2017]. 16

[53] A. de Gouvêa. "Neutrino Mass Models." *Ann. Rev. Nucl. Part. Sci.*, 66(1):197–217, 2016. URL `http://dx.doi.org/10.1146/annurev-nucl-102115-044600`. 17

[54] P. Minkowski. "$\mu \to e\gamma$ at a Rate of One Out of 10^9 Muon Decays?" *Phys. Lett.*, 67B:421–428, 1977. URL `http://dx.doi.org/10.1016/0370-2693(77)90435-X`. 17

[55] R. N. Mohapatra and G. Senjanović. "Neutrino Mass and Spontaneous Parity Nonconservation." *Phys. Rev. Lett.*, 44:912–915, 1980. URL `http://dx.doi.org/10.1103/PhysRevLett.44.912`. 17

[56] A. Nucciotti. "The use of low temperature detectors for direct measurements of the mass of the electron neutrino." *Adv. High Energy Phys.*, 2016:9153024, 2016. URL `http://dx.doi.org/10.1155/2016/9153024`. 18, 30, 31

[57] Creative Commons Corporation. "Attribution 4.0 International." URL `https://creativecommons.org/licenses/by/4.0/legalcode`. 18

[58] A. Yu. Smirnov. "The MSW effect and matter effects in neutrino oscillations." *Phys. Scripta*, T121:57–64, 2005. URL `http://dx.doi.org/10.1088/0031-8949/2005/T121/008`. 18

[59] P. F. De Salas et al. "Neutrino Mass Ordering from Oscillations and Beyond: 2018 Status and Future Prospects." *Front. Astron. Space Sci.*, 5:36, 2018. URL `http://dx.doi.org/10.3389/fspas.2018.00036`. 18

[60] I. Esteban et al. "Global analysis of three-flavour neutrino oscillations: synergies and tensions in the determination of $\theta_{23}, \delta_{\mathrm{CP}}$, and the mass ordering." *J. High Energy Phys.*, 01:106, 2019. URL `http://dx.doi.org/10.1007/JHEP01(2019)106`. 18

[61] Y. Kudenko. "Neutrino detectors for oscillation experiments." *J. Instrum.*, 12(06):C06003, 2017. URL `http://dx.doi.org/10.1088/1748-0221/12/06/C06003`. 18

[62] A. A. Penzias and R. W. Wilson. "A Measurement of Excess Antenna Temperature at 4080 Mc/s." *Astrophys. J.*, 142:419–421, 1965. URL `http://dx.doi.org/10.1086/148307`. 19

[63] K. Abazajian et al. "Neutrino physics from the cosmic microwave background and large scale structure." *Astropart. Phys.*, 63(Supplement C):66–80, 2015. ISSN 0927-6505. URL `http://dx.doi.org/10.1016/j.astropartphys.2014.05.014`. Dark Energy and CMB. 19

[64] A. G. Riess et al. "New Parallaxes of Galactic Cepheids from Spatially Scanning the Hubble Space Telescope : Implications for the Hubble Constant." *Astrophys. J.*, 855(2):136, 2018. URL `http://dx.doi.org/10.3847/1538-4357/aaadb7`. 20

[65] B. Pritychenko. "Systematics of Evaluated Half-Lives of Double-Beta Decay." *Nucl. Data Sheets*, 120:102–105, 2014. URL `http://dx.doi.org/10.1016/j.nds.2014.07.018`. 20

[66] A. Gando et al. "Search for Majorana Neutrinos Near the Inverted Mass Hierarchy Region with KamLAND-Zen." *Phys. Rev. Lett.*, 117:082503, 2016. URL `http://dx.doi.org/10.1103/PhysRevLett.117.082503`. 21

[67] C. Alduino et al. "First Results from CUORE: A Search for Lepton Number Violation via $0\nu\beta\beta$ Decay of ^{130}Te." *Phys. Rev. Lett.*, 120(13):132501, 2018. URL `http://dx.doi.org/10.1103/PhysRevLett.120.132501`. 21

[68] C. E. Aalseth et al. "Search for Neutrinoless Double-β Decay in ^{76}Ge with the MAJORANA DEMONSTRATOR." *Phys. Rev. Lett.*, 120(13):132502, 2018. URL `http://dx.doi.org/10.1103/PhysRevLett.120.132502`. 21, 51

[69] M. Agostini et al. "Improved Limit on Neutrinoless Double-β Decay of ^{76}Ge from GERDA Phase II." *Phys. Rev. Lett.*, 120(13):132503, 2018. URL `http://dx.doi.org/10.1103/PhysRevLett.120.132503`. 21

[70] T. J. Loredo and D. Q. Lamb. "Bayesian analysis of neutrinos observed from supernova SN 1987A." *Phys. Rev. D*, 65:063002, 2002. URL `http://dx.doi.org/10.1103/PhysRevD.65.063002`. 21, 22

[71] E. Otten and C. Weinheimer. "Neutrino mass limit from tritium β decay." *Rep. Prog. Phys.*, 71(8):086201, 2008. URL `http://dx.doi.org/10.1088/0034-4885/71/8/086201`. 22, 23, 25, 26, 171

[72] G. Pagliaroli, F. Rossi-Torres, and F. Vissani. "Neutrino mass bound in the standard scenario for supernova electronic antineutrino emission." *Astropart. Phys.*, 33(5–6):287 – 291, 2010. ISSN 0927-6505. URL `http://dx.doi.org/10.1016/j.astropartphys.2010.02.007`. 22, 155

[73] G. Drexlin et al. "Current Direct Neutrino Mass Experiments." *Adv. High Energy Phys.*, 2013:39, 2013. URL `http://dx.doi.org/10.1155/2013/293986`. 22, 26, 28, 33, 36, 88

[74] KATRIN collaboration. "KATRIN Design Report." *FZKA scientific report*, 7090, 2005. URL `http://bibliothek.fzk.de/zb/berichte/FZKA7090.pdf`. 22, 23, 25, 26, 30, 34, 35, 36, 37, 41, 43, 45, 55, 59, 90, 132, 148

[75] M. Kleesiek et al. "β-Decay Spectrum, Response Function and Statistical Model for Neutrino Mass Measurements with the KATRIN Experiment." 2018. URL `https://arxiv.org/abs/1806.00369`. 25, 54

[76] M. Kleesiek. "A data-analysis and sensitivity-optimization framework for the KATRIN experiment." Ph.D. thesis, Karlsruher Institut für Technologie, 2014. URL `http://nbn-resolving.org/urn:nbn:de:swb:90-433013`. 26, 51, 53, 55

[77] G. Beamson, H. Porter, and D. Turner. "The collimating and magnifying properties of a superconducting field photoelectron spectrometer." *J. Phys. E: Sci. Instrum.*, 13(1):64, 1980. URL `http://dx.doi.org/10.1088/0022-3735/13/1/018`. 27

[78] V. Lobashev and P. Spivak. "A method for measuring the electron antineutrino rest mass." *Nucl. Instrum. Methods Phys. Res. A*, 240(2):305–310, 1985. URL `http://dx.doi.org/10.1016/0168-9002(85)90640-0`.

[79] A. Picard et al. "A solenoid retarding spectrometer with high resolution and transmission for keV electrons." *Nucl. Instrum. Methods Phys. Res. B*, 63(3):345–358, 1992. URL `http://dx.doi.org/10.1016/0168-583X(92)95119-C`. 27

[80] N. Wandkowsky. "Study of background and transmission properties of the KATRIN spectrometers." Ph.D. thesis, Karlsruher Institut für Technologie, 2013. URL `http://digbib.ubka.uni-karlsruhe.de/volltexte/1000036631`. 29, 92, 94, 95, 97, 118, 125, 159, 180

[81] C. Kraus et al. "Final results from phase II of the Mainz neutrino mass search in tritium β decay." *Eur. Phys. J. C*, 40(4):447–468, 2005. ISSN 1434-6052. URL `http://dx.doi.org/10.1140/epjc/s2005-02139-7`. 28, 30, 117

[82] V. N. Aseev et al. "Upper limit on the electron antineutrino mass from the Troitsk experiment." *Phys. Rev. D*, 84:112003, 2011. URL `http://dx.doi.org/10.1103/PhysRevD.84.112003`. 28, 30

[83] M. Galeazzi et al. “End-point energy and half-life of the ^{187}Re β decay.” *Phys. Rev. C*, 63:014302, 2000. URL `http://dx.doi.org/10.1103/PhysRevC.63.014302`. 31

[84] M. Sisti et al. “New limits from the Milano neutrino mass experiment with thermal microcalorimeters.” *Nucl. Instrum. Methods Phys. Res. A*, A520:125–131, 2004. URL `http://dx.doi.org/10.1016/j.nima.2003.11.273`. 31

[85] E. Ferri et al. “The Status of the MARE Experiment with ^{187}Re and ^{163}Ho Isotopes.” *Phys. Procedia*, 61:227–231, 2015. ISSN 1875-3892. URL `http://dx.doi.org/10.1016/j.phpro.2014.12.037`. 31

[86] C. Hassel et al. “Recent Results for the ECHo Experiment.” *J. Low. Temp. Phys.*, 184(3):910–921, 2016. ISSN 1573-7357. URL `http://dx.doi.org/10.1007/s10909-016-1541-9`. 31

[87] L. Gastaldo et al. “The electron capture in^{163}Ho experiment – ECHo.” *Eur. Phys. J. ST*, 226(8):1623–1694, 2017. URL `http://dx.doi.org/10.1140/epjst/e2017-70071-y`. 31

[88] B. Alpert et al. “HOLMES.” *Eur. Phys. J. C*, 75(3):112, 2015. ISSN 1434-6052. URL `http://dx.doi.org/10.1140/epjc/s10052-015-3329-5`. 31

[89] A. Giachero et al. “Measuring the electron neutrino mass with improved sensitivity: the HOLMES experiment.” *J. Instrum.*, 12(02):C02046, 2017. URL `http://dx.doi.org/10.1088/1748-0221/12/02/C02046`. 31

[90] A. Nucciotti et al. “Status of the HOLMES Experiment to Directly Measure the Neutrino Mass.” *J. Low. Temp. Phys.*, 2018. URL `http://dx.doi.org/10.1007/s10909-018-2025-x`. 31

[91] A. Ashtari Esfahani et al. “Determining the neutrino mass with cyclotron radiation emission spectroscopy—Project 8.” *J. Phys.*, G44(5):054004, 2017. URL `http://dx.doi.org/10.1088/1361-6471/aa5b4f`. 32

[92] D. M. Asner et al. “Single-electron detection and spectroscopy via relativistic cyclotron radiation.” *Phys. Rev. Lett.*, 114:162501, 2015. URL `http://dx.doi.org/10.1103/PhysRevLett.114.162501`. 32

[93] L. Kuckert. “The windowless gaseous tritium source of the KATRIN experiment – characterisation of gas dynamical and plasma properties.” Ph.D. thesis, Karlsruher Institut für Technologie, 2016. URL `http://dx.doi.org/10.5445/IR/1000065077`. 34, 37

[94] F. Priester, M. Sturm, and B. Bornschein. “Commissioning and detailed results of KATRIN inner loop tritium processing system at Tritium Laboratory Karlsruhe.” *Vacuum*, 116:42–47, 2015. URL `http://dx.doi.org/10.1016/j.vacuum.2015.02.030`. 34

[95] S. Welte et al. “Experimental Performance Test of Key Components of the KATRIN Outer Tritium Loop.” *Fusion Sci. Technol.*, 71(3):316–320, 2017. URL `http://dx.doi.org/10.1080/15361055.2017.1291233`. 34

[96] M. Schlösser et al. “Accurate calibration of the laser Raman system for the Karlsruhe Tritium Neutrino Experiment.” *J. Mol. Struct.*, 1044(0):61–66, 2013. URL `http://dx.doi.org/10.1016/j.molstruc.2012.11.022`. 34

[97] M. Arenz et al. “The KATRIN superconducting magnets: overview and first performance results.” *J. Instrum.*, 13(08):T08005, 2018. URL `http://dx.doi.org/10.1088/1748-0221/13/08/T08005`. 35, 41, 48

[98] L. Kuckert et al. “Modelling of gas dynamical properties of the KATRIN tritium source and implications for the neutrino mass measurement.” *Vacuum*, 158:195–205, 2018. URL `http://dx.doi.org/10.1016/j.vacuum.2018.09.036`. 35

[99] A. Marsteller. “Measurement of Temperature Stability and Homogeneity of the KATRIN WGTS Cryostat.” Master thesis, Karlsruher Institut für Technologie, 2017. URL `http://www.katrin.kit.edu/publikationen/mth_marsteller.pdf`. 35, 36

[100] S. Grohmann et al. “The thermal behaviour of the tritium source in KATRIN.” *Cryogenics*, 55-56(0):5–11, 2013. URL `http://dx.doi.org/10.1016/j.cryogenics.2013.01.001`. 35

[101] A. Jansen. “The cryogenic pumping section of the KATRIN experiment - design studies and experiments for the commissioning.” Ph.D. thesis, Karlsruher Institut für Technologie, 2015. URL `http://nbn-resolving.org/urn:nbn:de:swb:90-471467`. 36, 37, 38

[102] S. Lukić et al. “Measurement of the gas-flow reduction factor of the KATRIN DPS2-F differential pumping section.” *Vacuum*, 86(8):1126–1133, 2012. URL `http://dx.doi.org/10.1016/j.vacuum.2011.10.017`. 36

[103] M. Arenz et al. “First transmission of electrons and ions through the KATRIN beamline.” *J. Instrum.*, 13(04):P04020, 2018. URL `http://dx.doi.org/10.1088/1748-0221/13/04/P04020`. 36, 37, 38, 39, 46, 55, 89, 90

[104] C. Röttele. “Results of the first Cool-down of the KATRIN Cryogenic Pumping Section.” *J. Phys. Conf. Ser.*, 888(1):012228, 2017. URL `http://dx.doi.org/10.1088/1742-6596/888/1/012228`. 37

[105] F. Friedel et al. “Time-dependent simulation of the flow reduction of D_2 and T_2 in the KATRIN experiment.” *Vacuum*, 159:161–172, 2019. ISSN 0042-207X. URL `http://dx.doi.org/10.1016/j.vacuum.2018.10.002`. 37

[106] S. Bauer. “Energy calibration and stability monitoring of the KATRIN experiment.” Ph.D. thesis, Westfälische Wilhelms-Universität Münster, 2014. URL `http://nbn-resolving.de/urn:nbn:de:hbz:6-04329567654`. 37

[107] E. Ellinger et al. “Monitoring the KATRIN source properties within the beamline.” *J. Phys. Conf. Ser.*, 888(1):012229, 2017. URL `http://dx.doi.org/10.1088/1742-6596/888/1/012229`. 38

[108] M. T. Hackenjos. “Katrin - first light commissioning and modelling of the beam line.” Ph.D. thesis, Karlsruher Institut für Technologie, 2017. URL `http://dx.doi.org/10.5445/IR/1000078933`. 38, 39, 191

[109] M. Babutzka. “Design and development for the Rearsection of the KATRIN experiment.” Ph.D. thesis, Karlsruher Institut für Technologie, 2014. URL `http://nbn-resolving.org/urn:nbn:de:swb:90-455986`. 38

[110] J. Behrens et al. “A pulsed, mono-energetic and angular-selective UV photo-electron source for the commissioning of the KATRIN experiment.” *Eur. Phys. J. C*, 77(6):410, 2017. URL `http://dx.doi.org/10.1140/epjc/s10052-017-4972-9`. 39, 110

[111] M. Schöppner. “A Prototype Ion Source for the Functionality Test of the KATRIN Transport Section.” Diploma thesis, Westfälische Wilhelms-Universität Münster, 2008. URL `http://www.uni-muenster.de/Physik.KP/AGWeinheimer/theses/Diplom_Michael_Schoeppner.pdf`. 39

[112] M. Zoll. “Development of tools and methods for KATRIN DPS2-F test experiments.” Diploma thesis, Universität Karlsruhe (TH), 2009. URL `http://www.katrin.kit.edu/publikationen/dth-zoll.pdf`.

[113] S. Lukić et al. “Ion source for tests of ion behavior in the Karlsruhe tritium neutrino experiment beam line.” *Rev. Sci. Instrum.*, 82(1), 2011. URL `http://dx.doi.org/10.1063/1.3504372`. 39

[114] F. M. Fränkle. “Background Investigations of the KATRIN Pre-Spectrometer.” Ph.D. thesis, Karlsruher Institut für Technologie, 2010. URL `http://nbn-resolving.org/urn:nbn:de:swb:90-193929`. 39, 40, 41, 42, 91, 149, 203

[115] S. Görhardt. “Background Reduction Methods and Vacuum Technology at the KATRIN Spectrometers.” Ph.D. thesis, Karlsruher Institut für Technologie, 2014. URL `http://nbn-resolving.org/urn:nbn:de:swb:90-380506`. 41, 42, 43, 96, 203

[116] M. Prall et al. "The KATRIN pre-spectrometer at reduced filter energy." *New J. Phys.*, 14(7):073054, 2012. URL `http://dx.doi.org/10.1088/1367-2630/14/7/073054`. 41, 89

[117] M. Arenz et al. (KATRIN Collaboration). "Commissioning of the vacuum system of the KATRIN Main Spectrometer." *J. Instrum.*, 11(04):P04011, 2016. URL `http://dx.doi.org/10.1088/1748-0221/11/04/P04011`. 41, 43, 44, 45, 46, 92, 93, 161, 166

[118] F. Glück et al. "Electromagnetic design of the large-volume air coil system of the KATRIN experiment." *New J. Phys.*, 15:083025, 2013. URL `http://dx.doi.org/10.1088/1367-2630/15/8/083025`. 43, 44, 233

[119] M. Erhard et al. "Technical design and commissioning of the KATRIN large-volume air coil system." *J. Instrum.*, 13(02):P02003, 2018. URL `http://dx.doi.org/10.1088/1748-0221/13/02/P02003`. 43, 44

[120] Creative Commons Corporation. "Attribution 3.0 Unported." URL `https://creativecommons.org/licenses/by/3.0/legalcode`. 44, 89, 101, 103

[121] K. Valerius. "The wire electrode system for the KATRIN main spectrometer." *Prog. Part. Nucl. Phys.*, 64:291–293, 2010. URL `http://dx.doi.org/10.1016/j.ppnp.2009.12.032`. 45, 93

[122] M. Kraus. "Energy-Scale Systematics at the KATRIN Main Spectrometer." Ph.D. thesis, Karlsruher Institut für Technologie, 2016. URL `http://nbn-resolving.org/urn:nbn:de:swb:90-544471`. 45, 46

[123] J. S. Schwarz. "The Detector System of the KATRIN Experiment - Implementation and First Measurements with the Spectrometer." Ph.D. thesis, Karlsruher Institut für Technologie, 2014. URL `http://nbn-resolving.org/urn:nbn:de:swb:90-427724`. 46, 47, 50, 52, 53, 57, 59, 60, 62, 63, 64, 83, 92, 111, 192, 194

[124] M. Arenz et al. "Calibration of high voltages at the ppm level by the difference of $^{83\mathrm{m}}$Kr conversion electron lines at the KATRIN experiment." *Eur. Phys. J.*, C78(5):368, 2018. URL `http://dx.doi.org/10.1140/epjc/s10052-018-5832-y`. 45, 46

[125] T. Thummler, R. Marx, and C. Weinheimer. "Precision high voltage divider for the KATRIN experiment." *New J. Phys.*, 11:103007, 2009. URL `http://dx.doi.org/10.1088/1367-2630/11/10/103007`. 45

[126] S. Bauer et al. "Next generation KATRIN high precision voltage divider for voltages up to 65kV." *J. Instrum.*, 8:P10026, 2013. URL `http://dx.doi.org/10.1088/1748-0221/8/10/P10026`. 45

[127] M. Erhard et al. "High-voltage monitoring with a solenoid retarding spectrometer at the KATRIN experiment." *J. Instrum.*, 9:P06022, 2014. URL `http://dx.doi.org/10.1088/1748-0221/9/06/P06022`. 46

[128] M. Zbořil et al. "Ultra-stable implanted ^{83}Rb/$^{83\mathrm{m}}$Kr electron sources for the energy scale monitoring in the KATRIN experiment." *J. Instrum.*, 8(03):P03009, 2013. URL `http://dx.doi.org/10.1088/1748-0221/8/03/P03009`. 46

[129] M. Slezák. "Monitoring of the energy scale in the KATRIN neutrino experiment." Ph.D. thesis, Czech Academy of Sciences, 2015. URL `http://www.katrin.kit.edu/publikationen/phd-Martin_Slezak.pdf`. 46

[130] J. Amsbaugh et al. "Focal-plane detector system for the KATRIN experiment." *Nucl. Instrum. Methods Phys. Res. A*, 778:40–60, 2015. URL `http://dx.doi.org/10.1016/j.nima.2014.12.116`. 47, 48, 49, 50, 51, 53, 59, 62, 78, 111, 143

[131] V. T. Jordanov and G. F. Knoll. "Digital synthesis of pulse shapes in real time for high resolution radiation spectroscopy." *Nucl. Instrum. Methods Phys. Res. A*, 345(2):337 – 345, 1994. ISSN 0168-9002. URL `http://dx.doi.org/10.1016/0168-9002(94)91011-1`. 50

[132] M. Howe et al. "Sudbury Neutrino Observatory neutral current detector acquisition software overview." *IEEE Trans. Nucl. Sci.*, 51(3):878 – 883, 2004. URL `http://dx.doi.org/10.1109/TNS.2004.829527`. See also `http://orca.physics.unc.edu/`. 50

[133] Center for Experimental Nuclear Physics and Astrophysics, University of Washington. "Annual Report.", 2013. URL `https://www.npl.washington.edu/cenpa-annual-reports`. 51, 70

[134] —. "Annual Report.", 2014. URL `https://www.npl.washington.edu/cenpa-annual-reports`. 51, 70

[135] R. Brun and F. Rademakers. "ROOT: An object oriented data analysis framework." *Nucl. Instrum. Meth.*, A389:81–86, 1997. URL `http://dx.doi.org/10.1016/S0168-9002(97)00048-X`. 52, 165, 168

[136] J. Schwarz. "The Focal-Plane Detector System Of KATRIN.", 2013. Institute presentation. 52

[137] E. L. Martin. "Electron Detection Systems for KATRIN Detector and Spectrometer Section." Ph.D. thesis, University of Washington, 2017. URL `http://hdl.handle.net/1773/40285`. 53, 72, 75

[138] H. Seitz-Moskaliuk. "Characterisation of the KATRIN tritium source and evaluation of systematic effects." Ph.D. thesis, Karlsruher Institut für Technologie, 2019. URL `http://dx.doi.org/10.5445/IR/1000090748`. 53

[139] S. Mertens. "Study of background processes in the electrostatic spectrometers of the KATRIN experiment." Ph.D. thesis, Karlsruher Institut für Technologie, 2012. URL `http://digbib.ubka.uni-karlsruhe.de/volltexte/1000027058`. 55, 90, 92, 96, 97, 152

[140] B. Bornschein et al. "The Five Phases to Standard Tritium Operation of KATRIN." *Fusion Sci. Technol.*, 71(3):231–235, 2017. URL `http://dx.doi.org/10.1080/15361055.2016.1273703`. 56

[141] F. Block. "Characterisation of the Background in the KATRIN Experiment." Master thesis, Karlsruher Institut für Technologie, 2018. URL `http://www.katrin.kit.edu/publikationen/mth_fblock.pdf`. 57, 99, 113, 194, 195, 206

[142] K. Wierman. "Studies of charge accumulation in the KATRIN main spectrometer." Ph.D. thesis, University of North Carolina at Chapel Hill, 2016. URL `https://cdr.lib.unc.edu/record/uuid:116cdd53-957b-4b40-bd8f-0203556ee1b4`. 59

[143] S. Enomoto, J. Canright, and P. Doe. "Performance of the New Detector Veto and SDS3-Christmas Muon Analysis.", 2018. Internal presentation. 59, 62

[144] Center for Experimental Nuclear Physics and Astrophysics, University of Washington. "Annual Report.", 2017. URL `https://www.npl.washington.edu/cenpa-annual-reports`. 59

[145] A. Seher. "Characterization Measurements of the KATRIN Focal-Plane Detector System." Master thesis, Karlsruher Institut für Technologie, 2016. 60, 64, 73

[146] S. Enomoto. "Data-Driven Noise Investigation.", 2016. Internal presentation. 62, 66, 69, 71, 72

[147] H. Spieler. *Semiconductor Detector Systems*. Oxford University Press, 2005. ISBN 978-0-19-852784-8. URL `https://app.knovel.com/hotlink/toc/id:kpSDS00001/semiconductor-detector/semiconductor-detector`. 64, 67

[148] V. Barzdėnas and R. Navickas. "Leakage Current Compensation for the 0.13 μm CMOS Charge Sensitive Preamplifier." *Elektronika ir Elektrotechnika*, 77(5), 2015. ISSN 2029-5731. URL `http://eejournal.ktu.lt/index.php/elt/article/view/10734`. 64

[149] W. Bludau, A. Onton, and W. Heinke. "Temperature dependence of the band gap of silicon." *J. Appl. Phys.*, 45(4):1846–1848, 1974. URL `http://dx.doi.org/10.1063/1.1663501`. 67

[150] S. Enomoto. "FPD Noise Analysis.", 2013. Internal presentation. 71, 83

[151] B. A. VanDevender et al. "Performance of a TiN-coated monolithic silicon pin-diode array under mechanical stress." *Nucl. Instrum. Meth.*, A673:46–50, 2012. URL `http://dx.doi.org/10.1016/j.nima.2012.01.033`. 83

[152] Center for Experimental Nuclear Physics and Astrophysics, University of Washington. "Annual Report.", 2018. URL `https://www.npl.washington.edu/cenpa-annual-reports`. 84

[153] M. Klein and F. Glück. "Tritium ion blocking and detection in the KATRIN experiment." *J. Phys. Conf. Ser.*, 888(1):012073, 2017. URL `http://dx.doi.org/10.1088/1742-6596/888/1/012073`. 88, 89

[154] M. Klein. "Tritium ions in KATRIN – Detection, blocking and removal." Ph.D. thesis, Karlsruher Institut für Technologie, 2018. 88, 191

[155] F. Fränkle et al. "Penning discharge in the KATRIN pre-spectrometer." *J. Instrum.*, 9(7):P07028, 2014. URL `http://dx.doi.org/10.1088/1748-0221/9/07/P07028`. 91, 147, 149

[156] M. Zacher. "High-field electrodes design and an angular-selective photoelectron source for the KATRIN spectrometers." Ph.D. thesis, Westfälische Wilhelms-Universität Münster, 2015. 91

[157] B. Leiber. "Investigations of background due to secondary electron emission in the KATRIN-experiment." Ph.D. thesis, Karlsruher Institut für Technologie, 2014. URL `http://nbn-resolving.org/urn:nbn:de:swb:90-424154`. 91, 92, 105, 107, 117, 118, 120, 121

[158] K. Altenmüller et al. "Gamma-induced background in the KATRIN main spectrometer." 2019. URL `https://arxiv.org/abs/1903.00563`. 92, 131, 136, 140

[159] M. A. Furman and M. T. F. Pivi. "Probabilistic model for the simulation of secondary electron emission." *Phys. Rev. ST Accel. Beams*, 5:124404, 2002. URL `http://dx.doi.org/10.1103/PhysRevSTAB.5.124404`. 92, 107, 111

[160] M. Arenz et al. "Reduction of stored-particle background by a magnetic pulse method at the KATRIN experiment." *Eur. Phys. J.*, C78(9):778, 2018. URL `http://dx.doi.org/10.1140/epjc/s10052-018-6244-8`. 94, 97, 98

[161] J. Barrett et al. "Results of the first KATRIN SDS measurement phase.", 2014. Internal report. 95

[162] S. Mertens et al. "Background due to stored electrons following nuclear decays in the KATRIN spectrometers and its impact on the neutrino mass sensitivity." *Astropart. Phys.*, 41:52–62, 2013. URL `http://dx.doi.org/10.1016/j.astropartphys.2012.10.005`. 94

[163] N. Wandkowsky et al. “Validation of a model for Radon-induced background processes in electrostatic spectrometers.” *J. Phys.*, G40:085102, 2013. URL `http://dx.doi.org/10.1088/0954-3899/40/8/085102`.

[164] KATRIN collaboration. “Radon-Induced Stored-Particle Background in the KATRIN Main Spectrometer.” In preparation. 94, 96

[165] F. Fränkle et al. “Radon induced background processes in the KATRIN pre-spectrometer.” *Astropart. Phys.*, 35(3):128–134, 2011. URL `http://dx.doi.org/10.1016/j.astropartphys.2011.06.009`. 94

[166] N. Wandkowsky et al. “Modeling of electron emission processes accompanying radon-α-decays within electrostatic spectrometers.” *New J. Phys.*, 15(8):083040, 2013. URL `http://dx.doi.org/10.1088/1367-2630/15/8/083040`. 95

[167] S. Mertens et al. “Stochastic heating by ECR as a novel means of background reduction in the KATRIN spectrometers.” *J. Instrum.*, 7:P08025, 2012. URL `http://dx.doi.org/doi:10.1088/1748-0221/7/08/P08025`. 97

[168] J. D. Behrens. “Design and commissioning of a mono-energetic photoelectron source and active background reduction by magnetic pulse at the KATRIN spectrometers.” Ph.D. thesis, Westfälische Wilhelms-Universität Münster, 2016. URL `https://www.uni-muenster.de/imperia/md/content/physik_kp/agweinheimer/theses/phd-behrens.pdf`. 97, 105, 110

[169] D. F. R. Hilk. “Electric field simulations and electric dipole investigations at the KATRIN main spectrometer.” Ph.D. thesis, Karlsruhe Institut für Technologie, 2016. URL `http://nbn-resolving.org/urn:nbn:de:swb:90-658697`. 97, 98

[170] D. F. Hinz. “Ionisation mechanisms of ^{206}Pb induced Rydberg atoms.” Master thesis, Karlsruher Institut für Technologie, 2018. URL `http://www.katrin.kit.edu/publikationen/mth-hinz.pdf`. 98, 113

[171] N. Trost. “Modeling and measurement of Rydberg-State mediated Background at the KATRIN Main Spectrometer.” Ph.D. thesis, Karlsruher Institut für Technologie, 2018. URL `http://dx.doi.org/10.5445/IR/1000090450`. 98

[172] W.-J. Baek. “Investigation of background processes of ions and Rydberg atoms in the KATRIN spectrometers.” Master thesis, Karlsruher Institut für Technologie, 2017. URL `http://www.katrin.kit.edu/publikationen/mth-baek.pdf`. 98, 99, 103, 166, 168, 181

[173] J. Hempfling. “Study on the Impact of Radon Decay Products on the KATRIN Background Level.” Bachelor thesis, Karlsruher Institut für Technologie, 2017. 99

[174] D. Furse et al. “Kassiopeia: A Modern, Extensible C++ Particle Tracking Package.” *New J. Phys.*, 19(5):053012, 2017. URL `http://dx.doi.org/10.1088/1367-2630/aa6950`. 99, 101, 102, 103, 159, 180

[175] T. Corona. “Methodology and application of high performance electrostatic field simulation in the KATRIN experiment.” Ph.D. thesis, University of North Carolina at Chapel Hill, 2014. URL `https://cdr.lib.unc.edu/record/uuid:6f44a9c2-f053-404a-b726-b960d5772619`. 100

[176] S. Groh. “Modeling of the response function and measurement of transmission properties of the KATRIN experiment.” Ph.D. thesis, Karlsruher Institut für Technologie, 2015. URL `http://nbn-resolving.org/urn:nbn:de:swb:90-465464`. 102

[177] A. Müller. “Investigation of the secondary electron emission characteristics of the KATRIN main spectrometer.” Master thesis, Karlsruher Institut für Technologie, 2016. URL `http://www.katrin.kit.edu/publikationen/mth_mueller_axel.pdf`. 105, 113, 126, 131, 234, 236

[178] M. G. Erhard. “Influence of the magnetic field on the transmission characteristics and neutrino mass systematic of the KATRIN experiment.” Ph.D. thesis, Karlsruher Institut für Technologie, 2016. URL `http://doi.org/10.5445/IR/1000065003`. 105

[179] iseg Spezialelektronik GmbH, Germany. “EHS High Voltage Power Supply series: Technical documentation, version 2.2.”, 2018. URL `https://www.iseg-hv.com/files/media/iseg_datasheet_EHS_en_22.pdf`. [Online; accessed 20-Sept-2018]. 106

[180] M. S. Chung and T. E. Everhart. “Simple calculation of energy distribution of low-energy secondary electrons emitted from metals under electron bombardment.” *J. Appl. Phys.*, 45(2):707–709, 1974. URL `http://dx.doi.org/10.1063/1.1663306`. 109

[181] H. Seiler. “Secondary electron emission in the scanning electron microscope.” *J. Appl. Phys.*, 54(11):R1–R18, 1983. URL `http://dx.doi.org/10.1063/1.332840`. 111

[182] D. C. Joy, M. S. Prasad, and H. M. Meyer. “Experimental secondary electron spectra under SEM conditions.” *J. Microscopy*, 215(1):77–85, 2004. ISSN 1365-2818. URL `http://dx.doi.org/10.1111/j.0022-2720.2004.01345.x`. 109

[183] D. W. Kim et al. “Evaluation of the creep–fatigue damage mechanism of Type 316L and Type 316LN stainless steel.” *Int. J. Press. Vessels Pip.*, 85(6):378–384, 2008. ISSN 0308-0161. URL `http://dx.doi.org/10.1016/j.ijpvp.2007.11.013`. 110

[184] N. Barrett et al. “Microscopic work function anisotropy and surface chemistry of 316L stainless steel using photoelectron emission microscopy.” *J. Electron Spectrosc. Relat. Phenom.*, 195:117–124, 2014. ISSN 0368-2048. URL `http://dx.doi.org/10.1016/j.elspec.2014.05.015`. 110

[185] F. Fränkle. "SDS3 measurements - status and outlook.", 2017. Presentation at the 32nd KATRIN Collaboration Meeting. 111

[186] B. L. Henke, J. A. Smith, and D. T. Attwood. "0.1–10-keV x-ray-induced electron emissions from solids—Models and secondary electron measurements." *J. Appl. Phys.*, 48(5):1852–1866, 1977. URL `http://dx.doi.org/10.1063/1.323938`. 111

[187] J. Greenwood. "The correct and incorrect generation of a cosine distribution of scattered particles for Monte-Carlo modelling of vacuum systems." *Vacuum*, 67(2):217 – 222, 2002. ISSN 0042-207X. URL `http://dx.doi.org/10.1016/S0042-207X(02)00173-2`. 111

[188] K. Altenmüller et al. "Muon-induced background in the KATRIN main spectrometer." *Astropart. Phys.*, 108:40–49, 2019. ISSN 0927-6505. URL `http://dx.doi.org/10.1016/j.astropartphys.2019.01.003`. 111, 113, 117, 118, 119, 127

[189] P. Renschler. "KESS - A new Monte Carlo simulation code for low-energy electron interactions in silicon detectors." Ph.D. thesis, Karlsruher Institut für Technologie (KIT), 2011. URL `https://publikationen.bibliothek.kit.edu/1000024959`. 111

[190] G. J. Feldman and R. D. Cousins. "A Unified approach to the classical statistical analysis of small signals." *Phys. Rev.*, D57:3873–3889, 1998. URL `http://dx.doi.org/10.1103/PhysRevD.57.3873`. 115, 116, 144

[191] G. Cowan. "Statistical errors, confidence intervals and limits." In *Statistical Data Analysis*, chapter 9, pages 118–142. Oxford University Press, 1998. 116

[192] S. Agostinelli et al. "Geant4—a simulation toolkit." *Nucl. Instrum. Methods Phys. Res. A*, 506(3):250 – 303, 2003. ISSN 0168-9002. URL `http://dx.doi.org/10.1016/S0168-9002(03)01368-8`. 117, 133

[193] J. Allison et al. "Geant4 developments and applications." *IEEE Trans. Nucl. Sci.*, 53(1):270–278, 2006. ISSN 0018-9499. URL `http://dx.doi.org/10.1109/TNS.2006.869826`.

[194] —. "Recent developments in Geant4." *Nucl. Instrum. Methods Phys. Res. A*, 835:186 – 225, 2016. ISSN 0168-9002. URL `http://dx.doi.org/10.1016/j.nima.2016.06.125`. 117, 133

[195] H. Arlinghaus. "Investigation of the muon-induced secondary electron background in the KATRIN experiment." Diploma thesis, Westfälische Wilhelms-Universität Münster, 2009. URL `http://www.uni-muenster.de/Physik.KP/AGWeinheimer/Files/theses/Diplom_Henrik_Arlinghaus.pdf`. 117, 128

[196] B. Jung. "Simulation des Myon-induzierten Untergrundes und dessen Speicherwahrscheinlichkeit am KATRIN Hauptspektrometer." Diploma thesis, Karlsruher Institut für Technologie (KIT), 2011. URL `http://www.katrin.kit.edu/publikationen/dth-jung.pdf`.

[197] P. Rovedo. "Muon induced secondary electrons at the KATRIN experiment: Detector installation and setup & data analysis." Diploma thesis, Karlsruher Institut für Technologie, 2013. URL `http://www.katrin.kit.edu/publikationen/dth_rovedo.compressed.pdf`. 118

[198] R. Rink. "Measurements and Simulations with the Extended KATRIN Muon Detector System." Master thesis, Karlsruher Institut für Technologie (KIT), 2014. URL `http://www.katrin.kit.edu/publikationen/mth-rink.pdf`. 117, 120

[199] L. N. Bogdanova et al. "Cosmic muon flux at shallow depths underground." *Phys. Atom. Nucl.*, 69:1293–1298, 2006. URL `http://dx.doi.org/10.1134/S1063778806080047`. 117

[200] T. K. Gaisser, R. Engel, and E. Resconi. *Cosmic Rays and Particle Physics.* Cambridge University Press, 2016. 117

[201] J. A. Formaggio and C. J. Martoff. "Backgrounds to sensitive experiments underground." *Ann. Rev. Nucl. Part. Sci.*, 54:361–412, 2004. URL `http://dx.doi.org/10.1146/annurev.nucl.54.070103.181248`.

[202] S. Chatzidakis, S. Chrysikopoulou, and L. Tsoukalas. "Developing a cosmic ray muon sampling capability for muon tomography and monitoring applications." *Nucl. Instr. and Meth. A*, 804:33–42, 2015. ISSN 0168-9002. URL `http://dx.doi.org/10.1016/j.nima.2015.09.033`. 117

[203] "Geant4 User's Guide: For Application Developers, Section 5.3." URL `http://geant4-userdoc.web.cern.ch/geant4-userdoc/UsersGuides/ForApplicationDeveloper/html/TrackingAndPhysics/particle.html`. 118

[204] G. Drexlin. "KARMEN upgrade and prospects at ESS." *Prog. Part. Nucl. Phys.*, 40:193–202, 1998. URL `http://dx.doi.org/10.1016/S0146-6410(98)00025-8`. 118

[205] P. Rovedo. "Status of the muon detection system.", 2013. Presentation at the 24th KATRIN Collaboration Meeting. 119

[206] J. Linek. "Investigation of the muon induced background at the KATRIN main spectrometer." Master thesis, Karlsruher Institut für Technologie, 2015. URL `http://www.katrin.kit.edu/publikationen/mth-Linek.pdf`. 126

[207] T. Abrahão et al. “Cosmic-muon characterization and annual modulation measurement with Double Chooz detectors.” *J. Cosmol. Astropart. Phys.*, 1702(02):017, 2017. URL `http://dx.doi.org/10.1088/1475-7516/2017/02/017`. 127

[208] B. Flatt. “Voruntersuchungen zu den Spektrometern des KATRIN-Experiments.” Ph.D. thesis, Johannes Gutenberg-Universität Mainz, 2004. URL `http://nbn-resolving.de/urn:nbn:de:hebis:77-7154`. 131

[209] M. Lammers. “Untersuchung der Untergrundrate des KATRIN Vorspektrometers im Bereich hoher Feldstärken.” Diploma thesis, Karlsruher Institut für Technologie (KIT), 2009. 131

[210] A. R. Smith et al. “Low Background Counting at LBNL.” *Phys. Procedia*, 61:787–795, 2015. URL `https://doi.org/10.1016/j.phpro.2014.12.101`. 132

[211] World Health Organization. “International Radon Project: Survey on Radon Guidelines, Programmes and Activities.”, 2007. URL `http://www.who.int/ionizing_radiation/env/radon/IRP_Survey_on_Radon.pdf`. 133

[212] National Nuclear Data Center. “Evaluated Nuclear Structure Data Files.” URL `http://www.nndc.bnl.gov/ensdf`. 133

[213] Geant4 Collaboration. “Guide For Physics Lists, Release 10.4.”, 2017. URL `http://geant4-userdoc.web.cern.ch/geant4-userdoc/UsersGuides/PhysicsListGuide/fo/PhysicsListGuide.pdf`. 134

[214] J. Chen. “Nuclear Data Sheets for A=40.” *Nucl. Data Sheets*, 140:1–376, 2017. URL `https://doi.org/10.1016/j.nds.2017.02.001`. 134

[215] E. Browne and J. Tuli. “Nuclear data sheets for a = 60.” *Nucl. Data Sheets*, 114(12):1849 – 2022, 2013. ISSN 0090-3752. URL `https://doi.org/10.1016/j.nds.2013.11.002`. 135

[216] KATRIN collaboration. “Addendum to the Letter of Intent.” *FZKA scientific report*, 6752, 2002. 148

[217] K. Essig. “Untersuchungen zur Penningfalle zwischen den Spektrometern des KATRIN Experiments.” Diploma thesis, Rheinische Friedrich-Wilhelms-Universität Bonn, 2004. URL `http://www.uni-muenster.de/Physik.KP/AGWeinheimer/theses/Diplom_Kathrin_Essig.pdf`. 148

[218] K. Valerius. “Spectrometer-related background processes and their suppression in the KATRIN experiment.” Ph.D. thesis, Westfälische Wilhelms-Universität Münster, 2009. URL `http://nbn-resolving.de/urn:nbn:de:hbz:6-28479494638`. 148, 149, 152, 153, 168, 171, 179

[219] B. Hillen. “Untersuchung von Methoden zur Unterdrückung des Spektrometeruntergrunds beim KATRIN Experiment.” Ph.D. thesis, Westfälische Wilhelms-Universität Münster, 2011. URL `http://nbn-resolving.de/urn:nbn:de:hbz:6-22429660310`. 152, 154, 168, 171

[220] J. Behrens. “Simulations of stored electrons in the Penning trap between the KATRIN spectrometers.” Diploma thesis, Westfälische Wilhelms-Universität Münster, 2012. URL `http://www.katrin.kit.edu/publikationen/dth_Jan_Behrens_2012.pdf`. 152, 153, 154, 168, 171, 176, 179, 180

[221] M. Beck et al. “Effect of a sweeping conductive wire on electrons stored in a Penning-like trap between the KATRIN spectrometers.” *Eur. Phys. J. A*, 44(3):499–511, 2010. URL `http://dx.doi.org/10.1140/epja/i2010-10959-1`. 153

[222] T. Trippe and G. Lynch. *Particle ID numbers, decay tables, and other possible contributions of the Particle Data Group to Monte Carlo standards*. 1987. URL `http://www.osti.gov/scitech/servlets/purl/5545302`. 155

[223] R. S. Mulliken. “Report on Notation for Spectra of Diatomic Molecules.” *Phys. Rev.*, 36:611–629, 1930. URL `http://dx.doi.org/10.1103/PhysRev.36.611`. 155

[224] R. Dörner et al. “Cold Target Recoil Ion Momentum Spectroscopy: a ‘momentum microscope’ to view atomic collision dynamics.” *Phys. Rep.*, 330(2):95–192, 2000. ISSN 0370-1573. URL `http://dx.doi.org/10.1016/S0370-1573(99)00109-X`. 160

[225] Y.-S. Chung. “Charge and energy distributions of recoil ions with small E/q from 70-keV H^+ + Ar collisions.” *J. Korean Phys. Soc.*, 38(2):103–106, 2001. URL `http://www.jkps.or.kr/journal/list.html?pn=vol&TG=vol&s_v=38&s_n=2&year=2001`. 161

[226] A. Itoh and M. E. Rudd. “Recoil-ion production from zero-impact-parameter H^+-Ar and H^+-Kr collisions at 20–70 keV.” *Phys. Rev. A*, 35:66–69, 1987. URL `http://dx.doi.org/10.1103/PhysRevA.35.66`. 161

[227] A. V. Phelps. “Cross Sections and Swarm Coefficients for H^+, H_2^+, H_3^+, H, H_2, and H^- in H_2 for Energies from 0.1 eV to 10 keV.” *J. Phys. Chem. Ref. Data*, 19(3):653–675, 1990. URL `http://dx.doi.org/10.1063/1.555858`. 161, 162, 163

[228] T. Tabata and T. Shirai. “Analytic cross sections for collisions of H^+, H_2^+, H_3^+, H, H_2, and H^- with hydrogen molecules.” *At. Data Nucl. Data Tables*, 76(1):1–25, 2000. URL `http://dx.doi.org/10.1006/adnd.2000.0835`. 162, 163

[229] National Institutes for Quantum and Radiological Science and Technology. “Japanese evaluated A&M data library (JEAMDL).” URL `http://www-jt60.naka.qst.go.jp/english/JEAMDL/jeamdl2.html`. [Online; accessed 16-August-2018]. 162

[230] M. E. Rudd et al. "Cross sections for ionization of water vapor by 7–4000-keV protons." *Phys. Rev. A*, 31:492–494, 1985. URL `http://dx.doi.org/10.1103/PhysRevA.31.492`. 163, 166, 167

[231] N. Tokoro and N. Oda. "Energy and angular distributions of ejected electrons for hydrogen-cluster-ion (H_n^+ , D_n^+ , n=1-3) impacts on helium in the intermediate energy region." *J. Phys. B: At. Mol. Phys.*, 18(9):1771, 1985. URL `http://dx.doi.org/10.1088/0022-3700/18/9/012`. 163

[232] M. E. Rudd. "Differential cross sections for secondary electron production by proton impact." *Phys. Rev. A*, 38:6129–6137, 1988. URL `http://dx.doi.org/10.1103/PhysRevA.38.6129`. 163

[233] M. E. Rudd et al. "Electron production in proton collisions with atoms and molecules: energy distributions." *Rev. Mod. Phys.*, 64:441–490, 1992. URL `http://dx.doi.org/10.1103/RevModPhys.64.441`. 163, 164, 167, 168

[234] M. W. Gealy et al. "Energy and angular distributions of electrons from ion impact on atomic and molecular hydrogen. I. 20–114-keV $\mathrm{H}^+ + \mathrm{H}_2$." *Phys. Rev. A*, 51:2247–2255, 1995. URL `http://dx.doi.org/10.1103/PhysRevA.51.2247`. 164, 165, 166

[235] M. Rudd. "Secondary electrons from charged particle collisions with atoms and molecules." *Nucl. Instrum. Methods Phys. Res. B*, 56-57:162–165, 1991. ISSN 0168-583X. URL `http://dx.doi.org/10.1016/0168-583X(91)95996-Q`. 164

[236] MyAssays Ltd. "MyCurveFit." URL `https://mycurvefit.com/`. [Online; accessed 19-December-2018]. 165, 168

[237] M. E. Rudd. "Energy and angular distributions of secondary electrons from 5-100-keV-proton collisions with hydrogen and nitrogen molecules." *Phys. Rev. A*, 20:787–796, 1979. URL `http://dx.doi.org/10.1103/PhysRevA.20.787`. 165

[238] M. A. Bolorizadeh and M. E. Rudd. "Angular and energy dependence of cross sections for ejection of electrons from water vapor. II. 15–150-keV proton impact." *Phys. Rev. A*, 33:888–892, 1986. URL `http://dx.doi.org/10.1103/PhysRevA.33.888`. 167, 168

[239] J. Ahrens, B. Geveci, and C. Law. "ParaView: An End-User Tool for Large-Data Visualization." In C. D. Hansen and C. R. Johnson, editors, *Visualization Handbook*, pages 717–731. Butterworth-Heinemann, Burlington, 2005. ISBN 978-0-12-387582-2. URL `http://dx.doi.org/10.1016/B978-012387582-2/50038-1`. 169

[240] J. Dilling et al. "Penning-Trap Mass Measurements in Atomic and Nuclear Physics." *Annu. Rev. Nucl. Part. Sci.*, 68(1):45–74, 2018. URL `http://dx.doi.org/10.1146/annurev-nucl-102711-094939`. 172

[241] KATRIN Collaboration. “Suppression of Penning discharges between the KATRIN spectrometers.” In preparation. 189, 190

[242] T. Thümmler. “Status of the Spectrometer and Detector Section.”, 2017. Presentation at the 33rd KATRIN Collaboration Meeting. 198

[243] K. Jousten. “Total Pressure Vacuum Gauges.” In *Handbook of Vacuum Technology*, chapter 13, pages 565–642. John Wiley & Sons, Ltd, 2016. ISBN 9783527688265. URL `http://dx.doi.org/10.1002/9783527688265.ch13`. 203

Appendix A

MAGNETIC FIELD SETTINGS

This appendix gives a detailed overview of the magnetic field configurations used in the context of this thesis. The currents used to generate these magnetic fields are listed in Table A.1 and Table A.2. Visualizations of the asymmetric and symmetric magnetic fields are shown in Figure A.1.

The EMCS coils play an important role in the magnetic field setup by cancelling out the x and y components of the Earth's magnetic field. However, a residual magnetic field in the z-direction remains. Instead of including the Earth's magnetic field and the field from the EMCS coils, a constant magnetic field in the z-direction was simulated ($+20\,\mu\mathrm{T}$), corresponding to the uncanceled portion of the Earth's magnetic field [118]. This method was applied to all magnetic fields listed in this appendix.

For the asymmetric magnetic field configurations, certain pixel rings were excluded from the analysis. Inner rings which did not correspond to a well-defined region of the MS wall were excluded. Outer rings which showed low rates, indicative of some kind of blocking or shadowing effect, were also excluded. The effect of these cuts can be seen in Appendix B.

	SDS-I	SDS-IIa	SDS-IIb		
Setting name	A	B	C	D	E
Beamline field	100%	83.3%	100%	100%	100%
Magnet	Current (A)				
PS1	0.0	104.0	157.3	0.0	0.0
PS2	0.0	156.0	156.9	155.8	155.8
LFCS 1	100.0	−100.0	−98.0	−98.0	−98.0
LFCS 2	100.0	−100.0	−98.0	−70.0	−98.0
LFCS 3	100.0	−50.0	98.0	0.0	−98.0
LFCS 4	100.0	20.0	−70.0	0.0	−80.0
LFCS 5	100.0	20.0	0.0	30.0	−60.0
LFCS 6	100.0	50.0	0.0	60.0	−60.0
LFCS 7	100.0	60.0	0.0	60.0	−60.0
LFCS 8	100.0	60.0	0.0	60.0	−30.0
LFCS 9	100.0	40.0	0.0	60.0	0.0
LFCS 10	100.0	30.0	40.0	60.0	40.0
LFCS 11	100.0	0.0	40.0	0.0	40.0
LFCS 12	100.0	0.0	60.0	0.0	40.0
LFCS 13	100.0	0.0	60.0	0.0	40.0
LFCS 14	0.0	0.0	0.0	0.0	0.0
PCH	72.6	72.6	87.0	87.0	87.0
DET	54.6	46.8	56.2	56.2	56.2
Pixel rings	6–12	2–11	2–12	3–12	1–12
z_{min} (m)	−9.460	−3.145	−2.437	−3.876	1.316
z_{max} (m)	−7.659	−0.696	1.576	−0.988	3.698
Surface area (m^2)	39.6	75.4	123.6	88.9	73.4

Table A.1: Asymmetric magnetic field configurations used during the SDS measurements described in this thesis. The beamline field is the percentage of maximum field at which the solenoids were operated. The listed pixel rings are those which image the MS surface (area from z_{min} to z_{max}) and are included in the analysis. The surface area only includes the contribution from the MS hull (the IE system is ignored). Table adapted from [34, 177].

	SDS-IIIa			SDS-IIIb	STS-IIIa
Setting name	F	G	H	I	J
Beamline field	70%	70%	20%	70%	70%
Magnet	Current (A)				
PS1	0.0	0.0	0.0	0.0	109.3
PS2	0.0	0.0	0.0	108.8	109.0
LFCS 1	0.0	0.0	−32.3	0.0	−95.0
LFCS 2	−50.0	0.0	−3.6	−25.0	−95.0
LFCS 3	−25.0	0.0	−4.8	−25.0	−20.0
LFCS 4	0.0	0.0	−0.4	−15.0	0.0
LFCS 5	0.0	−50.0	−27.4	0.0	0.0
LFCS 6	0.0	−50.0	25.1	0.0	40.0
LFCS 7	0.0	−50.0	2.5	0.0	50.0
LFCS 8	0.0	−50.0	2.6	0.0	60.0
LFCS 9	0.0	0.0	34.9	25.0	30.0
LFCS 10	0.0	0.0	0.8	−25.0	30.0
LFCS 11	0.0	0.0	22.4	25.0	0.0
LFCS 12	30.0	0.0	10.7	50.0	0.0
LFCS 13	80.0	20.0	11.5	50.0	0.0
LFCS 14	−50.0	−20.0	10.0	0.0	0.0
PCH	60.9	60.9	17.4	60.9	60.9
DET	39.3	39.3	11.2	39.3	39.3
Pixel rings	1–12	1–11	1–11	3–12	2–10
z_{min} (m)	−2.368	2.013	−1.721	−2.853	−2.549
z_{max} (m)	1.560	4.422	0.540	1.787	−0.421
Surface area (m^2)	120.9	74.2	69.6	142.9	65.5

Table A.1: (Continued from previous page)

	SDS-IIa	SDS-IIb		SDS-IIIa	SDS-IIIb	SDS-IIIc
Setting name	K	L	M	N	O	P
Beamline field	83.3%	100%	100%	20%	70%	70%
Analyzing plane	3.8G	3.8G	3.8G	∼3.8G	3.8G	6.0G
Magnet	Current (A)					
PS1	104.0	157.0	0.0	125.7	109.3	143.0
PS2	156.0	157.0	157.0	124.9	108.7	143.0
LFCS 1	21.1	74.8	79.9	32.3	21.6	48.2
LFCS 2	25.7	9.8	36.0	3.6	21.3	49.5
LFCS 3	20.3	12.8	19.6	4.8	33.2	90.0
LFCS 4	28.4	15.1	22.1	0.4	7.4	52.3
LFCS 5	38.8	14.6	21.7	27.4	55.9	52.0
LFCS 6	27.5	27.4	34.8	25.1	32.0	27.8
LFCS 7	34.4	65.0	72.9	2.5	61.0	91.8
LFCS 8	50.7	58.9	64.3	2.7	56.8	64.7
LFCS 9	10.4	30.7	36.2	34.9	35.8	63.0
LFCS 10	44.4	20.0	26.8	0.9	36.0	13.4
LFCS 11	37.2	15.7	22.8	22.4	42.3	60.5
LFCS 12	21.0	25.3	33.3	10.7	33.9	94.1
LFCS 13	43.3	25.9	33.8	11.5	15.8	10.1
LFCS 14	50.4	50.1	49.7	10.0	45.2	1.1
PCH	72.6	87.0	87.0	17.4	60.9	60.9
DET	47.0	56.2	56.2	11.2	39.3	39.3

Table A.2: Symmetric magnetic field configurations used during the SDS measurements described in this thesis. The beamline field is the percentage of maximum field at which the solenoids were operated. Table adapted from [34, 177].

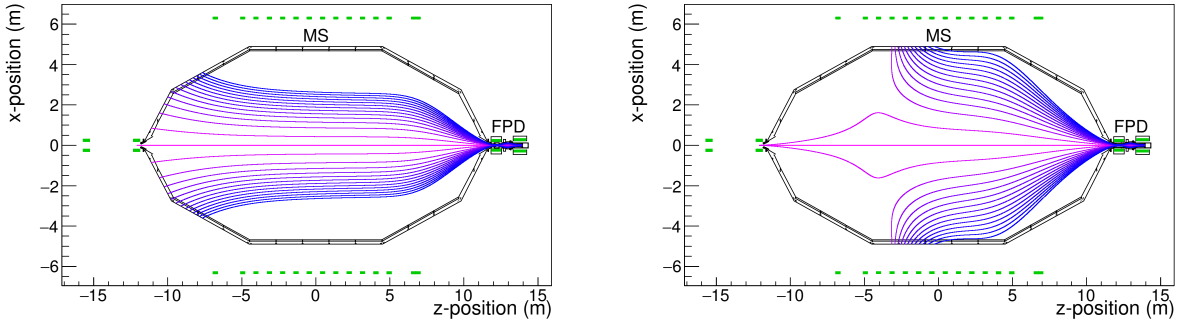

(a) Setting A

(b) Setting B

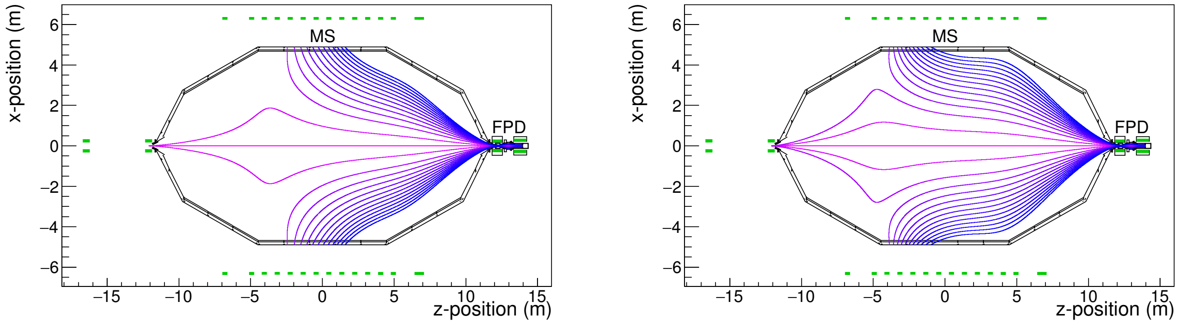

(c) Setting C

(d) Setting D

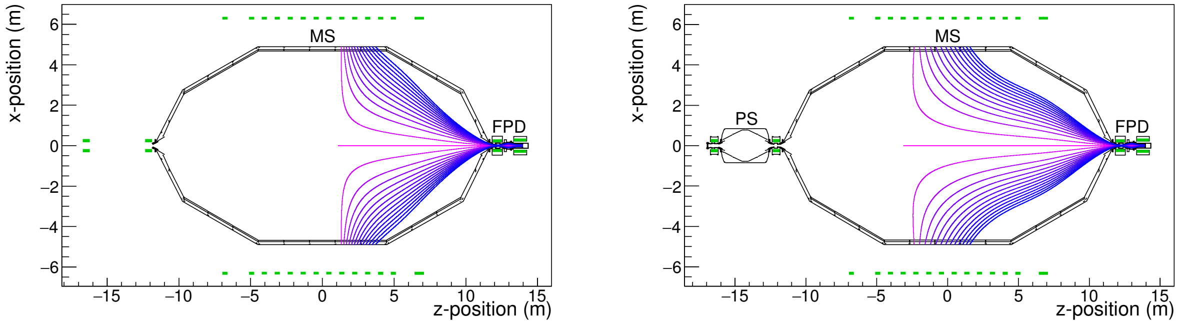

(e) Setting E

(f) Setting F

Figure A.1: Magnetic field configurations used during the SDS measurements described in this thesis. The displayed magnetic field lines intersect the FPD rings and are produced by the beamline solenoids and air-coils, shown in green.

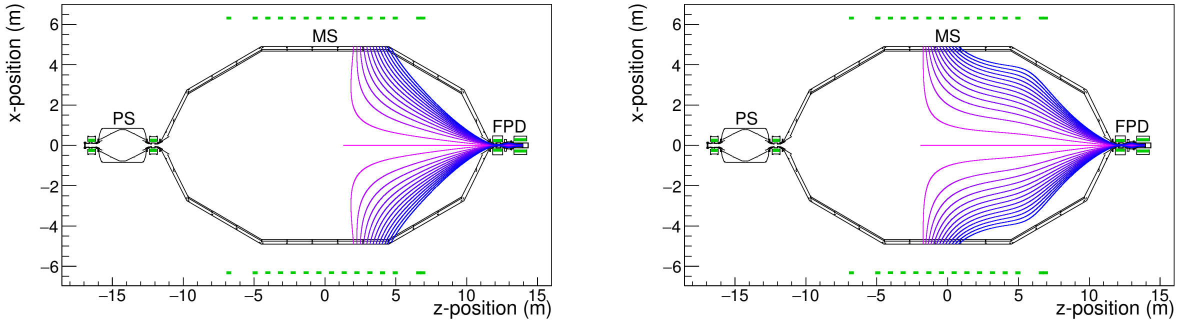

(g) Setting G (h) Setting H

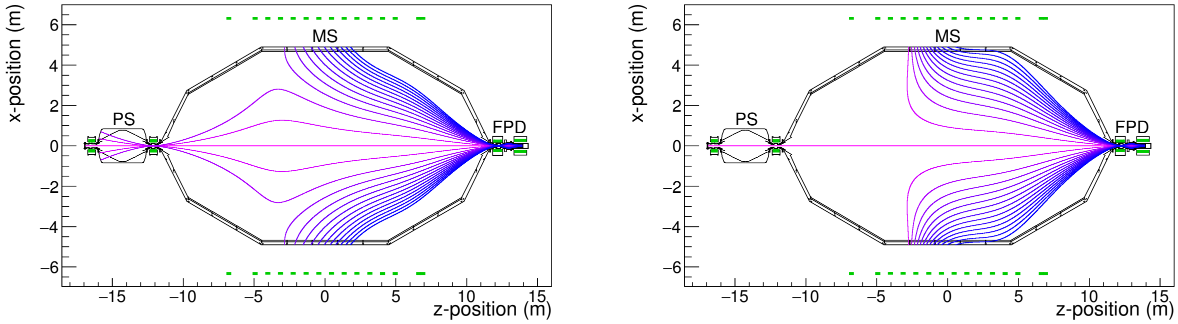

(i) Setting I (j) Setting J

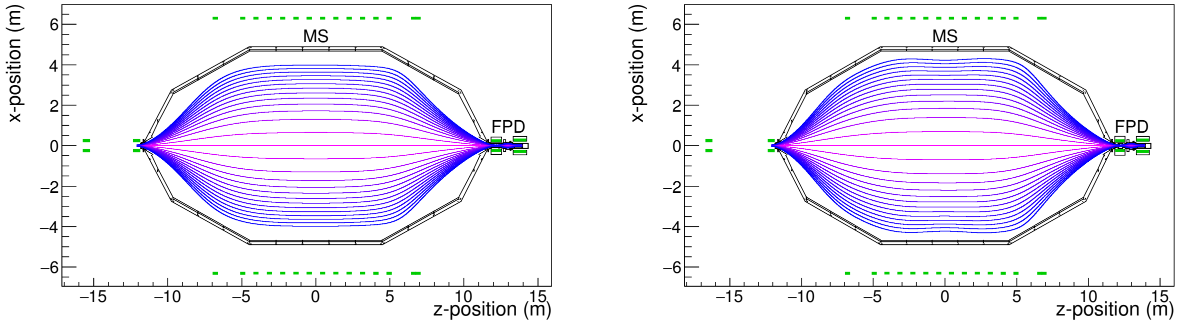

(k) Setting K (l) Setting L

Figure A.1: (Continued from previous page)

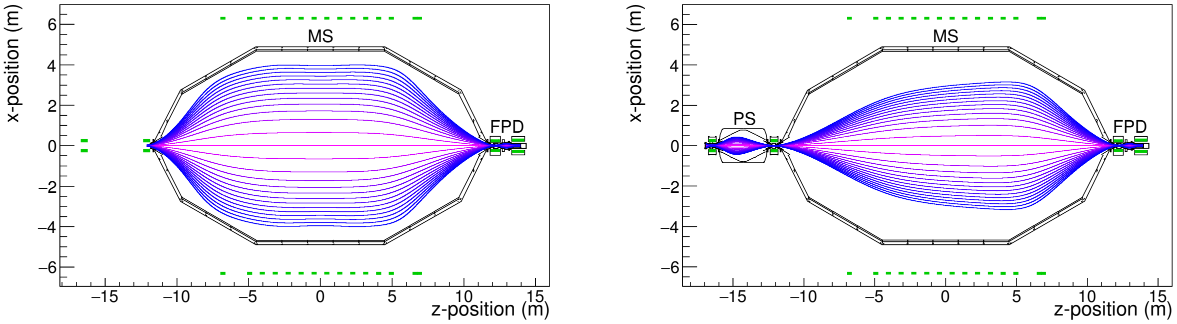

(m) Setting M (n) Setting N

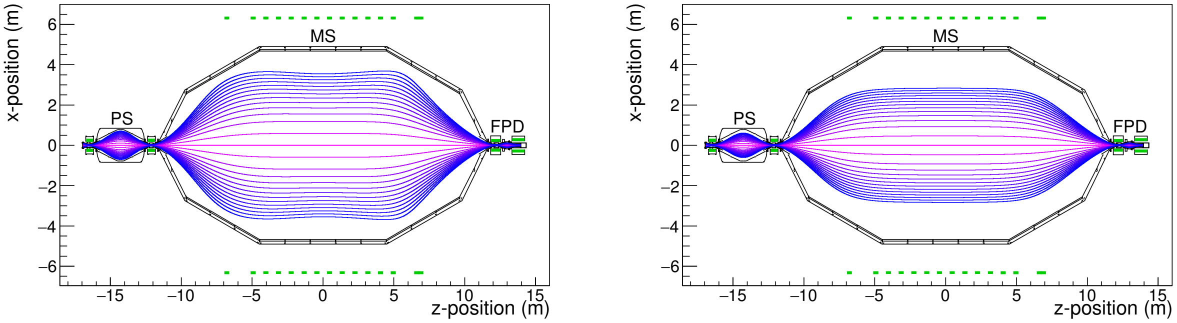

(o) Setting O (p) Setting P

Figure A.1: (Continued from previous page)

Appendix B

PIXEL CUTS AND ARRIVAL PROBABILITIES FOR SECONDARY EMISSION ANALYSIS

This appendix provides visualizations of the pixel cuts applied in the secondary electron emission rate analysis discussed in section 4.3.3. Figure B.1 shows the rate distributions across the detector wafer and arrival probability for each detector pixel ring, for each magnetic field setting. In Figure B.1f onwards, a sizable rate increase can be observed in the pixel rate distribution for the bottom-right region of the detector wafer. This rate increase is a result of the accidental contamination of the MS surface with ^{228}Th.

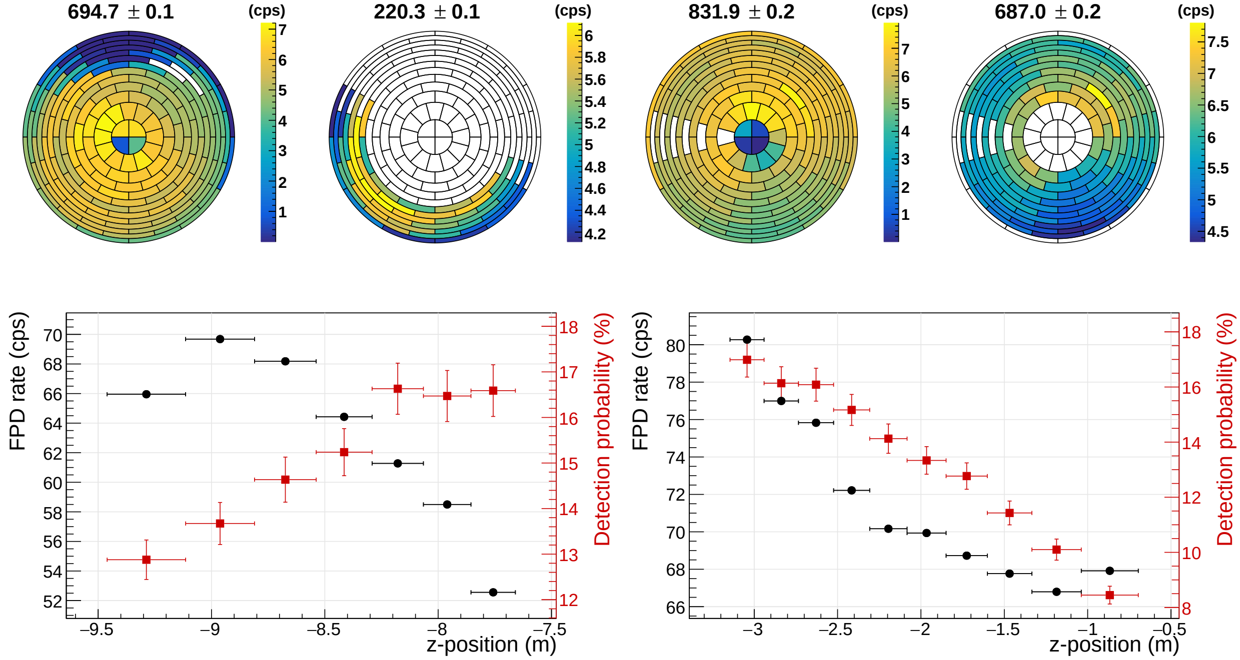

(a) Setting A

(b) Setting B

Figure B.1: Electron rates measured with asymmetric magnetic field settings. The upper left plot of each subfigure shows the rate distribution across the entire detector. The upper right plot of each subfigure shows the rate distribution after applying ring and/or pixel cuts. The value above each pixel distribution is the summed rate for the entire detector. The bottom plot of each subfigure shows the FPD rate (corrected for missing/excluded pixels) and the arrival probability (determined from simulation) as a function of axial position (i.e., detector pixel ring). The arrival probability is the average probability for an electron emitted from the MS hull to reach the FPD.

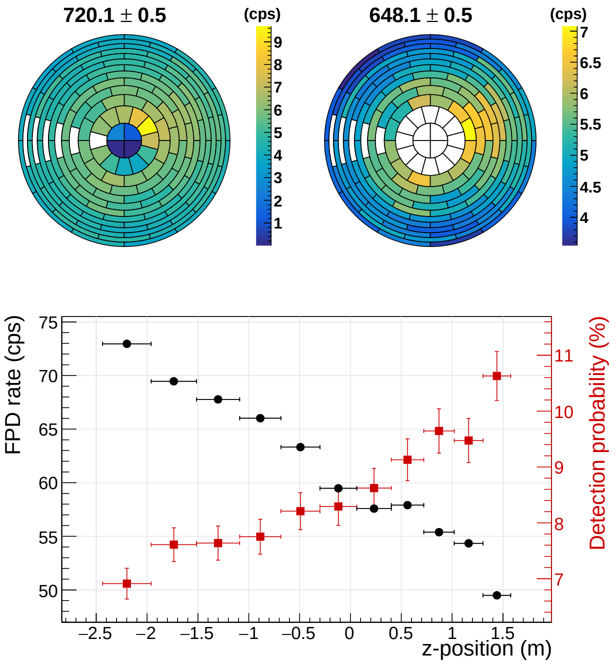

(c) Setting C

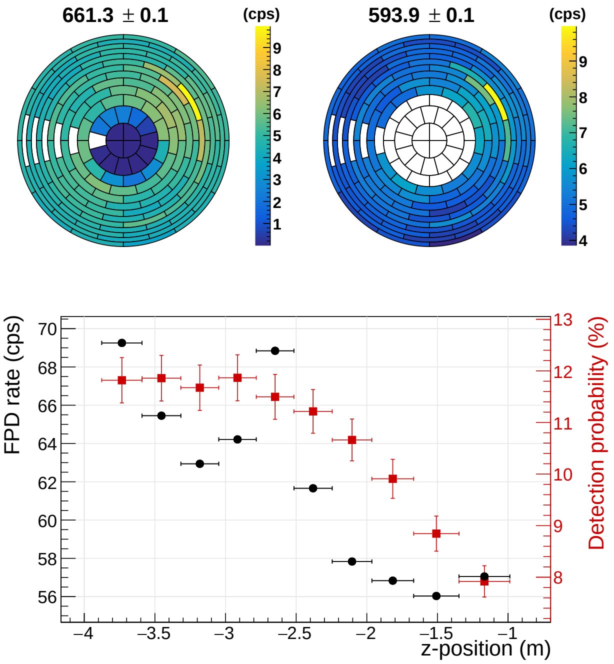

(d) Setting D

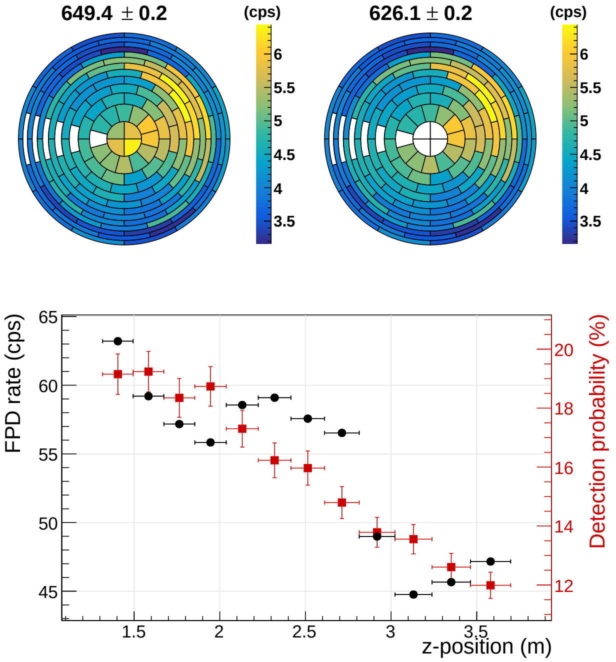

(e) Setting E

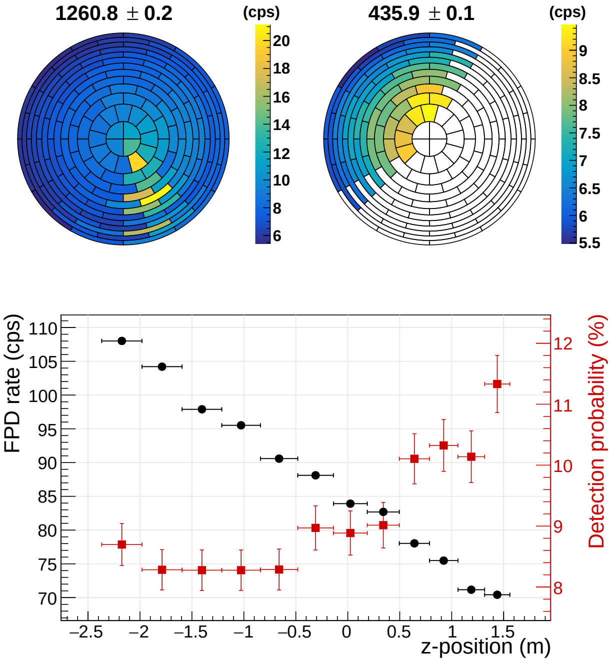

(f) Setting F

Figure B.1: (Continued from previous page)

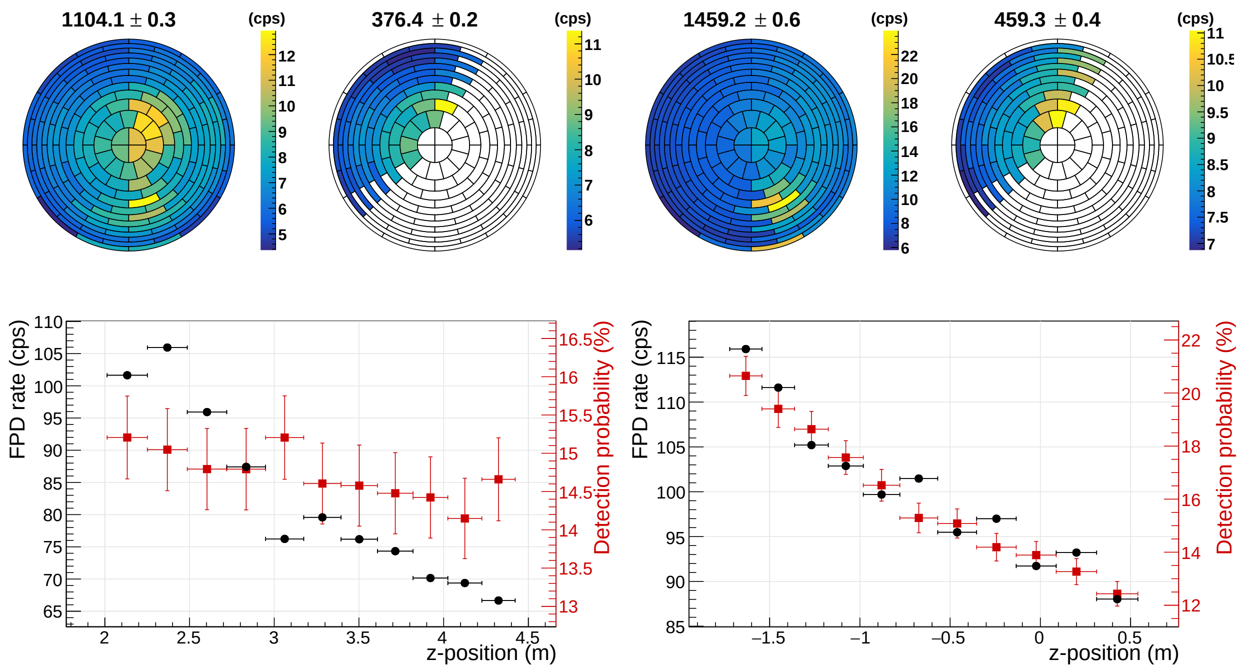

(g) Setting G

(h) Setting H

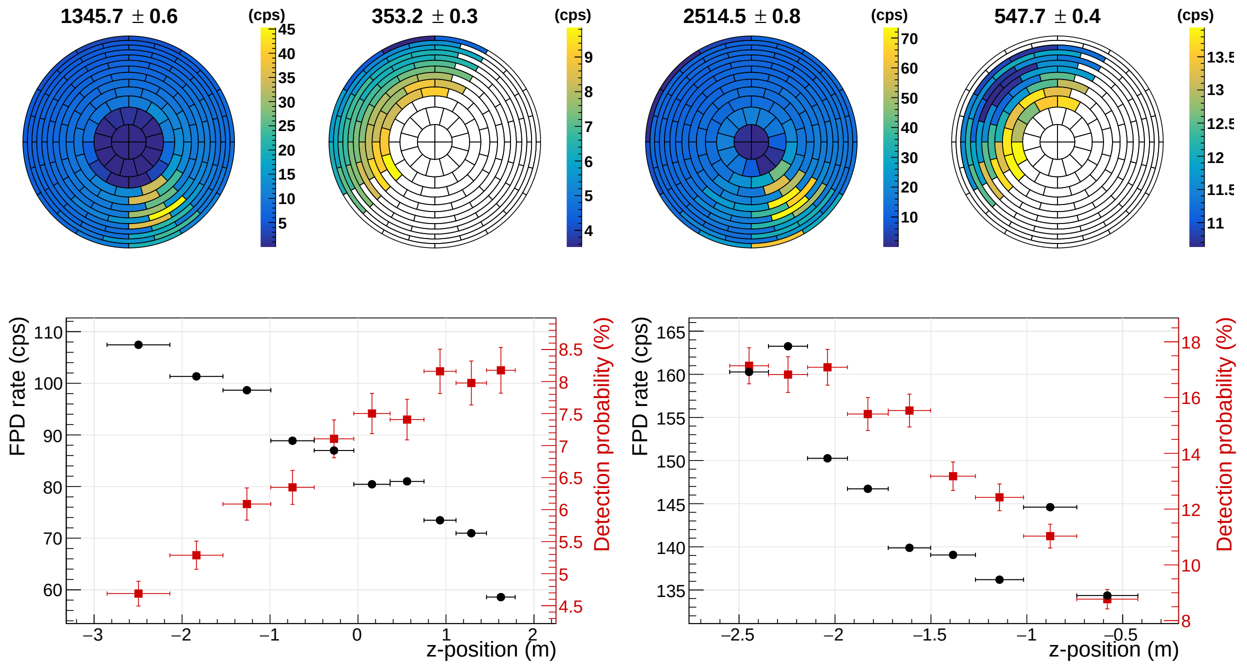

(i) Setting I

(j) Setting J

Figure B.1: (Continued from previous page)